Synthesis and modifications of shape memory alloys thin films using energetic ions

Submitted in

fulfillment of the requirements for the degree of ***Doctor of Philosophy***

by

VEERESH KUMAR

(ID No. 2013RPH9002)

Under the Supervision of

Dr. Rahul Singhal

DEPARTMENT OF PHYSICS

MALAVIYA NATIONAL INSTITUTE OF TECHNOLOGY
JAIPUR

December 2018

Dedicated to My Beloved Family

DECLARATION

I, **Veeresh Kumar**, declare that this thesis titled, "***Synthesis and modifications of shape memory alloys thin films using energetic ions***" and the work presented in it, are my own. I confirm that:

- This work was done wholly or mainly while in candidature for a research degree at this university.
- Where any part of this thesis has previously been submitted for a degree or any other qualification at this university or any other institution, this has been clearly stated.
- Where I have consulted the published work of others, this is always clearly attributed.
- Where I have quoted from the work of others, the source is always given. With the exception of such quotations, this thesis is entirely my own work.
- I have acknowledged all main sources of help.
- Where the thesis is based on work done by myself, jointly with others, I have made clear exactly what was done by others and what I have con-tributed myself.

Date: Veeresh Kumar

(ID No. 2013RPH9002)

CERTIFICATE

This is to certify that the thesis entitled "***Synthesis and Modifications of Shape Memory Alloys Thin Films Using Energetic Ions***" being submitted by Mr. Veeresh Kumar (ID No: 2013RPH9002) is a bonafide research work carried out under my supervision and guidance in fulfillment of the requirement for the award of the degree of **Doctor of Philosophy** in the Department of Physics, Malaviya National Institute of Technology, Jaipur, India. The matter embodied in this thesis is original and has not been submitted to any other University or Institute for the award of any other degree.

Place: Jaipur
Date:

Dr. Rahul Singhal
Department of Physics
Malaviya National Institute of
Technology, Jaipur

ACKNOWLEDGEMENT

Now, I am about to finish a long journey of receiving the doctorate degree. I sincerely realize that it would have never been possible without the support, help, encouragement and guidance of a number of peoples around me. From the bottom of my heart, I would sincerely thank all those who have contributed to this journey in direct or indirect ways.

First and foremost, I would like to express my sincere gratitude to my thesis supervisor, Dr. Rahul Singhal, Department of Physics, MNIT Jaipur, for his kind support, help, suggestions and valuable guidance. The discussions on problems with him have always been enlightening and enjoyable. His advice and enthusiasm towards the research work put me on the new platform of research which is more wonderful and challenging.

I wish to express my sincere gratitude to Prof. M.K. Banerjee, Department of Metallurgical and Materials Engineering and Dr. Ritu Vishnoi, Department of Physics, MNIT Jaipur for generation of initial spark of research spirit in my academic attitude and their valuable suggestions and kind support during my research work. Although, they were not my official co-supervisor; even they made significant efforts to make this thesis noteworthy. The tremendous knowledge of the subject and their passion both fundamental and experimental things motivated me to approach different ideas to discover the new things. It is a great pleasure for me to meet such knowledgeable and intellectual personalities during my Ph.D. work.

I am grateful to Prof. S.K. Sharma, (HOD), Dr. K. Sachdev, Dr. N. S. Rao, Dr. K. Awasthi, Dr. M. Kumar, Dr. K.V. Kamma, Dr. K. Lalwani, & Dr. S. Mandal, Department of Physics, MNIT Jaipur (Rajasthan) for their constant help and suggestions during my research work.

I would also like to extend my sincere thanks to Dr. D. Kanjilal (Director) and Dr. Asokan Kandasami, (Scientist), Inter University Accelerator Centre, New Delhi, for their encouragement, suggestions and fruitful discussion. During my Ph.D. experimental works at IUAC, we were always in touch and their doors were always open for discussions on both scientific and personal issues.

I am very thankful to Dr. Mukul Gupta, Scientist, UGC-DAE CSR Indore for providing the dc-sputtering and XRD characterization facilities and his many hours of fruitful discussions and last but not least hundreds of stimulative suggestions, corrections and advice. I am also very thankful to Prof. Ajay Gupta, Amity Centre for Spintronic Materials, Amity University, Noida, for his help and support in carrying out the synthesis of Ni-Ti films and suggestions regarding the targets preparation.

I would also like to express my sincere regard to Dr. Manvendra Kumar, Scientist, Nanotechnology Application Centre, University of Allahabad, Allahabad, for providing the nanoindentation characterization technique. I am grateful to Dr. Kumar for his hard work during the nanoindentation measurement. I am highly impressed with the way of thinking and approaching the problems in research that he has. Moreover, the Material Research Centre, MNIT Jaipur is also highly acknowledged for providing the research facility.

I express my deep appreciation to my friends and Colleagues Mr. Shushant Kumar Singh, Mr. Himanshu Sharma, Ms. Trupti Sharma and Ms. Pooja Sharma (Optical material Laboratory) Department of Physics, MNIT Jaipur. I also would like to acknowledge to all research scholar, Department of Physics especially Mr. Dinesh satrawla, Mr. Satyaveer Singh, Mr. Arun Vinod, Mr. Mahendra Singh, Mr. Radhe Shyam, Dr. Yogita Kumari, Mr. Lokesh Jangir, Ms. Mamta Yadav and Ms. Ranu Dhayal for their valuable suggestions and continuous help and support. Also warmest thanks to my childhood friend Mr. Chandra Mohan, Mr. Munesh Kumar, Kapil Kumar, Rajkrishan, Dharmendra Kumar and many more. All of them have been great friends and colleagues and have helped me a lot, professionally as well as personally. I hope they will continue to help me, guide me, and provide their support in future as well.

The financial supports provided by Department of Science & Technology, New Delhi in terms of DST FAST Young Scientist project (SR/FTP/PS-081/2011) is highly acknowledged.

Finally, this thesis would not have been possible without the tremendous support and encouragement from my parents and my sister who have always encouraged me to follow my dreams and happiness. I am thankful to my wife Shivani Vishnoi and my little child Akarsh, who gave me confidence with my abilities during the thesis writing and Ph.D.

Veeresh Kumar

ABSTRACT

In the thesis, binary Ni-Ti alloy thin films have been synthesized on Si substrate by dc-magnetron co-sputtering technique. Furthermore, prepared Ni-Ti thin films have been irradiated by using different ion species and fluence to enhance the various properties of Ni-Ti films for MEMS applications. Additionally, implantation of Ni-Ti films has also been done by Ag ions. The present research work reports the process parameters and mechanism of formation of the precipitate and ductile phase by using SHI irradiation technique.

A systematic investigation of the effect of Ag implantation and Au, Ag, Ni irradiation with different fluences on structural properties, lattice strain behavior, mechanical and phase transformation behavior of Ni-Ti alloy thin films has been made. X-ray diffraction measurements were performed in the θ-2θ mode. The XRD measurement reveals the formation of austenite and martensite phases in the deposited Ni-Ti films. XRD measurement of films irradiated at different fluences also shows that irradiation of Ni-Ti films at higher fluence suppresses the austenite and martensite phases. AFM and FESEM measurements show the change in surface morphology of the films with the increase in the fluence. For the films irradiated by 100 MeV Ag ions, the surface roughness increases continuously. In contrary, the surface roughness of the films irradiated by Au and Ni ions increases up to certain fluence and after that surface roughness of the films decreases. It has been observed that the small surface roughness contributed by the shallower depression exhibits smooth film surface and higher surface roughness occurs probably due to the ion irradiation induced sputtering effect. The four probe resistivity measurement of implanted and 120 MeV Au ions irradiated Ni-Ti films show the two-way transformation from cubic to rhombohedral and from rhombohedral to monoclinic phase in the films. Transformation temperature decreases with increase in the fluence. Influence of implantation/irradiation on mechanical properties is studied by nanoindentation measurement. It is found that introduction of Ag implantation in Ni-Ti alloy films lead to the mechanical properties (hardness and elastic modulus) by grain refinement; however, irradiation of Ag ions lead to mechanical behavior by precipitation formation.

Contents

Chapter 1: Introduction to Ni-Ti Shape Memory Alloy

Chapter 2: Literature Review

Chapter 3: Thin Films Deposition Methods and Characterization Techniques

Chapter 4: Synthesis of Ni-Ti Shape Memory Alloy Thin Film and Their Low Energy Ion Beam Effects (Ion Implantation)

Chapter 5: Swift Heavy Ion Irradiation Induced Modifications in Ni-Ti Shape Memory Alloy Thin Film

Chapter 6: Conclusion and Future Work

Appendix

Bio-data.

List of Tables

List of Figures

List of abbreviations

Ni-Ti	Nickel-Titanium
SME	Shape memory effect
SMAs	Shape memory alloys
AFM	Atomic Force Microscopy
RBS	Rutherford Back Scattering
FESEM	Field Emission Scanning Electron Microscopy
SHI	Swift Heavy Ion
XRD	X-ray diffraction
a_0	Lattice parameter
λ	Wavelength
β (FWHM)	Full-width half maxima
SRIM	The stopping and range of ions in matter
CPDS	Joint committee on powder diffraction standards

Chapter 1

Introduction to Ni-Ti Shape Memory Alloy

In this chapter, the properties of Ni-Ti shape memory alloy are described in detail to understand the basic phenomena associated with the shape memory behaviour and superelasticity effect. The microstructural behaviour and characteristic properties of Ni-Ti shape memory alloy are also discussed in profoundly. The objectives of the thesis problems are also stated at the end of this chapter.

1.1. Introduction: Overview of shape memory alloys

During the last several decades, smart or intelligent materials have received great interest of scientific community due to their excellent potential applications [1-3]. However, the definition of smart and intelligent materials has not been reached to the consensus yet in the scientific community. In general, a smart material is a multicomponent system consisting of three components: sensor, actuator and controller. A sensor is designed to sense external stimuli, such as temperature, stress, strain, pH, magnetic field, electric field and environmental changes. Actuator enables the system to respond in an appropriate time in a controlled manner while the controller is responsible for information processing between different components. In this way, any physical change in smart materials in response to a given stimulus is detected by the system. Once the stimulus is removed, smart materials regain their original shape [4-6]. It is well known that the varieties of smart materials are already available and being investigated significantly. These materials include shape memory alloy, magnetostrictive materials, piezoelectric materials, pH-sensing polymer and electrostrictive materials [7, 8]. Each smart or intelligent material has its one or more own characteristic properties such as viscosity, stiffness, shape, volume and temperature that can be significantly modified. Due to unique capability of these materials to respond the stimuli, these materials can be used in various applications in the field of microsensors and microactuators [9, 10]. Among the many smart/intelligent materials, shape memory alloys (SMAs) are the major elements due to their unique properties such as shape memory effect (SME), superelasticity (pseudoelasticity), high power density, good chemical resistance, high damping capacity and excellent biocompatibility [11-13]. SMAs may sense some physical changes such as heating (thermal), mechanical, electric or magnetic stimulus and give the pre-determined response. It is also possible to tune some critical parameters such as shape, natural frequency, strain, position, stiffness, damping, and other dynamical and static characteristics of materials which observed due to the environmental changes.

1.2. Nickel-Titanium (Ni-Ti) shape memory alloy

Ni-Ti shape memory alloy is the significant dominant element, due to its extraordinary properties such as shape memory effect, high damping capacity, high specific energy output and superelasticity (or pseudoelasticity). This novel alloy was discovered by Buehler et al. in 1963s at Naval Ordnance Laboratory (NOL) [14-15]. The Ni-Ti alloy also called NiTiNOL due to the equiatomic composition of Ni and Ti and its place of discovery (NiTi-Naval Ordnance Laboratory). The discovery of this alloy was considered as a breakthrough in research and the practical applications of shape memory alloys. The unique shape memory effect was first observed in AuCd alloy by Chang and Read in 1951, while the pseudoelasticity effect in this alloy was observed by Olander in 1932. Since the discovery of SMA, Ni-Ti alloy has grown as the best shape memory alloy with excellent properties among all SMAs [16, 17]. The various properties of Ni-Ti alloy are summarized in **table 1.1** as given below:

Density	6.4-6.5 g/cm^3
Melting point	1240-1300 ^{o}C
Latent Heat	24,200 J/Kg
Specific Heat	470-620J/Kg
Transformation Hysteresis	30-50 ^{o}C
Transformation range	-200 to 110 ^{o}C
Thermal conductivity (martensite)	8.6 W/m.K
Thermal conductivity (austenite)	18W/m.K
Yield Strength (austenite)	200-800MPa
Young's Modulus (austenite)	50-90 GPa
Yield Strength (martensite)	150-300MPa
Young's Modulus (martensite)	28-41GPa
Resistivity (martensite)	40-80 μ Ω cm
Resistivity (austenite)	70-110 μ Ω cm
Shape memory Strain (max.)	~8-10%

Table 1.1. Various properties of Ni-Ti SMA.

The phase transformation in Ni-Ti SMAs is quite exciting phenomena which arise with the variation in temperature and applied load. From the last three decades, the research on Ni-Ti SMA has the attracted attention of materials scientist and engineers [18]. Various approaches, experimental and theoretical are being used to study the martensite transformation and shape memory behavior. The phase transformation in crystallized Ni-Ti SMAs takes place martensitically from high-temperature austenite

(B2) phase to low-temperature martensite (B19) phase either directly or by introducing an intermediate R (rhombohedral) phase. The phenomena of intermediate transformation to R phase before achieving the martensite phase transformations has been the subject of great interest for several researchers [19-21]. The formation of R-phase in Ni-Ti SMA is observed if the alloy has prepared by some specific processing condition such as; higher Ni content, higher temperature annealing, cold working or thermal cycle, introduction of third element and the formation of precipitate. The R-phase to austenite transformation has the small temperature hysteresis in comparison to that of austenite to martensite transformation. Furthermore, the transformation from austenite to R-phase gives very small strain (~1%); whereas austenite to martensite transformation induces a very high strain (~10%). Decrease in strain by twinning plays a major role in the formation of R phase because it proceeds by nucleation and subsequent growth in parent phase [22].

1.3. Introduction to shape memory effect and superelasticity effect

1.3.1. Shape memory effect

Shape memory effect (SME) refers to the ability of a material to regain its original shape after deformation if heated above a particular temperature. The deformed state of the material is known as martensite phase which is a lower temperature phase, whereas high-temperature phase is termed as austenite phase. The phenomena of SME can be explained by schematic diagram as shown in figure given below [23]. This effect is based on the solid state diffusionless phase transformation which is also known as martensite phase transformation. Martensite transformation occurs by the nucleation and subsequent growth of martensitic plates during the quenching of austenite phase [24, 25]. This diffusionless transformation is governed by homogeneous and cooperative movement of atoms resulting in the change of the crystal structure and phases. During the diffusion process, atoms travel the distance which is less than the interatomic distance, therefore maintaining their relative positions in such a way that the material remains in solid form. All the atoms move in variants/domains resulting in the macroscopic change in shape. This magical phenomenon is responsible for shape memory and superelastic effects. Martensitic transformation is explained by a shear-like mechanism and is shown in Fig. 1.2(a) and (b) [18]. When austenite phase (B2 parent phase) (Fig. 1.2(a)) is allowed to cool below M_s (martensite start) temperature, transforms to martensite phase as demonstrated in Fig. 1.2(b).

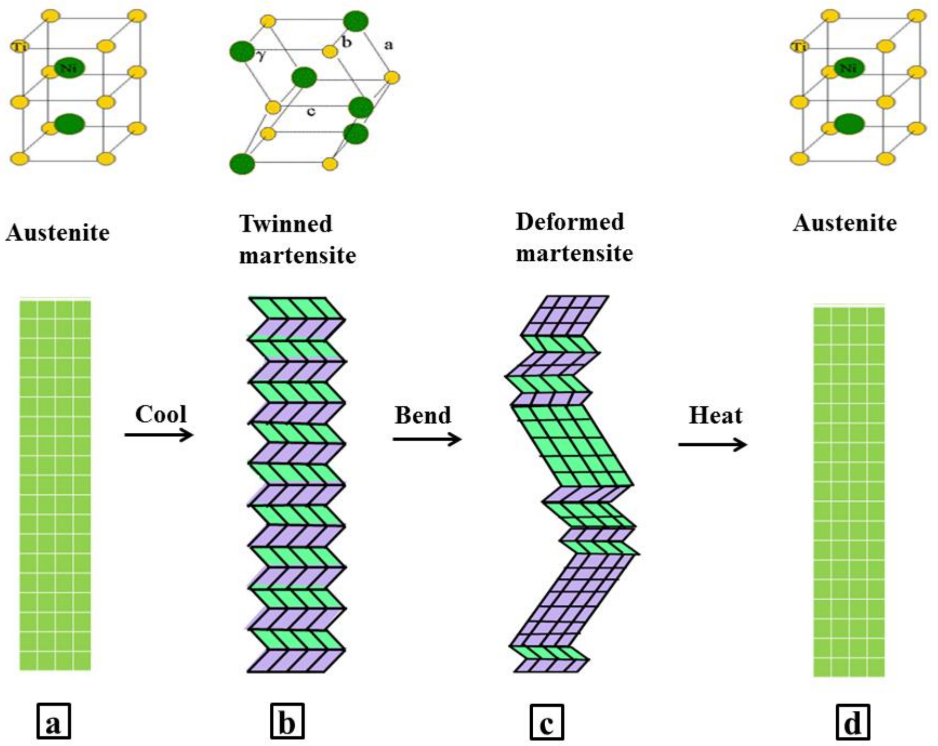

Figure 1.1. The schematic illustrations of shape memory effect phenomena.

Such transformation is known as athermal transformation since the amount of martensite phase depends only upon the temperature, not on time. In Ni-Ti shape memory alloy, martensite transformation is accompanied by twinning of martensitic variants responsible for reversible shape change and hence for SME. Martensitic twin boundaries are low energy and highly mobile which is favoring the formation of martensite plates. As the temperature is increased above A_s, martensite phase becomes unstable and reverse martensite transformation takes place (Fig. 1.2(b) to (a)). Although, if stress is imposed on the martensite phase, twin boundaries move and form a new phase as shown in Fig. 1.2 (b) to (c). The deformation of the shape of martensite in Ni-Ti shape memory alloy is governed by twin boundary motion which promotes shrinkage and coalescence of variants. In the case of Ni-Ti shape memory alloy, the maximum recoverable strain of martensite variants is about 10%. If martensite phase is heated above A_f temperature, martensite domains revert to their original parent austenite phase (Fig. 1.2(c) to (a)). During heating and cooling processes, the path of transformation does not overlap which implies that the martensite phase transformation is accompanied by transformation hysteresis (A_f - M_s).

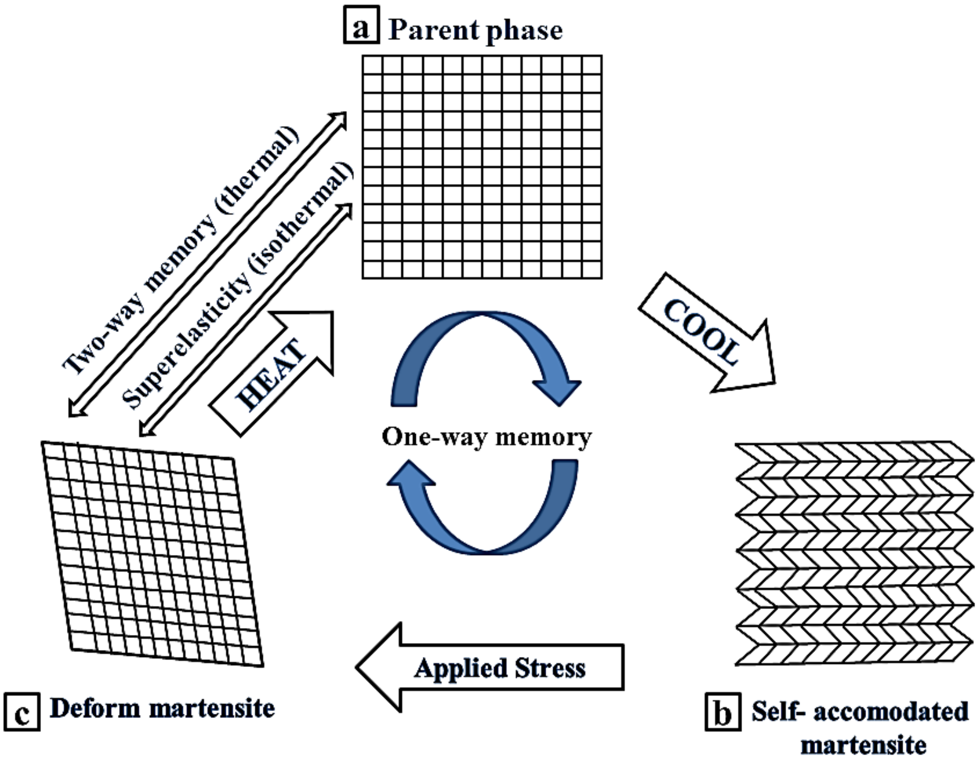

Figure 1.2. The schematic representation of the mechanism of SME and SE.

For high-frequency actuators, small hysteresis is recommended therefore a transformation with short temperature range (heating and cooling) is desirable. It is reported that R-phase shows very small thermal hysteresis. This interesting property makes this phase attractive for MEMS applications (e.g., actuators) [26].

There are two types of shape memory effect

1.3.1.1. One way shape memory effect

In one way SME, material remembers only high-temperature phase. After deformation, heating above a specific temperature brings the material into its original shape. Since in one way SME, shape change occurs during heating only, therefore, it is termed as one way SME. One-way SME occurs by very strong reversibility along with lattice correspondence during reverse phase transformation.

1.3.1.2. Two-way shape memory effect

In this phenomenon, material remembers both high and low-temperature crystal structures. Martensite and austenite both phases remember their original shape without the application of external stress unlike one way SME. This phenomenon is known as two-way SME. Two-way SME occurs by selective nucleation and growth of some martensite variants. For MEMS applications, two-way shape memory effect is highly desirable, but it is difficult to make a material able to exhibit two-way shape memory effect. Material needs rigorous and repetitive training under certain conditions to achieve this effect which is not economical. As an alternate, materials with one-way shape memory effect are used with external reset forces. It can be much easier to optimize the design about weight and size if there is no consideration should be paid to resetting spring. In order to understand the shape of martensite phase some martensite variants need to be selected. It is known that martensitic transformation is stress dependent process. During the nucleation process, the stress related variants are arranged in such a way that the elastic energy in minimized and thus the martensite phase of a particular shape is formed [27]. There are several reports concerning about, various synthesis methods to get the two-way SME such as (1) utilization of precipitation, (2) introduction of plastic deformation, (3) thermal cycle, (4) constraint aging of material and (5) aging of martensite due symmetry-conforming short-range order, etc.

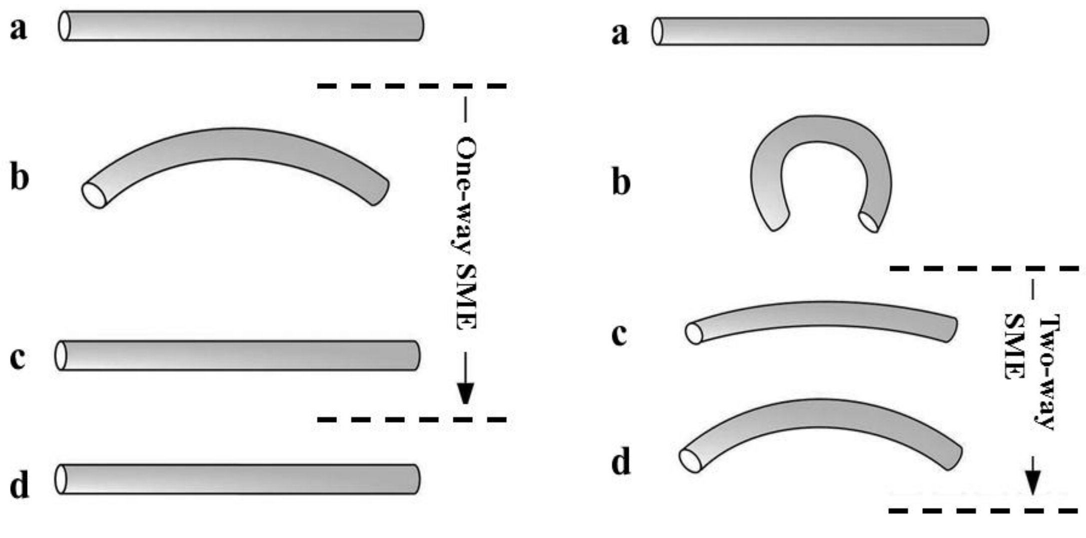

Figure 1.3. Schematic diagram illustrating the one-way and two-way SME: the phenomena are very similar: starting with martensite state (a), reversible deformation

for the one way SME or severe deformation with an irreversible amount for two way SME (b), heating the sample (c) and cooling the sample again (d).

Since freestanding thin films of Ni-Ti exhibit intrinsic two-way shape memory effect accompanied by large displacement and small actuation force. This behavior of two-way shape memory effect is attributed to the: residual stress present in films, the formation of precipitates along certain planes during the heating process, non-uniformity in composition through film thickness [28-30]. The constraint actuators can generate large actuation force between film and substrate, but the value of strain is sacrificed. On the other side, the substrate provides a biasing force giving rise two way shape memory effect [31, 32].

1.3.2. Superelasticity effect (SE)

Superelasticity (SE) or pseudoelasticity is a reversible and elastic phenomenon which occurs against an externally applied stress. This phenomenon is based on the phase transformation between the low symmetric martensite and high symmetric austenite phase of shape memory alloys [33]. Pseudoelasticity occurs at high temperature where parent phase or austenite phase is stable. At sufficiently high temperature, a good amount of mechanical strain stimulates the transformation of parent phase to the de-twinned martensite phase. Since this transformation does not depend on the temperature; rather it is induced by applied stress therefore also known as the stress-induced martensitic transformation. The applied strain is accommodated by the local shear mechanism. When the load is removed, strain is recovered back and material turns back to its original parent phase. This phenomenon is shown in figure 1.2. It is reported that Ni-Ti shape memory alloy can recover up to ~10% strain without plastic deformation [34]. This amount of recoverable strain is quite high than that obtained in the conventional metallic shape memory alloys (~0.5%) [35]. Pseudoelasticity is possible only if the total amount of deformation is accommodated by diffusionless martensite phase transformation. In case, if an excessive strain is applied, there is a chance that dislocation glide may occur, which will inhibit the reversibility of pseudoelasticity.

1.4. Ni-Ti crystal structures

The Ni-Ti SMA has three types of crystal structure (phases), austenite, martensite and rhombohedral (R-phase). The austenite and martensite are the temperature dependent structures, whereas the rhombohedral (R-phase) is a compositional dependent structure. The austenite phase is known as the parent phase of equiatomic Ni-Ti alloy and has a CsCl -type B2 cubic ordered structure with a lattice constant of 0.3015 nm and space group $Pm\bar{3}m$. The crystal arrangement of austenite phase is shown in figure 1.4 (a) [36]. Martensite is a low- temperature phase, the formation of this phase takes place by the diffusionless shearing of atoms with the same composition as parent phase and has an AuCd type (e.g., monoclinic, orthorhombic or tetragonal) crystal structure, denoted by B19’, as shown in figure 1.4 (b). In this structure, the cooperative movement of atoms is less than that the interatomic distance, unlike diffusional solid-state transformation. Through this cooperative arrangement, atoms maintain a relation, known as lattice correspondence, between high symmetrical austenite and low symmetrical martensite phase. The B19’ structure belongs to $P2_{1/m}$ space group. The lattice parameters for the monoclinic structure in equiatomic Ni-Ti (Ni50.8 at.pct.Ti tested at 50 C°) alloy was observed by Kudoh et al. and found a = 0.2898 nm, b = 0.4108 and c = 0.4646 at an angle β = 97.78° [37, 38]. The table 1.2 shows the different crystal structures of Ni-Ti SMAs [39, 40].

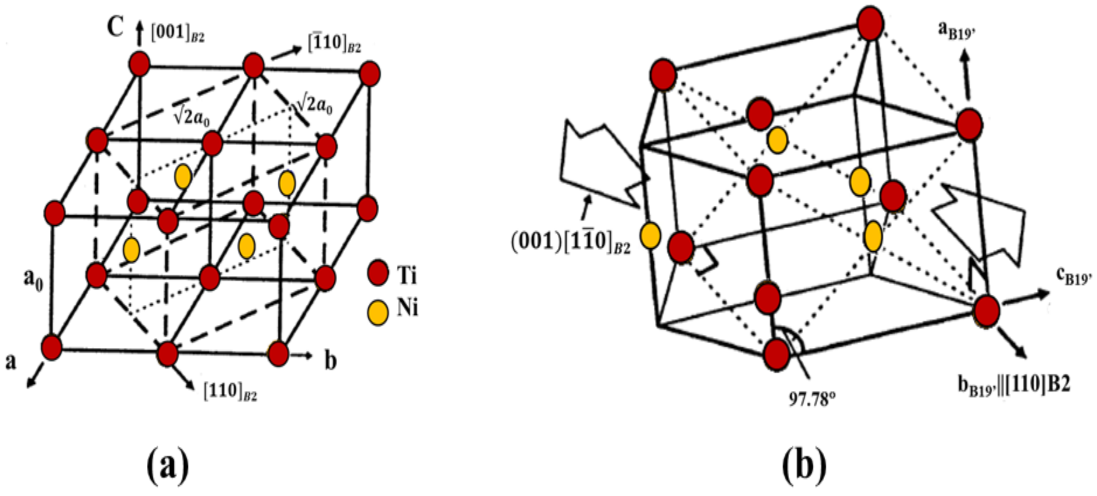

(a) (b)

Figure 1.4. Crystal structures of austenite (a) and martensite phases (b).

Ni-Ti alloy phases	**Crystal structure**	**Lattice Parameters (nm)**	**Observed in**
Martensite (B19')	Monoclinic	β = 97.78° a = 0.289 b = 0.410 c = 0.464	Alloy quenched from parent B2 phase (noticeable from surface relief)
Austenite (B2)	Cubic	A = 0.3015 nm	
Martensite (B19)	Orthorhombic	a = 0.288 b = 0.427 c = 0.451	50at.% Ti-(50at.%-X) Ni-X (where X is an third elements)
R -phase	Trigonal	a = 0.738 c = 0.532	In Ni rich Ni-Ti alloy, Thermal annealing or cold work, NiTiX (ternary alloys)

Table 1.2. Detailed information about Ni-Ti phases with their crystal structures.

Austenite phase to R phase transformation is a thermoelastic phenomenon with unique properties such as high fatigue, narrow hysteresis. Owing to these multifunctional properties, this material has become an excellent choice for practical applications [41]. The R phase transformation can be observed under certain conditions during cooling and heating cycles prior to the formation of martensite and austenite phase. The observation of intermediate R-phase between austenite and martensite phase frequently changes the transformation path as from B2→B19' into B2→R→B19'. The R-phase transformation is recognized as pre-martensite transformation. Moreover, R-phase transformation is considered as a second order phase transformation which occurs before B19' transformation by rhombohedral distortion of the austenite phase. The lattice parameter can be described by stretching the cubic B2 lattice along the <111> diagonal direction. If we consider the corner angle α, which is 90° in B2 cubic austenite, as clearly seen in figure 1.5, changes its position (90°) with the change in temperature [42].

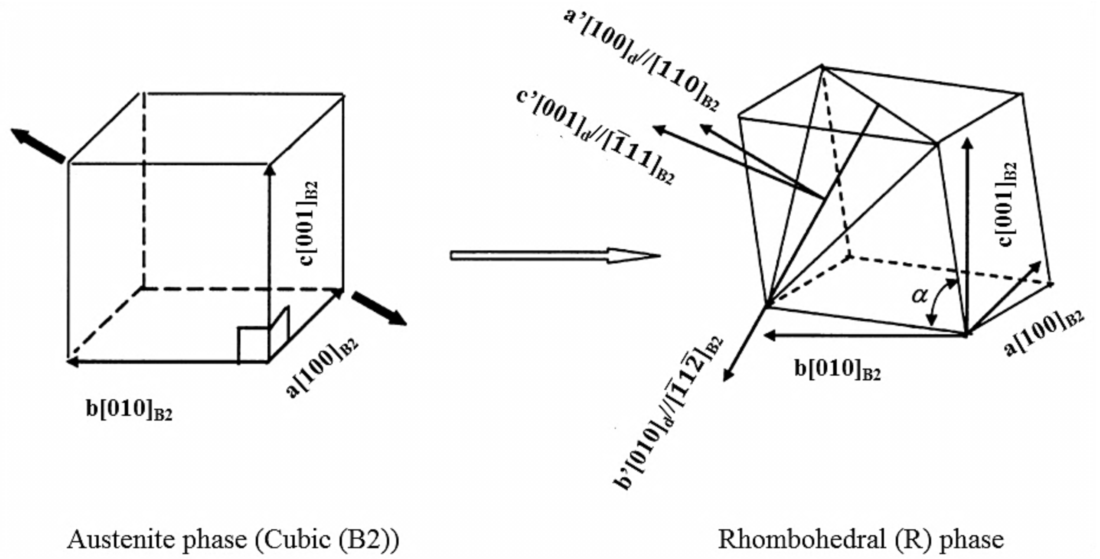
Austenite phase (Cubic (B2))

Rhombohedral (R) phase

Figure 1.5. Phase transformation from cubic austenite (B2) structure to rhombohedral (R) structure.

1.5. Ni-Ti SMA Phase diagram

A phase diagram of a metallic alloys system shows the graphical representation of the equilibrium conditions of different phases. Phase diagram of the alloys consists distinct phase boundaries which separate the different phases from each other. For a binary alloy system, the concentration of the element is a very important factor and is always represented along X-axis. Another most widely used variable is the temperature, which is represented along the Y-axis.

The phase transformation in Ni-Ti SMAs system is a very interesting phenomenon; shape memory properties of this alloy can be enhanced by tuning phase transformations temperature. The SE and SME take place in nearly equiatomic Ni-Ti alloy with Ni concentration in the range of 45 to 50 atomic%. Figure 1.6 shows the phase diagram of Ni-Ti binary alloy [3]. From phase diagram, it is clear that the solubility in Ni-Ti alloys is gradual changes with temperature in Ni-rich side whereas in the Ti side presence of a steep solvus boundary is observed. A small variation in the stoichiometry of Ni-Ti alloys can significantly lead to the formation of precipitation of the second phase. It was observed that diffusion less phase transformation takes place in Ni-rich Ni-Ti alloy, during slow cooling or aging from high temperature. In Ni-rich side, Ni-Ti alloy follows the following precipitation sequence, B2$\rightarrow$$Ni_4Ti_3$$\rightarrow$-$Ni_3Ti_2$$\rightarrow$$Ni_3Ti$ as reported in reference [36]. In these phases, the Ni_4Ti_3 phase is a metastable phase, which is observed at low temperature and short aging time, whereas Ni_3Ti phase is known as the stable precipitation phase. The existence of Ni_4Ti_3 precipitation phase in the alloy is primarily important to increase the shape memory characteristic properties and strength of material. The inset of phase diagram (Fig.1.6) shows the different equilibrium metastable phases between Ni-Ti and Ti_3Ni_4.

Furthermore, the mechanism of formation of precipitates in Ni-Ti alloys is extremely important to adjust the transformation temperatures for practical applications. It is known that martensite transformation temperature is very sensitive to the alloys composition, as 1 at. % variation in the composition of alloys changes the martensite transformation temperature more than 100 K [12].

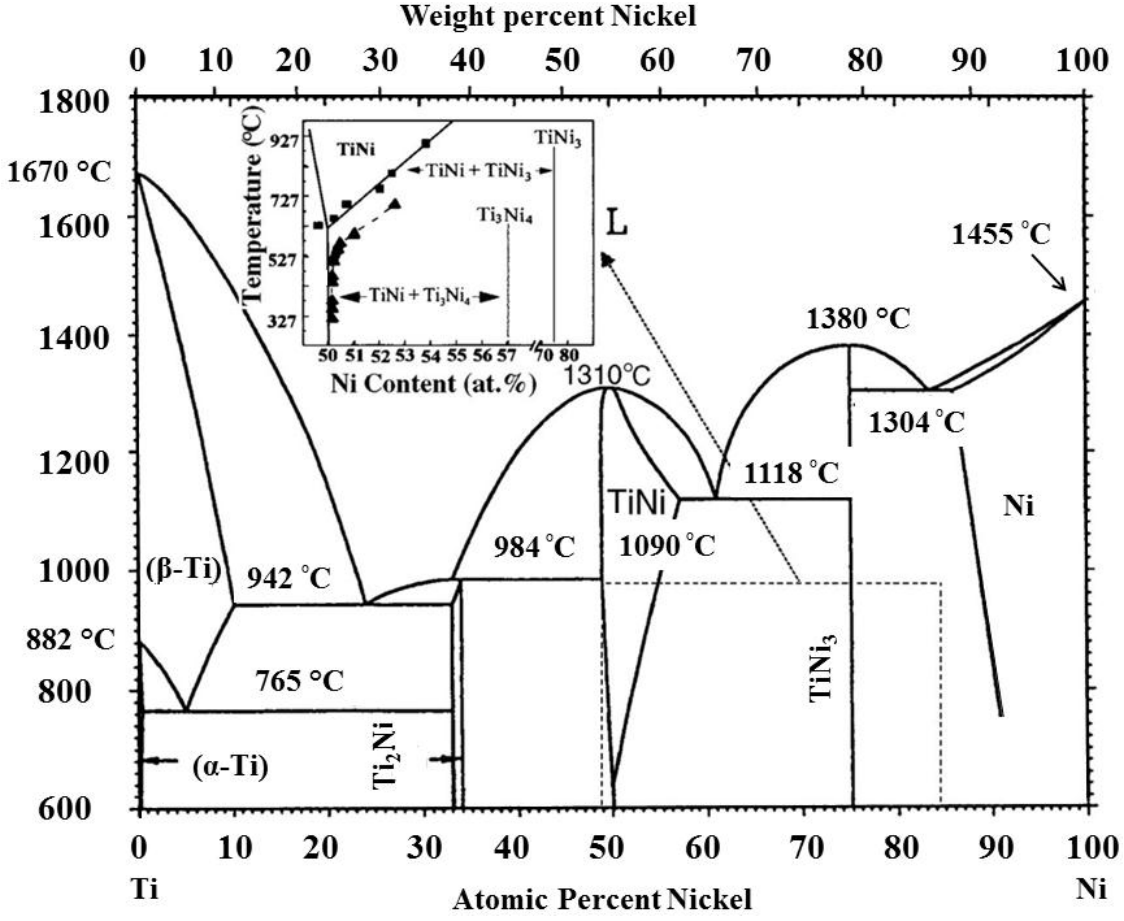

Figure 1.6. Ni-Ti binary alloy phase diagram.

For the practical applications observation of, metastable equilibrium phases in between Ni-Ti and Ni_4Ti_3 is of very much important. Precipitation hardening in bulk Ni-Ti SMA on Ti-rich side cannot be used since the solubility limit is found to be almost vertical and manipulation of Ti_2Ni phase cannot be simply used to improve the properties of SMAs. However, this situation changes in sputtered deposited Ti-rich Ni-Ti films crystallized via the amorphous state, which is a non-equilibrium process. The microstructure of the film is entirely different from that of the bulk alloy.

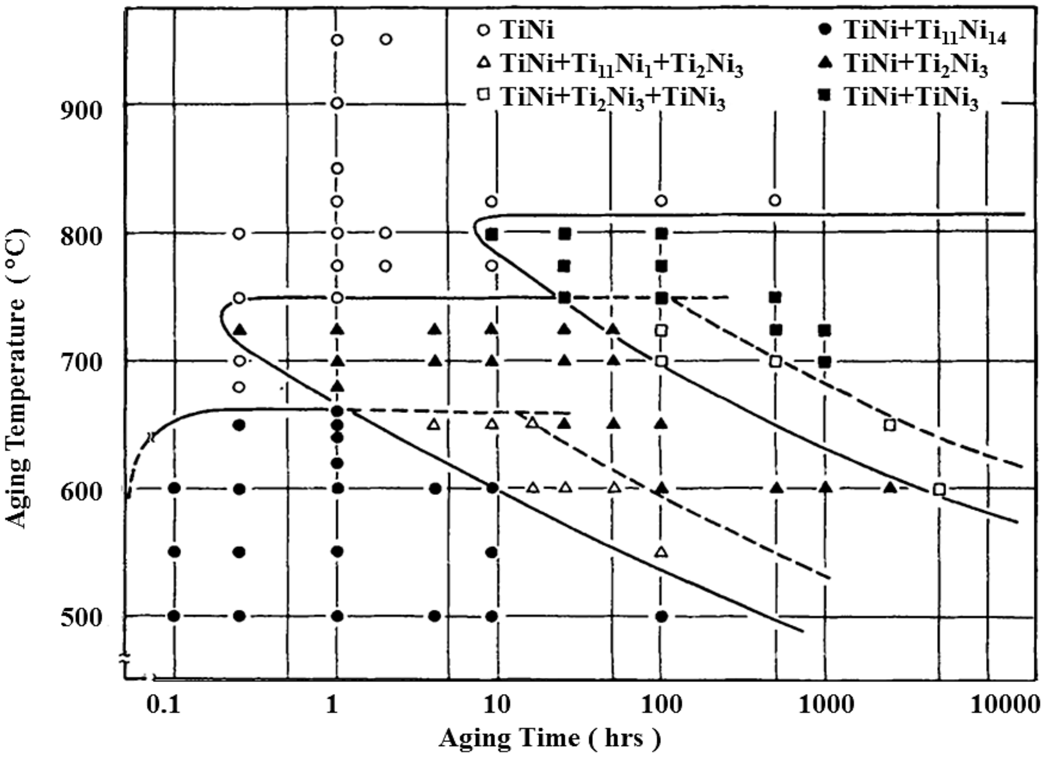

Figure 1.7. The schematic representation of TTT diagram for aging behavior in Ni-rich Ni-Ti alloys.

Nishida et al. [36] investigated the effect of composition on precipitation process in Ni-rich Ni-Ti alloys based on aging time and temperature. The observed TTT (Time-temperature-phase transformation) diagram for different compositions of the alloy is presented in figure 1.7. The TTT diagram shows that at the short aging time and lower aging temperature, Ni_4Ti_3 phase is observed, while at longer aging time and higher aging temperature, the Ni_3Ti phase appears and at an intermediate aging time and temperature Ni_3Ti_2 phase is formed. Further, Nunomura et al. [43] studied the phase relation and microstructure of SMAs based on Ni_3Ti, Ni_3Nb and Ni_3Al pseudo-ternary alloy. Later, Hara et al. [41] performed a study on Ni_3Ti_2 precipitate phase to determine the crystal structure and phase transformation characteristic from the crystallographic point of view. The crystal orientation of both low and high-temperature phases and twinning of low-temperature phase was also investigated in detail. High-temperature phase exhibit a tetragonal crystal structure with Pd_3Ti_2 type symmetry and space: group14/mmm. The values of lattice parameters were determined by using the Rietveld method and found: a = 0.3095(38) and c = 1.3585(169) nm. The crystal structure of low-temperature phase is orthorhombic with Al_3Os_2 type symmetry and space group: Bbmm. The lattice parameters for this structure were obtained: a = 0.4398(49), b = 0.4370(48) and c = 1.3544(150) nm, respectively.

1.6. Phase transformation in Ni-Ti alloy

The most important aspect of this alloy is related to the variation in characteristic temperature at which the SMA transformed from one crystal structure to another. There are six different characteristic temperatures related to the phase transformation. These transformation temperatures can be obtained by measuring the physical property such as electrical resistivity as a function of temperature. The typical characteristic temperatures of phase transformation are given as follows:

- A_s: austenite start temperature (during heating);
- A_f: austenite finish temperature (temperature at which the martensite phase is complete transforms to austenite);
- M_s: martensite start temperature (during cooling);
- M_f: martensite finish temperature (temperature where the austenite phase complete transforms to martensite phase);
- $R_{s,}$: R-phase start temperature (during cooling);
- $R_{f,}$: R-phase finish temperature (during cooling);
- R_s': R-phase start temperature (during heating);
- R_f': R-phase final temperature (during heating).

The transformation temperatures of SMAs strongly depend upon the elemental composition, heat treatment and alloying process, etc. [12]. Furthermore, stress generated in the Ni-Ti system alloy also affects the phase transformation properties. The effective way to control the transformation temperature is changing the composition of the alloy. In several cases, 0.1 at.pct change in composition, affects transformation temperatures more than 10 °C. In equiatomic Ni-Ti SMA the transformation temperature is very sensitive to the Ni composition since Ni-rich side has some solubility limit at high temperature. Continuously, increase in Ni concentration can cause the drastic decrease in transformation temperature. Since on the Ti-rich side, there is no such dependency of transformation temperature was found, most probably because in Ni-Ti phase diagram the solubility of Ti side is almost vertical [44].

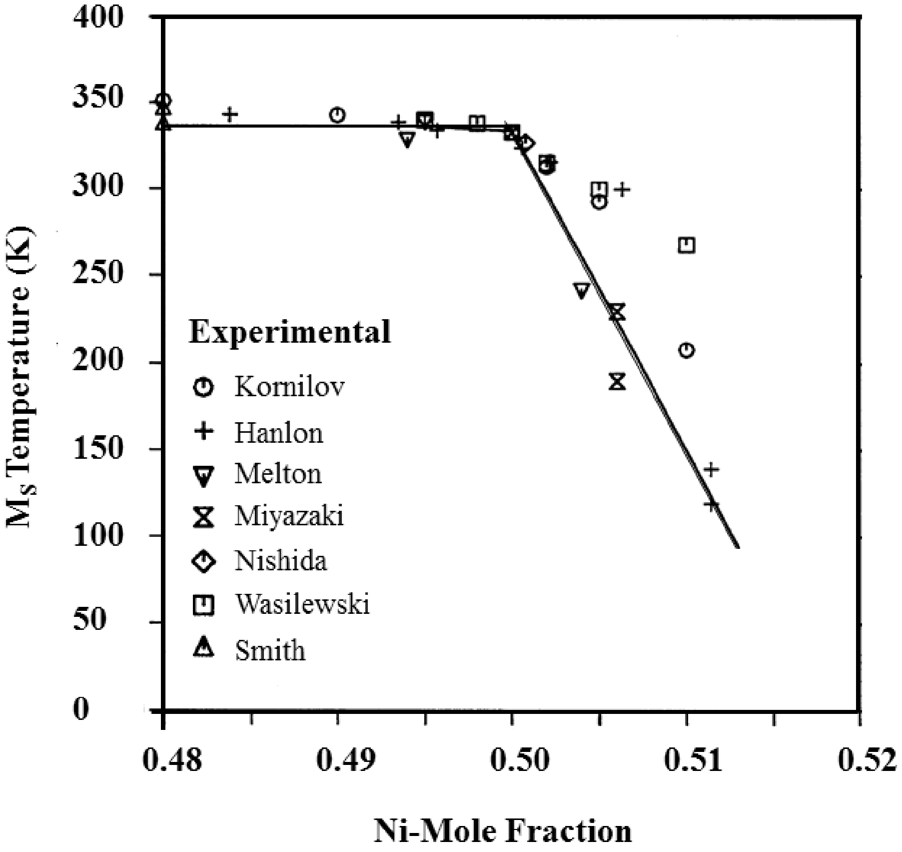

Figure 1.8. Martensite temperature (M_S) as function of Ni composition for binary Ni-Ti SMA. The data has been plotted for different authors using different symbols, and solid line represents thermodynamic calculation.

1.7. Ni-Ti thin films

A large number of concepts on bulk Ni-Ti SMAs have been implemented successfully. However, for some special applications (such as robotic manipulators and temperature dependent switching) bulk Ni-Ti has very less attention due to its slow response during heating and cooling cycles [45, 46]. Therefore, Ni-Ti thin films or special thin wires are explored for their possible use in miniature robotics and MEMS system at micro to millimeter scale. In the form of thin film, Ni-Ti SMAs have received great interest of scientific community due to their excellent properties for MEMS applications, such as high power density, high power to weight ratio, good chemical resistance, pseudoelasticity (or superelasticity) and excellent biocompatibility [47, 48]. The work output per unit volume for SMA thin film is quite large in comparison to other micro-actuation mechanisms. Phase transformation in Ni-Ti SMA thin film is accompanied by significant changes in physical, electrical, chemical and mechanical properties, such as shape recovery, thermal expansion coefficient, surface roughness, electrical resistivity, dielectric constant, yield stress, young modulus, hardness and damping [49-51]. These changes can be fully utilized in design and fabrication of micropumps, micro-switch and micro-grippers, etc. for MEMS applications. The SMA materials also posses higher sensitivity for the environmental changes, e.g., stress, or thermal and are ideal for the microsensors applications [52].

1.8. Importance of Ni-Ti thin films

Nowadays, the demand for micromachines has increased significantly in various fields such as biotechnology, aerospace, nanotechnology, micro-electro-mechanical systems (MEMS), industries including various biomedical applications [53-55]. Thin films of Ni-Ti alloy can be used to produce such microactuators because of their unique properties such as large stress sustainability without deforming permanently [56], low voltage controllability, biocompatibility and shape memory behavior, etc. Also, the work output per unit volume of these films is quite large as compared to other micro-actuation mechanisms [57]. Recently, NiTiCu based ultralow-fatigue SMA films containing Ti_2Cu precipitates for 10 million transformation cycles were reported for artificial heart valve or elastocaloric cooling [58]. These unique properties in Ni-Ti films are due to their distinct crystalline structure (B2 at high temperature exhibiting austenite phase and monoclinic at low temperature exhibiting martensite phase) and phase transformation behavior. The phase transformation is accompanied by significant changes in the structural, electrical, mechanical and chemical properties of films, thus controlling the design and fabrication of micro-actuators out of several methods one of the effective way to produce phase transformation in shape memory alloys is swift heavy ion irradiation.

The ion irradiation has the unique capability to enhance the properties of the shape memory alloys.

1.9. Modification of material properties induced by swift heavy ion irradiation (SHI)

The development of advanced materials with novel properties without compromising with their bulk properties is one of the main challenges for the scientific and technological revolution. Advanced technological applications demand tailor of shape, size distribution, and surfaces and interfaces along with excellent mechanical and physical properties. SHI has attracted the attention of research community for tuning the materials properties which would be a rapid advancement in the field of materials science. At present, ion beam technology has grown as a versatile technology for the development of miniaturized devices which require basic fundamental understanding about the interaction between ions and matter [59-63]. Deposition of localized energy density into a specified volume is the main advantage of SHI over thermal equilibrium process. Furthermore, the study of the interaction between ions and matter establishes an interdisciplinary connection between condensed and atomic physics.

As the beam of energetic ions interacts with the materials, loses its energy into the materials and significantly modifies the various properties of materials. The modifications of materials properties depend upon the amount of energy deposited into the materials by swift heavy ions; therefore a desired modification in material property can be achieved by choosing the particular beam and fluence, which is not possible by using any other technique [64-65]. However, energy deposited by SHI is much more localized, and process of deposition of energy into the material is far from equilibrium condition. The controlled deposition with spatial selectivity of energy and fluence is the special feature of SHI beam.

Nowadays, the swift heavy ions technique has been emerged out as a versatile technique for tailoring the materials properties in order to make them multifunctional. SHI technique is capable to tailor mechanical, magnetic, structural, optical, thermodynamical and chemical properties of a material. When the swift heavy ions impart on the material, a number of phenomena can occur such as plastic deformation, epitaxial crystallization, mixing of materials, amorphization, sputtering, and nanophase & nanostructure formation in the material, etc. [66-69]. The methods employing ion beams cover a huge range of ion species, energy and fluence. Use of these methods in combination with other materials preparation technique allows the production of multifunctional materials with extra processing degree of freedom.

When the energetic ions pass through the material, lose their energy into the material mainly through collision either with the nucleus of target material or electron of the target [70-73]. There are two types of energy loss of energetic ions into the material; one is nuclear energy loss and other is electronic energy loss. In nuclear energy loss, the velocity of the incident ions is relatively as minute as compared with Bohr velocity of orbital electrons. Hence, incident ions hit the material nuclei elastically and energy of the ions is directly transferred to nuclei, which results in displacement of material atoms. This energy loss is dominant at low energy range (energy< MeV) and is very useful for ion implantation and mixing of materials in semiconductor industries [74]. While in electronic energy loss, the velocity of incident ions is higher than the Bohr velocity of orbital electron and is dominant in the higher energy range (energy in the range of few MeV to few GeV).

When the electronic energy charge ions pass through the material, a large amount of energy is deposited in a confined volume [61]. Due to this large amount of electronic energy deposition, material goes into molten state for very short time duration (~few pico-second) and generates a cylindrical track along their path termed as ion track. The motivation of the present thesis work is based on the ion beam induced modifications of Ni-Ti shape memory alloy thin films for various applications for MEMS device. Chapter 2 gives the glimpse of the work performed on SHI irradiation induced modifications in SMAs materials; which inspired me to formulate the thesis problem.

1.10. Objectives of the thesis

Ni-Ti thin films are important for the application of SMA in the emerging field of micro devices such as MEMS, which demands high quality of SMA thin films deposited on silicon substrate. In addition to the growth of SMA thin films, precise control on properties of SMA is essential for various applications. The main focus of the present research is to acquire precise control on the various properties of Ni-Ti thin films associated with shape memory behavior by using low energy and high energy ion beam; due to its unique capability to modify the materials at the nanometre scale. After considering all issues given in the previous section, the main objectives of my thesis are formulated as;

- The optimization of deposition parameters of Ni-Ti films to get the highly crystalline films on Si substrate.
- To deposit Ni-Ti thin films with both phases (low-temperature martensite and high-temperature austenite) to understand the interaction mechanism of SHI ion irradiation on both phases.
- To tailor the structural, electrical and mechanical properties of Ni-Ti films by SHI irradiation for MEMS applications.
- To understand the strengthening mechanism of Ni-Ti films by using ion implantation and irradiation.
- To modify the Ni-Ti film surface by ion-beam irradiation and to investigate its effect on mechanical properties for MEMS application.

Chapter 2

Literature Review

This chapter plan to offer the background for the research work presented in this thesis. The subsequent part of this chapter deals with the literature review carried out for investigation of various properties of binary Ni-Ti alloy for MEMS. Various modification methods available in the literature are discussed. Special attention has been given to the effect of swift heavy ion irradiation in Ni-Ti alloy films. Moreover, the effect of ion implantation on Ni-Ti alloy thin films is also explained profoundly. The effect of metallic and non-metallic ions on phase transformation behaviour and various properties are also discussed. The last section of this chapter deals with the identification of some grey areas (research gap) related to the research on Ni-Ti alloy thin films.

2.1. Introduction

Intermetallic binary alloys are promising materials with superior shape memory properties which make them a suitable candidate for various applications such as robotics, medicine, electronics, telecommunication and optics, etc. [75, 76]. The shape memory behavior in these alloys is governed by thermoelastic martensitic transformation. During thermoelastic martensitic transformation, highly symmetric cubic parent phase is converted into low symmetric monoclinic martensite phase. It is interesting to note that the martensite phase can exist in twenty-four type of variants with the significant difference in their geometry. Each variant has its characteristic geometric configuration [77]. After the deformation, martensite phase converts into that variant which has the lowest internal energy for stabilization. Upon heating above A_f temperature, atoms of the deformed martensite phase re-occupy their original position giving the shape memory effect.

Over the past few years, thin films of Ni-Ti alloy have attracted much attention of research community due to their increasing demand for MEMS applications [78, 79]. It has been reported that the transformation from austenite to martensite phase takes place not only directly but also by an intermediate phase known as R-phase. This R-phase transformation is accompanied by very small thermal hysteresis compared to direct transformation (austenite to martensite), which makes it very useful for actuator applications such as microsensors and microswitches [80, 81]. The martensite transformation can be triggered by changes the temperature, stress or external magnetic field. Both the stress and thermally induced martensitic transformations have diverse practical applications.

Although, binary Ni-Ti thin films possess excellent superelasticity, shape memory behavior, biocompatibility, and resistance against corrosion and are widely being used in the industry. Even though, the tribological properties of thin films are very inferior. To improve the tribological properties of Ni-Ti films, surface treatments are used; which consequently enhance the mechanical and tribological properties. Therefore, surface modifications of Ni-Ti thin films could be more advantageous to enhance the various properties. There are several reports indicating the improvement in surface properties of Ni-Ti thin films by surface treatments [82-86]. In general, the surface modification is achieved by SHI irradiation and ion implantation methods. These methods are precise enough to alter the surface structure of thin films including their microstructure, chemical composition, and physical properties.

2.2. Studies based on the investigation of various properties of Ni-Ti SMA thin films for MEMS.

[1] **Kumar et al.** [87] synthesized Ni-Ti thin films by dc-sputtering technique and studied the variation in phase transformation path as a function of film thickness. The XRD results reveal the presence of austenitic (1 1 0) phase in the films from the beginning of the deposition, which could be due to the minimum surface energy of bcc plane. The reflection (211) corresponding to austenite structure was observed in films having the thickness greater than 2.3 μm due to the release of strain energy at higher thickness. The electrical measurement results infer that the film with thickness ≤300 nm experiences resistance force due to the inter diffusion between substrate and film and small grain size. The films with higher thickness (634 nm and 1.1 μm) exhibit the constrained martensite to austenite phase transformation via intermediate R phase followed by a small temperature hysteresis width, which makes the material suitable for the actuator application. The film with thickness 2.3 μm shows the complete phase transformation.

In another study, the same author investigated the effects of grain size on structural, mechanical and electrical properties of Ni-Ti films deposited at three different temperatures 350, 450, 550, and 650 °C [88]. From this study, it was observed that substrate temperature play a significant role on surface morphology, structural and phase transformation behavior of Ni-Ti SMA. The crystallinity and grain size increased with increasing the substrate temperature. The low hardness and depth recovery ratio were observed in all the films deposited at different substrate temperatures. This was due to the dominance of martensite phase at room temperature. The resistance versus temperature curves represents an increase in phase transformation behavior with increase the grain size. The films deposited at a temperature of 350 °C show the negative temperature coefficient of resistance and non-metallic behavior. But, the film deposited at substrate temperature ≥ 350 °C showed the metallic behavior.

[2] The effect of film thickness on shape memory behavior of equiatomic Ni-Ti is studied by **Ishida et al.** [89]. It was observed that transformation strain and residual strain under the constant stress are very sensitive to the film thickness, below 5 μm. The strain generated in Ni-Ti films are affected by the two types of constraints: surrounding grains and surface oxide layer. With increasing the thickness, the former effect becomes dominant, but the latter effect becomes weak. As a consequence, the residual strain and transformation strain are found the maximum for 2 μm films thickness. In contrary to this, no significant effect was noticed for the films above 5 μm thickness. They proposed that the formation of TiO_2 on the film surface reduces Ti concentration beneath the surface oxide layer. As a result, the changes in composition leads to decrease in transformation temperature with simultaneous increases transformation start and finish temperatures.

[3] The effect of elemental concentration on structure, electrical and mechanical properties of Ni-Ti films was studied by **Sanjabi et al.** [90]. The expected superelasticity and shape memory behavior was observed corresponding to different film compositions, comparable with bulk alloy. The electrical measurement confirmed that in near equiatomic and Ti-rich films, phase transformation occurs from low-temperature martensite phase to high-temperature austenite phase above the room temperature. Whereas in Ni-rich films, it occurs below room temperature. Nano indentation measurement demonstrated the superelastic effect in Ni-rich films and martensite deformation in equiatomic and Ti-rich films.

[4] **Reddy et al.** [91] investigated the effect of annealing temperature on microstructure, morphology and mechanical properties of Ni-rich Ni-Ti films. The prepared Ni-Ti films were annealed at four different temperatures 350, 450 550 and 650 °C. They observed that the degree of crystallization increased with increasing the annealing temperature as confirmed by XRD. The mechanical properties such as hardness and elastic modulus increased at higher annealing temperature due to the nucleation, growth process of grains

and segregation of Ni_3Ti precipitation phase. The surface morphology of the films changed with the variation in annealing temperature. As the temperature increased, grain growth was noticed. As a result; microstructure changed from wavy topography to globular type of structure.

[5] **Tong et al.** [92] investigated the effects of annealing temperature on mechanical and phase transformation behavior of Ni-Ti thin films deposited on glass substrate. The annealed films at different temperatures show the formation of Ni_4Ti_3 and Ni_3Ti precipitation phases and decomposition of Ni_4Ti phase into Ni_3Ti phase at 600 °C temperature. The nanoindentation measurement showed the increase in hardness and elastic modulus with increasing the annealing temperature. This improvement in mechanical property was attributed due to the formation of Ni_3Ti precipitation phases. The martensite transformation temperature was also increased with increasing the annealing temperature.

2.3. Modification of Ni-Ti SMA by post-deposition treatment: Ion irradiation

The different properties of bulk Ni-Ti SMA_S such as structural, mechanical, electrical with different types of particle irradiation such as electron irradiation, neutron irradiation, proton irradiation and high or low energy ion irradiation have been studied by several research groups. But there are very few reports available on SHI irradiation induced modifications in Ni-Ti SMA thin films.

[1] **Barbu et al**. [93] studied the condition for track formation in Ni-Ti intermetallic compound by irradiation with swift heavy ions. The irradiation of the bulk alloys has been done by using the large range of energy with different ions to cover the large range of S_e (from 17- 52 keV). It was revealed that ions track were only induced in the monoclinic structure but not in cubic one; only when the linear rate of energy deposition by electronic excitation was greater than 46 keV/nm. They described that the tracks were amorphous in their center which decreases phase transformation temperature from monoclinic to cubic at the periphery of track region. At electronic excitation rate (S_e) = 32 keV/nm, no individual tracks were formed, and only monoclinic to cubic structure transformation was seen. For (S_e <17 keV/nm), swift heavy ions was unable to

create any visible crystal structure modifications by electronic excitation. The formation of track in Ni-Ti SMAs was discussed with the framework of “thermal spike” and “coulomb explosion” models.

[2] **Lagrange et al.** [94] observed that SHI induced damaging effects can benefit the shape memorial behavior and bias the shape recovery if the detrimental effects are more controlled. Using this concept, high energy ion beam is used to alter the martensite phase transformation and bias the motion of SMAs thin films. They observed that the sample irradiated at a fluence of 1×10^{14} ions/cm^2 by 5 MeV Ni ions shows maximum amorphous fraction at a depth of 1.2 μm, it was 0.7 μm shallower than the maximum atomic displacement from nuclear collisions calculated by TRIM simulations. This study reveals the possible influence of electronic stopping power on the damaging process. A significant phase transformation was observed below the threshold electronic stopping power reported by Barbu et al. (17 keV/nm). In case of 80 MeV Ar ions study, the amorphous zone was found at a fluence of 1×10^{15} ions/cm^2. They found significant damaging effects from ions having lower electronic stooping power (< 9 keV/nm) near to 5 MeV Ni ions energy (3 keV/nm). This observation confirmed that electronic stopping plays the major role in the damaging process.

In another study, they investigated the effect of 5 MeV Ni ions irradiation on unstrained and pre-strained microstructure of Ni-Ti thin films [95]. They observed that irradiation of the films suppressed the martensite transformation and stabilized the high-temperature austenite phase at room temperature in both strained and pre-strained films. The phase transformation or amorphization of the films at high fluences were observed due to the damage accumulation mechanism. At higher fluence, defect accumulates to a critical value increasing the free energy of the system high enough to induce a transition to the amorphous state. They also concluded that the irradiation-induced transition was higher in the pre-strained films as compared to undeformed film, which confirms the strain sensitive irradiation induced transformation.

[3] **Goldberg et al.** [96] deposited the thin films of Ni-Ti by sputtering and characterized by X-Ray diffraction (XRD), differential scanning calorimetry (DSC) and Rutherford backscattering spectroscopy (RBS). They found that irradiation of the films with MeV He ions below 0.01 dpa causes a decrease in pre-martensitic transformation temperature by 5 ^{o}C during both heating and cooling. The stabilization of austenite phase with fluence was also observed. They conclude that the displacement of atoms from their original site increased the internal energy of alloy system via broken bond around newly formed vacancies. The increase in disorder and entropy of the system modified the Ni-Ti phase diagram showing the shifting of phase transformation towards lower temperature side.

[4] **Konopleva et al.** [97] investigated the effect of neutron irradiation on martensite transformation and shape memory behavior in Ni-Ti alloy at the low-temperature helium circuit. The irradiation of alloys at 170 K in martensite phase revealed that the transformation from cubic austenite phase to rhombohedral (R) phase and from rhombohedral (R) phase to martensite phase decreases exponentially with increasing the ion dose. However, there was no change occurred in shape memory behavior and transformation plasticity of the alloy up to a dose of 6.7×10^{22} n/m^2.

[5] **Vishnoi et al.** [98] studied the effect of 450 keV Ar ion irradiation on the first order phase transformation behavior of NiMnSn ferromagnetic shape memory alloys thin films prepared by dc magnetron sputtering on Si (100) substrate at 550 °C. The prepared thin films were characterized by using X-ray diffraction (XRD), Scanning electron microscopy (SEM), and Transmission electron microscopy (TEM). The XRD study showed the improvement in the crystallinity of films up to a certain fluence of 1×10^{15} ions/cm^2, and above this fluence (3×10^{16} ions/cm^2) the crystallinity of the alloy films decreased result into complete amorphization of the films. This result was further authenticated by TEM bright field images and SEM micrographs. In addition to this, at the higher fluence of Ar ions also deteriorates various properties of the alloy is attributed to the formation of precipitates and facilitation of defect diffusion.

[6] **Wang et al.** [99] investigated the effects of 1.7 MeV electron irradiation and subsequently heat treatment on multistep phase transformation in Ni-rich Ni-Ti alloy at different fluences. They observed that the irradiation and heat treatment of the alloys had prominent effects on transformation temperatures, but with different characteristics. There was a minor change from first orthorhombic (R phase) to monoclinic (martensite phase) transformation after irradiation. But second R-phase to monoclinic phase transformation temperature was significantly decreased with increase in electron fluence and completely suppressed at a fluence of $12.8\times10^{20}/m^2$. Whereas, after heat treatment, R-phase transformation (start/finish) shifts to lower temperature and R-phase to martensite phase transformation shifts to the higher temperature. They concluded that the effects of electron irradiation and heat treatment on transformation characteristics are not exchangeable. However, irradiation is considered as a prominent technique for modification of the alloys properties.

[7] **Waitz et al. [**35] studied the effects of electron irradiation on martensite transformation temperature of TiNi shape memory alloys by using TEM and differential scanning calorimeter (DSC). The electron irradiation was performed by using TEMs with the different accelerating voltage of 200, 300, 400 and 1000 keV. After irradiation, the voltage of TEM was changed to investigate the critical value of voltage for irradiated induced martensite transformation. The phase transformation in Ni-Ti bulk alloys occurred under electron irradiation above 350 kV, but not observed at 340kV or below this accelerating voltage. It was interesting to note that the phase transformation took place in very less time (few second) of irradiation. They found that the phenomena of electron irradiation induce martensite transformation was observed due to the displacement of atoms from their lattice position by the accelerating voltage. The critical value of displacement energy was found 18 eV for bulk Ni-Ti SMA.

[8] The effect of electron irradiation on martensite transformation temperature of Ni-Ti bulk SMAs has been investigated by **Zu et al**. [100,101]. The Ni-Ti alloy samples were annealed at 673 K for 1 hrs before irradiation and then irradiated by 1.7 MeV-energy. The DSC results show the two-step phase transformation during both heating and cooling. The R-phase to martensite

transformation decreases with increasing the electron dose. The change in transformation characteristics was due to the elastic stress relaxation around the Ti_3Ni_4 precipitate phase, and the migration and accumulation of irradiation-induced point defect.

[9] **Wang et al.** [102] studied the effects of 18 MeV proton beam irradiation on R-phase transformation in bulk Ni-Ti alloy at two different doses 1.5×10^{13} and 1.5×10^{14} H^+/cm^2. The microstructure and transformations characteristics of alloy before and after irradiation have been investigated by TEM and DSC. After irradiation, R-phase start transformation temperature (R_s) and reverse martensite finish transformation temperature (A_f) decreased with the increase of proton irradiation. The R_s temperature decreased about 3-6 K while the A_f temperature decreased about 9-13 K. The results show that parent austenite phase was stabilized in all doses. The variation in transformation temperature was observed due to the local stress field generation, and ordering of austenite phase originated by proton beam irradiation through point defect cluster and small displacement cascades.

[10] The effect of proton beam irradiation on mechanical and phase transformation behavior of Ni-Ti alloy wire has been investigated by **Afzal et al.** [103]. The Ni-Ti wire in parents phase has been irradiated by 2 MeV proton beam for the different time 15, 30, 45 and 60 minutes at room temperature. After irradiation, obtained results indicate that an intermediate R-phase is introduced between parent austenite phase and the martensite phase, which results in suppression of direct transformation between austenite and the martensite phase. The hardness of Ni-Ti wire increased linearly with the increase of exposer time up to 60 minutes. The formation of R-phase, variation in transformation temperature and improvement in mechanical properties of irradiated alloys was attribute due to the lattice disorder and associated change in crystal structure after irradiation.

[11] The influence of electron beam irradiation on the mechanical response of Nitinol at room temperature has been studied by **Yousaf et al**. [104]. The Ni-Ti alloy in parent phase was irradiated with 6, 9, 12, 15 and 18 MeV electron beam for 10 min. at a dose rate of 300 cGy/min. The crystalline to amorphous

phase transformation is observed in the specimen irradiated with high energy, i.e., 15 and 18 MeV electron energy. This significant reduction in crystallinity of the Ni-Ti alloy was noticed due to the displacement damage caused by electron-irradiation. Moreover, mechanical properties, ultimate tensile strength are also decreased with the increase of electron energy and thus making the material less ductile.

2.4. Modification of Ni-Ti SMA by post-deposition treatment: Ion implantation

[1] **Ikenga et al.** [105] studied the microstructure of Ni-Ti bulk alloy implanted by Cu^{2+} ions at the energy of 3 MeV and 100 K and 300 K temperature. The implanted microstructure was studied by using Transmission electron microscopy (TEM) and XRD. TEM images of the implanted sample (300 K) at a fluence of 10^{14} ion cm^{-2} indicates the formation of the amorphous phase, whereas, ion implantation at 100 K did not show the amorphization even at the fluence of 10^{15} ion cm^{-2}. The crystalline nature of alloy implanted at 100 K confirmed by XRD study. The XRD pattern of the alloy also confirms the formation of the amorphous state in alloy implanted at 300 K.

[2] **Zhao et al. [**106**]** investigated the effects of Niobium (Nb) ion implantation with a MEVVA ion source, on the surface characteristic, mechanical and corrosion behavior of Ni-Ti alloy. It was observed that Nb implantation at different dose leads to the formation of Nb_2O_5/TiO_2 compact precipitate phase on the surface of Ni-Ti alloy. The formation of precipitation phase takes place up to 30 nm depth on the surface, resulting in depletion of Ni content. The nanoindentation measurement shows that hardness and Young modulus of the alloy decrease with increasing the fluence. This reduction in mechanical properties was attributed to the damaging effects, caused by the Nb ion implantation. The potentiodynamic polarisation test shows the improvement in corrosion resistance of the Ni-Ti alloy after implantation. The alloy implanted at a moderated fluence of 1.5×10^{17} ion/cm^2 and 2 mA current shows the best corrosion resistance.

[3] The mechanical and structural properties of Boron and Nitrogen ion implanted Ni-Ti SMA with several doses (1×10^{16}, 5×10^{16} and 1×10^{17} at.cm^{-2}) have been

investigated by **Pelletier et al.** [107,108]. As a function of ions fluence and species, different phases and microstructures were obtained using grazing incident XRD. The low dose boron and nitrogen ion implantation in the near-surface region significantly improve the mechanical properties such as hardness and elastic modulus. The GIXRD measurement has revealed that the main hardening mechanism was generated by the formation of the partial amorphous layer around the ion projected. The formation of partial amorphous layer seems to be independent of the implanted dose and species.

To confirm the actual hardening mechanism, the same author conducts another study in which alloy with the same composition was irradiated by 1.5 Ar ions. They conclude that main hardening mechanism was occurred due to the formation of the irregular, amorphous layers around the ions projected range. These implanted layers divided into several sub-layers, correlated to the amorphous zone density through the thickness. The volume of amorphous layered also seems to be independent of the dose of argon ions. That indicates that overlapping of damage region is needed for crystalline to amorphous phase transformation. At long range, the disappearance of crystal structure corresponding to the austenite phase is related to the ballistic effects, i.e., generates of dislocation, vacancies in austenite crystal lattice. However, the mechanism of phase transformation in Ni-Ti under SHI is very complex, and recrystallization and partial restoration phenomenon may take place.

[4] **Gorji et al.** [109] studied the effect of carbon and nitrogen ion implantation on Ni-Ti alloy thin films at 80 keV energy and 3×10^{17}cm^{-2} ion dose to improve the wear resistance of the films. The implanted films were characterized by using different techniques such as X-ray photo electron spectroscopy (XPS), GIXRD, AFM and nanoindentation. The XPS and GIXRD studies showed the formation of different phases such as TiN, Ti_2Ni and different kind of oxide phases after implantation. The nanoindentation measurement revealed the improvement in wear behavior of the implanted films via increasing the nano-hardness and decreasing the scratch coefficient of the films. This improvement in mechanical properties was observed due to change in chemical composition of films and formation of the different types of new phase such as carbide, oxide, and nitride.

[5] **Zhao et al.** [110] modified Ni-Ti SMA by hafnium (Hf) ion implantation to improve its surface integrity and wear resistance against deformation. They observed the formation of TiO_2/HfO_2 layer on the surface of Ni-Ti alloy after implantation. XPS and Auger electron spectroscopy techniques revealed that the thickness of this layer increases with increase in fluence. The alloy implanted with moderate fluences possessed thickest oxide layer and highest amount of Hf concentration. The composite HfO_2/TiO_2 layer formed after implantation consists very less amount of Ni on the alloy surface. The nano-hardness of implanted alloy decreased even up to the depth larger than the implanted ion range. They conclude that, at a moderated incident dose, the Hf implanted Ni-Ti alloy possess better wear resistance than the unimplanted one. Moreover, the pseudoelastic behavior of the alloys improved with the increase of implanted dose and retained their integrity even after being deformed in tension to 10%.

[6] The mechanical and phase transformation behavior of nitrogen ion implanted Ni-Ti SMA was investigated by **Kucharski et al.** [111]. The indentation test at micro and nano-scale and tension test were performed to study the local superelastic effects in different volume of unimplanted and nitrogen implanted alloy. Furthermore, changes in characteristic temperatures after implantation treatment were measured by DSC. It was observed that ion implantation modifies the properties not only in the thin surface layer but also in bulk material. The superelastic effect of the super facial layer up to the depth of implanted ion was destroyed. The martensite characteristic transformation temperatures (start/ finish) were shifted to the higher values after the nitrogen ion implantation. It was found that martensite content increases with ion dose. Consequently, the residual depth of indenter also increased and due to the soft nature of martensite phase and therefore load versus depth curve become more similar to those detected for the elastic-plastic behavior.

[7] **Li et al.** [112] modified the Ni-Ti alloy by plasma immersion ion implantation (PIII) with Ta at different incident current to improve the mechanical properties and corrosion resistance of the alloy. It was observed that Ta implantation leads to the formation of composite Ta_2O_5/TiO_2 layer on the Ni-

Ti alloy surface. Augur electron microscopy revealed the suppression of Ni from the superficial surface layer of implanted Ni-Ti alloy. The nanoindentation measurement results showed the obvious reduction in hardness and Young modulus after Ta implantation. The Potentiodynamic anodic polarization test showed the improvement in corrosion resistance after PIII implantation. The Ni-Ti SMAs alloy implanted at a moderated incident current acquires a uniform surface morphology and higher surface roughness, which gives the best corrosion resistance. This work suggested that Ta implantation in Ni-Ti SMAs alloy is an effective way to improve the cytocompatibility and corrosion resistance in future biomedical applications.

[8] **Levintan et al.** [113] analyzed shape memory and mechanical properties of nitrogen ion-implanted Ni-Ti alloy for orthopaedic device and surgical tools. The Ni-Ti alloy in martensite phase has been implanted by the high-dose ion with low energy 65 keV at different fluences 1×10^{17} 5×10^{17} and 1×10^{18} J/cm^2. It was observed that after implantation, the nitrogen and carbon implanted layers are formes on Ni-Ti surface. The formation of these layers plays a complex multifunctional role to change the mechanical properties of the alloy. The change in Ti to Ni concentration ratio was noticed due to preferential sputtering of Ni atoms over Ti atoms after implantation.

[9] **Oliveira et al.** [114] observed that nitrogen plasma based ion implantation process (PBII) was able to modify the surface layer of Ni-Ti SMA. Such surface modifications of Ni-Ti alloy by ion implantation are very efficient to improve many important properties, thus extending the applications of this alloy in the harsh space environment. After implantation, a huge amount of nitrogen concentration was observed on the surface and implanted nitrogen ions diffused to large absolute depth in the direction of bulk Ni-Ti alloy. As a result, a clear suppression of Ni atoms was observed on the top surface of the alloy. The formation of TiN layer was identified by XRD and intensity of martensite peaks increased with increasing the incident angle of XRD. They suggest that PBII caused a significant reduction in the friction coefficient of the implanted samples, which is more noticeable in the begging of the test. This reduction in friction coefficient was attributed to the presence of nitrogen ions to a large depth towards the bulk material. The implanted ions caused a

significant change in the wear behavior of Ni-Ti alloy, which avoided the realizing of material during friction tests and increase the corrosion resistance of material after implantation.

[10] **Zayonts et al.** [115] studied wear resistance and surface tribological properties of Ni-Ti bulk alloy implanted by 50 keV nitrogen ions at different fluences, 1×10^{17}, 1×10^{18} and 2×10^{18} cm^{-2}. The surface characteristic and wear test on the implanted surface was done by using depth sensing indentation test, dry sliding-wear test, and scanning profilometry method. The observation shows that implanted treatment modifies the near-surface layer up to 190-220 nm and lead to suppression of Ni content from the surface in 40-50 nm depth. The significant depletion of Ni content in the layer down to 100 nm thickness was observed after implantation. The hardness and mechanical properties (wear resistance) of the alloy were significantly enhanced after implantation. The improvement in hardness is ascribed to the formation of different precipitation phases, harden solid solution. Furthermore, the Ti-based compounds (Included TiN) were formed after treatment in the depth of 30 nm to 120 nm.

After the extensive literature review, it was found that the binary Ni-Ti alloy has immense technological importance, if the irradiation-induced damaging effects and unpredictable martensite transformation can be controlled and also irradiation parameters such as the energy of the beam, mass of the beam and fluence are properly chosen. The main focus of the current interest is to achieve precise control on the various properties related to martensite transformation temperature and shape memory behaviours. After literature survey, we have determined following grey areas as research gap in Ni-Ti alloy which needs further investigations;

These are as follows:

I. There is no systematic study on Ni-Ti thin films irradiated or implanted by various metallic ion beams.
II. There is no systematic study of the effects of ion irradiation on high symmetric austenite and low symmetric martensite phases simultaneously.
III. There is lack of systematic investigation describing the effect of ion irradiation on precipitation hardening mechanism of Ni-Ti films.

IV. Modification of Ni-Ti binary alloy thin films by negative ions implantation is less explored work; therefore it needs further investigation.

The paramount interest of the present study lies in the fact that it will enhance the existing knowledge in the field of irradiation-induced modifications in Ni-Ti alloy thin film. There are no systematic studies on the effect of metallic ions on the structural, electrical and mechanical behavior of Ni-Ti thin films; hence the investigations itself will be a new contribution to the research. The current study will open a new path to control the irradiation induce damaging effects and shape memory behavior of the alloy. The controlled effects of energetic ions on various properties are immense technological importance for various MEMS applications.

Chapter 3

Thin Films Deposition Methods and Characterization Techniques

This chapter comprises the details about the synthesis method used for the present research work. Apart from this, a brief description of Swift heavy Ion Irradiation, implantation methods and characterization techniques used in this work are appended under several sections. Methodology of various characterization techniques such as Rutherford backscattering spectrometry, X-Ray Diffraction, Atomic force microscopy, Field Emission Scanning Electron Microscopy, Energy-dispersive spectroscopy, Four probe electrical resistivity measurement and nanoindentation used to accomplish the present research work are elaborated in this chapter.

3.1. Thin films deposition techniques

The properties of Ni-Ti thin films differ significantly from their bulk counterpart with a variation in deposition methods, composition and other practical parameters such as the area of deposition, vacuum level [116]. Although several methods have been developed to deposit Ni-Ti thin films, among them vacuum evaporation, arc plasma, ion plating, laser ablations, and sputtering technique are the popular and widely used methods. In above methods, thin films deposited by sputtering techniques are more suitable for MEMS applications because of uniform thickness, compositions, and better processing rates [117,118]. Sputtering technique is one of the extensively employed technique to fabricate thin films due to it is ability to deposit multi-component thin films with controlled thickness and composition. Besides, thin films deposited by sputtering process exhibit excellent mechanical properties due to fine grains size. Sputtering technique is also used to fabricate highly adherent films with the substrate and with complex shaped objects. Thin films of Ni-Ti first synthesized by Thomas et al. in 1982's by electron irradiation. The obtained films were amorphous even this discovery was a milestone in the area of shape memory alloys [119]. In 1983 Sekiguchi et al. firstly synthesized the crystallized Ni-Ti thin films by vacuum deposition and found the phenomenon of shape memory effect [120]. Later in 1987, Ti-56Ni alloy thin film was deposited by Kim et al. by using magnetron sputtering. However, the composition of the obtained thin film was not equiatomic, and these films did not show the martensitic phase transformation. Even this attempt opened up a possibility of using sputtering techniques for Ni-Ti shape memory thin films [121]. In this study, magnetron co-sputtering technique has been employed for depositing Ni-Ti thin film samples.

3.1.1. Sputtering techniques

In the sputtering process, a solid target is bombarded by highly energetic ions which cause the ejection of surface atoms from the target material. This phenomenon occurs only when the energy of the incident ions is higher than the binding energy of target material [122]. Prolonged bombardment of highly energetic ions causes depletion of target material which subsequently deposits on the substrate in the form of thin film. Sputtering is performed either by dc voltage or rf voltage.

Advantages of sputtering technique

There are so many advantages of the sputtering technique over the other techniques.

(1) The film can be deposited in a large area with higher uniformity.
(2) Deposited films have better reproducibility.
(3) Higher adhesion between deposited film and substrate.
(4) Desire control on film growth and thickness.
(5) It can deposit the higher melting point materials.
(6) Ability to deposit the thin films with different composition and morphology.

There are various types of sputtering techniques:

3.1.1.1. Physical sputtering

Physical sputtering is based on the principle of moment transfer between incident ions and target atoms [123,124]. As highly energetic plasma ions fall on the surface of the target material, momentum exchange takes place due to severe collision cascades. When the energy of incoming ions is high enough to break the bonds of target atoms, makes them eject out leading to sputtering process. Sputtering yield is defined as the ratio of the average number of atoms ejected out per incident plasma ions. Sputtering yield depends on so many parameters such as the mass of the bombarding ion and target material, incident angle, energy of bombarding ions and surface binding energy of target atoms.

3.1.1.2. Potential sputtering

When the multiple charge ions projectile at the solid surface, a special form of electronic sputtering take place which is known as potential sputtering[125]. In this process, the potential energy is always stored in the form of multiply charged ions and separated out when the ions recombine during impact on a solid surface. This type of sputtering process is strongly dependent upon the sputtering yield and charge state of the incident ions and takes place when the energy of incident ions is well below the threshold of physical sputtering. This type of sputtering has only been observed for certain target materials [126].

3.1.1.3. Electronic sputtering

In this technique, highly energetic electrons or highly charged heavy ions incident on the target material and lose their energy by electronic stopping power [127]. This energy promotes electronic excitations causing sputtering of the atoms from the surface of the target material. This technique is widely used for the sputtering of insulator target material because of very slow quenching rate of electronic excitations unlike in conductors.

3.1.1.4. Etching and chemical sputtering

The removing of atoms from the surface of the target material with the sputtering of inert gas ions is called “ion etching” or “ion milling”. This type of sputtering gives higher sputtering yield in comparison to physical sputtering process because; plasma process has large numbers of chemically active ions and radicals. The reactive ions are often used in secondary ion mass spectroscopy (SIMS) technique to increase the sputtering rate.

The sputtering which is observed below the threshold energy limit of physical sputtering is known as chemical sputtering [128]. In this sputtering, the target material is bombarded with a highly chemical reactive species causing the material to sputter out. The chemical reaction between target atoms and projectile atoms knocks out the loosely bounded atoms of the target surface which subsequently deposit onto the substrate. This technique has been extensively used in the semiconductor industries for etching and structuring of surface patterns.

3.1.2. Magnetron co-sputtering

Sputtering is a physical vapor deposition method used to prepare highly uniform nanocrystalline thin films. In the present work, Ni-Ti thin films were synthesized by using dc magnetron co-sputtering technique at UGC DAE CSR Indore. The geometry and fundamental principle of magnetron sputtering are described here. The details of deposition parameter of Ni-Ti films are discussed in next chapter (section 4.1). The schematic of the sputtering deposition process is shown in figure 3.1[129].

Magnetron sputtering technique is a type of plasma vapor deposition process where plasma ions promote the ejection of atoms from the surface of target materials working as the negative electrode. Positively charged ions of the plasma are allowed to accelerate towards the target by the application of electric field. These positively charged plasma ions have sufficient energy to eject out the atoms of the target material. The target atoms eject out in a line-of-sight cosine distribution pattern and condense on the surface of the substrate which works like a cathode. The target material depends on the choice of the film to be fabricated on the substrate according to the requirement. For conducting targets, deposition can be done by dc power supply while for insulating target materials RF power source is used.

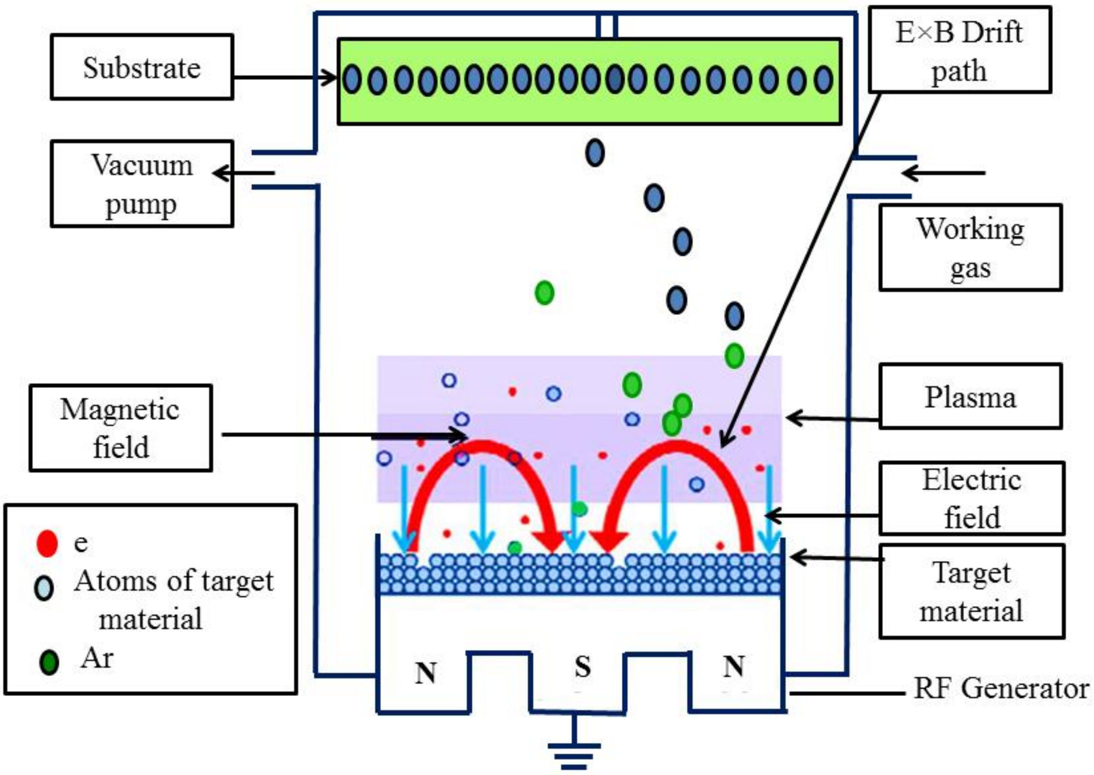

Figure 3.1. Schematic representation of magnetron sputtering deposition process.

This technique is known as magnetron sputtering because it makes use of the magnetic field to trap the electrons which promote the ionization process at low pressure. Magnetron sputtering was pioneered in 1852, but it took around 100 years for commercialization in the industry. At present, the sources of magnetron sputtering are available many geometric configurations. Simultaneously, the target materials are also available in tubular, rectangular or circular shape.

In the sputtering process, the high ion current is required for the better sputtering rate. The collision of sputtering gas ions with target material causes:

- Emission of secondary electrons;

- Emission of atoms from target surface;
- Backscattering of the sputtering gas atoms.

The deposition rate also depends upon the flow of gas atoms. The mean free path of the gas atoms is given as (130);

$$l = kT/\sqrt{\pi}.\sigma.p \text{---------------------} (3.1)$$

where k is Boltzmann constant, T temperature and σ is the cross section and p is the gas pressure. The above equation shows that pressure of the gas should be lower than a certain maximum to obtaining the maximum deposition rate. The magnetron co-sputtering setup used in the present is given below:

Figure 3.2. Magnetron co-sputtering setup (AJA International, Model- SHQ OR) used in present study at UGC-DAE CSR Indore.

3.2. Post Treatment Methods

3.2.1. Swift heavy ion irradiation

The ions which have the energy in the range of MeV to GeV are known as Swift Heavy Ions (SHI) [131]. Swift heavy ion irradiation technique has been extensively used for engineering the various properties of materials [132]. The alteration of material properties by SHI irradiation depends upon the interaction between the incident ions and the target material. The incident ions interact with the target material and lose their energy into the material by two independent ways (a) through the elastic collision with the nucleus of target material which is termed as the nuclear energy loss (S_n), and (b) through inelastic collision with the electron of the target material known as the electronic energy loss (S_e). The nuclear energy loss is mainly dominant in the low energy range (S_n< MeV) or the energy range of few keV to few hundreds of keV, while the electronic energy loss (S_e) or high energy heavy ions is dominant in the high energy range, i.e., energy is in the range of few MeV to few GeV. For SHI, the electronic energy loss (S_e) in the target material is (>1MeV/amu) via inelastic collision. In SHI irradiation, the projectile ions impart energy to electrons and these electrons transfer their energy to lattice via the electron-phonon coupling. The Figure given below shows the variation of electronic and nuclear energy loss for the SiO_2 target material [133].

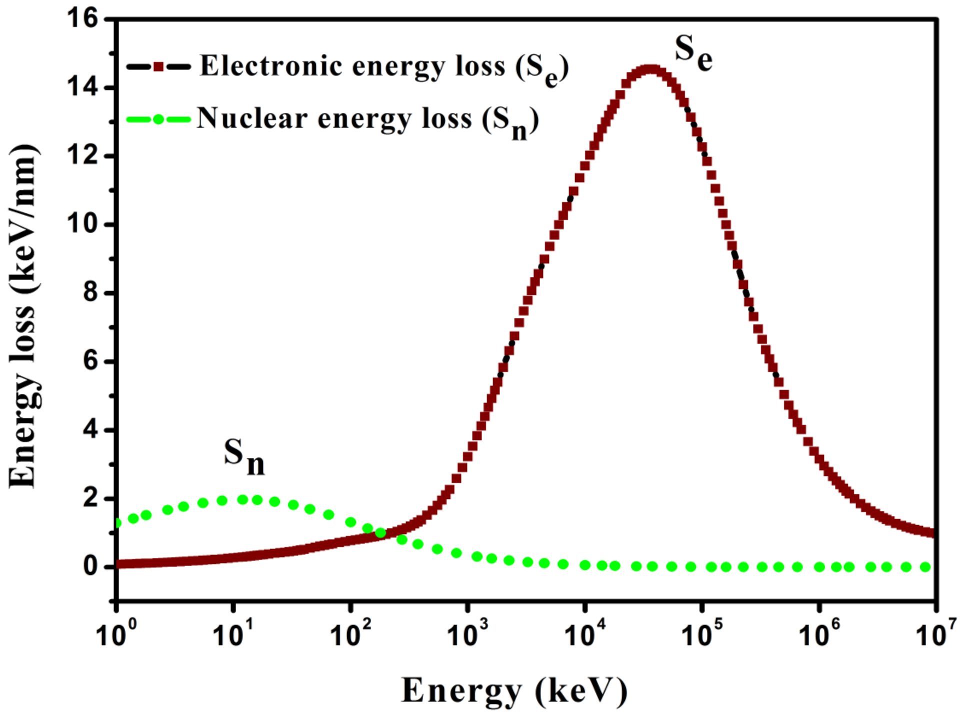

Figure 3.3. Energy loss distributions for Ag-ions in SiO_2 matrix calculated by SRIM 2008 code.

3.2.1.1. Introduction to 15UD Pelletron accelerator

In the last few decades, ion beam technique has become very much popular to tune the properties of engineering materials. Since the 1960s, ion implanters or accelerators have become the essential component of semiconductor electronics industry. At present, ion implanters are widely being used for many biomedical applications such as cancer therapy, etc. Such possibility of engineering the properties of materials has opened the new avenue of interdisciplinary research for the betterment of human life. At present, IUAC is having the facility of 15 UD tadem accelerator which is capable to attaining terminal potential 15 MV [134, 135]. This accelerator is capable of accelerating a large range of ions from proton (H^{1+}) to uranium (except inert gases) with energy ranging from few MeV to 100 of MeV depending on the ion species to be accelerated. Fig 3.4 shows a diagram of 15 UD tandem Pelletron accelerator. The Pelletron is installed in a stainless steel tank with 26.5-meter height and 5.5-meter diameter. The middle part of the tank is connected to high voltage terminal with the grounding of top and bottom part.

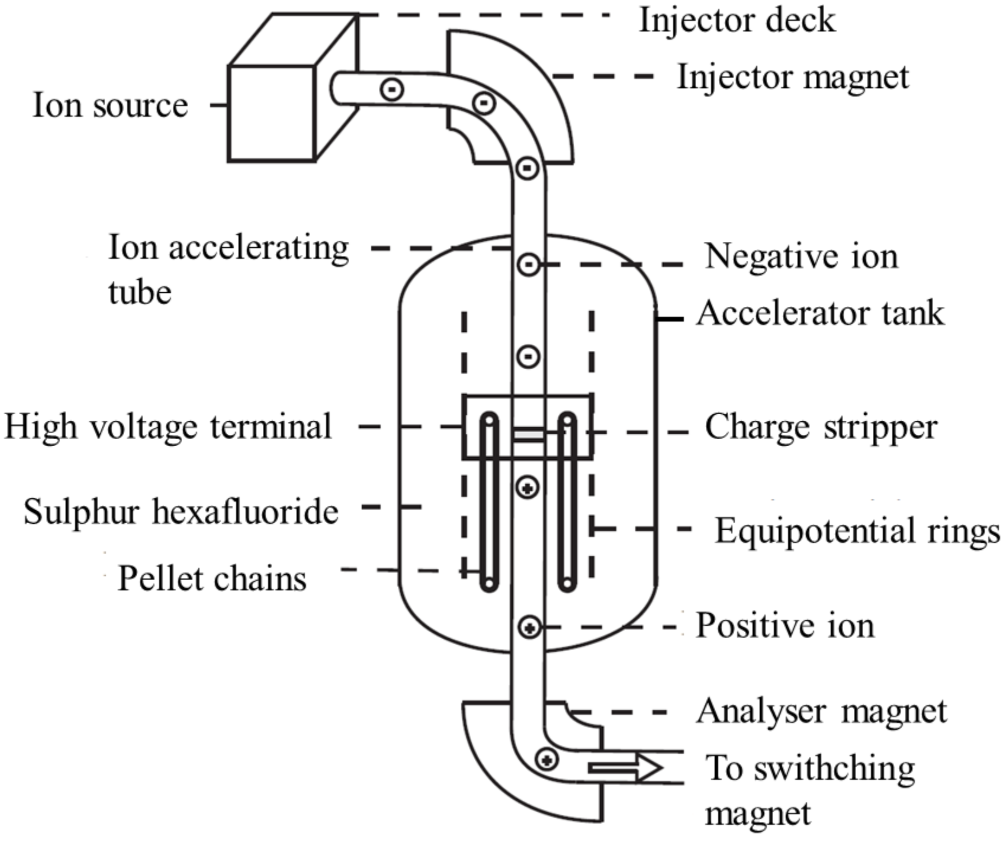

Figure 3.4. Schematic diagram of Pelletron Accelerator situated at IUAC, New Delhi.

The diameter and height of this tank are 1.52-meter and 3.81-meters respectively. The charging of this terminal can be done form 4 to 16 MV potential gradient. To maintain the potential gradient between the terminal and the ground of the tank, accelerating ceramic titanium diffusion bonded tubes are used. A highly insulating sulfurhexafluoride gas is filled into the tank with a pressure of 6-7 bar, to prevent spark which possibly may occur with high terminal potential. The source of negative ions is situated at the top part of the building. MC-SNICS (Multi-Cathode- Source of Negative Ion by Cesium Sputtering) is used as the negative ion source. The negative ions generated by the source have -1 charge state and further accelerated under the influence of high voltage power supply. Further, ions are selected according to their respective mass under the application of varying magnetic field applied by the injector magnet. The filtered ions with particular mass are allowed to bend at downward angle 90° in connection with the upper ground of the tank. These negative charge ions at the top of tank (grounded) attract towards the terminal with an energy gain of V_T MeV. Further, these negatively charged ions are accelerated through a C foil or N_2 stripper by changing the polarity. The role of the stripper is to strip the electrons from the negatively charged ions giving rise to positive ions with q charge state. These ions are further accelerated with an energy q times V_T due to the ground potential at the bottom of the tank. The final energy of the ions coming out of the accelerator can be defined by following equation [136]:

$$E = [E_{deck} + (1+q)V_T] -------------------(3.2)$$

where q is the charge state of ions after stripping, V_T is terminal potential in MV, and E_{deck} is the deck potential of MC-SNICS source.

After crossing the stripper, ions have different energies with different charge states. These ions are energetically analyzed by using a 900 bending magnet termed as analyzer magnet. At this stage, the ion with desired energy and charge state are filtered by analyzer magnet. Once a beam of ions with desired energy are achieved, transferred to the experimental beam line through the switcher magnets. By using the multiport switching magnet, it is possible to deflect the beam in any of the seven beam lines situated in the beam hall as per the experimental requirement. To achieve the ultra-high vacuum in the accelerator, ions and getter pumps are used. As the ion beam passes through the accelerator beam line, it is mandatory to align the beam in the center, and this is done by using steering and quadruple triple magnets. For visual monitoring of the beam, quartz or beam profile monitors are used and beam current is measured by Faraday cups.

3.2.1.2. Material Science beam line

Multi-port switching magnet is used to provide the direction to the ion beam in any one of the beam line out of seven. Material science beam line is available in beam hall 1, which is situated in the right side of the zero degrees beam line with an angle of 15 degrees. The high vacuum irradiation chamber of material science beam line is made up of stainless steel with 68 cm diameter. Figure 3.5 shows the diagram of the high vacuum chamber. To create the high vacuum, the system is equipped with the rotary pump and turbo molecular pump. The operation of rotary pump followed by turbo pump creates 10^{-7} mbar vacuum in the chamber during the experiment. Copper made four-sided sample holder also known as target ladder can mount 24 samples at a time. After mounting the samples, target ladder is placed into the chamber. The movement of the ladder is managed by a stepper motor attached to a mechanical assembly. Apart from this, the motion of the ladder can also be controlled by electronic system available in the data acquisition room. The sample is brought in the path of the ion beam by monitoring the luminescence of the ion beam falling on the quartz crystal. To look inside the chamber during the experiment, an arrangement of CCD camera and a light bulb is provided. CCTV screen of the data acquisition room shows the exact position of the beam.

After locating the beam position on CCTV monitor, sample is placed in that position by horizontal and vertical movement of the ladder. The beam is focused with the help of a steerer and a magnetic quadrupole. To irradiate the sample, beam performs scanning in x and y directions with the help of an electromagnetic scanner. Scanning is performed in an area of 10×20 mm^2. Scanning is performed in such a way that it covers most of the area of the sample to maintain the uniformity of the irradiation effects. Target ladder is surrounded by a secondary electron suppressor kept at -120 V. The suppressor is designed with an opening which allows the ion beam to an incident on the sample. Finally, target ladder collects the electric potential which is further measured by the current integrator device.

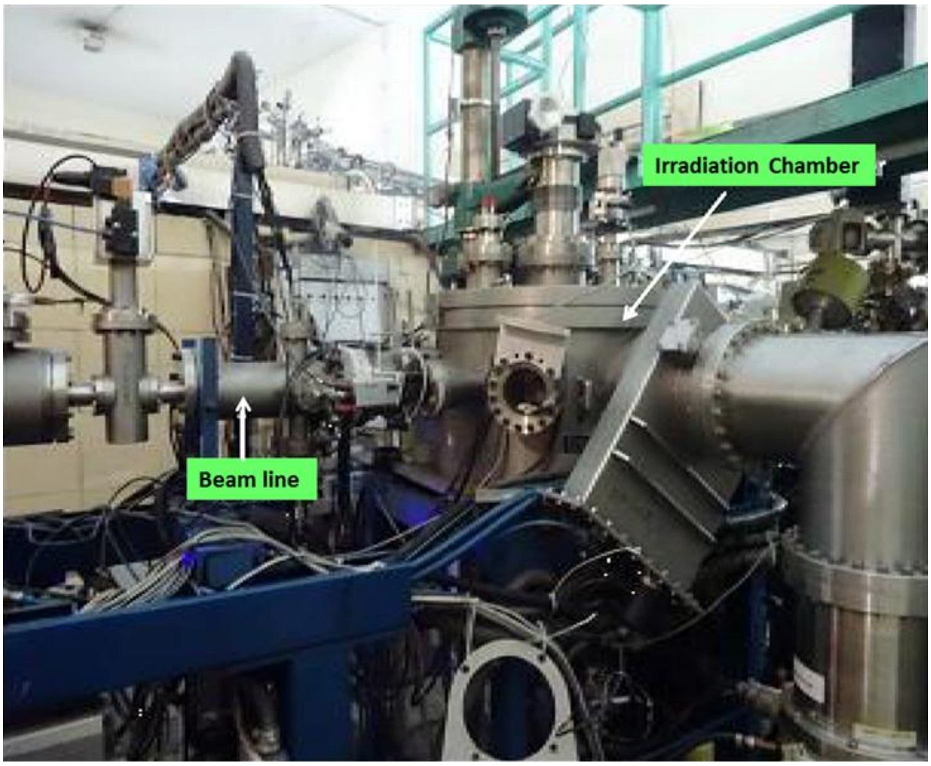

Figure 3.5. Photograph of vacuum chamber of Material Science beam line at IUAC New Delhi.

In the present study, we have taken 120 MeV Au, 100 MeV Ag ions and 90 MeV Ni from Pelletron accelerator for the modification of Ni-Ti thin films deposited on Si substrate in materials science beam line.

3.2.2. Low energy accelerator (Ion implanter)

Ion implantation technique is an excellent technique to introduce the dopant atoms into the target materials, especially for the semiconductor industry. This technique offers higher flexibility, higher homogeneity over large surface areas. Apart from this, the possibility of adjusting the implantation doping during the multiple ion implantation is the main benefit of this technique which is not possible by conventional diffusion technique. The ion implanter system consists of different subsystems given as (1) ion source, (2) mass separator or mass analyzer, (3) accelerator stage, (4) beam scan system and finally the (5) target chamber. These different subsystems can be utilized in the different configuration as shown in figure 3.6. The design of early implanter was usually based on the single accelerator and a magnetic analyzer (Fig 3.6 a), in which the ions travel only in the straight line through the magnetic analyzer. The mass analyzer used in these systems has very less resolving power.

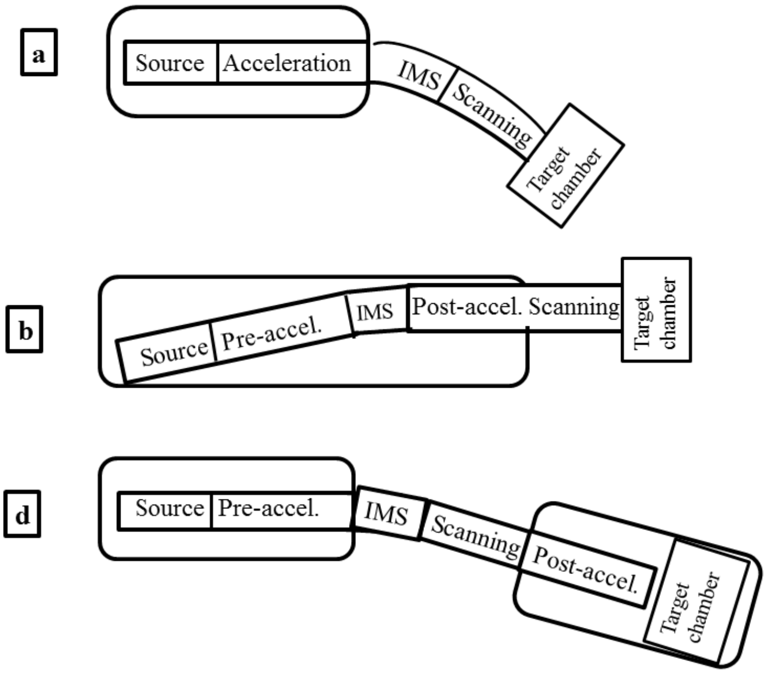

Figure 3.6. Three basic implanter configurations.

Therefore, this accelerator can only be used for atomic research to accelerate the light mass ions such as helium and hydrogen. For the mass separation of heavier ions, large magnetic field is needed. This large electromagnet requires large amount of electric power for water cooling. Later, to save the energy, design of accelerator was split into two major parts, (a) preacceleration and (b) postacceleration as given in figure 3.6(b) and (c). The preacceleration part accelerates the ions to 10-30 keV energy before mass separation. After mass separation, some of the selected ions are re-accelerated with the final energy of 80-500 keV. This design of the accelerator reduces the power consumption, X-ray generation and has the advantage to accelerate only the required ion species to very high energy.

The designs of latest ion implanters are included the optimization of low power consumption, size of implanter and vacuum requirement. The schematic of latest implanter is shown in figure 3.6 b. The important part of the implanter is the placement of beam scanning system before the postaccelertion stage. This arrangement reduces beam deflection to minimum levels which is desired for higher ion energies. The technical construction of the ion accelerator is shown in figure 3.7.

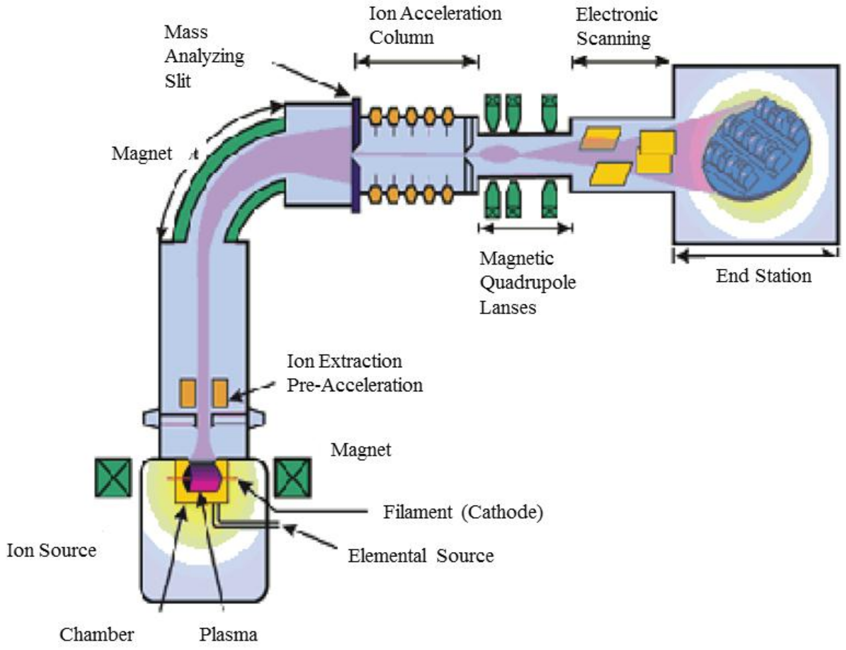

Figure 3.7. Schematic diagram of low energy ion beam implanter at IUAC, New Delhi.

The figure shows that the ions are extracted from the high potential ion source (0–500 kV) by applying the addition voltage 10-30 kV. The extracted ions subsequently enter to entrance slit of mass separation magnet. After mass separation, beam passes through the analysing magnet into the entrance side of acceleration tube. Here, the ions are accelerated to the required energy. Further, the beam is focused through the acceleration tube and quadrupole lens (e.g., ion optical elements) and is directed to the target material in XY-scan direction. The X and Y- scanning are used to get the uniform distribution of ions on the target surface. The current of incident ions is measured by using the Faraday cups near the target position or around the target connected to current integration.

3.3. Characterization techniques

The different characterization techniques such as Rutherford backscattering spectrometry, X-ray diffraction, Atomic force microscopy, Field emission scanning electron microscopy, Four Probe electrical resistivity (ER) measurement and Nano-indentation were employed to characterize the various properties of as-deposited and irradiated/implanted Ni-Ti thin films on Si substrate. All these techniques are extensively explained in the literature. A brief discussion and fundamental principle behind these techniques are presented here, relevant to thesis work.

3.3.1. Rutherford backscattering spectrometry

Rutherford backscattering spectrometry (RBS) is a non-destructive characterization technique which is used to determine both elemental composition and depth of a thin layer within several nm [137]. In RBS a beam of low mass ions bombarded into the surface of sample and energy of backscattering ions is recorded at an angle with an energy sensitive detector. RBS is based on elastic scattering of α-particles from different nuclei of the target material. In the elastic scattering of α-particles, there is no energy transferred between the incident particle and target atoms during the collision and the state of target atoms remains unchanged. In collision process, the energy of projected α-particles transfers elastically to the target atoms, which depends upon the mass of both projectile and target atoms [138]. The measurement of this method may be performed for both crystalline and amorphous materials. The determination of energy of scattered α-particles from target atoms provided the information of atomic species. RBS is performed with He^+ (α-particles) ions in the energy range of 0.5 to 3 MeV and backscattering α-particles are identified by using a semiconductor detector subtending a small solid angle [139]. In RBS energy of scattered ions and signal are analyzed by using conventional nuclear electronic. The energy (E) of backscatter α-particle from the surface atoms of target materials at an angle θ is given by the following relation [140]:

$$E = KE_o \text{------------------------}(3.3)$$

where E_o denotes the energy of projectile and K is the kinetic factor. The kinetic factor is defined as:

$$k = \frac{[(m_2{}^2 - m_1{}^2 Sin\theta)^{1/2} \pm m_1 Cos\theta]}{m_1 + m_2} \text{----------}(3.4)$$

where m_1 and m_2 are the mass of the projectile and target atom and θ is the scattering angle of projectile respectively. In above equation, the positive sign is taken when the mass of projectile is less than the target materials, otherwise negative sign is taken.

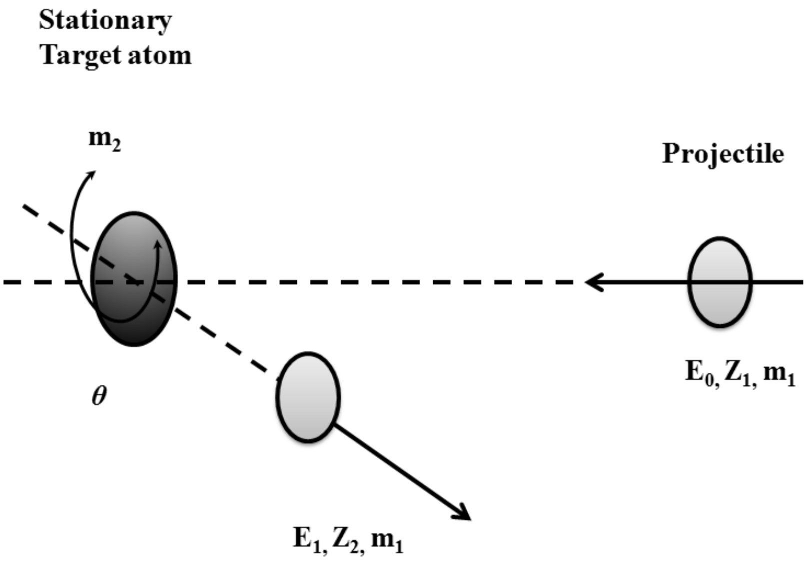

Figure 3.8. Scattering processes of RBS technique.

The total number of backscattering particle per unit area can be calculated by measuring the total number of backscattered particles form the surface of the target material at which the beam has targeted and given as:

$$N_s = \frac{Y.Sin\alpha}{N_p.d\Omega.\left(\frac{d\sigma}{d\Omega}\right)} \text{------------------}(3.5)$$

where Y is the yield (total number of detected particles), N_p is number of projectile atom, dΩ is detector solid angle, dσ/dΩ is differential Rutherford scattering cross section and α tilt angle on the sample surface with respect to the incident beam.

The differential cross section ($d\sigma / d\Omega$) for backscattering in the laboratory system gives the equation:

$$\frac{d\sigma}{d\Omega} = \left[\frac{Z_1 Z_2 e^2}{2E\sin^2\theta}\right] \frac{\left(\left[1-(\frac{m_1}{m_2}\sin^2\theta)^2\right]^{1/2} + \cos\theta\right)^2}{\left[1-(\frac{m_1}{m_2}\sin^2\theta)^2\right]^{1/2}} \text{------------}(3.6)$$

where,

Z_1 and Z_2 …………………… Atomic number of projectile and target material nuclei,
m_1, m_2 …………………………Mass of the projectile and target nucleus,
e…………………………………Electronic charge,
E………………………………...Initial energy,
θ…………………. ……………Backscattering angle.

When $m_1 << m_2$, the above equation can be written as;

$$\frac{d\sigma}{d\Omega}=\left[\frac{Z_1Z_2e^2}{4E}\right]^2\frac{1}{\sin^4(\theta/2)}-------------(3.7)$$

In the present study, RBS characterization facility was done by 1.7 MV Pelletron Accelerator installed at IUAC New Delhi. RBS data is analyzed by using the SIMNRA simulation developed by Max-Planck- Institute for Plasmaphysics in Germany to find the elemental stoichiometry, film thickness and depth profile [141].

3.3.2. X-Ray Diffraction (XRD)

XRD is a versatile characterization technique used to element identifies and quantitative determination of lattice parameter and phase present in the solid materials. It is based on the principle of elastic scattering of X-ray by periodic lattice [142]. In addition to this, XRD also gives the information about physical properties and chemical composition of bulk materials and thin films deposited on the substrate. X-rays are the electromagnetic radiation, which is produced by the copper (Cu) source. The wavelength of the Cu Kα radiation is 1.548 Å, and it comparable to the size of the atom (1.5 Å). In 1913, Sir W. H. Bragg and his son Sir W. L. Bragg developed an equation to explain as to why the cleavage faces of crystals appear to reflect the X-ray beam at certain angles of incidence. In a crystal lattice, if d is the interplanar distance between atomic layers and λ is the wavelength of the incident X-ray beam and small n is the integer then the Bragg's equation for constructive interference is given by the relation:

$$2d\sin\theta=n\lambda--------------------(3.8)$$

by using the above equation one can calculate the atomic and molecular structure of the crystals. Figure 3.9 represents the fundamental schematic diagram for Bragg's equation.

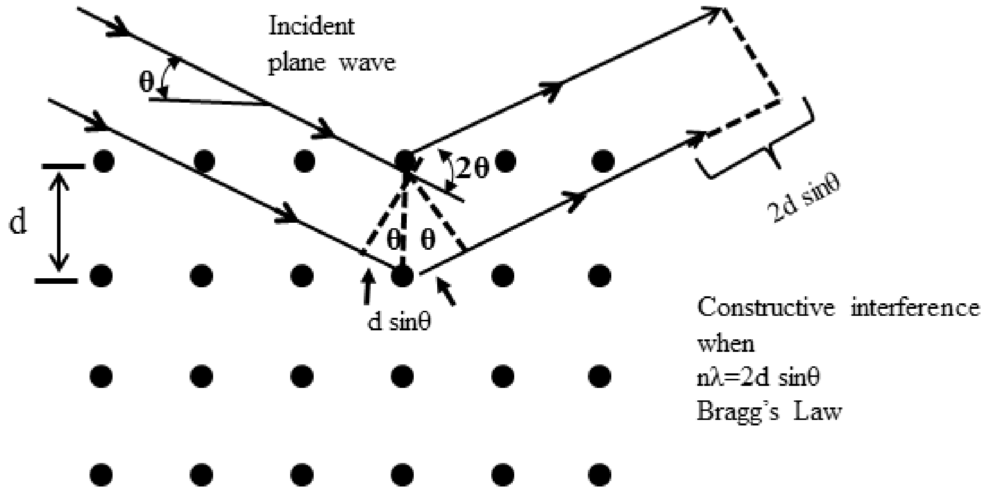

Figure 3.9. Fundamental beam optics schematic diagram of X-ray diffraction.

The XRD pattern of films was obtained using the Bruker D8 Advance X-Ray Diffractometer from Analytical using a Cu-K_α (λ= 1.54 Å) source. The incident optics was set to 1° and 1 cm slits. These measurements were carried out in a 2θ range of 35-52 degree at a scan speed of 0.6°/minute. The lattice spacing "d" was calculated using Bragg's equation (eq. 3.9) which is further utilized to calculate lattice constant. Monochromators sources are used to stop the undesired portion of the radiation. To focus irradiated area of specimen the aperture diaphragm is set between the tube and specimen as shown in fig. 3.10. The source of X-ray is classified into two ways, one is sealed tube and another is rotating anode. Both sources are used to generate the monochromatic X-ray. The X-rays are generated when a beam of high energy such as the electron is interacting with mater. In this process a filament usually made-up of tungsten is heated to generate the electron. The generated electrons are accelerated due to the potential difference toward the Cu target. These accelerated electrons create a characteristic spectrum by ejected the electron from the core-shell of target materials (Cu). This spectrum is composed of several discrete energy levels, which is suppressed by using the suitable filter to get the monochromatic X-ray on the surface samples.

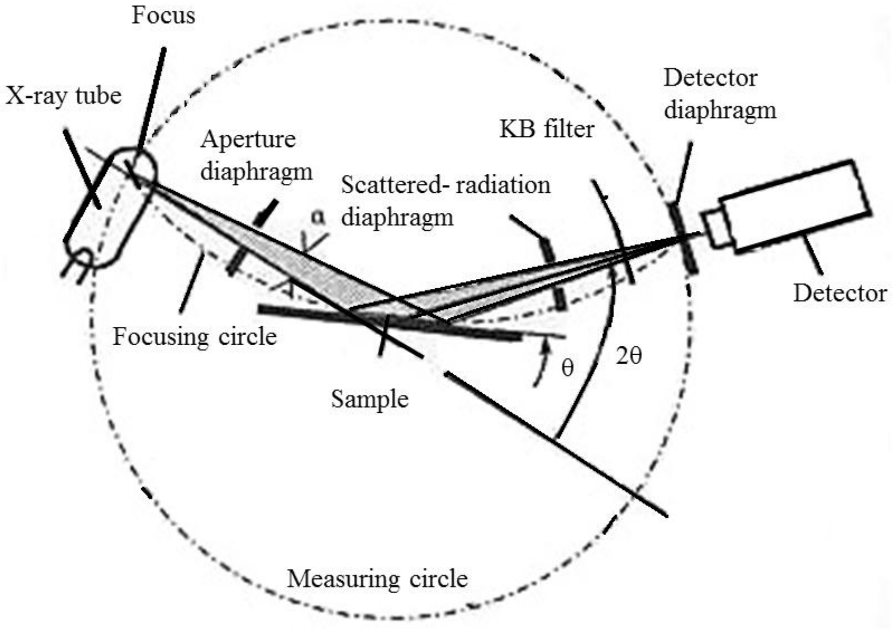

Figure 3.10. Schematic diagram of the beam path.

Determination of Particle Size

The qualitative analysis of target materials is accomplished by knows the crystal arrangement of that material. For a material, the important parameter is crystallite size, which can be calculated by the width of Bragg reflection. The mean crystallographic crystallite size (*D*) of the crystalline material can be calculated from the XRD data by applying the Scherrer's formula [142].

$$D = \frac{0.9\lambda}{\beta \cos\theta} \text{------------------------} (3.9)$$

where λ is the wavelength of Cu-Kα (λ=0.154 nm) radiation, β and θ are full width at half maxima (FWHM) in radian on the 2θ scale and Bragg's angle respectively.

Effect of lattice strain on peak position and width

The orientation of crystal lattice changed with the change in peak position, which can be further utilized to calculate the information about lattice strain such as compressive or tensile and shear. The fig. given below shows the variation of peak position at a fixed 2θ angle [143].

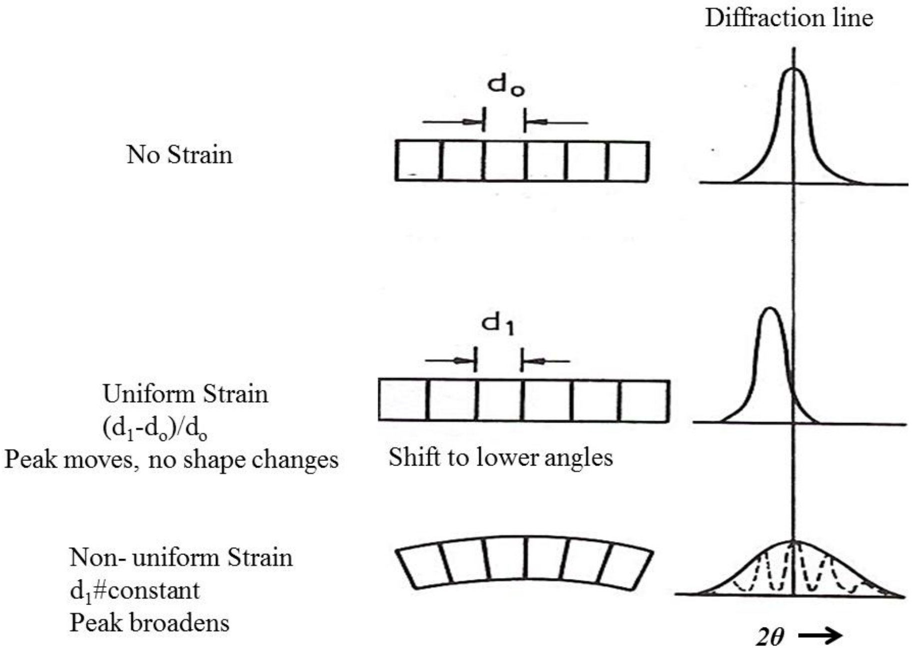

Figure 3.11. Schematic of strain effects.

3.3.3. Atomic force microscopy

Atomic force microscopy (AFM) is a form of scanning probe microscopy, which has the very high resolution of the order of nanometre to 1000 times better than the optical diffraction limit. The information associated with AFM is obtained by sweeping the surface of the solid materials by using a mechanical probe. The probe is made up of piezoelectric element which has very exact and accurate movements on electronic command. In 1980s Gerd Binning and Heinrich Rohrer developed the precursor to AFM, the scanning tunneling microscope (STM) at IBM Research-Zurich and for this work both got the noble prized in physics in 1986s [144, 145].The first experiment on AFM was performed by Binnig, Quate, and Gerber in 1986s.

The first commercial AFM was introduced in 1989s. AFM is a paramount technique for imaging, measuring and manipulating of materials from angstrom to microns scale. For scanning the top surface of the test specimen, AFM instrument consists of a microscale cantilever along with the sharp tip (probe). The cantilever used in AFM instrument is typically made of silicon or silicon nitride. In the event that the tip is helped bring into proximity of the sample surface, various forces between the sample surface and tip lead to deflection of the cantilever according to Hooke's law:

$$F = -kX \text{ ------------------------- } (3.10)$$

where k is constant, and X is the displacement. The value of k depends upon the dimension and shape of the elastic materials.

Depending on the various conditions, AFM can be used to measure various types of forces including van der Waals forces, electrostatic forces, mechanical contact forces, Casimir forces, capillary forces, salvation forces and magnetic forces (through Magnetic force microscope), etc. In addition to forces, it is also possible to measure some other additional quantities by using Scanning Thermal Microscopy (STM) or photothermal microspectroscopy. For this purpose, specialized probes are designed as per the requirement [146]. For example, an array of photodiode equipped with Al or Au-coated cantilever is used to measure the deflection with the aid of a laser spot reflected from the surface. Moreover, piezoresistive AFM cantilevers, capacitive sensing, and optical interferometry are the other prominent techniques for the measurements. At the time of measurement, a constant force is maintained between the sample surface and tip through a feedback mechanism which accommodates the distance between the sample surface and tip. A vertical piezo scanner holds the tip, and the sample surface is scanned in X and Y direction by another piezo block. The obtained 2-D image of the scanned area shows the topographical features of the scanned part of the sample surface.

The AFM device can be operated in three different imaging modes [147]:

1. Static mode- which is also known as contact mode.
2. Dynamic mode- also known as non-contact mode.
3. Tapping mode.

1. Static mode

The probe is "dragged" over the sample surface, and the curves of the surface are taken by using the deflection of the cantilever or by using the feedback signal which is used to maintain cantilever at a constant position. Since static signal measurement is prone to drift and noise. Therefore, to achieve sufficient deflection signal with low interaction force, low stiffness cantilevers are used. During the measurement near the surface of the sample, an attractive force is quite high, and forces cause the tip to “fall into” on the sample surface. Thus, AFM in contact mode is always done in depth where the attractive force has minimal effect and repulsive force is dominant, i.e., tip is always in “contact” with the solid surface. There is one disadvantage over the contact mode that is large lateral forces exist on sample as the drip is move over the specimen. The present mode is useful for high-speed atomic resolution scans and also known as the variable-deflection mode. The schematic diagram of the AFM is shown in figure 3.12.

2. Dynamic mode or noncontact mode

In the dynamic mode of AFM, surface of sample does not contact with tip of cantilever. The cantilever is highly oscillated close to their resonance frequency or just above the amplitude modulation. In this mode, the spacing between the sample surface and tip is on the order of 10 to several 100 of angstroms.

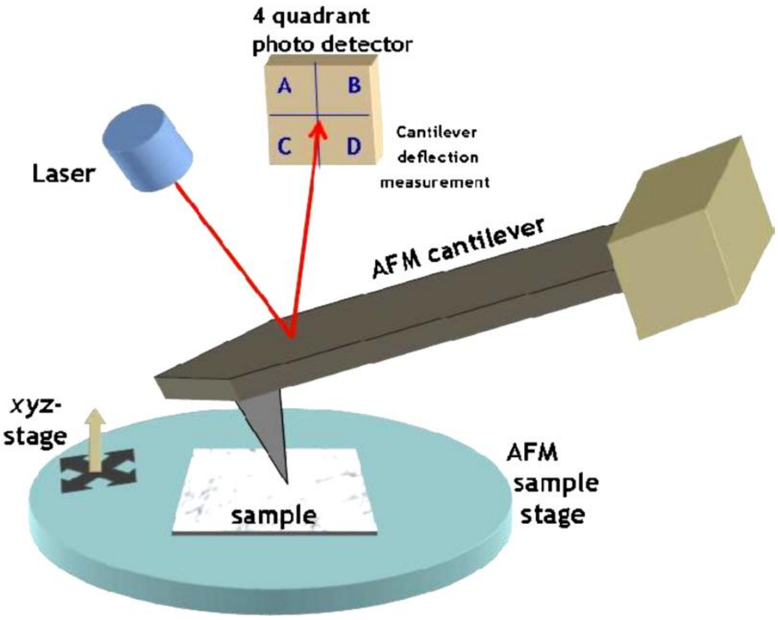

Figure 3.12. Schematic diagram of basic constituents of the AFM instrument.

The amplitude of oscillations including phase and resonance frequency is altered by interaction forces between tip and sample surface. Change is oscillation frequency with respect to the standard reference oscillation gives information about the sample’s surface characteristics. These changes are measured, collected and recorded for image processing. The schematic illustration of AFM for image processing is show in Fig. 3.13.

3. Tapping mode

This is a well-known dynamic mode of AFM which is operated in the presence of gases/air. The Cantilever is positioned above the surface and oscillates at its resonance frequency. In this way, cantilever taps the surface only for a small fraction of its oscillation period. Although, it seems that the sample is in contact with cantilever but this contact occurs for a very short period of time. In the meantime, as the tip scans the surface, lateral forces are reduced dramatically. This mode is most suitable for soft and poorly immobilized samples rather than contact mode. In addition, this mode is also used for phase imaging where phase shift of the oscillating cantilever is measured with respect to the driving signal. This phase shift is the characteristic feature of the materials properties which affect the interaction between the tip and sample surface. On the basis of this phase shift, total sample area can be differentiated with different properties like adhesion, friction and viscoelasticity.

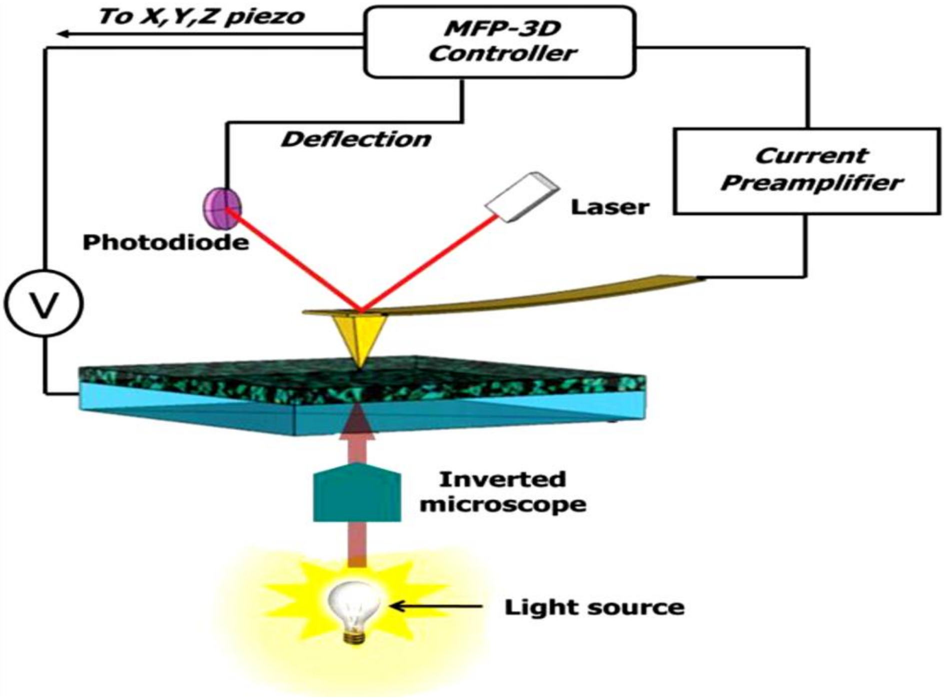

Figure 3.13. Schematic illustration of AFM setup.

In present thesis works, we deposited the Ni-Ti thin films on Si substrate by using dc-magnetron co-sputtering. The topography views were characterized by using a Bruker make Nanoscope V system with a Si_3N_4 cantilever.

3.3.4. Field emission scanning electron microscopy (FESEM)

Field emission scanning electron microscopy characterization technique is used to visualize the nanometre topographic arrangement of an object. It is a high-resolution type scanning electron microscopy which is used to characterize the Nano-dimension of both either conducting or non-conducting materials such as metals, polymer, ceramics, and composite [148]. It is also analysis the chemical composition in attachment with the Energy Dispersive X-Ray Spectroscopy (EDX).

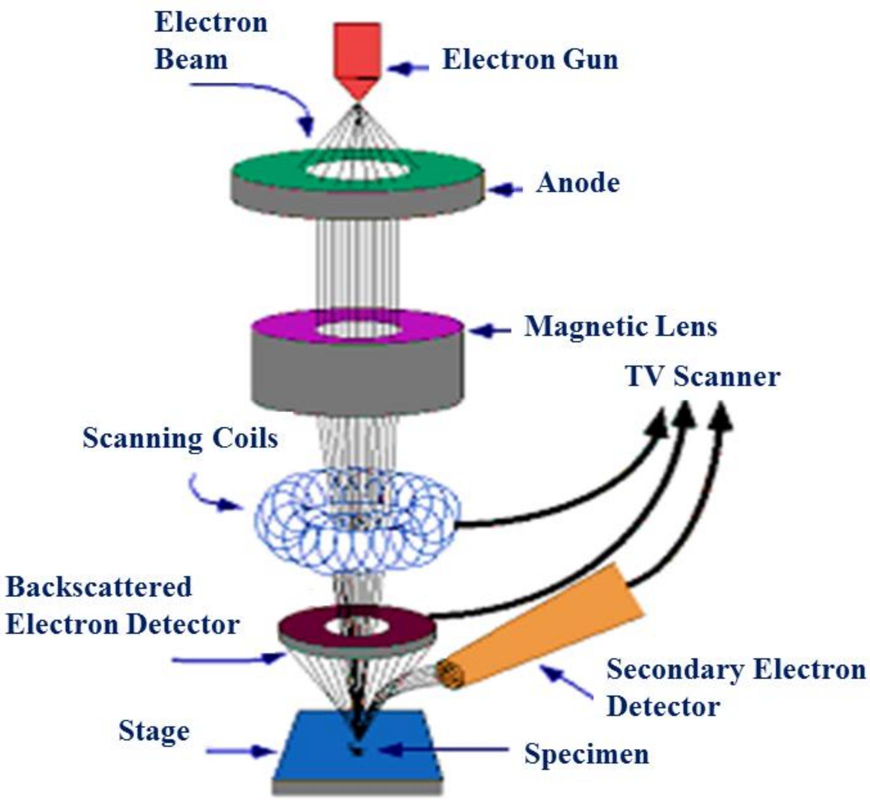

Figure 3.14. Schematic representation of Field emission scanning electron microscopy.

FESEM is a type of electron microscope which performs raster pattern scan on the surface of the sample. Scanning is done through a high energy electron beam. As the beam of the electrons incidents on the sample surface, high energy electrons interacts the atoms. As a result of the interaction, sample produces signals which contain information about the surface characteristics, composition and electrical conductivity of the sample [149]. The schematic diagram of FE-SEM is given in figure 3.14. The main component of the SEM is electron gun which generates a high and stable current in a small beam [150]. There are two types of emission sources embedded with the electron gun: field emitter and thermionic emitter. The main difference between Field Emission Scanning Electron Microscope (FE-SEM) and Scanning Electron Microscope (SEM) is the type of emitter used.

In thermionic emitters, electric current heats up the filament. The Filament is made up of either Tungsten (W) or Lanthanum hexaboride (LaB6). As the voltage is supplied to the filament, it heats up. When the voltage is sufficiently high to cross the energy work function, electrons eject out of the material. The source of thermionic emission has relative low evaporation of cathode material, thermal drift, and low brightness during operation.

To avoid these shortcomings, a new technology based on the field emission effect was developed. This advanced technology does not produce electron beam by heating the filament, unlike thermionic emission. Here, emission of electrons is achieved by placing the filament under the influence of electric potential gradient. A sharp pointed and small tip Tungsten (W) wire is used as a Field Emission Source (FES). The radius of the tip is maintained less than ~ 100 nm to concentrate the electric field potential up to the extreme level. Concentrated potential lowers the work function of the material (cathode) to facilitate the emission of the electrons from the cathode.

A very high vacuum (~10–6 Pa) is maintained inside the column to avoid the unwanted collision of air/dust particles with electron the beam. The acceleration voltage between anode and cathode is maintained of the magnitude of 0.5 to 30 kV. An electron beam generated by FE source is of the order of 1000 times smaller than that of the thermal electron gun used in a standard microscope. Therefore, image quality is markedly enhanced in FE source embedded microscope. To resolve and differentiate the surface features, the wavelength of the electron beam must be smaller than the features. Hence, the concentrated electron beam is required. This lower level of beam condensation makes the FESEM instrument with the highest resolution. This feature makes FESEM as a very useful technique for surface imaging at very high resolution in the field of nanotechnology and materials science [151].

Applications of the FE-SEM

1:- Thickness measurement of multilayer and thin films.

2:- To measure the surface morphology of different crystalline solid or amorphous materials.

3:- To measure the shape, size distribution of grains on the surface of characterized materials.

4:- Fracture and failure analysis of materials.

5:- Analysis of defect production in the materials by different techniques.

6:- Analysis and measurement of the dimension and height of nanometre size objects.

7:- Elemental composition measurement and analysis of micron-sized features.

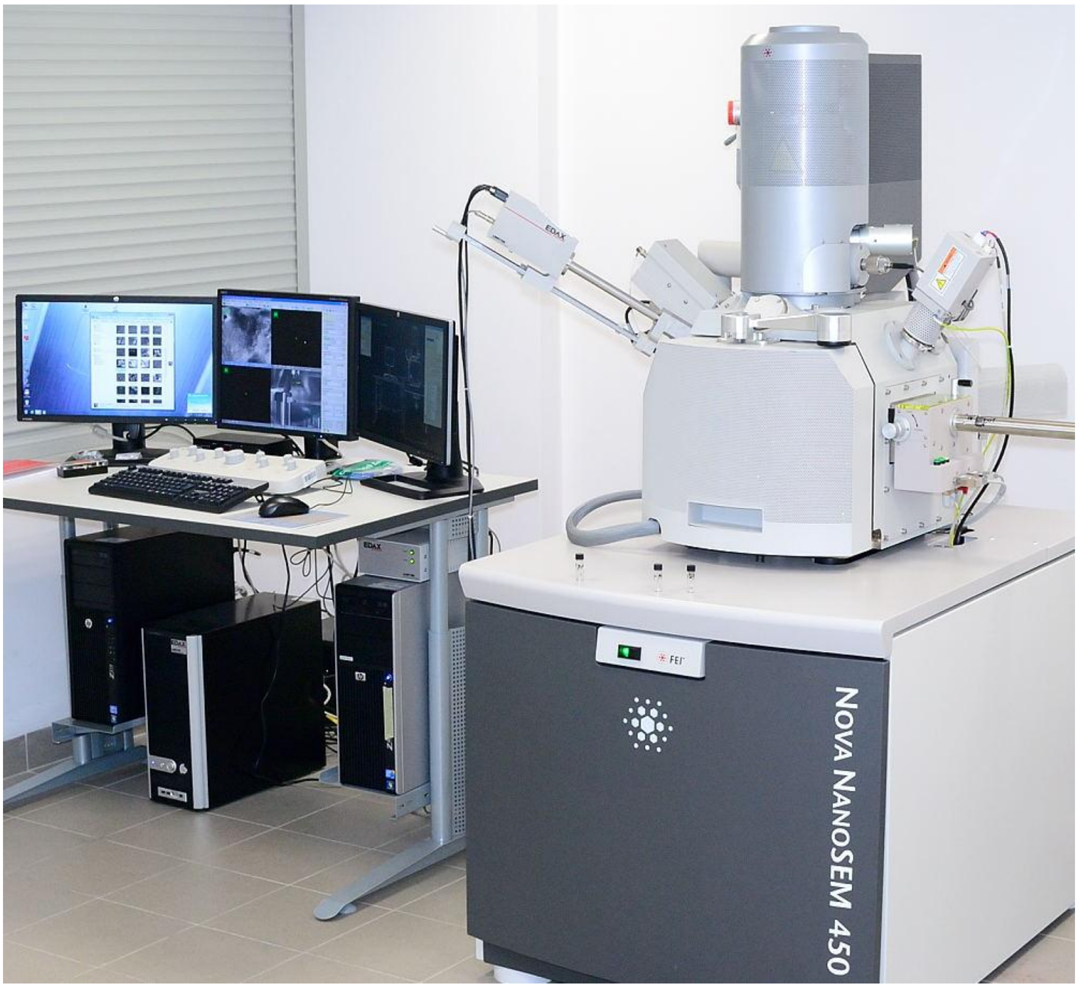

Figure 3.15. Quanta FEG 450 FESEM used for study at MRC, MNIT Jaipur.

3.3.5. Energy dispersive X-Ray spectroscopy (EDX/EDAX)

Energy Dispersive X-Ray Spectroscopy (EDS or EDX) is the type of a chemical analysis technique which is used in combination with scanning electron microscopy (SEM).

In this technique, an electron beam is allowed to bombard on the sample surface. As a result, X-rays are produced, and sample composition is analyzed by the detector. EDS technique is capable to analyzed phases which are as small as 1µm or less. An electron beam moves on the sample in raster pattern. These high energy electrons interact with inner shell electrons of the material and transfer their energy. As a result, inner shell electrons eject out leaving a hole behind. This hole is occupied by outer shell electron. The energy difference between inner shell and outer shell is emitted as X-ray. The energy of these X-rays is a characteristic feature of the element. Attached energy-dispersive spectrometer detects emitted X-rays in terms of number and energy. Since the energy of the emitted X-rays are the specific characteristic of the elements (due to the energy difference between two shells) from which they have ejected out, allows the quantitative measurement of the elemental composition of the given specimen [152]. The EDS detector plots a graph between emitted X-rays versus corresponding energy. EDS detector is a solid-state device made up of lithium-drifted silicon. As the emitted X-rays strikes to EDs detector, a charge signal is generated which is proportional to the X-ray energy. This charge signal is converted to voltage pulse by using an amplifier. This voltage pulse is received by a multichannel analyzer and sorted according to potential. The energy corresponding to each X-ray is determined by voltage measurement and sent to a computer for further analysis. The computer generates a graph between X-ray energy and counts to evaluate the composition the element to be analyzed [152, 153].

In present study, Ni-Ti thin films irradiated with different energy and beam with a thickness of ~270 were characterized by using FE-SEM (Nova Nano FE-SEM 450 FEI) at Material research centre, MNIT Jaipur and scanning electron microscopy SEM (Model :MRAII LMH, TESCAN) at Inter University Centre (IUAC), New Delhi in material science division. The SEM images of investigation Ni-Ti films are discussed in next chapter.

3.3.6. Four probe electrical resistivity (ER) measurement

Four-probe electrical resistivity method is a non-destructive and most common method to measure the resistivity of a thin film and bulk samples.

The schematic diagram of this method is shown in figure 3.16. To measure the resistivity of the samples the contact over the surface is made by using the silver past in a linear arrangement as the distance between all probes remain equal. A heater is attached to the system to heat the sample linearly so that the behavior of the sample is measured with temperature. The two outer side prove used to inject the current into the sample and inner two probes used to measure the resultant electric potential distribution. Due to the high input impedance voltmeter connect to the circuit there is no current flow in the inner two probes [154]. Therefore voltage drops at terminal 2 and 3 caused by the contact resistance between the sample and probe are eliminated from potential measurements. Since the contact resistance is extremely sensitive to the surface condition (such as oxidation) and pressure.

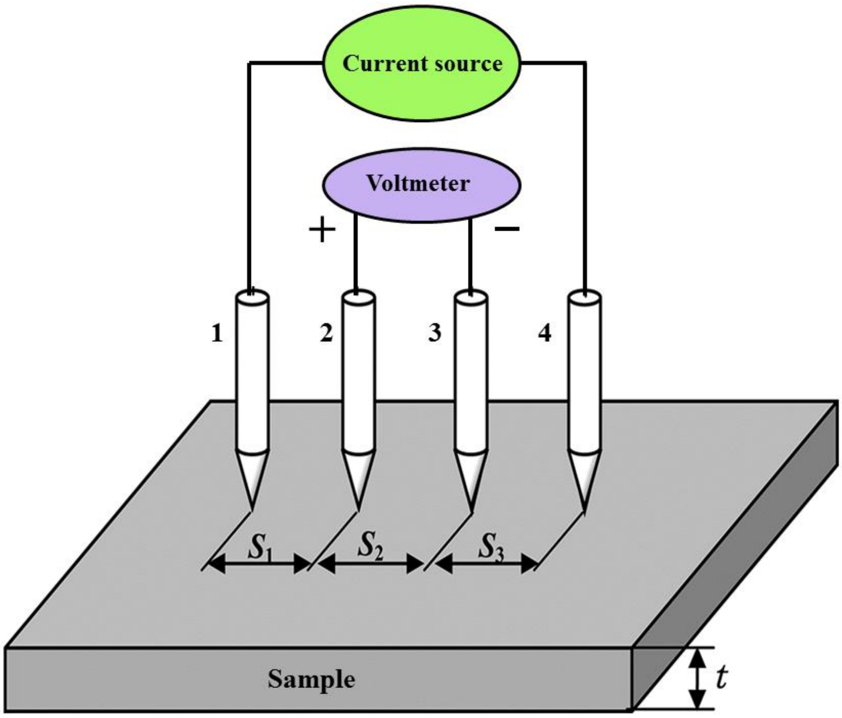

Figure 3.16. Schematic diagram of four point-probe resistivity measurement.

The resistivity of the thin films and bulk materials are calculated by using the following relation [155]:

$$\rho = \frac{\pi t}{\ln 2}\left(\frac{V}{I}\right) ------------------------ (3.11)$$

$$\rho = 2\pi s\left(\frac{V}{I}\right) ------------------------ (3.12)$$

where, V is the voltage, I current, t film thickness and s is the distance between probe.

The experiment of electrical resistivity was performed at IUAC New Delhi in materials science division. The measurement was carried in liquid nitrogen cryostat by using the standard Keithley 2612 Source meter. The temperature of the sample during the experiment was controlled by using the Lakeshore temperature controller (Modal 340). The setup used in present study was fully automated, and program is written using Lab-View software.

3.3.7. Nanoindentation

As far as the mechanical properties are concerned the hardness of the material is the primary mechanical properties, and history is as old as human being started using the materials. However, referring the material as hard or soft is very old but not so easy to present quantitatively. Hardness can be explained as ‘resistance developed in material for plastic deformation. The hardness depends upon the physical and chemical properties of the materials. However, in the case of nanostructured materials, it is associated with the detailed microstructure analysis as well as the technique used for its measurements. There are some sorts of certain limitation for mechanical properties analysis of Nano-structured thin films which cannot be accessed by the conventional technique by visualizing the optical image.

Indentation techniques emerged for the precise measurement of the hardness of thin films in the era of 20th century. The techniques for fabrication of sub-micron tip as indenters, e.g., Berkovich tip, Knoop tip, Cube corner tip and Vickers, etc. with different geometry and angles facilitates to make the nanoindentation techniques more profound and useful for specific mechanical properties. Increasing sensitivity to noise reduction of the instruments motivated the nanoindentation technique to measure of smaller dimensions, e.g., nanometres mechanical analyses. The geometry of indenter tip introduces a different stress state in the material beneath the indenter. The working principal of nanoindentation technique relies on applying a maximum load continuously or stepwise on the tip and measuring the permanent impression based on the continuous depth sensing mechanism.

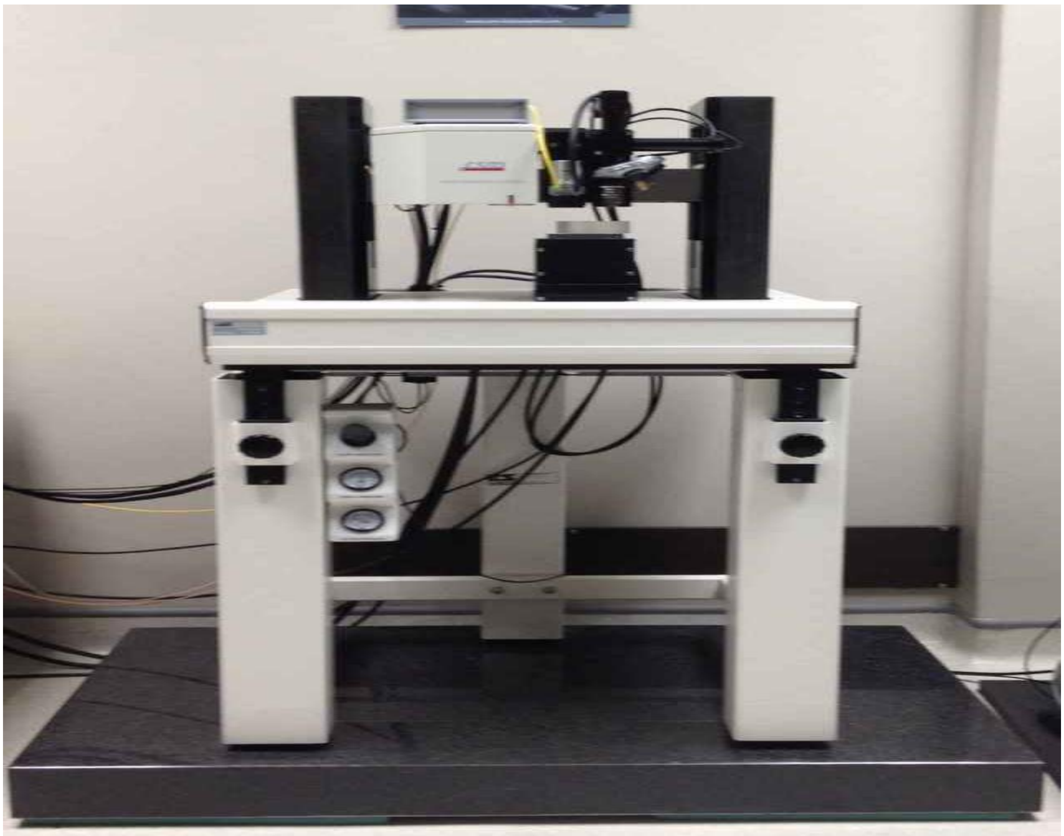

Figure 3.17. CSM instrument Nano-indentation tester at Nanotechnology Application centre, University of Allahabad.

Methods have been developed to extract the hardness and Young's modulus from the applied load-penetration depth results [156]. In all, Oliver and Pharr's method was developed as a key assumption and unloading curve during indentation at maximum load is believed to be entirely elastic [157]. For area function calibration which is used to find out by indenting on a sample of isotropic and known properties. After getting the area function the hardness can be calculated by

$$H = \frac{P}{A} ------------------------ (3.13)$$

where H is hardness, P is the maximum load and A is the projected area during indentation. The elastic modulus can be evaluated by unloading section of stiffness and contact area.

$$S = \frac{2\beta}{\sqrt{\pi}} E_{eff} \sqrt{A} -------------------- (3.14)$$

where is S is the stiffness, E_{eff} is the effective elastic modulus,

$$\frac{1}{E_{eff}} = \frac{1-\upsilon^2}{E} - \frac{1-\upsilon_i^2}{E_i} ----------------- (3.15)$$

where ν_i, E_i , ν, E denoted the indenter, and specimen passions ratio and elastic modulus. The parameter β is a dimensionless constant. So these mentioned equations provide the hardness and elastic modulus by the resulting testing data of nanoindentation. However, in the case of nanomaterial's, mechanical testing using nanoindentation favoured by smaller interaction area of nanostructure dimension [157]. The very initial interaction of indenter and material will be elastic in nature and plastic deformation takes place depending upon the applied load, stress accumulation beneath the indenter and materials properties. However, the fracture in the thin films is also observed after the critical applied load.

Chapter 4

Synthesis of Ni-Ti Shape Memory Alloy Thin Film and Their Low Energy Ion Beam Effects (Ion Implantation)

This chapter deals with the synthesis of Ni-Ti shape memory alloy thin films by magnetron co-sputtering technique. Apart from this, the prepared Ni-Ti thin films have been implanted by Ag ions is also discussed in detail. The Ni-Ti compositions are verified by Rutherford backscattering spectrometry study. The implanted thin films are structurally characterized by X-ray diffraction, Atomic force microscopy. The phase transformation temperatures of the films are determined by four probe resistivity measurement. Nanoindentation study has been conducted to know the mechanical behavior of the Ni-Ti films.

4.1. Synthesis of Ni-Ti SMAs thin films

In a general way, the fabrication of films of a particular material and choice of synthesis technique normally depends on fulfilling the requirements and material properties as well on practical limitation such as the area of coverage, cost, and vacuum requirements. Non-thermal growth techniques, such as sputtering, have proved to be most preferred technique regarding the optimization of growth parameter such as crystallinity and morphology during growth of films. Sputtering deposition technique is lead to unusual and frequently advantageous growth kinetic and force a film to deposit under far thermal equilibrium. Sputtering technique is much more suited to deposited films because Ni-Ti thin films can directly deposit on the semiconductor substrate or IC. Considering the potential advantage of the sputtering deposition in the field of MEMS, in the present study, magnetron co-sputtering technique has been applied for preparation of Ni-Ti thin films by using two different targets and powers.

The shape memory effect, superelasticity and transformation temperature of sputtered deposited Ni-Ti thin films are very sensitive to alloy composition and deposition conditions. By using sputtering method, films can be deposited at high temperature or room temperature. The sputtered deposited Ni-Ti thin films at room temperature are always amorphous, thus, a post-annealing is needed to crystalline the deposited films because the thermally induced phase transformation only occurs in the crystalline films. In the present study, the thin films of Ni-Ti were synthesized at an elevated temperature (550 ^{o}C) to get the fully crystalline films.

A brief description of sputtering techniques includes growth and morphology control is already present in section 3, the experimental deposition parameters and sputtering power are present in this section. The study of ion implantation induces modification of Ni-Ti thin films by metallic ions are also present in this chapter.

4.1.2. Experimental details

Ni-Ti thin films were deposited on p-type Si (100) (Matsurf Tech. Inc, USA) substrate using the dc-magnetron co-sputtering technique. To achieve the uniform growth of Ni-Ti films Si substrate was rotated (60 rpm) in the horizontal plane of the targets. High purity targets of Ni (99.99%) and Ti (99.99%) of 3 mm thick and 50 mm diameter (Neyco supplier, France) were used for deposition. The substrates were cleaned in an ultrasonic bath containing a mixture of (1:4) trichloroethylene and distilled water, respectively. Before deposition, the sputtering chamber was evacuated to a base pressure of about 2×10^{-7} torr, while during deposition the pressure was kept at 3×10^{-3} torr. The pressure of Ar gas (99.99 at. %) was regulated to be 9×10^{-3} torr inside the chamber before deposition and sputtering of both the targets and Si substrate for ten minutes performed for cleaning. After cleaning, the deposition was performed for 1 hour 40 minutes using direct current powers of 100 W for Ti and 50 W for Ni target. The target to substrate holder distance was fixed approximate 16 cm. During deposition, the substrate temperature was kept at 550 °C to achieve the crystalline NiTi thin films. The surface morphology and microstructure of the films were studied using FESEM (Nova Nano FE-SEM 450 FEI) and AFM using a Bruker make Nanoscope V system with a Si_3N_4 cantilever in tapping mode at Material Research Centre, MNIT Jaipur. The thickness and elemental composition of the films were measured using Rutherford backscattering spectrometer. The orientation, crystallinity and room temperature phase of the pristine and irradiated films were studied using X-ray diffractometer (Bruker D8 Advance) equipped with Cu K_α X-ray source in θ-2θ geometry having a scan speed of 0.6°/minute. The electrical resistivity of Ni-Ti films at different temperatures was measured using Four-terminal resistivity method over a temperature range from 100 to 400 K. The temperature of the films was measured by using Lake Shore thermocouple, and temperature ramp was set at 2 K/minute during heating and cooling cycles. The contacts on the films were made by using silver paint.

4.2. Ag (120 keV) implantation-induced modification of Ni-Ti shape memory alloy thin films

In order to enhance Ni-Ti SMAs properties, various surface modification techniques such as oxidation treatment [158], gas nitriding [159], various coating [160], laser melting [161), alkaline treatment and ion implantation techniques have been performed on Ni-Ti alloy [162,163]. The critical challenge for coating techniques focuses on the binding strength because of the problem of delamination. However, for surface modification of metals and alloys, ion implantation is a precise technique, which endows Ni-Ti SMA with the new modified surface layer with the ability to retain it’s superelastic and shape memory behavior in the thin films. The modified surface also affects the structural, electrical and mechanical properties by the presence of foreign ions [164,165]. It has been reported that the mechanical properties of the materials are strongly dependent upon the defect density, grain refinement, and precipitation, which lead to increase in resistance of materials against plastic deformation. However, these treatments result in change in martensite transformation temperature by change in internal stress and chemical composition of the matrix [166,167].

In the present study, Ni-Ti thin films were implanted with 120 keV Ag ions at different fluences ranging from 3×10^{15} to 3×10^{16} ions/cm^2. The correlation between the microstructure and mechanical properties of Ni-Ti thin films after implantation has been discussed in terms of crystallite size and dislocation density.

For implantation, prepared Ni-Ti thin films were implanted by 120 keV Ag ions (negative ion) using MC-SNICS ion source in the Low Energy Ion Beam Facility (LEIBF) of the Inter-University Accelerator Centre (IUAC), New Delhi. During implantation, the samples stage in the implantation chamber was kept under a pressure of ~6×10^{-7} torr. In the case of 120 keV Ag ions, the electronic and nuclear stopping power (S_e and S_n) in Ni-Ti thin film were calculated using SRIM 2008 code [168].

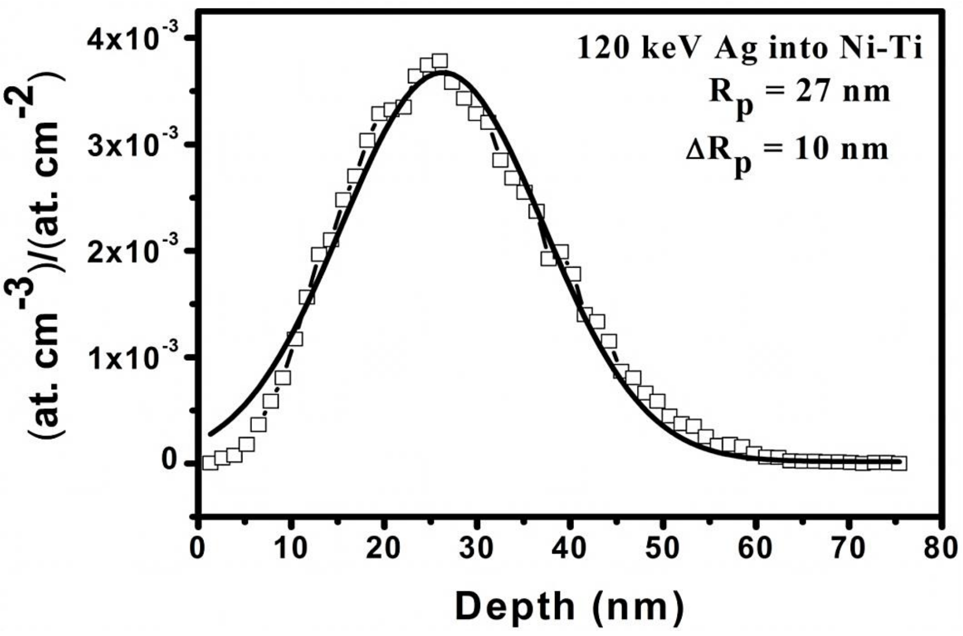

Figure 4.1. Depth distribution of Ag atoms in Ni-Ti films simulated by TRIM computer code for ten thousand 120 keV Ag ions.

The projected range of Ag ions was calculated by SRIM and found to be ~ 27.1 nm, where projected range denotes the average distance up to which Ag ions can penetrate into the film. The theoretical distribution of Ag ions was calculated by using TRIM 2008 computer simulation for ten thousand ions [168]. Assuming a normal Gaussian distribution the values of projected ion range R_p and the standard variation ΔR_p was obtained as shown in Figure 4.1.

Moreover, Figure 2 shows the SRIM simulation of ion trajectory (1000 Ag ions) for 120 keV Ag ions and defect production by implanted ions in ~270 nm film thickness. The separate histograms of Ni and Ti show the production of vacancies by implanted ions in the entire thickness.

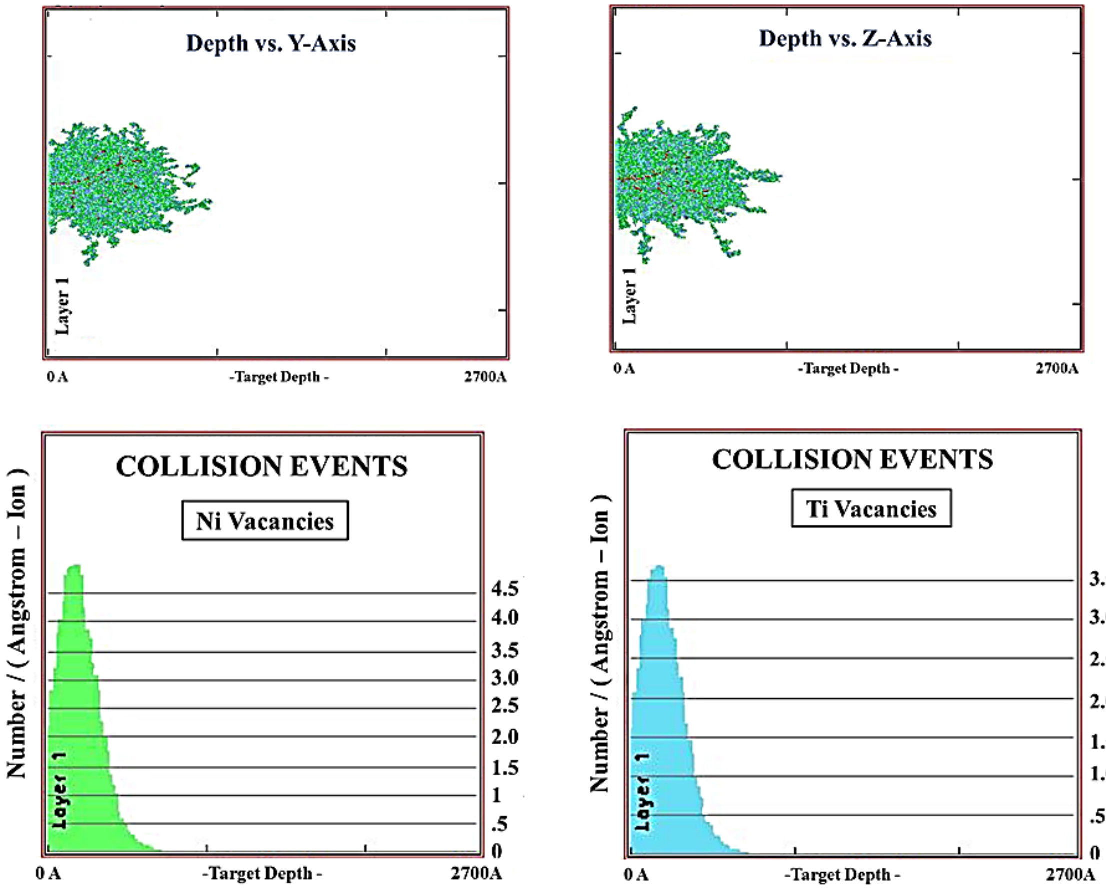

Figure 4.2. TRIM simulation for 1000 Ag ion of 120 keV energy in Ni-Ti film showing the ions trajectory for defects production by the energetic implanted ions in 270 nm thickness. The histograms of Ni and Ti showing the vacancies created by the passage of 120 keV Ag ions in Ni-Ti films.

It is noticed that the defects generated by incoming ions are in the range of energy of bombarded ions. The calculated number of vacancies for Ni is found to be 1.3×10^{24}

ions/cm^3 for the fluence of 3×10^{15} and for the fluence of 9×10^{15} and 3×10^{16} ions/cm^2, the number of vacancies are 4.0×10^{24} ions/cm^3 and 1.3×10^{25} ions/cm^3 respectively. Similarly, Ti vacancies created at different fluences of 3×10^{15}, 9×10^{15} and 3×10^{16} ions/cm^2 are found to be 1.0×10^{24}, 3.1×10^{24} and 1.0×10^{25} ions/cm^3 respectively. Thus the higher number of vacancies and hence higher damage is produced in Ni-Ti thin films.

4.2.1. Results and discussion

4.2.1.1. Rutherford Backscattering Spectrometry

RBS is used to determine the film thickness, atomic species, and their atomic concentration. Figure 3(a) displays the RBS spectrum of pristine Ni-Ti film on Si substrate at normal incidence with the detector positioned at 165° scattering angle. To measure the film thickness and quantify the atomic concentration of metals in film, the RBS spectrum was simulated by SIMNRA 12 [169], and a fit is shown in Figure 3. The Ni atomic concentration was calculated to be ~56.7 at% and Ti was found to be ~43.3 at%. The thickness of the film, estimated by SIMNRA simulation is found to be ~270 nm. Furthermore, the film implanted at a fluence of 3×10^{16} ions/cm^2 was also characterized by using RBS to know the preferential sputtering in the implanted film. The Ni to Ti ratio for the pristine and implanted films decreases from 1.3 to 1.26 at%; this change suggests that there is preferential sputtering in the Ni-Ti system during implantation process.

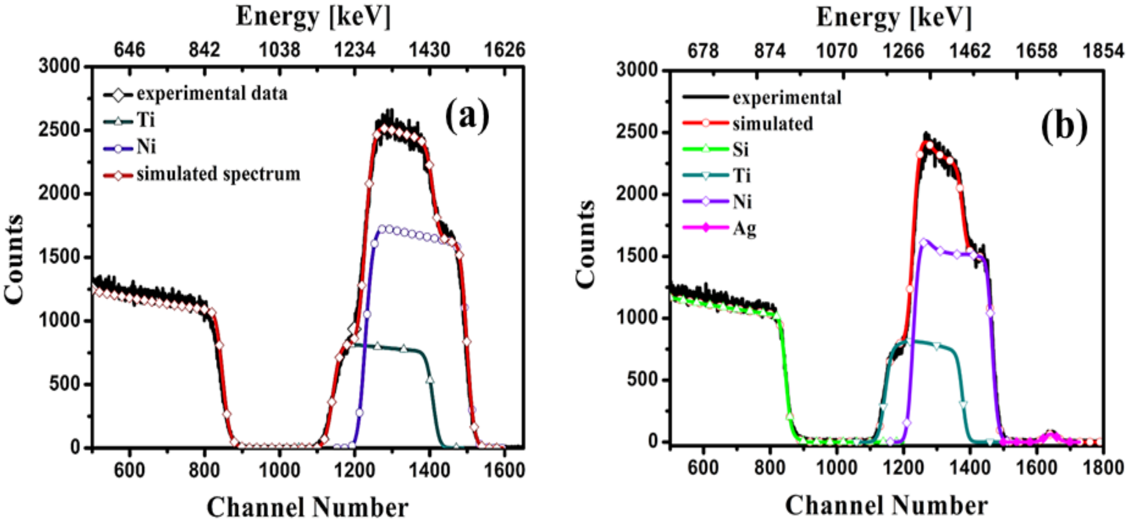

Figure 4.3. RBS spectrum for Ni-Ti pristine film (a) and implanted film at a fluence of 3×10^{16} ions/cm^2 (b) along with SIMNRA simulation.

Hence the variation in concentration of Ni from 56.7 in pristine to 55.2% in the implanted film is attributed; consequently, the preferential sputtering of Ni atoms over Ti atoms takes place.

4.2.1.2. X-ray diffraction

XRD pattern of Ni-Ti pristine film and also of those implanted by 120 keV Ag ions at fluences of 3×10^{15}, 9×10^{15} and 3×10^{16} ions/cm^2, respectively, are shown in Figure 4. XRD pattern reveals that both the phases, austenite phase (*A*) (cubic; JCPDS file no. 65-5537) as well as martensite phase (M) (monoclinic; JCPDS file no. 77-2170), were formed in Ni-Ti pristine films deposited at 550 °C, and planes corresponding to their structure are marked by corresponding Miller indices. The most intense peak at 2θ = 42.5° is due to the (110) fundamental reflection corresponding to cubic structure and the peak at 2θ = 43.9°, which is due to (002) fundamental reflection corresponding to monoclinic structure, respectively.

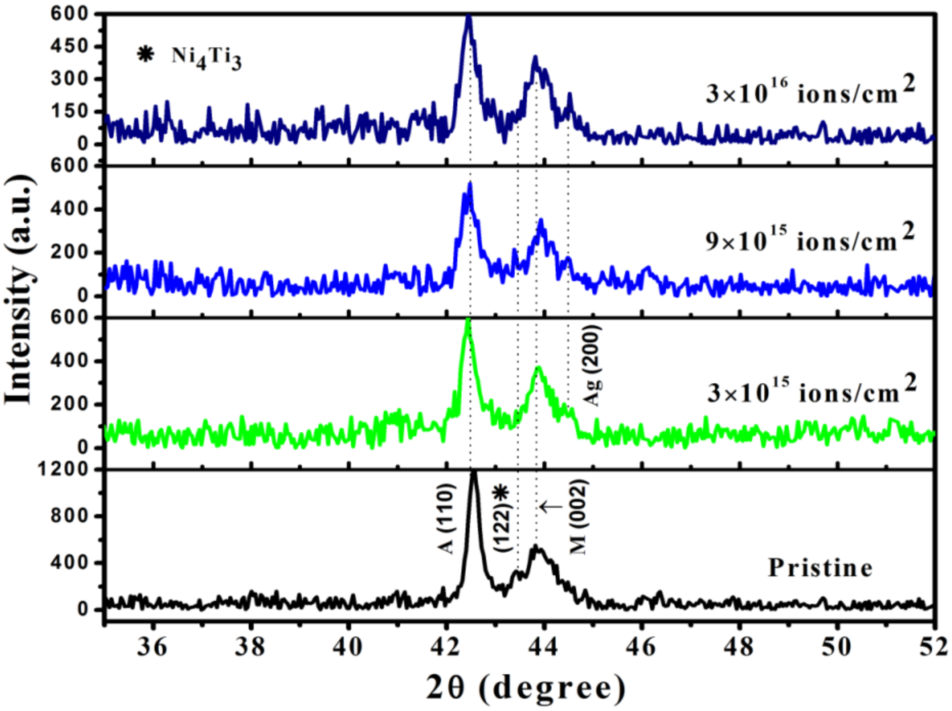

Figure 4.4. XRD spectra of pristine and 120 keV Ag ions implanted Ni-Ti thin films deposited at 550 °C by using the dc-magnetron co-sputtering technique.

Moreover, a small peak at 43.2° was observed due to Ni_4Ti_3 precipitation phase corresponding to (122) fundamental reflection. The evolution of the XRD peak with implantation fluences exhibits different trends. Figure 4.4 shows that at the lowest fluence of 3×10^{15} ions/cm^2, a small peak at $2\theta = 44.5°$ arises corresponding to Ag (200) plane (JCPDS file no. 03-0921), indicating the structural change produced by the implanted ions [170].

The mean crystallographic crystallite size (D) of the pristine and implanted thin films was calculated from the XRD data corresponding to austenite (110) and Ag (200) peaks by applying Scherrer's formula [142].

$$D = \frac{0.9\lambda}{\beta \cos\theta} ------------------------ (3.9)$$

where λ is the wavelength of Cu-K$_\alpha$ (λ = 0.154 nm) radiation, β and θ are full width at half maxima (FWHM) and Bragg's angle, respectively. The calculated value of crystallite size for the pristine film is 32.7 nm, and for the films implanted at different fluences 3×10^{15}, 9×10^{15}, and 3×10^{16} ions/cm^2 is found to be 30.2 nm, 20.6 nm and 23.7 nm, respectively, as summarized in Table 4.1. Also, the crystallite size corresponding to Ag (200) peak at fluences of 9×10^{15}, 3×10^{16} ions/cm^2 is calculated and found to be 22 nm and 27 nm, respectively. The crystallite size corresponding to film implanted at a fluence of 3×10^{15} ions/cm^2 by Ag ions could not be calculated due to small Ag signal.

The microstrain (ε) of pristine and implanted Ni–Ti thin films at different fluences was calculated by using the following equation [171,172]:

$$\varepsilon = \frac{\beta_G \cot\theta}{4} ------------------------ (4.1)$$

where β_G is FWHM (in radian) and θ = angle of diffraction, respectively. The calculated values of microstrain were observed to increase with a decrease in the crystallite size up to a fluence of 9×10^{15} ions/cm^2 and it decreases at the higher fluence of 3×10^{16} ions/cm^2. The calculated values of microstrain in pristine film are 0.29 and for the films implanted at different fluences 3×10^{15}, 9×10^{15}, 3×10^{16} ions/cm^2 was found to be 0.31, 0.46 and 0.40, respectively, as reported in Table 4.1.

Fluence (ions/cm^2)	**2θ (degree)**	**FWHM (degree)**	**Crystallite sized (D) (nm)**	**Micro-strain (ε)%**	**Dislocation density (δ)×(10^{15} line/m^2)**	**(R_{rms}) (nm)**
Pristine	42.56	0.26	32.7	0.29	0.93	2.14
3×10^{15}	42.44	0.28	30.2	0.31	1.09	1.18
9×10^{15}	42.46	0.41	20.6	0.46	2.35	0.80
3×10^{16}	42.46	0.35	23.7	0.40	1.78	0.37

Table 4.1. Microstructural parameters of pristine and implanted Ni-Ti thin films at different fluences.

The film implanted at higher fluence (3×10^{16} ions/cm^2) shows an increase in crystallite size, which was calculated corresponding to (110) plane. Moreover, a simultaneous increase in intensity indicates improvement in crystallinity of Ni-Ti thin films. Therefore, it can be concluded that at higher fluence, film releases strain energy, which is primarily responsible for the growth of (110) plane, because most of the body-centred cubic orientations have a lower surface energy [173]. The peak broadening in XRD lines without affecting the peak position could be due to the non-uniform displacement of atoms after implantation with respect to their lattice position.

The dislocation density (δ) of the pristine and implanted thin films was calculated from the crystallite size (D) using the following relation [174], and values are shown in table 4.1.

$$\delta = \frac{1}{D^2} line/cm^2 ---------------------(4.2)$$

The dislocation density is defined as the length of dislocation per unit volume, while the dislocation is a line defect. The calculated values of dislocation density were strongly dependent upon the number of defects produced by the Ag ions. The XRD data for the pristine and films implanted at different fluences were obtained at room temperature (300 K). The XRD data (Figure 4.4) shows the presence of Ni_4Ti_3 phase at 43.2° (JCPDF file no. 39-1113) in the film deposited at 550 °C and also in the films implanted at different fluences. The presence of Ni-rich (Ni_4Ti_3) phase in Ni-Ti films leads to the formation of *R* phase as reported by Sanjabi et al. [175] and Gyobu et al. [176]. Due to the existence of Ni_4Ti_3 precipitate phase, the *R*-phase was observed in the present result, which was further confirmed by electrical resistivity versus temperature curves (Figure 4.6) in both heating and cooling cycles.

4.2.1.3. Atomic force microscopy

The surface morphology of pristine and Ag implanted films at different fluences of 3×10^{15}, 9×10^{15} and 3×10^{16} ions/cm^2, respectively, was analyzed by AFM. Figures 4.5(a)-(d) show the two-dimensional AFM images of pristine and implanted thin films with a scan area of 1µm×1 µm.

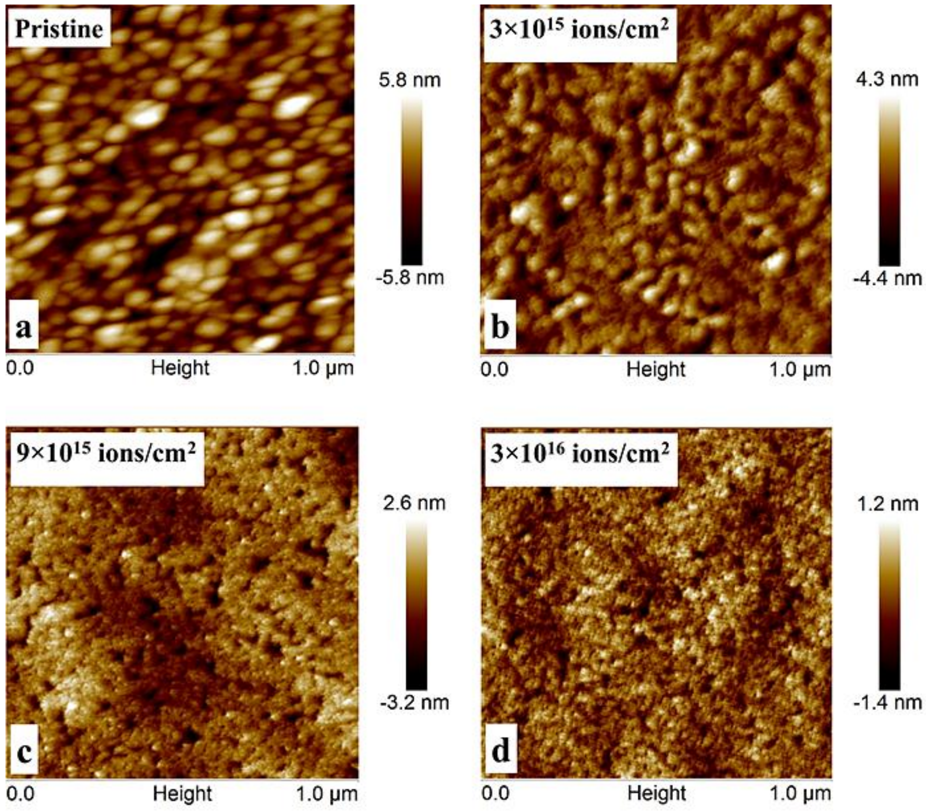

Figure 4.5. AFM surface micrograph of Ni-Ti thin films over a scan area 1×1 µm; (a) pristine Ni-Ti film, (b) Ni-Ti film implanted at 3×10^{15} ions/cm^2, (c) Ni-Ti films implanted at 9×10^{15} ions/cm^2 and (d) Ni-Ti thin film implanted at higher fluence 3×10^{16} ions/cm^2.

AFM images clearly show the change in morphology of films with an increase in incident ions per unit area on the films. The root means square (R_{rms}) surface roughness of Ni-Ti pristine and implanted films are given in Table 4.1. The root means square surface roughness was calculated based on the calculation of standard deviation in peak to valley difference in height within image area as reported in ref. [177].

$$\mathrm{R_{rms}} = \left[\frac{1}{N} \sum_{i=1}^{N} | Z_i - \overline{Z} |^2 \right]^{1/2} \text{----------------(4.3)}$$

where $\overline{Z}$ mean height distance and N is the number of surface height data. The R_{rms} value of pristine films is ∼2.14 nm, and for the films implanted at different fluences, it is found to be ∼1.09 nm, ∼0.80 nm and ∼0.37 nm, respectively. The R_{rms} values of surface roughness calculated by AFM images were observed to decrease with an increase in ion fluences, which could be due to a decrease in crystallite size and an increase in XRD peak broadening.

4.2.1.4. Electrical transport properties

Phase transformation behavior of pristine and 120 keV Ag-implanted thin films at different fluences 3×10^{15}, 9×10^{15} and 3×10^{16} ions/cm^2 was characterized by the four-point probe resistivity method. Figure 4.6(a)-(d) shows the resistivity versus temperature curves of pristine and implanted thin films at different fluences during heating and cooling cycles. At the time of experiment, the condition of stationary equilibrium was maintained by cycling the temperature stepwise with a sufficient time interval between every data point. In Figures 4.6(a)-(d), R_s, R_f, M_s and M_f denotes the start and finish temperature of formation of intermediate R phase [175], martensitic phase (B'_{19}) on cooling and R_s', R_f', A_s, A_f denotes the R phase, austenite phase (B_2) on heating, respectively. It was observed that austenite, martensitic and R phase are present in Ni-Ti pristine films and also in the films implanted at different fluences, as shown in Figures 4.6(a)-(d). A linear decrease of resistivity values was observed after implantation in Ni-Ti thin films with the continuous increase in the fluence; it may be explained as follows; during implantation, vacancy diffusion is increased and this increased diffusion of vacancies leads to the decrease in the resistivity values [178]. Figure 4.6(a) shows the resistivity versus temperature curves of pristine Ni-Ti film deposited at 550 °C, which reveals two-step phase transformation from martensitic (B'_{19}) to austenitic phase (B_2) and vice versa via R phase, during heating and cooling cycles. It was observed that upon heating, the value of electrical resistivity increases with an increase in the temperature up to 260 K because of the formation of *R* phase, but after phase transformation of martensite to austenite, the value of resistivity is found to decrease. The resistivity of films was measured by using the following equation [155]:

$$\rho = \frac{\pi t}{\ln 2}\left(\frac{V}{I}\right) \text{------------------} (4.4)$$

where *V* is the voltage, *I* current and *t* film thickness.

During heating and cooling cycles, *R*-phase transformation is observed in all the films implanted at different fluences. The formation of *R*-phase during phase transformation from austenite ($B_2 \leftrightarrow R$) induces significantly small transformation strain (~1%) when compared to the phase transformation from austenite to martensite ($B_2 \rightarrow B'_{19}$) phase transformation (~10%) [179]. Decrease in strain by twinning plays an important role in the formation of *R* phase because it proceeds by nucleation and growth in parent phase. Therefore, the formation of *R* phase is a self-accommodation process, which occurs gradually in the parent phase with decreasing temperature. The presence of *R*-phase transformation in the Ni-Ti shape memory alloy thin films are found to be very beneficial to the two ways shape memory effect which can remember both low and high temperatures shapes [180]. Due to this unique property, Ni-Ti SMA is considered as a promising material for actuation of some MEMS devices such as microsensors and microswitches [81]. Thin films of Ni-Ti SMA are very sensitive to environmental changes such as electrical field, magnetic field, stress, and temperature and thus they can be used for microsensor applications [181]. Other promising applications include optical fibre switching, probe tips for self-regulating equipment, fuel injectors, lens positioner, microrelay and switches embedded with on-chip circuit breakers to prevent overheating caused by accidental overload or short circuit, etc. [182]. In present work, two-way shape memory effect occurs due to the following reasons: existence of the Ni_4Ti_3 precipitate phase, intrinsic residual stress generation, higher Ni composition and biasing force generated by Si substrate.

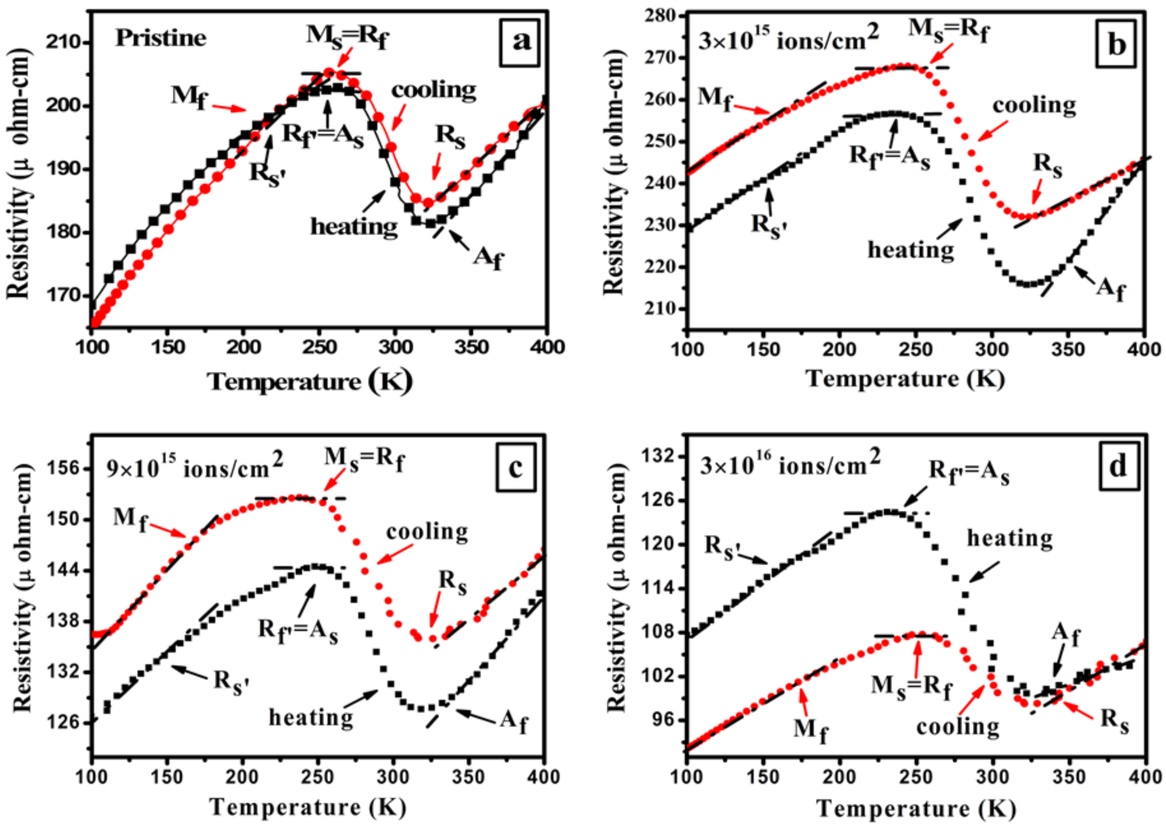

Figure 4.6. Electrical resistivity versus temperature curves of Ni-Ti pristine and implanted thin films at different fluences during heating and cooling cycles.

A two-step phase transformation in Ni–Ti films takes place in the following procedure as reported by Mohri et al. [183]:

A- phase →R- phase → M- phase (during cooling cycles),

M- phase → R - phase→ A- phase (during heating cycles).

Figure 4.6(b)-(d) accounts a two-step phase transformation (austenitic phase↔martensitic phase via *R* phase and vice versa) in Ni-Ti films implanted at 3×10^{15}, 9×10^{15} and 3×10^{16} ions/cm^2, respectively, during heating and cooling cycles. The values of austenitic A_f (finish temperature of austenitic phase) and martensitic phase M_s (start martensitic phase temperature) calculated from resistivity versus temperature curves were found to be 321 and 260 K for pristine film, 323 and 253 K for film implanted at 3×10^{15} ions/cm^2, 320 and 252 K for the film implanted at 9×10^{15} ions/cm^2, 330 and 238 K for the film implanted at a fluence of 3×10^{16} ions/cm^2. The thermal hysteresis width is defined by the temperature difference between the A_f and M_s and found to be 61, 70, 68 and 92 K for the pristine and the films implanted at different fluences. From resistivity versus temperature curves, it appears that film implanted at a fluence of 3×10^{16} ions/cm^2 shows much larger hysteresis width in comparison to pristine Ni-Ti films, which could be due to the structural defect and change in the chemical composition after ion implantation [184]. In case of the films implanted at different fluences at 3×10^{15}, 9×10^{15} and 3×10^{16} ions/cm^2, respectively, it is observed that hysteresis loop is not closed even at 100 K, which could be due to small grain size, lattice mismatching and intrinsic stress formed in films after implantation.

4.2.1.5. Nanoindentation

The mechanical properties of pristine and 120 keV Ag-implanted Ni-Ti films were determined by CSM nanoindentation. Figure 4.7 (a)-(d) shows the indenter load versus displacement curves as a function of ion fluences taken at room temperature. These curves are used to calculate the basic mechanical properties such as indent depth recovery ratio (δ), elastic modulus (E_r), hardness (H) and plastic resistance parameter (H/E_r). All results were calculated by using the Oliver and Pharr method [155]:

The elastic modulus is defined by the equation:

$$E_r = \frac{S\sqrt{\pi}}{2\sqrt{A}} ----------------------(4.5)$$

where S (unloading stiffness) $= dP/dh$ and A is the projected contact area. The elastic modulus of the material is related to the modulus of elasticity by the following relation:

$$\frac{1}{E_r} = \frac{(1-v_i^2)}{E_i} + \frac{(1-v_s^2)}{E_S} ----------------(4.6)$$

where subscript *i* represents the indenter material and subscript *s* corresponds to sample material, and ν is the Poisson's ratio.

The hardness (H) of the material is expressed by the following formula:

$$H = \frac{P_{\max}}{A} ------------------------(3.13)$$

where P_{max} is the maximum load and A is the projected contact area. The obtained values by nanoindentation test are listed in table 4.2. The elastic modulus of the pristine film was 161 GPa and for the films implanted at different fluences 3×10^{15}, 9×10^{15} and 3×10^{16} ions/cm^2, respectively, it was found to be 164, 173 and 170 GPa, respectively, as mentioned in table 4.2.

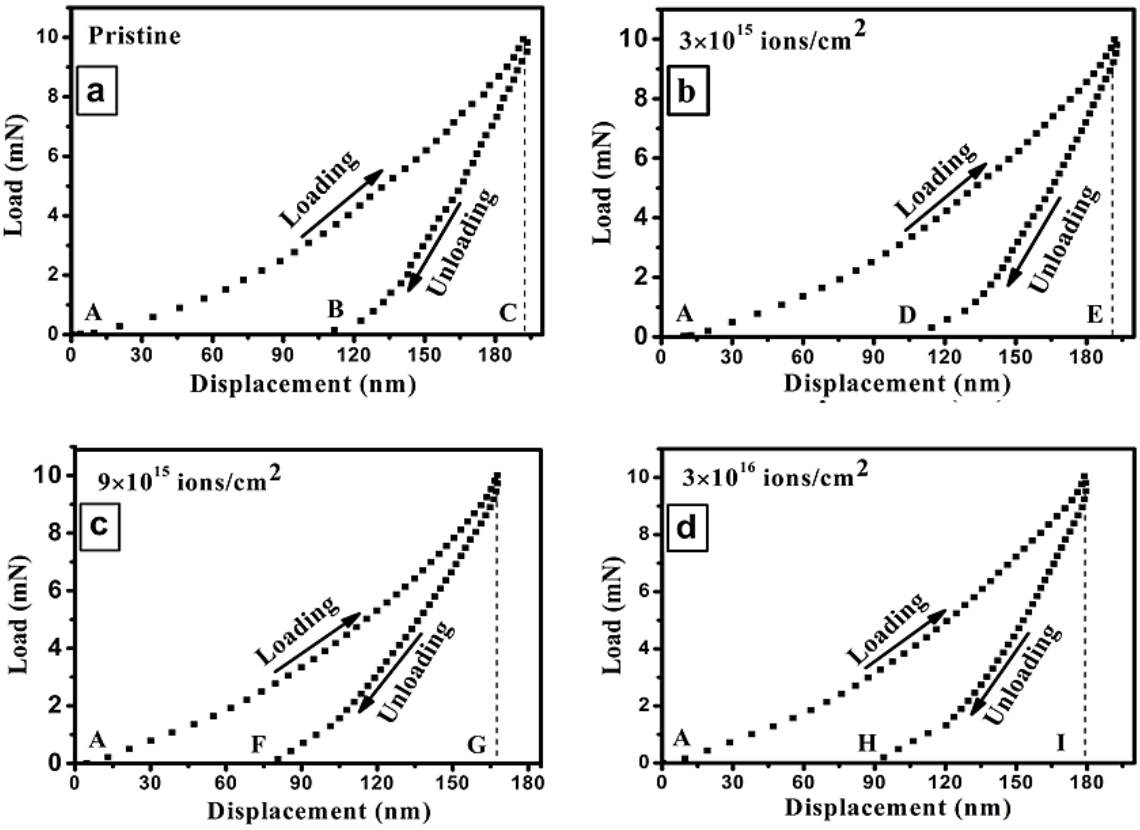

Figure 4.7. Load versus displacement curves of pristine and Ag implanted Ni-Ti thin films at different fluences.

The hardness of pristine film was 17.7 GPa and for the films implanted at 3×10^{15}, 9×10^{15} and 3×10^{16} ions/cm^2 respectively, it was found to be 20.1, 28.2 and 22.3 GPa, respectively. It has been observed that Ni-Ti film exhibits a higher value of hardness (28.2 GPa) at a fluence of 9×10^{15} ions/cm^2 in comparison to pristine (H = 17.7 GPa) film; this is ascribed to smaller crystallite size of the implanted film compared to pristine films, which is also confirmed by XRD analysis. It is found that a decrease in crystallite size is almost 1.5 times lower than the pristine film. Similar behavior was also reported by Choudhary and Vishnoi et al. in Ni-Ti/PZT/TiO_x heterostructures and NiMnSn thin films. They concluded that a large number of grain boundary leads to smaller crystallite size, which restricts the wear of the films to a large extent by acting as barriers to dislocation motion [185,186].

Table 4.2. A comparison of hardness and elastic modulus of pristine and 120 keV Ag implanted Ni-Ti thin films.

Fluence (ions/cm^2)	**Total depth h_{max} (nm)**	**Residual depth h_r (nm)**	**Depth recovery ratio (δ)**	**Hardness H (GPa)**	**Elastic modulus E_r (GPa)**	**H/E_r**
Pristine	192.3	112.3	0.41	17.7	161	0.10
3×10^{15}	190.6	114.2	0.40	20.1	164	0.12
9×10^{15}	167.4	80.9	0.51	28.2	173	0.16
3×10^{16}	178.9	94.2	0.47	22.3	170	0.13

It is also reported by several authors that smaller grain size and higher dislocation density increase the yield strength of the material [187, 188]. The Ni-Ti films implanted at a fluence of 9×10^{15} ions/cm^2 shows higher dislocation density and smaller crystallite size in comparison to the films implanted at different fluences as reported in Table 1. Hardness to-elastic modulus (H/E_r) ratio is also an important parameter to measure the elastic and elastic-plastic behavior of thin films. A higher H/E_r value is found for the film implanted at a fluence of 9×10^{15} ions/cm^2, which indicates small strain energy and better wear resistance to plastic deformation.

The indentation-induced superelastic effect can be characterized by depth recovery ratio, which is estimated from the load versus displacement curve by using the following relation [178]:

$$\text{Depth recovery ratio } (\delta) = \frac{(h_{\max} - h_r)}{h_{\max}} \text{---------------} (4.7)$$

where $h_{\max}$ and h_r correspond to penetration depth at maximum load, residual displacement when load returned to zero during unloading, respectively. The values of $h_{\max}$ and h_r indicated by *C*, *E*, *G*, *I* and *B*, *D*, *F*, *H* respectively for different fluences are shown in Figures 4.7 (a)-(d), and the values of depth recovery (δ) for the pristine and implanted films are shown in table 4.2. The h_r and $h_{\max}$ are the characteristics of elastic nature of the materials and hardness. The Lower the values of h_r, the higher is the elasticity of materials, and also lower values of $h_{\max}$ show higher hardness of materials.

Summary:

In this chapter, Ag ion implantation induced modifications of Ni-Ti alloy thin films have been investigated. Ag ion implantation at different fluences leads to the formation of new phases in the films and causes significant changes in microstructural parameters. AFM study reveals changes in the surface roughness values with increases in ion fluence. It is concluded that, a two-step phase transformation ($B_2 \leftrightarrow R \leftrightarrow B'_{19}$) take place in Ni-Ti and Ni-Ti-Ag films during heating and cooling cycles. The film implanted at a fluence of 3×10^{16} ions/cm^2 shows the large thermal hysteresis during heating and cooling cycles due to the generation of structural defects in the crystalline Ni-Ti matrix after the ion implantation. Significant improvement in mechanical properties is achieved in the film implanted at a fluence of 9×10^{15} ions/cm^2. Improved properties of Ni-Ti films pave the way to future MEMS application.

Chapter 5

Swift Heavy Ion Irradiation Induced Modifications in Ni-Ti Shape Memory Alloy Thin Film

In this chapter, the effect of swift heavy ion irradiation on Ni-Ti thin films has been investigated. This chapter has been divided into three parts. First part describes the reduction of the amount of shape memory behavior under swift heavy ion irradiation. Improvement in structural and mechanical behavior of Ni-Ti films under swift heavy ion is described in second section. The variation in structural and mechanical properties of Ni-Ti films associated with the crystallite sized are described in section three. The change in various properties of Ni-Ti films have been observed to depend on ion beam species and fluences. A summary of engineering of various properties by swift heavy ion irradiation is discussed in the last of the chapter.

5.1. Au (120 MeV) ion irradiation induced modifications in nanostructured Ni-Ti shape memory alloy thin films

Swift heavy ion (SHI) irradiation has unique capabilities for modification of surface layers on metals and alloys including their crystal structure, chemical composition, physical and mechanical properties. SHI induced damaging effects can benefit the shape memorial behavior and bias the shape recovery if the damaging effects are more controlled. It has been reported that structural, electrical and mechanical properties of the materials strongly depends upon the precipitation, defect density, grain refinement in the material produce by SHI irradiation [189,190].

In the present study, a preliminary work done by using SHI irradiation on Ni-Ti films is reported. This current work is focussed on ion-beam induced modifications of 120 MeV Au ion irradiated Ni-Ti sputter deposited thin films which are investigated using FESEM, AFM, RBS, XRD and Electrical resistivity measurements.

The main objective of the present study is to investigate the effects of SHI irradiation on both phases, austenite as well martensite phase simultaneously at room temperature for the future applications of these materials in harsh environments such as space or nuclear reactor. In the present experiment, the critical value of fluence for shape memory behaviour has been investigated, below this critical fluence Ni-Ti film shows the SMA behavior and above that fluence, the shape memory behavior degraded. Irradiation at low fluence below the critical value creates the defect in the materials in a controlled manner which increases the vacancies diffusion, and this diffusion of vacancies leads to higher mobility in the materials. The schematic diagram of the work presented is shown in Fig. 5.1. The modifications in the structural and electrical properties against SHI irradiation at different ions fluences of 120 MeV Au ions energy were characterized by FESEM, AFM, XRD and Four-terminal resistivity measurement.

Further, the Ni-Ti films deposited on Si substrate were irradiated with 120 MeV Au ion beam at IUAC New Delhi, India, using 15 UD pelletron accelerator facility. Ion fluence was varied from 1×10^{12} to 3×10^{13} ions/cm^2. The electronic energy loss S_e and nuclear energy loss S_n calculated for Ni-Ti SMA using 120 MeV Au ions were $\sim3.1\times10^3$ and 5.3×10^1 eV/Å, respectively, and the range of Au ions in Ni-Ti was $\sim$7.6 μm as calculated by SRIM programme [168], which was found to be much higher than the film thickness, so most of the Au ions after passing through the film get buried into the Si substrate.

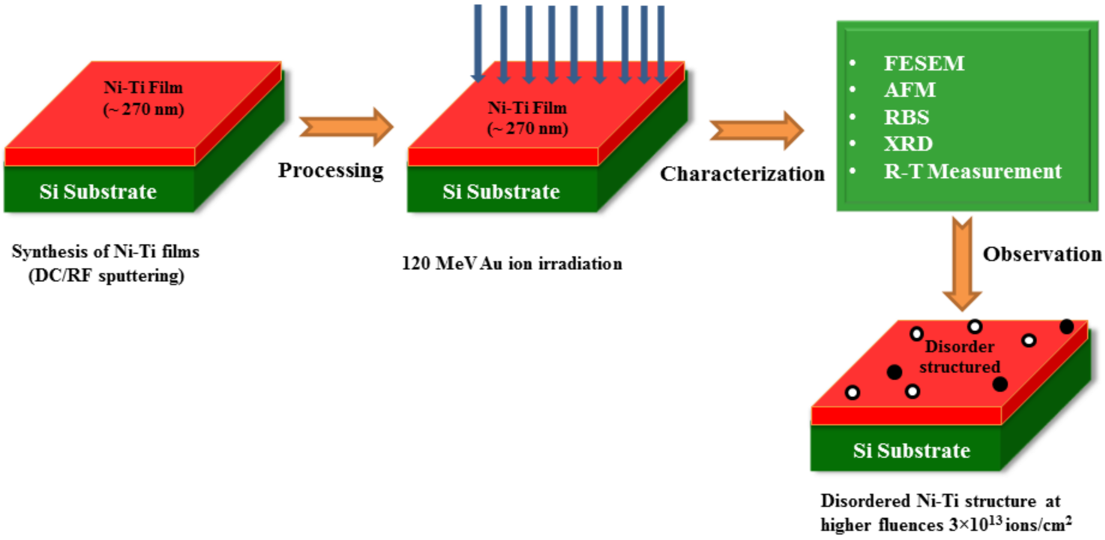

Figure 5.1. Schematic diagram of Ni-Ti thin films deposited at 550 ˚C and irradiated at different fluences.

5.1.1. Results and discussion

5.1.1.1. Field emission scanning electron microscopy

The surface properties of pristine and 120 MeV ion irradiated Ni-Ti films were determined by FE-SEM. Fig. 5.2(a) to (e) show the FE-SEM micrographs of pristine and irradiated films at different fluences ranging from 1×10^{12} to 3×10^{13} ions/cm^2. It is clear from these images that different shaped grains such as pyramidical and spherical, are formed and the grain size first increases with increase in the ion fluence, remain constant up to a certain fluence and then decreases first gradually and then considerably with the further increase in the fluence. Fig. 5.2(a) shows that in the pristine film pyramidical and spherical shaped grains are observed depicting the presence of both austenite and martensite phases in the films. But, the pyramidical grains are quite large in number as compared to spherical grains due to the dominance of austenite phase in the film. Fig. 5.2(b) shows diffused pyramidical and spherical grains present in the film irradiated at a fluence of 1×10^{12} ions/cm^2. The grain size increases but the number of pyramidical grains decreases while that of spherical grains increases due to the decrease of austenite phase and slight increment of martensite phase in the film in accordance with the XRD data which is later shown decrease in the intensity of (110) peak depicting austenite phase while broadening and slight increase in the intensity of (002) peak depicting martensite phase. With increase in fluence to 5×10^{12} ions/cm^2 (Fig. 5.2(c)), FESEM micrograph show grains of similar morphology and constant size as found in film irradiated at fluence 1×10^{12} ions/cm^2. At further increased fluence of 1×10^{13} ions/cm^2, smaller grains with diffused grain boundaries are observed (Fig. 5.2(d)). As the fluence is increased to 3×10^{13} ions/cm^2 (Fig. 5.2(e)), the grain size decreases considerably to the extent that surface morphology of the film completely disappears and a smooth film appears which may be due to the amorphization of the film at a fluence of 3×10^{13} ions/cm^2.

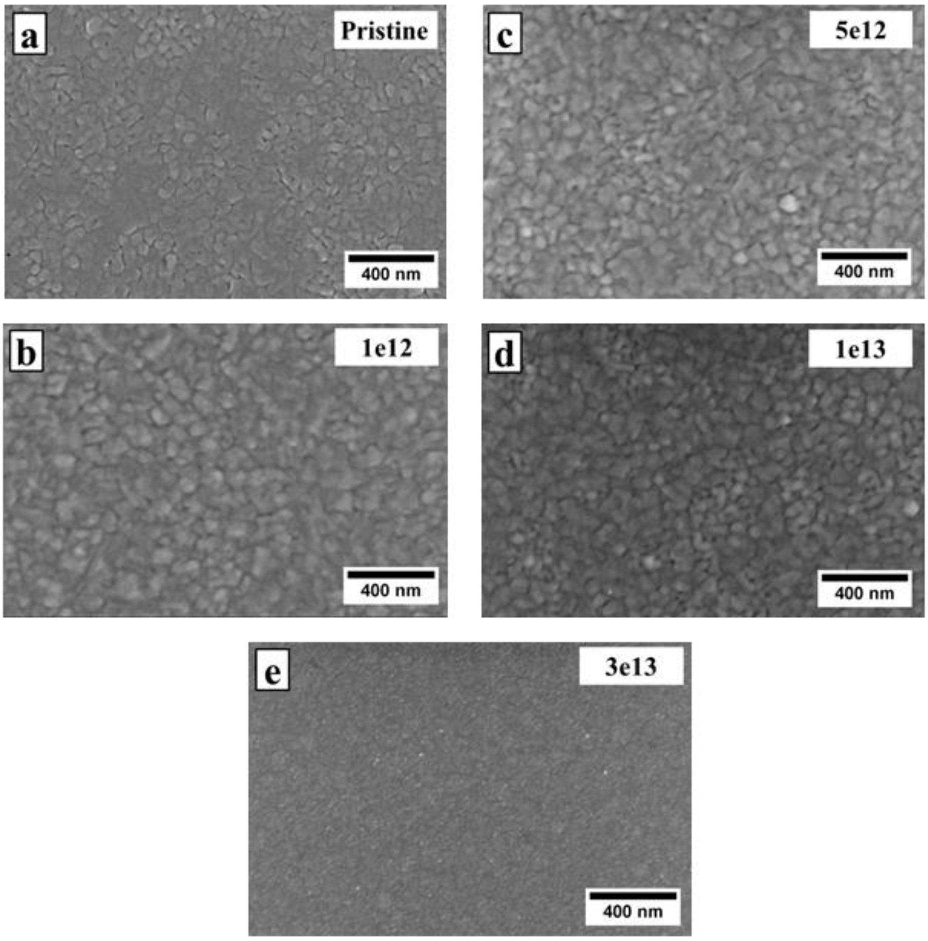

Figure 5.2. FESEM images of pristine and 120 MeV Au ion irradiated Ni-Ti thin films at different fluences.

5.1.1.2 Atomic force microscopy

Apart from FESEM, the surface morphology (grain size and surface roughness) of all the films was also analyzed using AFM. Fig. 5.3(a) to (e) shows the two dimensional

AFM images of as-deposited and 120 MeV Au ion irradiated Ni-Ti SMA films at a scale of 1µm×1µm. The root-mean-square roughness (R_{rms}) of the surfaces of the films was obtained from AFM scans over film areas of 2 µm×2 µm by scanning three times, each time at the different location for every film. R_{rms} of the films was calculated using the following formula,

$$R_{rms} = \left[\frac{1}{N} \sum_{i=1}^{N} | Z_i - \overline{Z} |^2 \right]^{1/2} \text{-----------------}(4.3)$$

where, R_{rms} is the root mean square roughness taken from the mean image data plane and Z_i is the current Z value, Z is the Peak-to-valley difference in height values within the analyzed region, N is the number of points within the box cursor in nm.

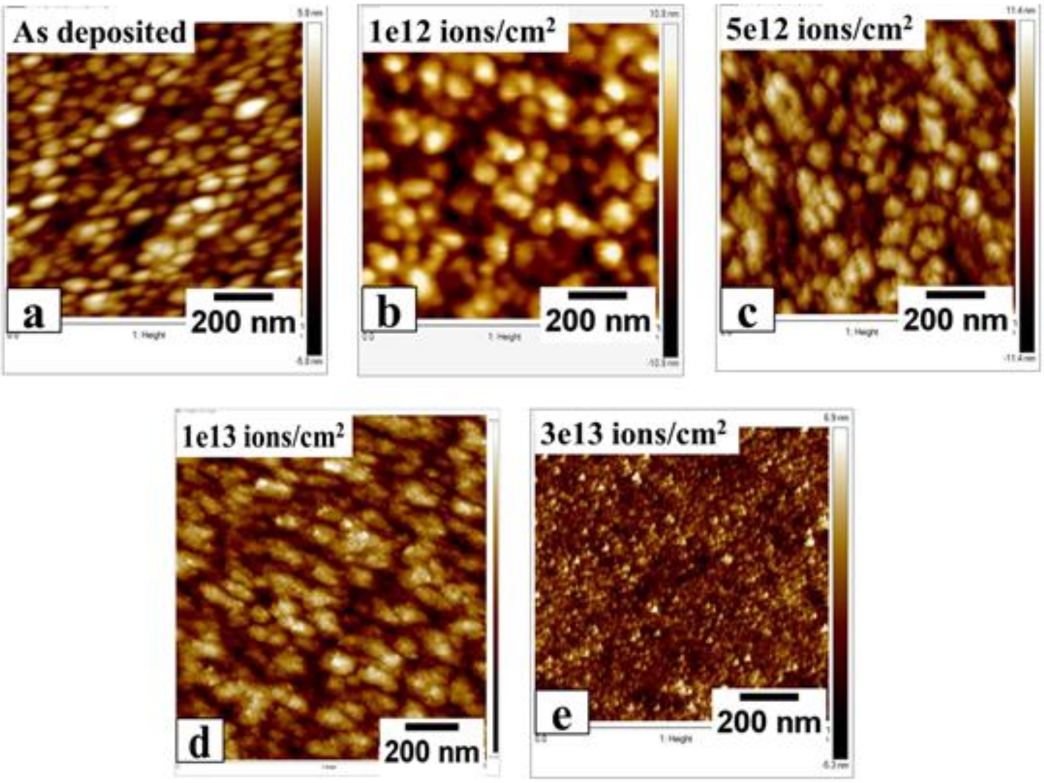

Figure 5.3. AFM images of pristine and 120 MeV Au ion irradiated Ni-Ti thin films at different fluences.

The average values of surface roughness of as-deposited and irradiated films at different fluences 1×10^{12}, 5×10^{12}, 1×10^{13} and 3×10^{13} ions/cm^2 was found to be ~ 2.9 nm, ~ 3.98 nm, ~ 3.85 nm, ~ 3.76 nm and 1.88 nm respectively. It was observed that root mean square surface roughness first increases with increase in fluence to 1×10^{12} ions/cm^2 due to the increased intensity of martensite phase in the film and then it again decreases but to a smaller extent for films irradiated at 5×10^{12} and 1×10^{13} ions/cm^2 respectively, whereas it decreases considerably for film irradiated at 3×10^{13} ions/cm^2 due to the complete amorphization of the film resulting in the disappearance of both the austenite and martensite phases, in accordance with the FESEM result as reported in Fig. 5. 2. The sizes of the grains calculated by AFM also show similar behaviour as calculated by AFM also show similar behavior as calculated by FESEM images.

5.1.1.3. Rutherford backscattering spectroscopy

The major problem in using Ni-Ti films for various applications is the difficulty in controlling their chemical composition. The transformation temperatures of Ni-Ti also depend considerably on the composition of films.

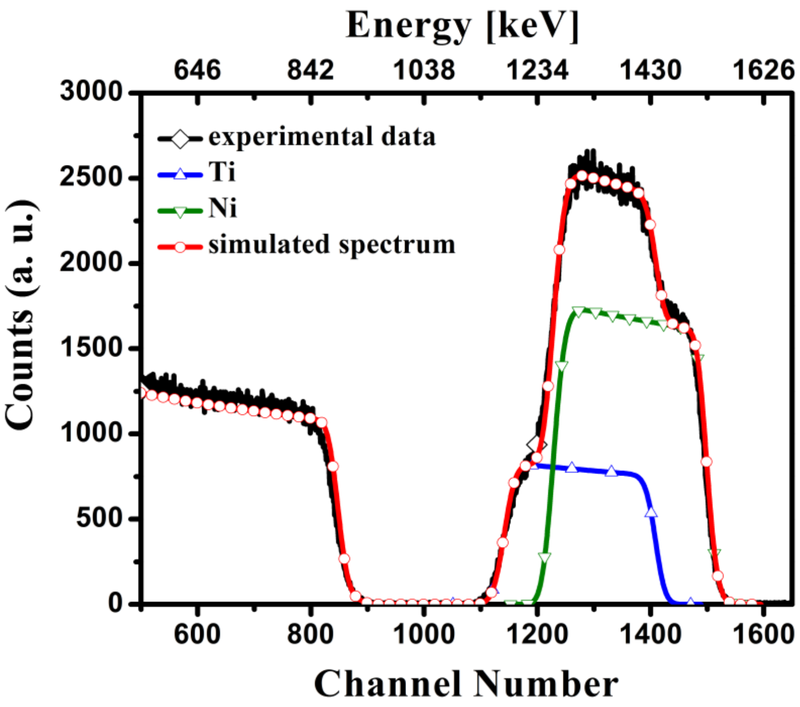

Figure 5.4. RBS spectra (2 MeV He^+) perform on as-deposited film shows Ni and Ti edges for the channel number in the range of 1100-1500 range.

A slight change in the composition results in a remarkable change in the transformation temperatures and thus the various properties of the films. So the formation of desired composition in the films and also the accurate determination of composition in the films after formation is very essential. Rutherford backscattering spectroscopy (RBS) is an efficient method to determine the composition of the films as well as film thickness, atomic species present in the films and their concentration. Fig. 5.4 shows Rutherford backscattering spectrum of as deposited Ni-Ti film on Si substrate. In order to measure the film thickness and to determine the atomic concentration of metals in the film, the RBS spectrum was simulated by SIMNRA **[**169**]**, and a fit is shown in Fig. 5.4 by continuous line. The Ni atomic fraction was calculated 56.7 at. % and Ti was found to be 43.3 at. %. The films thickness simulated by SIMNRA was found to be ~ 270 nm.

5.1.1.4. X-ray diffraction

Fig. 5.5 shows the room temperature X-ray diffraction (XRD) pattern of Ni-Ti pristine film and also of the films irradiated by 120 MeV Au ions at different fluences ranging from 1×10^{12} to 3×10^{13} ions/cm^2. In addition to substrate peak, XRD pattern reveals that both the phases, austenite (B2) as well as martensite (B19’) exist in the pristine sample. No traces of other phases like Ti_2Ni and Ti_3Ni_4 were observed in XRD pattern of these films. The planes corresponding to austenite and martensitic structure are marked by their Miller indices. The most intense peak at 2θ=42.5o which is due to the (110) fundamental reflection corresponds to cubic austenite structure, and the peak at 2θ = 43.9^o which is due to (002) fundamental reflection corresponds to monoclinic martensite structure. The peaks $(\bar{1}36)$, $(1\bar{3}6)$ and $(0\bar{4}4)$ correspond to oxidized Si substrate [167]. The film irradiated at a fluence of 1×10^{12} ions/cm^2 shows decrease in the intensity of (110) peak (corresponding to B2 phase) and the (002) peak, corresponding to B19’, becomes broad. It indicates the damage of austenite structure in the film upon ion irradiation. With increase in the fluence to 5×10^{12} ions/cm^2, the peak intensity of both the phases decreases. With further increase in fluence to 1×10^{13} ions/cm^2, the intensity of these peaks decreases considerably. The decrease in intensity of both the phases at this fluence shows the partial amorphization of the austenite and martensite phase and suppression of phase transformation by the electronic energy deposition in Ni-Ti regime. At a much higher fluence of 3×10^{13} ions/cm^2, all the peaks are vanished and the film gets completely amorphized due to excessive ion impact. Amorphization by electronic excitation and ionization is also possible, where the energy of the incoming ion is transferred to the atoms of lattice via electron-electron and electron-phonon coupling. Such electron excitations can also cause local heating followed by a rapid quenching (thermal spikes) producing lattice distortions which are so drastic that they relax into an amorphous state [191].

The XRD pattern shows the crystalline to amorphous phase transformation of Ni-Ti thin films by SHI irradiation at fluence of 3×10^{13} ions/cm^2. The suppression of both the phases under the SHI irradiation has been observed by introduction of lattice defects and high strain generation by the bombardment of Au ions on Ni-Ti films. The amorphization of materials depends on the irradiation conditions such as ion fluence, irradiation temperature and nature of the ions as reported by several authors [192, 193]. In the case of electron and proton irradiation, it has been well established in the literature that irradiation cause stress field and lattice disorder in the materials [194].

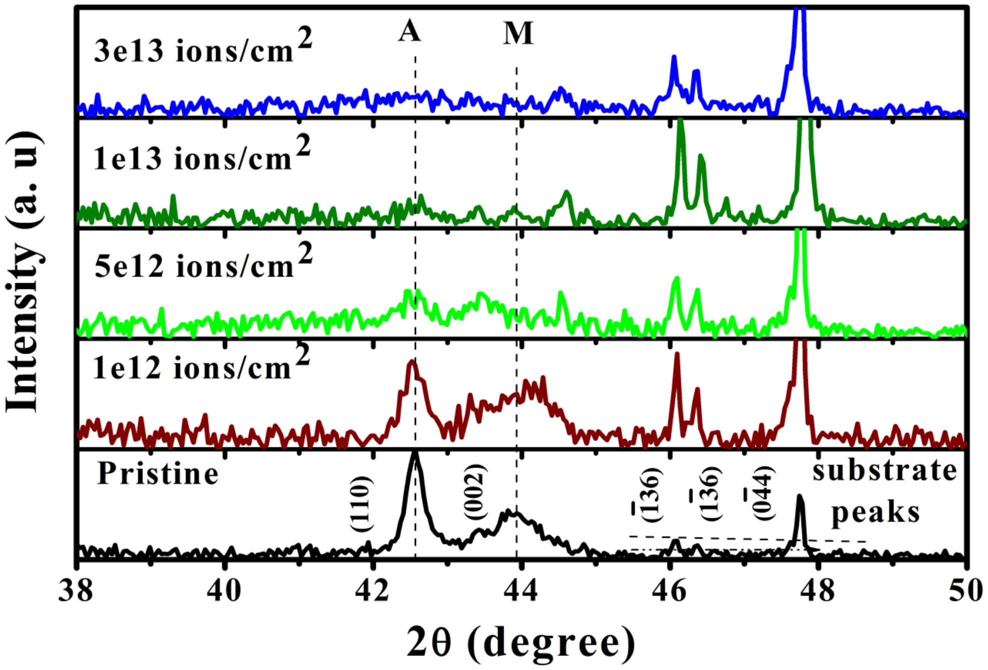

Figure 5.5. X-ray diffraction spectra of pristine and 120 MeV Au ion irradiated Ni-Ti thin films at different fluences.

The lattice disorder by electronic excitation produces the point defect (vacancy and interstitial pairs) which is evenly distributed in the material and suppress the transformation temperature and cause amorphization. Irradiation at critical fluences, produce isolated amorphous zone in a crystalline material and density of these amorphous zones is continuously increased with increase the fluences and at a higher fluence these amorphous zone starts to overlap and at a critical fluence, material become amorphous.

5.1.1.5. Electrical measurement

The variation of electrical resistance with temperature is an effective method for determining the formation of various phases in shape memory alloys thin films and studying their phase transformation behaviour since the high temperature ordered austenite phase, intermediate R phase and low-temperature disordered martensite phases are accompanied with changes in the electrical resistance due to their different crystal structures. Fig. 5.6(a) to (d) show the electrical resistance versus temperature curves of pristine and 120 MeV Au ion irradiated Ni- Ti films, measured by four-terminal resistivity method during cooling and heating cycles in the temperature range

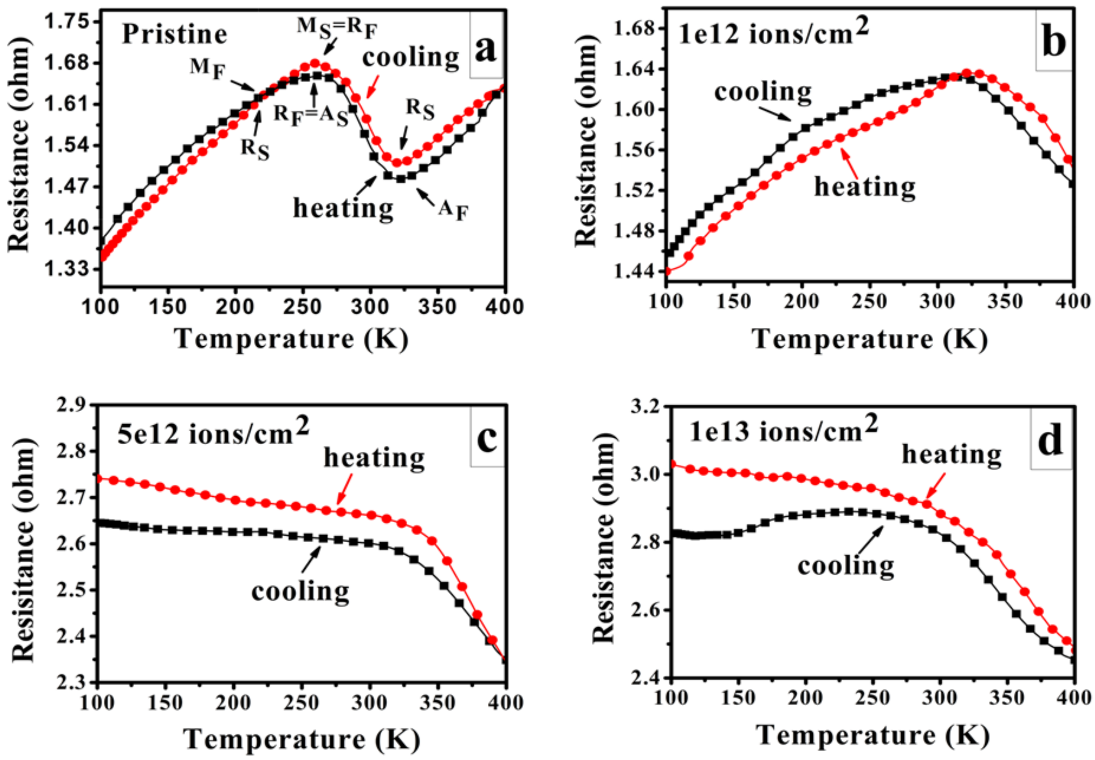

Figure 5.6. Electrical resistance versus temperature (R-T) curves of pristine and 120 MeV Au ion irradiated Ni-Ti films, during heating and cooling cycle.

100-400 K. At the time of experiment, the condition of stationary equilibrium was maintained by cycling the temperature stepwise with a sufficient time interval at every data point. In figures 5.6(a) to (d) R_s, R_f, M_s, M_f and A_s, A_f, denote the start and finish temperatures of formation of the intermediate R phase and martensitic (B19') phase on cooling, and austenitic (B2) transformation on heating, respectively.

Fig. 5.6(a) shows the electrical resistance versus temperature (R-T) curve of pristine Ni-Ti film. The pristine film shows a very clear two-step phase transformation B2↔R↔B19' during heating and cooling cycles. During heating cycle, electrical resistance of B2 phase was observed to increase with increase in the temperature because of the formation of R phase, but during cooling below 400 K, first the resistance value of B19' phase decreases linearly because of decrease in the intensity of electron-phonon interaction but at temperature below Rs (310 K), the electrical resistance again starts increasing with temperature because the austenite B19' phase gets distorted and starts transforming to R phase with higher electrical resistance, because in small sized grains the restriction imposed by the grain boundaries for the formation of R phase is small as compared to that offered for phase transformation from austenite to martensite phase [155**]**. On cooling the film further below R_f (260 K), the electrical resistance goes on decreasing with temperature because R phase to martensite transformation begins to occur which gets completed below M_f. Thus, during both heating and cooling cycles, formation of R phase was observed which possess higher electrical resistance in comparison to B2 and B19' phases. Fig. 5.6(b) shows the R-T curve of thin film irradiated at a fluence 1×10^{12} ions/cm^2, in which slightly different trend of electrical resistance was observed upon ion irradiation with 120 MeV Au ions. It was observed that irradiated film showed deteriorated hysteresis as compared to pristine film. Also, the R-T curves during heating and cooling cycles do not show the clear phase transformation behaviour. It could be due to the disorder occurring in the film due to ion impact as also confirmed by the decrease in intensity of ordered austenite phase from XRD data. R-T curves of films irradiated at fluences 5×10^{12} and 1×10^{13} ions/cm^2 as shown in figures 5.6(c) and (d) show the non-metallic behavior of both the films without any indication of phase transformation during subsequent heating and cooling cycles. At higher fluence (1×10^{13} ions/cm^2) the energy deposited by incoming ions in the film due to the electronic stopping is quite large and leads to degradation of shape memory behaviour and complete amorphization of the films. In the present case, the incomplete phase transformation could be attributed to the following reasons; (a) large resistance force as compared to driving force could be generated due to the constraints imposed by inter-diffusion of film and substrate due to ion irradiation (b) large number of grain boundaries due to small grain size restrict the growth of martensitic phase during cooling (c) presence of intrinsic defects created by 120 MeV Au ions in Ni-Ti thin films at higher fluences.

5.2 Ag^{7+} ion (100 MeV) irradiation induced modifications in Ni-Ti shape memory alloy thin films

The primary objective of the present study was to deposit the films with two different phases; ordered austenite and low-symmetry allotrope martensite phase with higher composition of Ni. The films are irradiated at different fluence to grow hard Ni_3Ti precipitate by using SHI irradiation. The results present here bring forth the understanding of the strengthening mechanisms and deformation behavior of Ni-Ti films by SHI irradiation. This study is also important to investigate the effects of SHI irradiation on shape memory alloy for future application of these materials in harsh radiation zones such as space or nuclear reactor. The schematic diagram of ion-solid interaction is shown in Fig.5.7. In previous study Ni-Ti thin films with same composition Ti57at.%Ni has been irradiated by using 120 MeV Au ions irradiation to investigate the critical values of fluence and acceptable radiation limit for this composition. This work does not involve the investigation on the growth of hard precipitation phase after irradiation with 120 MeV Au ions. Moreover, the interaction between Au ions and target material (Ni-Ti) is more in comparison of Ag ions due to higher mass (nearly twice) of Au ions which is confirmed by TRIM simulation on the basis of collision events. In case of 120 MeV Au ions irradiation, we observed the amorphization of Ni-Ti films, however, in case of Ag ions irradiation the partial amorphization of austenite and martensite phase and formation of Ni_3Ti phase was occurred.

In this study, we have used an innovative material modification technique namely SHI irradiation to engineer the surface structure and mechanical properties of Ni-Ti thin films. In the present study Ni-Ti thin films have been irradiated by 100 MeV Ag^{7+} ions at different fluences ranging from 1×10^{12} to 1×10^{13} ions/cm^2 and characterized by various characterization techniques such as RBS, XRD, AFM, FESEM and nanoindentation measurements.

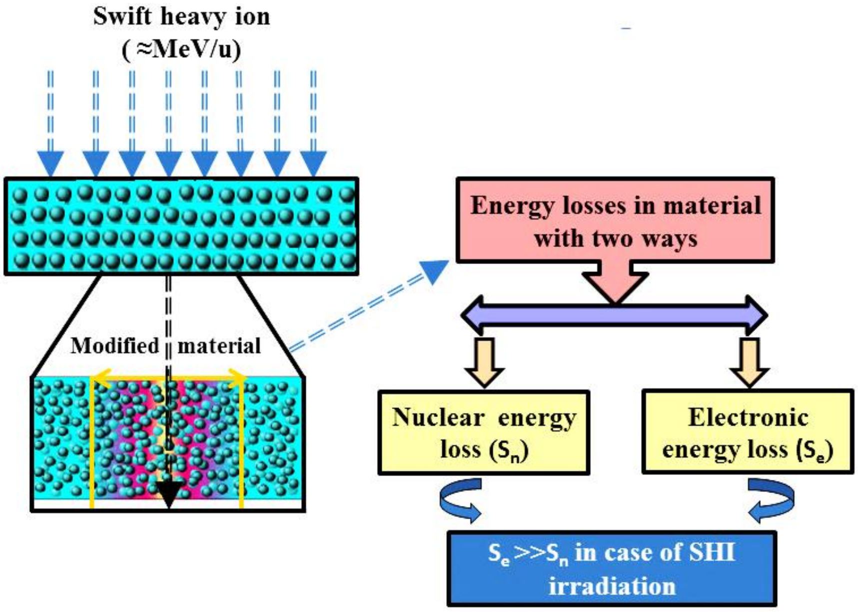

Figure 5.7. Schematics diagram for ion-solid interaction for SHI.

The prepared Ni-Ti films were irradiated by 100 MeV Ag^{7+} ion beam at Inter University Accelerator Centre (IUAC), New Delhi, at room temperature by using 15 UD Pelletron Tandem accelerator facility. During irradiation, a high vacuum of the order of ~6×10^{-7} torr was maintained inside the irradiation chamber. The values of nuclear energy loss (S_n) and electronic energy loss (S_e) were calculated by SRIM 2008 code [168] and found to be 0.01×10^3 eV/Å, 2.5 $\times10^3$ eV/Å, respectively. Moreover, range of 100 MeV Ag ions in Ni-Ti films (density 6.14 g/cm^3) was also calculated by SRIM 2008 code and determined as 8.23 µm. The calculated value of S_e is too high than that of S_n; that's why S_e dominates over S_n therefore modifications are mainly attributed due to S_e effect. The thickness of the films is very small in comparison of ion range; hence most of the ions will pass through the Ni-Ti films and get buried into the substrate. The ion beam was scanned over an area of 1×1 cm^2 to achieve the homogeneous irradiation of Ni-Ti films and the beam current was kept constant at ~ 2 pnA (particle nanoampere).

5.2.1 Results and discussion

5.2.1.1 Rutherford Backscattering spectrometry

RBS is a non-destructive technique and it capable to determine both elemental composition and depth of a thin layer within several nm. Fig. 5.8 shows simulated

RBS spectrum along with depth profile of pristine Ni-Ti film deposited at 550 °C. The elemental stoichiometry and film thickness was estimated by using the SIMNRA simulation of RBS data [169].

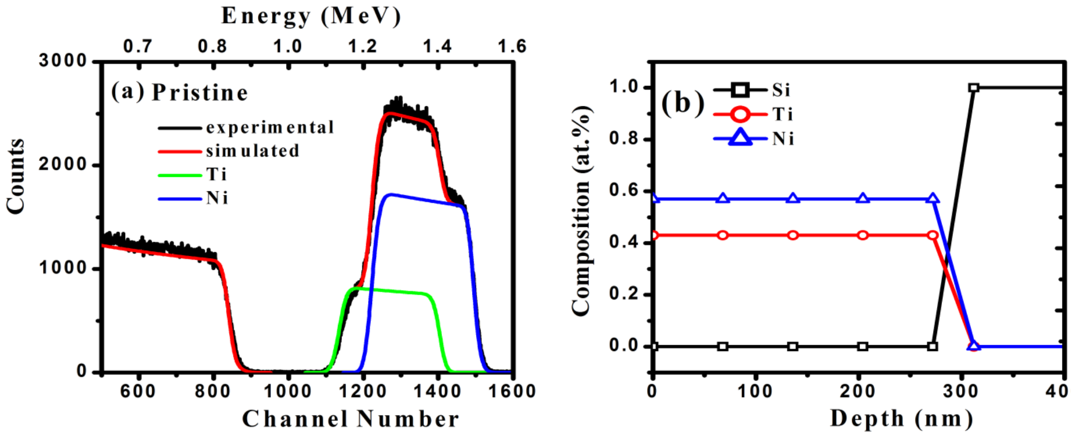

Figure 5.8. RBS spectra (2MeV He^{2+}) along with SIMNRA simulation (a) and depth profile (b) of Ni-Ti pristine film deposited at 550 ^{0}C.

The composition of Ni and Ti present in the film was determined by He^{2+} ions with a beam of 2 MeV energy and at normal incidence with detector positioned at 165° scattering angle. The calculated near surface concentration of Ti was found to be ~ 43.3 at. % and Ni concentration was found to be ~ 56.7 at. %. The thickness of the pristine film was found to be ~270 nm. The elemental composition versus depth profile for Ni and Ti is shown in Fig. 5.8(b) and it is showing the uniform distribution of Ni and Ti content through the film thickness.

5.2.1.2 X-Ray diffraction

Fig. 5.9 shows the room temperature XRD pattern of pristine and irradiated Ni-Ti thin films at different fluences in 2θ range of 35˚-54˚. The XRD pattern of pristine film exhibits three phases: martensite (monoclinic; JCPDS file no. 77-2170), austenite phase (cubic; JCPDS file no. 65-5537) and small amount of Ni_3Ti phase (Hexagonal; JCPD file no. 65-2038) in the film deposited at 550 ˚C. In addition to substrate peaks, XRD pattern of pristine film shows the strong austenite phase at 2θ = 42.5˚corresponding to (110) fundamental reflection, martensite peak at 43.9˚ corresponding to (002) fundamental reflection and a small amount of Ni enriched buried Ni_3Ti precipitate peak at 2θ = 43.5˚ corresponding to (004) plane, respectively. Two other peaks observed in pristine films at 46˚ and 47.7˚ are corresponding to oxidized Si substrate [167, 195]. The film irradiated at a fluence of 1×10^{12} ions/cm^2 shows decrease in intensity of both phases due to the phase transformation from austenite (110) and martensite (002) phase into Ni_3Ti phase on Ag ion bombardment. Further, the film irradiated at a fluence of 5×10^{12} ions/cm^2 shows the dominance of Ni_3Ti phase with concurrent decrease the intensity of austenite phase. The film irradiated at this fluence (5×10^{12} ions /cm^2) shows the ordering of Ni_3Ti phase, which corresponds to hexagonal crystal structure of films.

It is observed that film irradiated at this fluence releases strain energy which is primarily responsible for the ordering of (004) plane, because (004) plane of Ni-Ti possess the minimum surface energy in accordance of basic crystal growth theory [196]. Further, the film irradiated at a higher fluence of 1×10^{13} ions/cm^2 shows the dominance of Ni_3Ti phase and partial amorphization of austenite and martensite phase. The decreasing in intensity of austenite and martensite phase depends upon the amount of energy deposited in Ni-Ti films by the Ag^{7+} ions. When the SHI irradiation passess through the film, it causes ionization and excitation of Ni-Ti films, the ionization and excitation of the Ni-Ti atoms lead to modification in properties such as structure and phase of the deposited material.

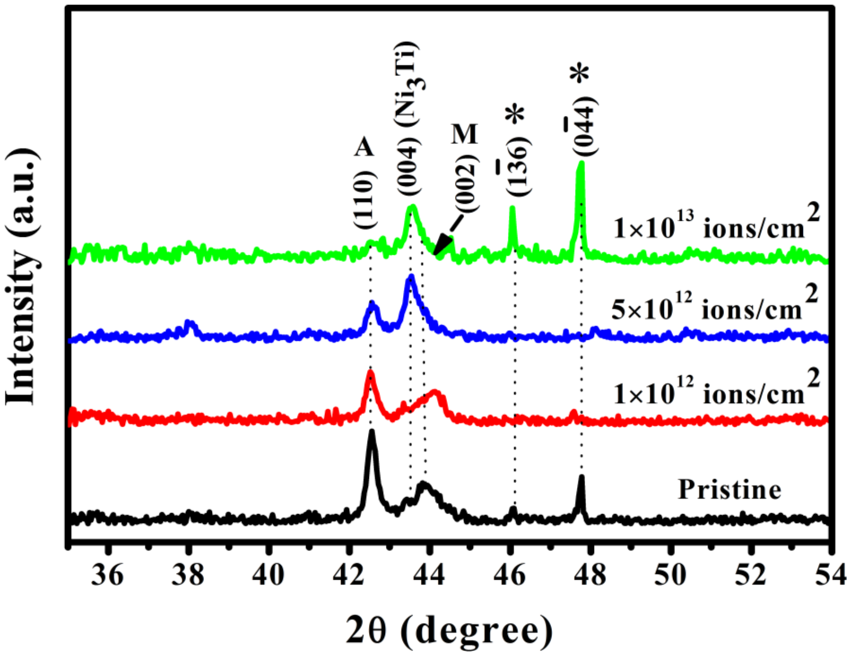

Figure 5.9. XRD spectra of pristine and 100 MeV Ag^{7+} ion irradiated Ni-Ti thin films at different fluences.

Such electron excitations can also cause local heating followed by a rapid quenching (thermal spikes) which subsequently produces lattice distortions. These lattice distortions are so drastic they relax into an amorphous state [191]. The modifications in materials structure or phases depend upon irradiation conditions such as ion fluence, irradiation temperature and the nature of ions as reported by several authors [167,197]. The precipitation of phases and recrystallization of monoclinic into cubic phase by 2 MeV proton beam irradiation has also been observed by Afzal et al. [103] in Ni-Ti alloy at room temperature. The irradiation of Nitinol by proton beam produces small displacement cascade and thus generates vacancies, interstitial or precipitates. Irradiation-induced defects in material increase the shear movement of atoms at the beginning of transformation and lead to increase in anti-phase boundary which decreases the martensite transformation.

5.2.1.3 Atomic force microscopy

The surface morphology (grain size and roughness) of pristine and Ag^{7+} irradiated Ni-Ti thin films at different fluences ranging from 1×10^{12} to 1×10^{13} ions/cm^2 is studied with AFM in tapping mode. Fig. 5.10(a)-(d) shows the two-dimensional AFM micrographs of pristine and irradiated Ni-Ti thin films at scan area of 1 μm^2. AFM micrograph of the pristine film (Fig. 5.10(a)), shows the very fine and dense grains of Ni-Ti with well define boundary. The film irradiated at a fluence of 1×10^{12} ions/cm^2 shows the change in surface morphology with fluence. Moreover, grains are non-uniformly distributed over the film surface due to electronic energy bombardment on Ni-Ti film. The modification of film surface can be understood on the reference of electronic energy deposited into the Ni-Ti thin film. When SHI passes through the Ni-Ti film, it loses its energy into the material followed by ionization and excitation of the atoms. Electronic energy deposited by SHI irradiation beyond a certain threshold (Se~32 keV/nm for Ni-Ti) can cause the significant movement of the atoms results into change in the crystal structure and surface roughness [93]. Further, it is found that irradiated at a higher fluence of 1×10^{13} ions/cm^2 decreases the grain size and promotes agglomeration of the grains. The agglomeration of the grains is attributed to multiply ions impact turning on Ni-Ti film by SHI irradiation. The average roughness (R_{avg}) and root-mean-square surface roughness (R_{rms}) of the pristine and irradiated Ni-Ti films are obtained from the AFM images of 1 μm ×1 μm scan area of films surface, three times at different position for each film and it has been taken as an average roughness estimated from AFM micrograph.

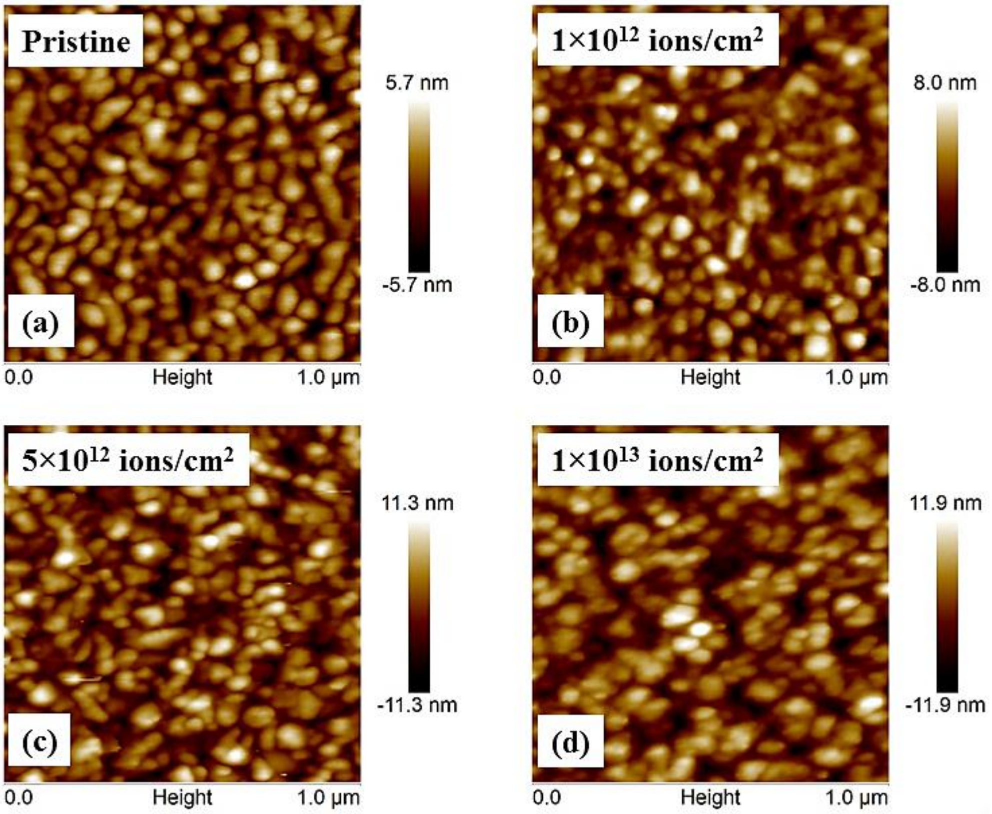

Figure 5.10. AFM two dimension surface micrograph of pristine and 100 MeV Ag^{7+} ion irradiated Ni-Ti films at different fluences over a scan area of 1×1 μm^2.

The R_{avg} and R_{rms} are defined by the following equations [177]:

$$R_{avg} = \left[\frac{1}{N} \sum_{i=1}^{N} | Z_i - \overline{Z} | \right] \text{------------------} (5.1)$$

$$R_{rms} = \left[\frac{1}{N} \sum_{i=1}^{N} | Z_i - \overline{Z} |^2 \right]^{1/2} \text{-----------------} (4.3)$$

where $\overline{Z}$ mean height distance and N is the number of surface height data. The R_{avg} and R_{rms} of the pristine and irradiated films are observed to increase with increasing the ion fluences. This could be due to agglomeration of grains and Ni_3Ti precipitate formation at higher fluences. The R_{avg} value of pristine film is ~2.06 nm and for the films irradiated at different fluence found to be ~2.82 nm, ~3.73 nm, ~4.10 nm, respectively. The R_{rms} values found to be ~1.61 nm for the pristine film and ~2.32 nm, ~3.02 nm and ~3.35 nm for the films irradiated at three different fluences respectively. AFM results indicated that the surface morphology of the Ni-Ti films strongly depends upon the ion fluences as shown in figure 5.11.

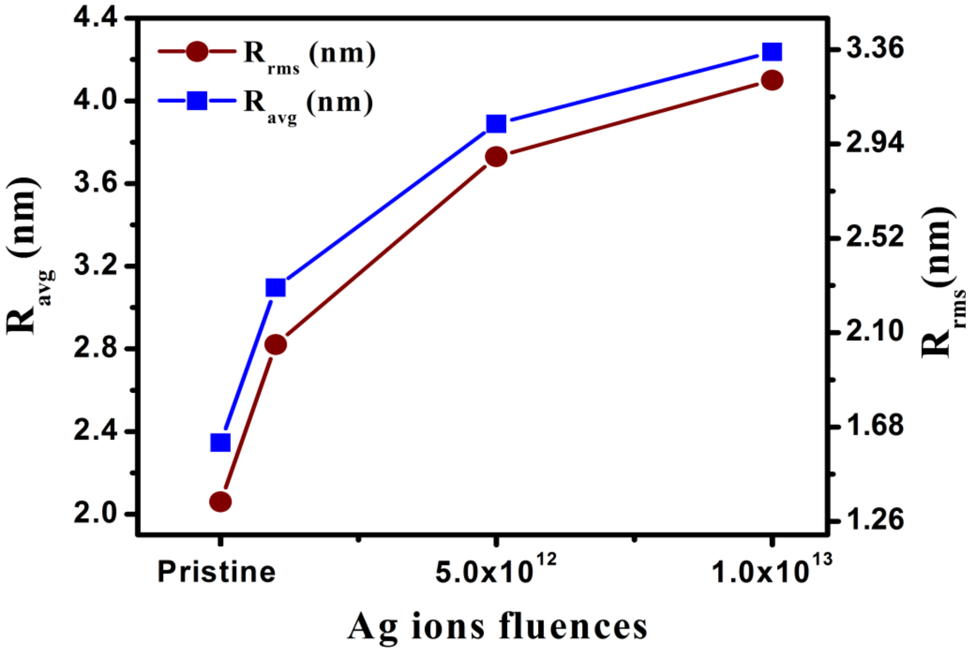

Figure 5.11. Variation of R_{avg} and R_{rms} with fluences for the pristine and the films irradiated at different fluences of 100 MeV Ag ions.

In the present study, the Ni-Ti films with same thickness are irradiated by using different fluences. The different fluences have different effects on the surface of the grown films such as clustering of grains, formation of creators, etc. [108]. The surface morphology is changed with fluences with simultaneous change in the Z-height of the sample. The Z-height of the sample depends upon the arrangement of grains and roughness of the films. The variation in roughness value of film also changes the Z-height of the film.

In present study, the Z- height of the four samples is different due to the difference in roughness values of the films.

5.2.1.4 Field Emission Scanning Electron Microscopy

Apart from AFM, the surface morphology of pristine and irradiated Ni-Ti thin films is also investigated by FESEM. Fig. 5.12(a)-(d) show the FESEM images of pristine and

Ag^{7+} irradiated Ni-Ti thin film at different fluences ranging from 1×10^{12} to 1×10^{13} ions/cm^2. The FESEM micrographs have confirmed the change in morphology of Ni-Ti films with ion irradiation at different fluences.

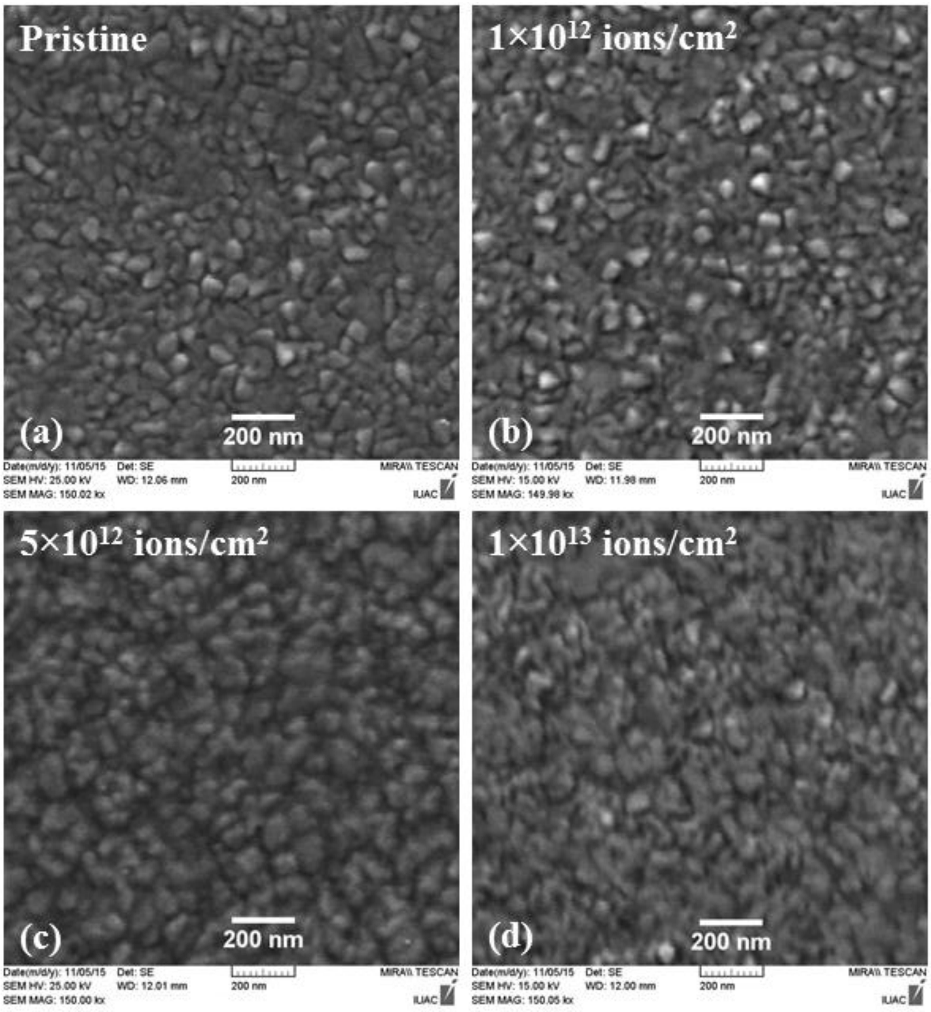

Figure 5.12. FESEM images of pristine and 100 MeV Ag^{7+} ion irradiated Ni-Ti films at different fluences.

Fig. 5.12(a) shows the dense granular morphology with nearly same granule sized in pristine film deposited at 550 °C. In Fig. 5.12(b) FESEM image of the irradiated film at a fluence of 1×10^{12} ions/cm^2 shows that the density of granular size grains decreases with increase in fluence. These SHI induced structural modifications are also supported by AFM analysis. Further, the film irradiated at fluence of 5×10^{12} ions/cm^2 shows the diffused grains morphology of the film; however, it is possible to observe the boundary of grains. The grains of the films are seemed to be agglomerated at this fluence. With further increase in the fluence (1×10^{13} ions/cm^2), the granular morphology of film is completely disappeared and it becomes difficult to observe the boundary of grains. The agglomeration of the grains can be ascribed due to electronic energy deposited by the incoming ions in Ni-Ti regime [178, 198]. The surface features of the pristine and irradiated films at different fluences of Ag ions have no evident default such as cracks and holes etc.

5.2.1.5. Nanoindentation

The change in crystal structure in nm-sized crystallites by SHI irradiation may play an important role to enhance the mechanical properties of nanocrystalline materials. Materials under the lattice contraction resist the large force thus decreasing the penetration depth of indentation and inhibiting the crack propagation [199]. This phenomenon leads to increase in toughness and hardness of materials; however, lattice expansion leads to opposite phenomena. Ni_3Ti precipitate leads to increase the mechanical strength promoting the interaction between grain boundaries and dislocations which subsequently increase the interactions in turn increases the average hardness and Young modulus values.

The CSM nanoindentation has been used to characterize the mechanical properties of pristine and the films irradiated at different fluences of 100 MeV Ag^{7+} ions. Fig. 5.13 shows the load versus displacement curves of Ni-Ti films irradiated at different fluences of 100 MeV Ag^{7+} ions. These curves are used to calculate the fundamental mechanical properties such as hardness (H), Young modulus (E_{eff}) and plastic resistance parameter (H/E_{eff}) etc. All results obtained by nanoindentation were analyzed by using the Oliver and Pharr method [155] and are summarized in Table 1. Five nanoindentation tests were performed on each film at different location to measure the average values of hardness and young modulus. Each indenter test consisted of 8-second linear loading segment to a peak load, 10- second holding and a 8-second linear unloading segments. Generally, the hold periods have used to reduces the time-dependent effects (creep effects) generated in the specimen. The load-displacement curves show (fig. 5.13) the behavior of each film is consistent from test to test, indicating surface of all the films are homogeneous over the area tested. The E_{eff} is a significant parameter of materials related to stiffness: the larger the value of E_{eff}, the stiffer the material. Furthermore, the H/E_{eff} is also an important parameter to differentiate in elastic and elastic-plastic nature of the materials. The higher value of

H/E$_{eff}$ shows higher elastic nature of material or higher resistance to plastic deformation while the lower value of H/E$_{eff}$ corresponds to its elastic-plastic behavior [200]. The Young modulus is calculated using the following relations:

$$E_{eff} = \frac{\sqrt{\pi}}{2}\frac{S}{\sqrt{A}} --------------------(4.5)$$

where, S is unloading stiffness at maximum load ($S = \frac{dP}{dh}$) and A is the projected contact area. The Young modulus of the material is related to the modulus of elasticity by the following relation:

$$\frac{1}{E_{eff}} = \frac{(1-v_i^2)}{E_i} + \frac{(1-v_s^2)}{E_S} ----------------(4.6)$$

where, subscript i represents the indenter material, and subscript s corresponds to sample material and v is the Poisson’s ratio. The hardness (H) of the deposited material can be calculated by the following equation:

$$H = \frac{P_{\max}}{A} --------------------------(3.13)$$

where, P$_{max}$ is the maximum indenter load and A is the projected contact area at that load.

Fig. 5.14(a) shows the bar chart of hardness versus ion fluences for pristine and for the film irradiated at different fluences ranging from 1×10^{12} to 1×10^{13} ions/cm^2. It depicts that hardness of Ni-Ti films is increase with increase in ion fluence and the film irradiated at a fluence of 1×10^{13} ions/cm^2 has higher hardness. The improvement in hardness of Ni-Ti films at different fluences is attributed due to the formation of lattice disorder and associated change in crystal structure. It is also reported that hardness of the metallic thin films increases vividly when the thickness of the deposited material falls below about 300 nm and the hall Petch relation, obeyed by thin films, is also dependent on film thickness [201].

The formation of defects such as precipitation, dislocation, and irradiation induced phase in material up to a certain limit contribute to increasing in resistivity and barrier strength. However, these treatments suppress the martensite transformation temperature by changeing the internal stress and chemical composition of the Ni-Ti matrix [108].

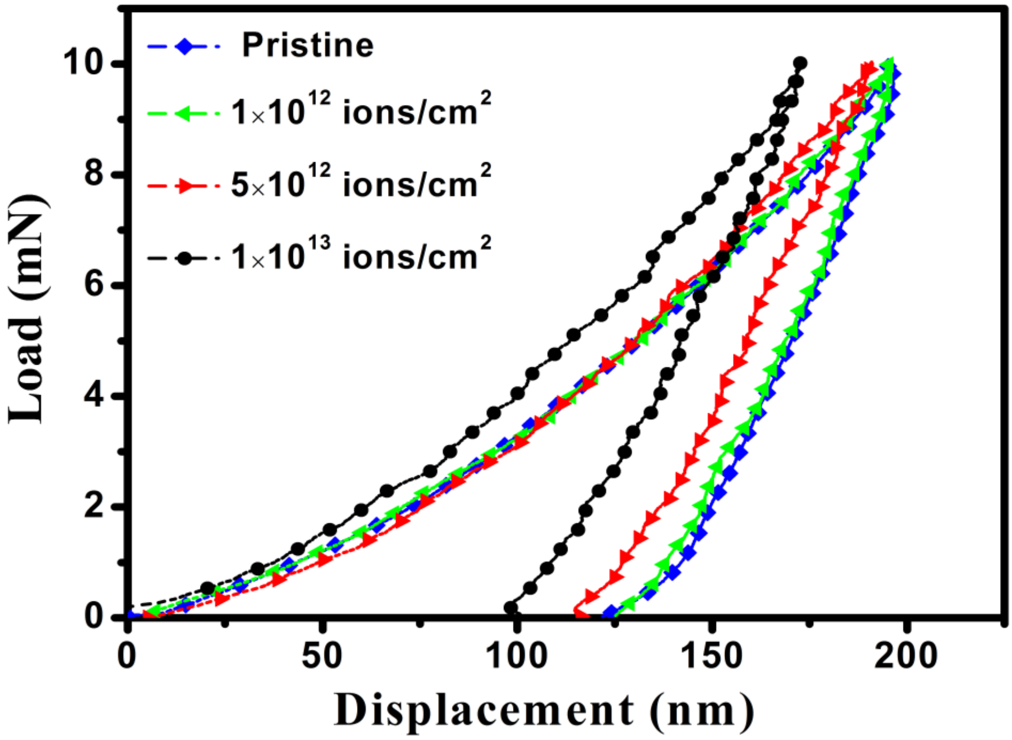

Figure 5.13. Load versus depth profile of pristine and 100 MeV Ag^{7+} ion irradiated Ni-Ti films at different fluences.

Table 5.1. Comparison of nanoindentation and AFM results obtained for pristine and irradiated Ni-Ti thin films.

Fluence (ions/cm^2)	**Hardness H (GPa)**	**Young modulus E_{eff} (GPa)**	**H/E_{eff}**
Pristine	11.62 ± 1	172.62 ± 1	0.067 ±0.005
1×10^{12}	12.81 ± 1	171.83 ± 3	0.074 ±0.007
5×10^{12}	13.58 ± 0	181.81 ± 1	0.074 ±0.01
1×10^{13}	16.12 ± 1	176.93 ± 1.	0.090 ±0.008

The hardness of pristine film is 11.62 ± 1GPa and for the films irradiated at different fluences are found to be 12.81 ± 1GPa, 13.58 ± 0 GPa and 16.12 ± 1 GPa respectively as reported in table 5.1. The Young modulus of the pristine film is 172.62 ± 1GPa and for the films irradiated at different fluence are 171.83 ± 3GPa, 181.81 ± 1GPa and 176.93 ± 1GPa respectively. The bar chart for hardness to Young modulus (H/E_{eff})

ratio versus ion fluences for Ni-Ti pristine and films irradiated at different fluences is shown in Fig. 5.14(c). The H/E_{eff} ratio is important parameter to measure the material elastic and elastic-plastic behaviors.

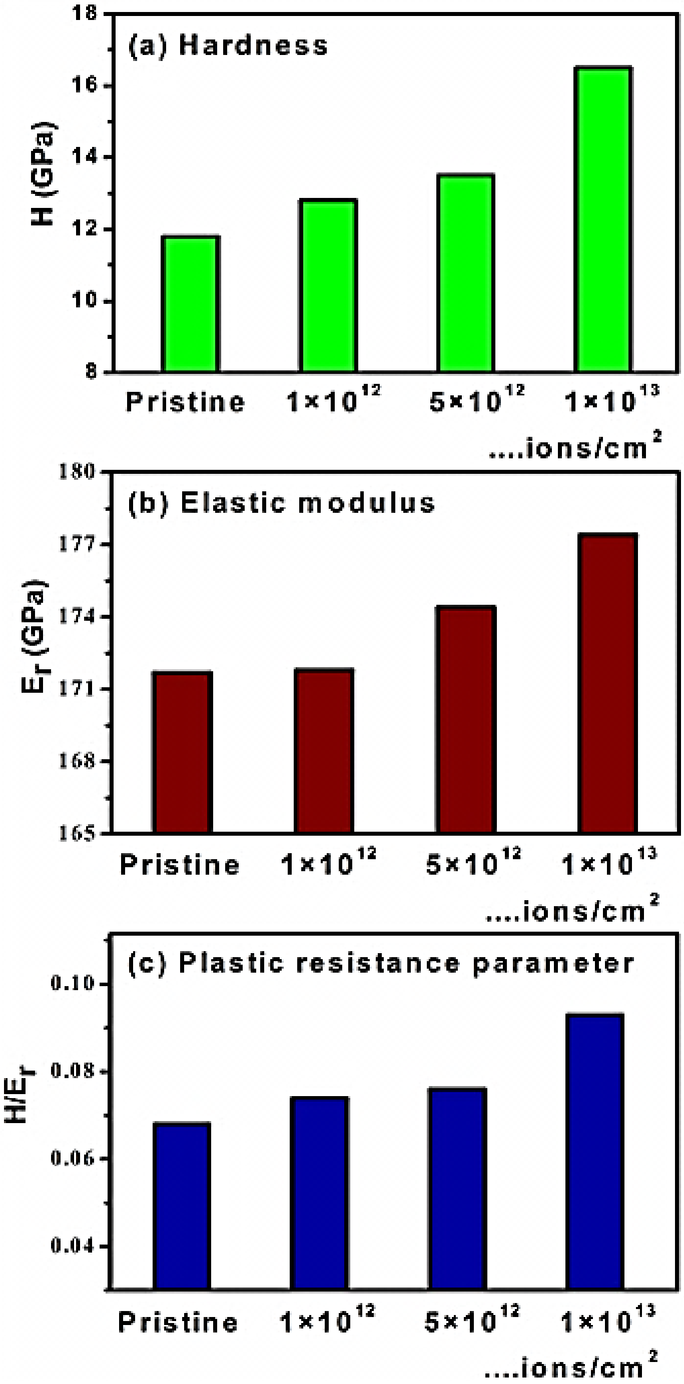

Figure 5.14. Bar chart of hardness (a), elastic modulus (b) and plastic resistance parameter of pristine and irradiated Ni-Ti films at different fluences of 100 MeV Ag^{7+} ions.

The higher value of H/E_{eff} ratio shows the excellent the wear resistance and better films quality, while a lower value of H/E_{eff} reveals large fraction of work is consumed in plastic deformation, and large strain energy is required when contacting a material [202]. A higher (H/E_{eff}) value (0.090 ±0.008) is obtained for the film irradiated at a fluence 1×10^{13} ions /cm^2. The higher value of H/E_{eff} shows the better wears resistance and small strain energy for deformation.

Fig. 5.15 shows the variation of electronic (S_e) and nuclear stopping (S_n) power versus energy for 100 MeV Ag^{7+} ions calculated by SRIM program in Ni-Ti matrix. The strength of interaction between incident ions and target atoms depends on charge, mass and energy of the incident ions. The energy deposited by bombardment ions can modify the structural and phase transformation properties of films. The electronic excitation and ionization of materials by SHI irradiation causes the significant displacement of atoms.

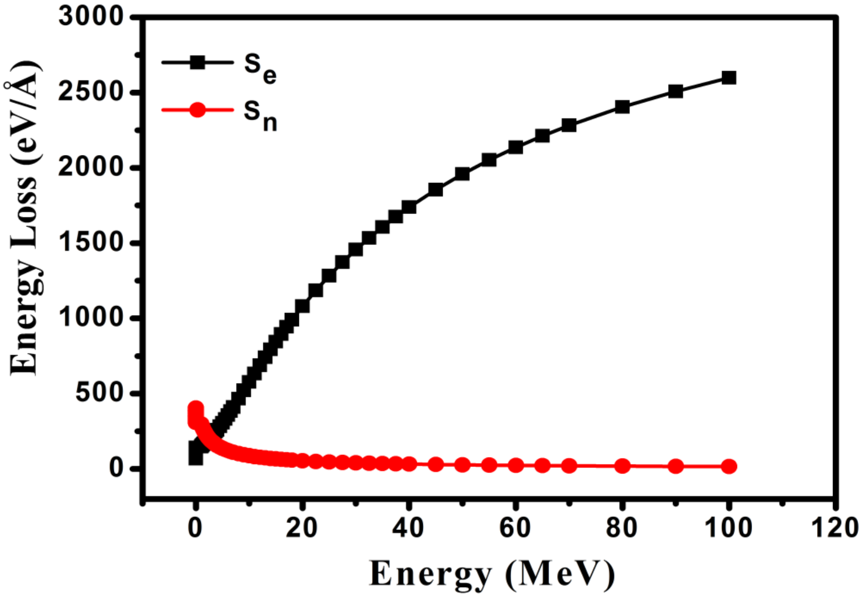

Figure 5.15. SRIM simulation of nuclear (S_n) and electronic stopping (S_e) power versus energy for Ag^{7+} ions in Ni-Ti matrix.

When energetic ions pass through the Ni-Ti films they lose their energy via two independent processes; (a) nuclear stopping (S_n) loss: incident ions transfer their energy to target lattice by elastic collision and cause significant atomic displacements, which further results in creation of frenkel defects (vacancies or interstitial), (b) electronic stopping (S_e) loss: incident ion transfer their energy to electron of target atoms by inelastic collision terms known as electronic stopping loss. In the high-energy region (energy range of the order of ~MeV) electronic stopping dominates over nuclear stopping and modifications are mainly due to the electronic stopping. In the present study, Ag ions are chosen due to its higher mass and energy regime. Fig. 5.16 shows the variation of S_e and S_n with projected depth of ~800 nm at 100 MeV for Ag^{7+} ions, which is much larger than~270 nm, film thickness of Ni-Ti films. Therefore, the effect of electronic stopping power on structural and mechanical properties of Ni-Ti films is anticipated to be uniform irradiation throughout the films thickness.

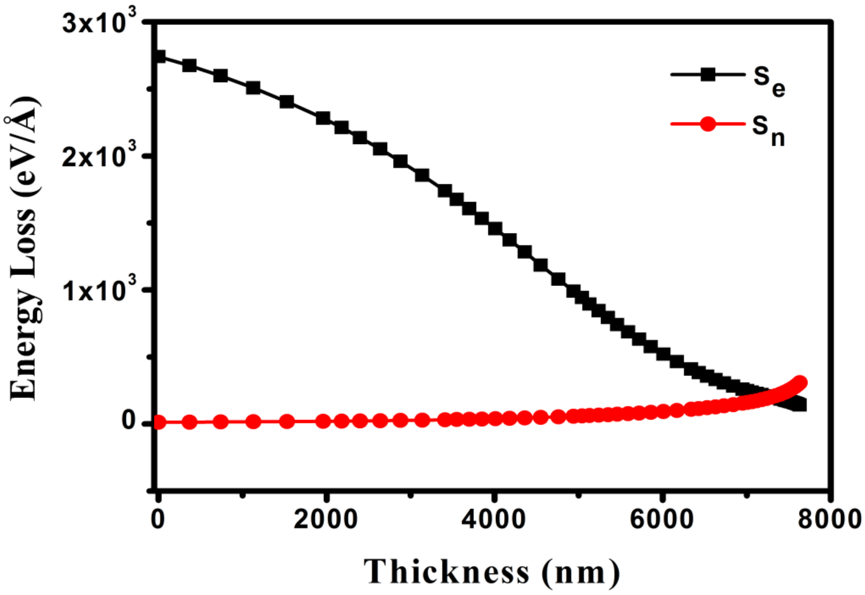

Figure 5.16. SRIM simulation, variation of electronic (S_e) and nuclear energy (S_n) loss of 100 MeV Ag^{7+} ions with thickness in Ni-Ti thin film.

5.3. Ni (90 MeV) ions irradiation induced modifications in Ni-Ti shape memory alloy thin films

Ni-Ti intermetallic alloy is a functional material not only as practical shape memory alloys with prominent strength and ductility but also as those demonstrates unique physical properties such as pre-deformation behavior. The work output per unit volume of Ni-Ti alloy is much higher in contrast to other micro-actuation mechanisms. The phase transformation path in Ni-Ti alloy is changed by the significant change in physical, chemical, electrical and mechanical properties such as; surface roughness, thermal expansion coefficient, electrical resistivity, dielectric constant, yield stress and damping [203, 204]. All these changes could be fully utilized in design and manufacturing of pumps and grippers for uses in MEMS applications. Therefore, modifications in deposited films by using different fluences of SHI irradiation is immense technically importance to explore the various properties of Ni-Ti SMAs.

In last decades, the effect of different type of perturbations such as the electron, proton, and ion irradiation on microstructure, phase transformation, and mechanical properties have been reported in literature [101,103,191], But investigation of surface characteristic and mechanical behavior of Ti-56.7at.%Ni thin films, irradiated by SHI irradiation are not adequate. The main motive of the present investigation was to improve the structural and mechanical properties of the Ni-Ti films for different MEMS applications by using SHI irradiation. Here, SHI ion irradiation demonstrated the enhancement in mechanical properties of Ni-Ti thin films up to certain fluences and decrements in the properties above that fluence. This study is also important to use Ni-Ti thin films in the harsh space environment, as is case of device deigned to remotely release the solar panels and antenna arrays of satellites, superior tribological and mechanical properties are required [114].

In the present experiment, the stability of austenite and martensite phases against SHI irradiation has been studied. The partial amorphization of the as-grown phases: austenite and martensite were occurred, which leads to change in structural and mechanical behavior of Ni-Ti SMA. Furthermore, the variation in hardness and Young modulus of the films occurred drastically after SHI irradiation at higher fluences of Ni ions. The irradiated Ni-Ti films at different fluences of 90 MeV Ni ions have been characterized by using different techniques such as RBS, XRD, AFM and nanoindentation measurements.

Moreover, the irradiation of Ni-Ti films was carried out by 90 MeV Ni ion beam by using the 15 UD Pelletron Tandem accelerator at IUAC, New Delhi at room temperature. During irradiation, a high vacuum of the order of ~6×10^{-7} torr was maintained inside the irradiation chamber to reduce the atmospherically impurity. The fluences of the beam were varying from 1×10^{12} to 1×10^{13} ions/cm^2. The dimension of each film during the irradiation was 1×1 cm^2 in the irradiation chamber. To cover the complete area and homogeneous irradiation, raster scan (1×1 cm^2) of ion beam was done over the films surface during irradiation. The values of nuclear energy loss (S_n)

and electronic energy loss (S_e) were calculated by SRIM 2008 code [168] and found to be 0.003×10^3 eV/Å, 1.5×10^3 eV/Å, respectively. Here the calculated value of S_e is too high than that of S_n; therefore the modifications in Ni-Ti films are mainly occurred due to S_e effects. Moreover, the range of 90 MeV Ag ions in Ni-Ti films (density 6.14 g/cm^3) was also calculated by SRIM 2008 code and found to be 8.73 μm, where range denotes the maximum distance up to which Ag ions can penetrate into the film, which is higher than the thickness of the film. During the irradiation, beam current was kept constant ~ 2 pnA (particle nanoampere) and Ni-Ti films surface was scanned over and area of 1×1 cm^2 to get the homogeneous irradiation.

5.3.1. Results and Discussion

5.3.1.1. Rutherford Backscattering spectrometry

RBS is a non-destructive technique and it gives the precise estimation of the composition and thickness of the deposited film. In present study, 5SDH-1.7 MV Tendem accelerator at IUAC, New Delhi, was used to perform the experiment. The Ni-Ti alloy thin film is very sensitive to the elemental composition and the composition uniformity over the surface. These two factors play an important role in the fabrication of thin film for shape memory applications. In addition, phase transformation behaviour and mechanical strength of the Ni-Ti alloy also depend upon the elemental composition.

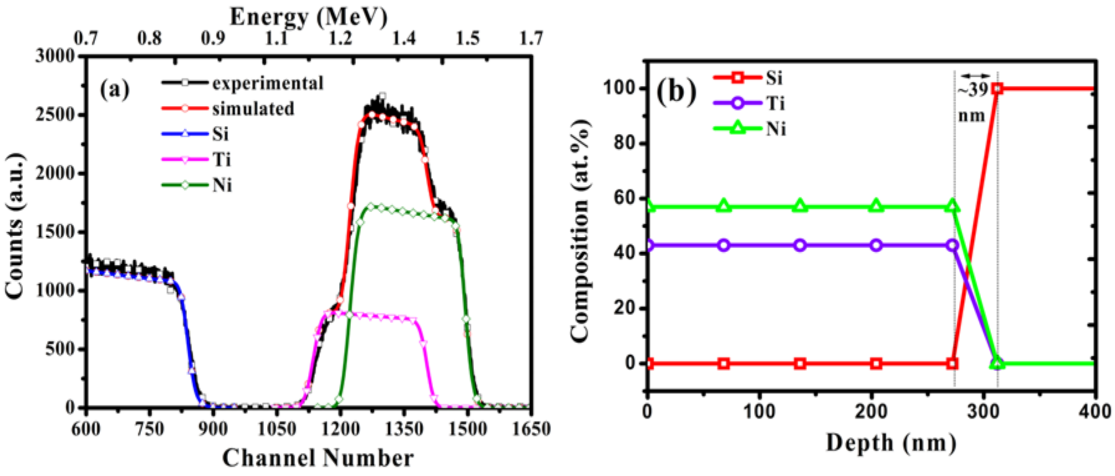

Figure 5.17. RBS spectra along with SIMNRA simulation of Ni-Ti pristine film deposited on Si substrate (a) and depth profile (b) performed by using 2 MeV He^{2+} ions.

A small variation in composition (0.1 at.%) can cause a shift in transformation temperature by around 10 °C; consequently, the temperature of shape memory effect is altered significantly [205]. Moreover, the superelastic behavior of the thin films is also affected by their elemental composition. Therefore, the fabrication of thin films with desired composition and exact determination of the elemental composition of the films is very essential. Figure 5.17(a)-(b) represent the simulated RBS spectrum and depth profile for the pristine film deposited on Si substrate at 550 °C. To obtain the film thickness and elemental composition present in the pristine film, the RBS data has been simulated by using the SIMNRA simulation and the fitting of data is shown in figure 5.17(a) [169]. The simulated concentration of the Ti near the surface was found to be ~43.3 at.% and the concentration of the Ni was found to be ~56.7 at.%. The thickness of the film was calculated ~270 nm. Furthermore, fig. 5.17(b) shows the graph between the atomic concentration of Ni and Ti versus depth of the film. The figure shows the uniform distribution of elements (Ni and Ti) through the films thickness. A significant diffusion of Ni-Ti into Si substrate (~39 nm) is also observed after the deposition, which may be due to higher temperature deposition of Ni and Ti on substrate.

5.3.1.2. X-Ray Diffraction

Figure 5.18 shows the room temperature X-ray diffraction patterns plotted for Ni-Ti pristine and films irradiated at different fluences of 90 MeV Ni ions. The pristine and irradiated Ni-Ti films show the several diffraction peaks which indicate the polycrystalline nature of films. In spite of similar composition and thickness, the Ni-Ti films irradiated with different fluences exhibits distinct phases at room temperature as authenticated by the XRD spectra.

The XRD pattern of the pristine and the films irradiated at different fluences exhibit two major peaks corresponding to Ni-Ti SMAs. The XRD pattern of the pristine film deposited at 550 °C exhibits two strong peaks corresponding to austenite and martensite phases. The peak corresponding to the austenite phase is located at 2θ = 42.5° (JCPDS file no. 65-5537) associated to cubic (110) plane, and the martensite phase at 43.9° (JCPDS file no. 77-2170) associated to monoclinic (002) plane, respectively. XRD analysis reveals that the martensite phase is disappeared in the films irradiated at the higher fluence of 1×10^{13} ions/cm^2. The presence of martensite phase at room temperature in the pristine film could be due to higher biaxial stress. This type of behavior of martensite phase is consistent with the data reported by Martins et al. [206]. The growth of austenite phase corresponding to (110) plane in the pristine film could be due to the fact that most of the body centred cubic crystal structure exhibit minimum surface energy along (110) plane. This surface energy is the most dominating driving force for structure formation [173]. The Ni-Ti film irradiated at the fluence of 1×10^{12} ions/cm^2 exhibits the decreases austenite and martensite peaks corresponding to (110) and (200) plane with reduced intensity. With further increase in the fluence to 3×10^{12} ions/cm^2, the intensity of the austenite peak decreases and the peak corresponding to martensite phase (200) became broad.

The broadening of the (200) plane shows the low stability of the martensite phase against the SHI irradiation. Moreover, the peak broadening also indicates the partial amorphization of the martensite phase at this fluence. With further increase in fluence to 9×10^{12} ions/cm^2, the intensity of both the phases decreases considerably.

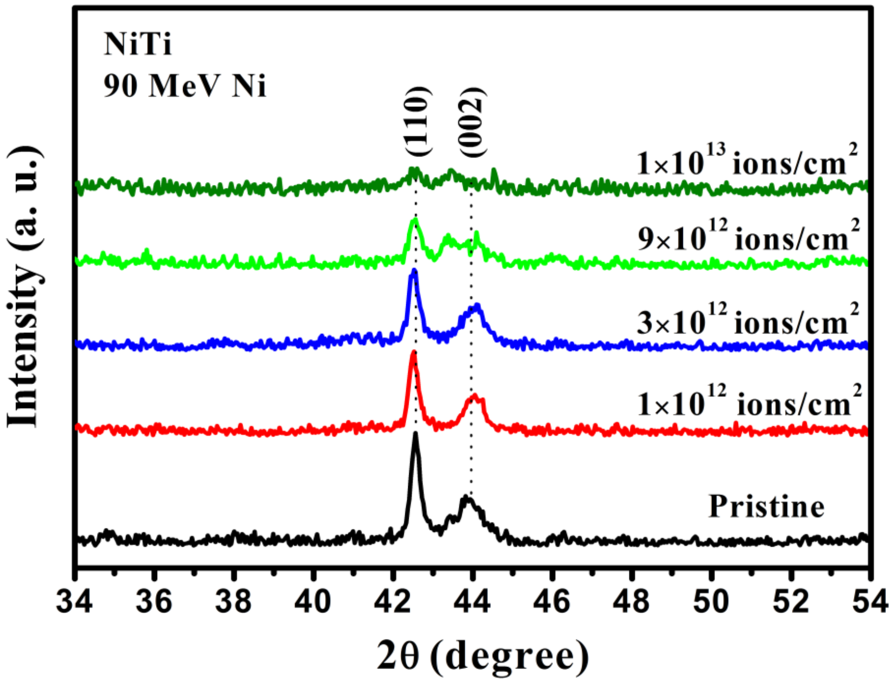

Figure 5.18. XRD patterns of pristine and irradiated Ni-Ti thin films at different fluences of 90 MeV Ni ions.

The decrease in intensity of both peaks corresponding to austenite and martensite phases shows partial amorphization of both the phases and suppression of phase transformation from austenite to martensite phase by electronic energy deposition in

Ni-Ti matrix. At higher fluence of 1×10^{13} ions/cm^2, the XRD peaks corresponding to austenite and martensite phase with low intensity and significant broadening shows the partial amorphization behaviour. The decrease in fraction of crystallinity of both phases depends upon the amount of energy deposited by SHI irradiation in Ni-Ti films by Ni ions. Which can be understand as: when the energetic ions pass through the Ni-Ti films, it causes ionization and excitation of alloy atoms, leading to modification in alloy properties such as structural and phase. Such high electronic excitations produce local heating followed by rapid quenching (thermal spike) which subsequently generates lattice distortions. Such drastic distortions in the lattice are responsible for the amorphization of material [191]. The partial amorphization of both the phases at higher fluence has been the introduction by lattice defect and high strain generation by the bombardment of 90 MeV Ni ions on Ni-Ti films. The changes in material crystallinity also depend upon the irradiation condition such as ion fluence, irradiation temperature and nature of the ions as reported by several authors [192,193]. In reference to electron and proton irradiation, it has been quite well reported in the literature that irradiation by these species causes lattice disorder and stress field around the materials [194]. The lattice disorder by electronic excitation generates the point defect (vacancy and interstitial pairs) which is evenly distributed in the materials and suppress the transformation temperature and cause amorphization. Irradiation of the materials at critical fluences, produce isolated amorphous zone called ion track and density of these ion tracks (amorphous zones) are continuously expended with increasing the fluences, and at a much higher fluence these amorphous zone started to overlap material become amorphous [93].

Furthermore, average particle size or crystalline size (D) of the pristine and the irradiated Ni-Ti thin film at different fluences has been calculated from line broadening of the XRD lines, corresponding to austenite (110) plane after removing the instrumental broadening by using the Debye-Scherrer's formula [142];

$$D = \frac{K\lambda}{\beta \cos\theta} \text{------------------------} (3.9)$$

where D = crystallite size, K = shape factor (0.9), β = integral half width, λ and θ are the wavelength of Cu-Kα (λ=0.154 nm) radiation, and Bragg angle, respectively. The calculated crystallite size (D) values for the pristine is 31.57±1and for the films irradiated at different fluences of 90 MeV Ni ions (1×10^{12}, 3×10^{12}, 9×10^{12} ions/cm^2) are found to be 30.44 ± 1 nm, 28.41 ± 1 nm, 26.63 ± 1 nm and 18.52 ± 1 nm respectively as summarized in table 5.2. Furthermore, the strain (ε_{zz}) developed in pristine and irradiated Ni-Ti thin films at different fluences due to SHI irradiation was computed along the austenite (110) plane by the following relation [142]:

$$\varepsilon_{zz}(\%)=\frac{(a-a_0)}{a_0}\times 100\text{----------------}(5.2)$$

where symbol 'a' represents the lattice parameter of strained Ni-Ti films and 'a_0' is represent the unstrained lattice parameter corresponds to bulk Ni-Ti alloy. The lattice parameter 'a' of Ni-Ti films has been calculated by using the equation for cubic structure [207];

$$\frac{1}{d^2}=\frac{(h^2+k^2+l^2)}{a^2}\text{--------------------}(5.3)$$

where d is the interplanar distance calculated from the position of the peak (110) by using the Bragg condition, a is the lattice parameter and h, k, l are the Miller indices. The calculated values of strain were observed to increase with the increase in the ion fluence and decrease in crystallite size.

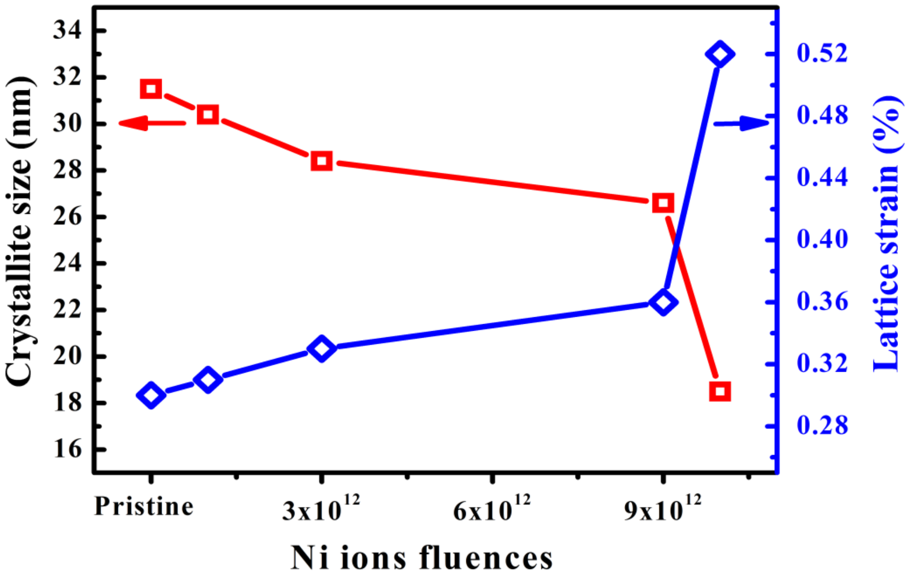

Figure 5.19. Variation of crystallite size and lattice strain with fluence for the pristine and the films irradiated at different fluences of 90 MeV Ni ions.

For the pristine thin film, the calculated strain value is 0.30 and for the films irradiated at different fluences 1×10^{12}, 3×10^{12}, 9×10^{12}, 1×10^{13} ions/cm^2 are found to be 0.31, 0.33, 0.36 and 0.52 respectively as reported in table 5.2. The calculated lattice parameter has been found to be smaller than the 'bulk' lattice parameter, suggesting a lattice compression in the direction perpendicular to the film plane. This behavior indicates the presence of compressive in plane stress in the films. A systematic increase in strain values was observed with the increase in ion fluence of 90 MeV Ni, which could be due to the increase in lattice defects, large number of grain boundaries (decrease in crystallite size) and decreased ordering as evident by the decrease in the peak intensity of preferred orientation of Ni-Ti films.

The dislocation density (δ) of the pristine and irradiated Ni-Ti films at different fluences has been calculated from the crystallite size (D) using the given relation [174], and the obtained values are given in table 5.2:

$$\delta = \frac{1}{D^2}\, line/m^2 \text{ ------------------ } (4.2)$$

The dislocation density is a line defect and it is defined as the length of dislocation per unit volume. The values of dislocation density increase with the increase in ion fluence and strongly depends upon the number of defects creates by the incident Ni ions in the Ni-Ti films.

Fluence (ions/cm^2)	**2θ (degree)**	**FWHM (degree)**	**Crystallite size (D) (nm) along (110) peak**	**Lattice strain (ε)% along (110) peak**	**Dislocation density (δ)×(10^{15} line/m^2)**
Pristine	42.56	0.27	31.57±1	0.30	1.00
1×10^{12}	42.51	0.28	30.44±1	0.31	1.07
3×10^{12}	42.52	0.30	28.41±1	0.33	1.23
9×10^{12}	42.54	0.32	26.63±1	0.36	1.41
1×10^{13}	42.52	0.46	18.52±1	0.52	2.91

Table 5.2. Microstructural parameters of pristine and 90 MeV Ni ion irradiated Ni-Ti thin films at different fluences.

5.3.1.3. Atomic Force Microscopy

The topographical features (roughness and grain size) of the pristine and 90 MeV Ni ion irradiated Ni-Ti thin films at different fluences ranging from 1×10^{12} to 3×10^{13} ions/cm^2 have been studied with AFM in tapping mode. Fig. 5.20(a)-(e) show two-dimensional representations of AFM micrographs of pristine and irradiated Ni-Ti thin films on the scan area of 2×2 μm^2. It is clear from the AFM micrographs that films irradiated at different fluences have different surface morphology. The AFM micrograph of the pristine film (Fig. 5.20 (a)) shows the very dense and fine grains with well define boundary of the Ni-Ti film deposited at 550 °C. The film irradiated by SHI irradiation at fluence of 1×10^{12} ions/cm^2 reveals the change in surface morphology with fluence. Further, the film irradiated at the fluence of 3×10^{12} ions/cm^2 represents the random distribution of crystalline grains over the film surface. Further increasing in fluence of 3×10^{12} ions/cm^2, no sharp grains boundary is observed, which indicates the featureless grain morphology. However, as the fluence of irradiation increased further from 3×10^{12} to 1×10^{13} ions/cm^2, (Fig. 5.20(d) to (e)) the amorphous state like topography appears which indicates the loss of crystallinity of film at this fluence. However, at this fluence some randomly distributed columnar grains are formed by the coalescence of adjacent grains due to the electronic energy deposited in Ni-Ti matrix by SHI. The change in surface morphology of the films could be understood by electron energy deposited into the films, which are given as when the SHI irradiation falls on the metallic films, it lose their energy into the films followed by excitation and ionization of the atoms of the deposited material. The electronic energy deposited by SHI irradiation into Ni-Ti alloy beyond a certain threshold (S_e~32 keV/nm for Ni-Ti alloy) promotes the significant movement of atoms resulting into the change in the surface morphology (shape of grains) and crystallinity of the film [93].

The surface topography of the pristine and irradiated Ni-Ti films at different fluences can be obtained by using the roughness parameter like average roughness (R_{avg}) and root-mean-square surface roughness (R_{rms}). The surface roughness of all the films was obtained from AFM scan over film area of 2×2 μm^2, three times at a different position for each film by using the following equations [177]:

$$R_{avg} = \left[\frac{1}{N} \sum_{i=1}^{N} | Z_i - \overline{Z} | \right] \text{------------------} (5.1)$$

$$R_{rms} = \left[\frac{1}{N} \sum_{i=1}^{N} | Z_i - \overline{Z} |^2 \right]^{1/2} \text{-----------------} (4.3)$$

where N represents the number of surface height data, and $\overline{Z}$ is the mean height distance.

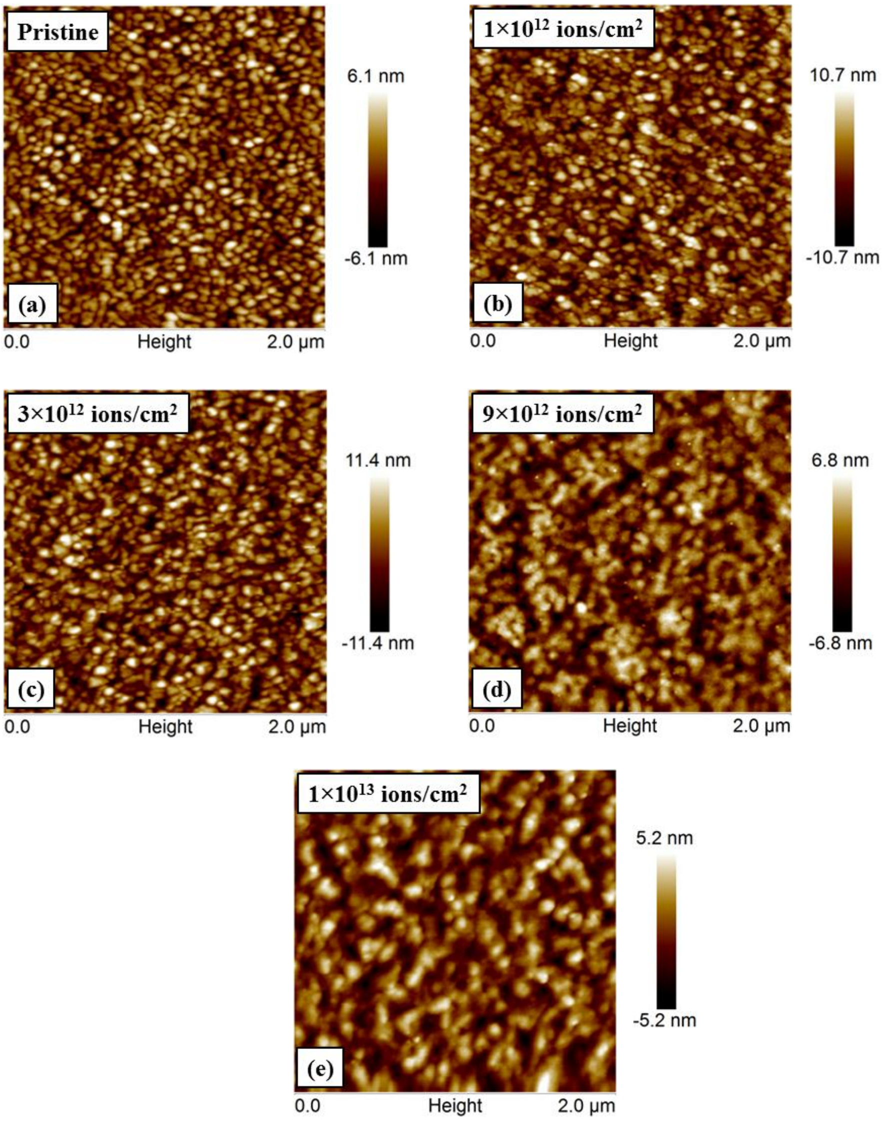

Figure 5.20. AFM (2D) surface morphological micrographs over scan 2×2 μm^2 areas for the pristine and irradiated Ni-Ti thin films at different fluence of (b) 1×10^{12} ions/cm^2 (c) 3×10^{12} ions/cm^2 (d) 9×10^{12} ions/cm^2 and (e) 1×10^{13} ions/cm^2.

The R_{avg} and R_{rms} values of the films increase with the increase in the fluences up to 3×10^{12} ions/cm^2 and then decrease considerably with the increase in the fluence. The R_{avg} value for the pristine film is ~2.14 and for the films irradiated at different fluences are found to be ~3.77 nm, ~4.31 nm, ~2.52 nm and ~1.75 nm, respectively, while the values of R_{rms} for the pristine and the films irradiated at different fluences were found to be ~1.81nm, ~2.23 nm, ~3.89 nm, ~1.83 nm and ~1.32 nm respectively. From the AFM measurement, it has been observed that the small surface roughness contributed by the shallower depression exhibits smooth film surface and higher surface roughness occurs most probably due to the ion irradiation induced sputtering effect during the ion irradiation [208].

5.3.1.4. Nanoindentation

The nanoindentation is a convenient tool to test the fundamental mechanical properties, i.e., elastic modulus and hardness and the extent of stress-induced phase transformation in a small volume of Ni-Ti films. It is employed to measure the penetration depth of an indenter into the film surface along with the applied load to measure the values of area of the contact depth and hardness of the materials deposited on the substrate. In the present study, three indents test were conducted on pristine and the irradiated Ni-Ti thin films at three different locations, each spaced 2 μm apart from each other. Each indenter test consisted of 8-second linear loading, 10-second holding to a peak load and 8-second unloading segment. Mostly the holding period has been used to diminish the time-dependent effects (creep effects) cause by the specimen. Fig 5.21(a)-(e) represents the load versus displacement curves for the pristine and the films irradiated at different fluences of $1\times10^{12,}$ 3×10^{12} 9×10^{12} and 1×10^{13} ions/cm^2, respectively. The mechanical properties such as hardness and elastic modulus of the films were obtained from load versus displacement curves (p-h) and analyzed by using the Oliver and Pharr method [156, 209]. The load versus displacement curves obtained for all the films were plotted in the figure 5.21(a)-(e). The pattern of load versus displacement curves for all the films was consistent from test to test, indicating that the surface of all the films is quite homogeneous over the areas tested. The load versus displacement graphs of all the films shows the overall elastic-plastic response [210]. The unloading curves (plastic response) of all the films are smooth demonstrating the stress recoveries on relaxation during indentation withdraw.

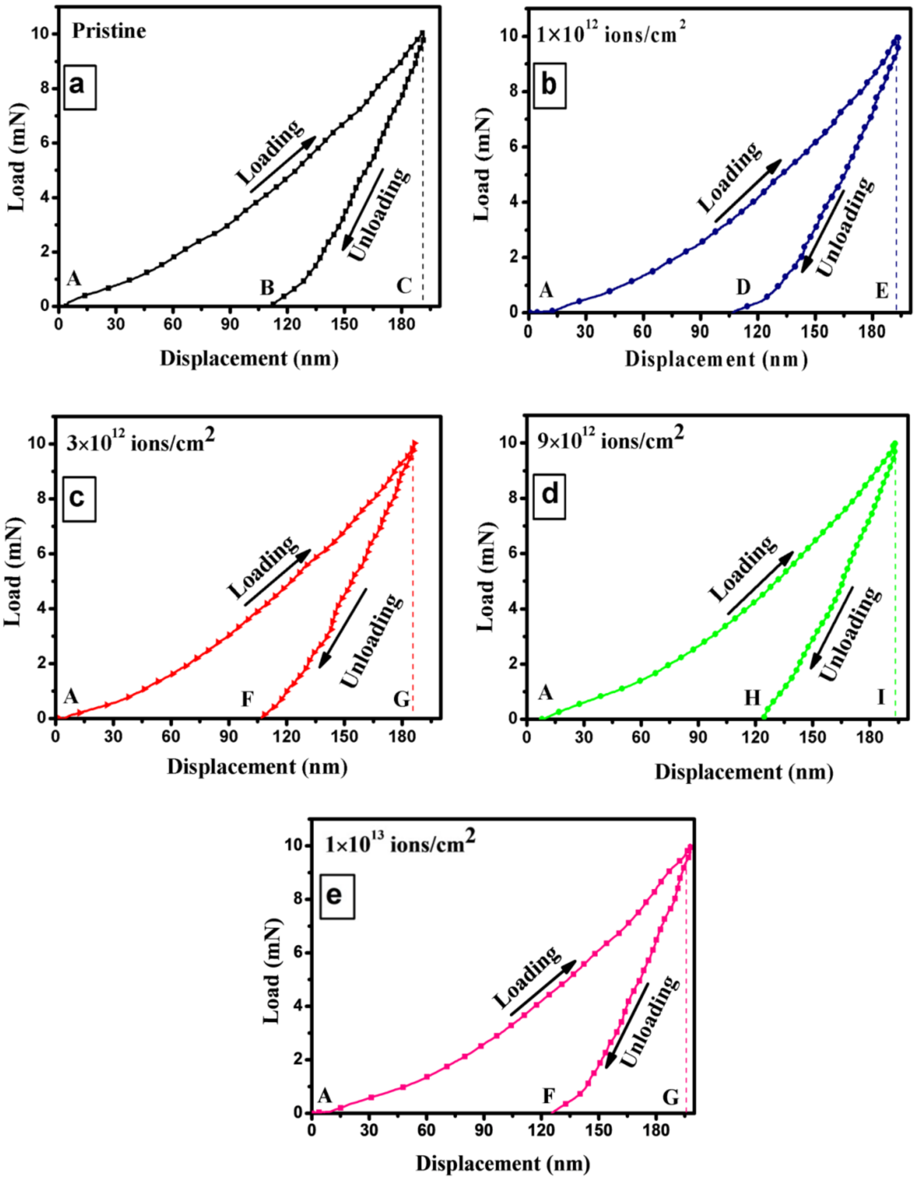

Figure 5.21. Load versus displacement curves for pristine and the films irradiated at different fluences of 90 MeV Ni ions.

It has been observed that irradiation of the films has a significant effect on the mechanical properties of the films irradiated at different fluences. Irradiation of the films up to certain fluence leads to an increase in mechanical strength by grain boundary and dislocation interaction with the consequent increase in average elastic modulus and hardness of the films. At low fluences, the hardness and elastic modulus of the films increase due to the nucleation and propagation of dislocations, but at higher fluence the value of hardness is decreased. The table 5.3 given below shows the variation of hardness and elastic modulus for the pristine and irradiated Ni-Ti thin films.

The elastic modulus of the films is calculated by using the following equation:

$$E_{eff} = \frac{\sqrt{\pi}}{2}\frac{S}{\sqrt{Ac}} ---------------------- (4.5)$$

where S is unloading stiffness at maximum load ($S = \frac{dP}{dh}$) and A_c is the projected contact area and E_{ff} is the effective modulus of the material related to the modulus of elasticity which is given by following equation:

$$\frac{1}{E_{eff}} = \frac{(1-v_i^2)}{E_i} + \frac{(1-v_s^2)}{E_S} ------------------ (4.6)$$

where, subscript *i* represents the indenter material, and subscript *s* corresponds to sample material and ν is the Poisson's ratio. The hardness (H) of the films can be calculated by the following equation:

$$H = \frac{P_{\max}}{A} ------------------------- (3.13)$$

where P_{max} is the maximum indenter load and A is the projected contact area at that load. The calculated values by nanoindentation measurement are shown in table 5.3. The hardness of the pristine film is 11.26 ± 0.4 GPa and for the films irradiated at different fluences of 90 MeV Ni ion are found to be 11.4 ± 0.9 GPa, 12.8 ± 0.9 GPa, 10.90 ± 0.5 GPa and 9.18±0.4 GPa respectively. The elastic modulus of the pristine film is 155.57 ± 4.06 GPa and for the films irradiated at different fluence are found to be 163.39 ± 2.62 GPa, 169.4 ± 2.46 GPa, 164.46 ± 3.92 GPa and 167.46±3.98 GPa respectively. The obtained values of the elastic modulus at different irradiated fluences follow the same trends as shown by the hardness. It illustrates that hardness of the Ni-Ti films increases up to the fluences 3×10^{12} ions/cm^2 and after that, the hardness of the films decreases with increasing the fluences. The decrease in hardness at higher fluences is due to the formation of lattice disorder and partial amorphization of the films. However, the formation of defects such as dislocation, precipitation and ion irradiation induced phases in the shape memory alloy up to certain limit leads to increase in resistivity and barrier strength. However, these treatments contribute to change the martensite transformation temperature by changing the internal stress and chemical composition of the film matrix [108, 211]. It is also reported that hardness of the metallic thin films improved drastically when the thickness of the deposited films on the substrate is below ~300 nm as per the Hall Petch relation [201].

Fluence (ions/cm^2)	**Hardness H (GPa)**	**elastic modulus E_{eff} (GPa)**	**H/E_{eff}**	**Depth recovery ratio**
Pristine	11.2 ± 0.4	155 ± 4.0	0.072 ± 0.001	0.41
1×10^{12}	11.4 ± 0.9	163 ± 2.6	0.069 ± 0.006	0.42
3×10^{12}	12.8 ± 0.9	169 ± 2.4	0.075 ± 0.006	0.42
9×10^{12}	10.9 ± 0.5	164 ± 3.9	0.066 ± 0.003	0.36
1×10^{13}	9.1 ± 0.4	167 ± 3.9	0.054 ± 0.003	0.34

Table 5.3. Variations of hardness and elastic modulus parameter for pristine and irradiated Ni-Ti thin films at different fluences.

The significant feature to examine the behavior of wear resistance of the films is ascribed by the ratio of hardness to elastic modulus. In addition, it is a major parameter to determine the elastic and elastic-plastic behavior of the films. Ni et al. observed that the deformation around the indenter surface arises due to the sink-in and piling-up of material and the tendency of sink-in increases with increasing the value of H/E ratio. The film with the higher ratio of (H/E), results into smaller accumulation strain and leading to excellent wear resistance, while the lower value of (H/E) demonstrates more fraction of work consumed during the plastic deformation and more strain energy is required when contracting a material [202]. The film irradiated at a fluence of 3×10^{12} ions /cm^2 has the higher (H/E_{eff}) value (0.075 ± 0.006). This higher (H/E) value shows the small strain energy and better wear resistance for deformation and thus it can be used in MEMS devices.

The indentation induced superelastic effect is analyzed by depth recovery ratio, which is estimated from the load versus displacement curves by using the following equation [212]:

$$\text{Depth recovery ratio } (\delta) = \frac{(h_{\max} - h_r)}{h_{\max}} \text{-----------------} (4.7)$$

where h_{max} and h_r correspond to the penetration depth at maximum load, and residual displacement when load returned to zero during indentation withdrawal respectively. The value of depth recovery ratio is increases for the pristine and the films irradiated up to the fluence of 3×10^{12} ions/cm^2 and decreases considerably for the films irradiated at fluence 3×10^{12} ions/cm^2 and 3×10^{12} ions/cm^2 as shown in table 5.3. The increment in depth-recovery ratio could be due to the higher hardness and higher degree of crystallization. However, the decrement is most probably due to the lower hardness and irradiation induced defects. The films irradiated at higher fluence of 9×10^{12} and 1×10^{13} ions/cm^2 show the increase in mechanical hysteresis due to the less crystallinity.

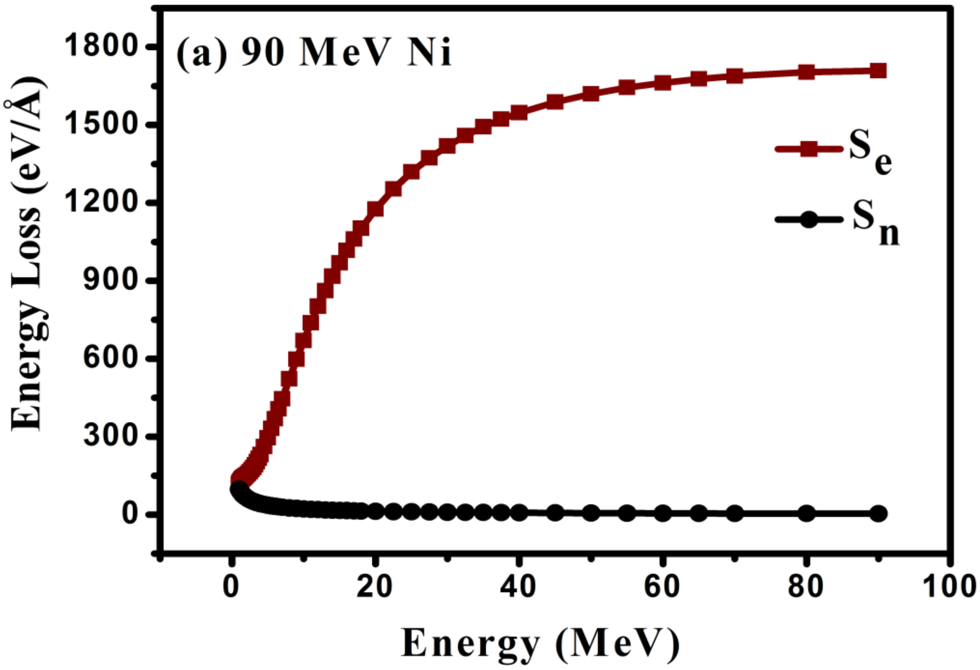

Figure 5.22. SRIM simulation of electronic and nuclear stopping potential versus energy for Ni-Ti film irradiated by Ni ions.

The fig. 5.22 shows the graph between electronic (S_e) and nuclear (S_n) stopping power versus energy (MeV) for the Ni-Ti thin films with composition Ti 57.7at.%-Ni. The variation of S_e and S_n versus energy of the incident 90 MeV Ni ions is simulated by using TRIM 2008 code. The interaction between the bombarded incident ions and the target atoms depends upon the energy, mass and charge of the incident ions species. Sufficient energy provided by the incident ions to the target Ni-Ti matrix can cause the significant moment of the atoms resulting in the change in structural and phase transformation properties of the films. In SHI irradiation process, the energy is deposited into the materials by two independent processes namely as electronic energy loss (S_e) and nuclear energy loss (S_n). In electronic energy loss: ions of indent beam transfer their energy to the electrons of target atoms by inelastic collision and terms known as the electronic energy loss. In nuclear energy loss: ions of incident beam deposited their energy into the material lattice by the elastic collision which causes significant movement of atoms resulting in formation of frenkel defects (vacancies or interstitial defect).

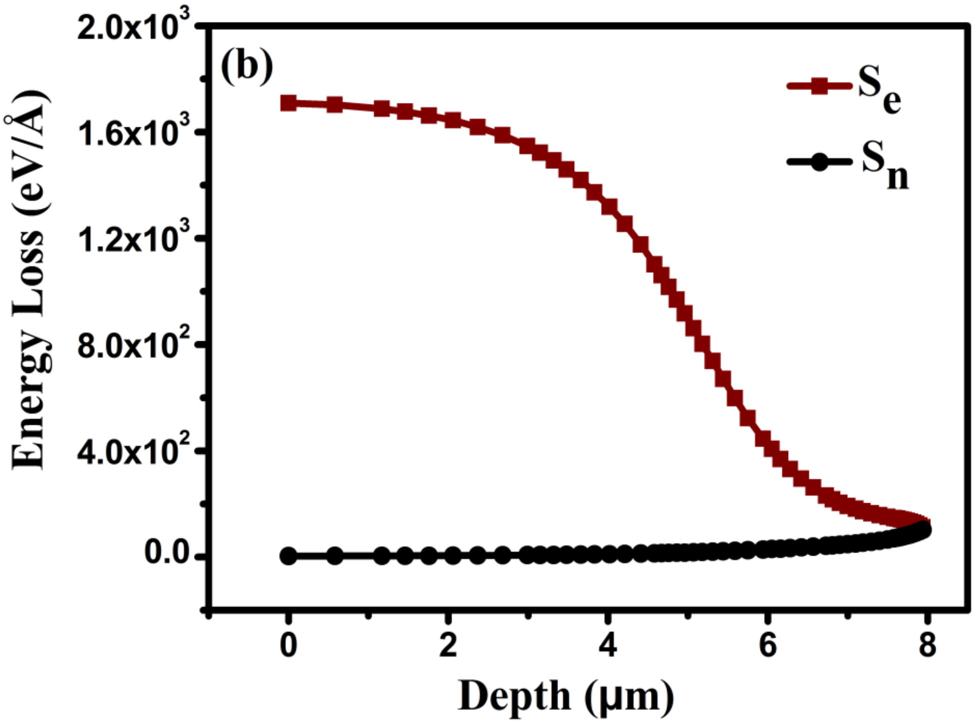

Figure 5.23. SRIM simulation, variation of electronic (S_e) and nuclear stooping ((S_n)) powers of 90 MeV Ni ions with variation in thickness in Ni-Ti thin film.

In the high energy range, energy of the order of MeV/amu, electronic stopping dominates over the nuclear stopping potential, therefore; modifications in the target materials are mainly observed due to the electronic stooping potential. Furthermore, fig.5.23 shows the variations of electronic and nuclear stopping potential with the penetration depth of incident ion beam (90 MeV Ni) in Ni-Ti film. The figure shows that the penetration depth of the incident beam is much larger than the thickness of the films therefore the incident beam could penetrate the Ni-Ti films and get buried into the Si substrate.

Summary:

In the present chapter, a systematic and preliminary investigation on Ni-Ti nanocrystalline thin films deposited on Si substrate at 550 ^{o}C has been done. The prepared Ni-Ti films were irradiated by using different ions species (Au, Ag & Ni) and energies, i.e., 120 MeV, 100 MeV, and 90 MeV respectively. The experimental results of surface modifications conditions and structural, electrical and mechanical properties of as-deposited and modified Ni-Ti thin films were analyzed, compared and discussed in this chapter. The study of surface modifications and enhancement in various properties of the Ni-Ti SMAs films at different fluences and ion species leads to conclusions. SHI irradiation was extensively applied to engineering the structural, electrical, mechanical and chemical properties of Ni-Ti SMA material near the surface region. This innovative materials modification treatment alters the initial surface, and following effects are observed:

In case of the films irradiated by 120 MeV Au ions at different fluence ranging from 1×10^{12} to 3×10^{13} ions/cm^2, the surface morphology of the films changes with the increase in fluence as confirmed by FESEM and AFM micrographs. As the fluence increases, spherical shaped grains increases as compared to pyramidical ones due to change in phase and at considerable the higher fluence of 3×10^{13} ion/cm^2, spherical grains also disappear due to the amorphization of the films at such high fluence. The crystallinity of the Ni-Ti SMAs decreases with increase in fluences and at a fluence of 3×10^{13} ions/cm^2 complete amorphization occurred as authenticated by XRD. Further, R-T measurement is revealed that clear phase transformation from martensite to austenite phase and vice versa via R- phase in pristine film during subsequent heating and cooling cycles. The R-T measurements also revealed the degradation of shape memory effect and occurrence of the non-metallic behavior of Ni-Ti films irradiated at higher fluences. Further, in the case of the films irradiated at 100 MeV Ag^{7+} ion irradiation at different fluences of 1×10^{12}, 5×10^{12} and 1×10^{13} ions/cm^2, the structural and mechanical properties significantly change with change in ion fluences. The films irradiated at a fluence of 1×10^{13} ions/cm^2 shows the formation of buried Ni_3Ti precipitate phases as authenticated by XRD. XRD measurement also evidences that irradiation of Ni-Ti film at higher fluence suppresses the austenite and martensite phases by introducing an intermediate Ni_3Ti precipitation phase. AFM and FESEM measurements show the change in surface morphology with fluence. The Ni-Ti films surface roughness was increased with increase in ion fluence, which may be due to the ion irradiation, induce sputtering effects. Furthermore, nanoindentation measurement revealed that hardness and Young modulus of Ni-Ti thin films improved with increase the ion fluences. In addition to that, Ni-Ti thin films are also irradiated by using 90 MeV Ni ions to investigate the stability of austenite and martensite phase against the SHI irradiation. The irradiated Ni-Ti films show the less stability of martensite and higher stability of austenite phase towards the SHI irradiation.

Chapter 6

Conclusion and Future Work

6.1 Summary of the work done

In the present research work, we have studied the synthesis and modifications of binary Ni-Ti SMAs thin films by using SHI irradiation. The Ni-Ti thin films have been prepared by using magnetron co-sputtering technique with two different targets (Ni and Ti). To enhance the various properties, modifications have been done by employing different energy and ion fluences. The various aspects of modified Ni-Ti alloy, including crystallographic mechanism of martensitic phase transformation and shape memory effect, the effects of implantation/irradiation on phase transformation path and on mechanical properties have been investigating using different characterization techniques. From these results following conclusions can be drawn:

It is concluded that-

(i) Sputter-deposited Ni-Ti thin films with composition Ti 57.7at.%Ni on Si substrate have been successfully synthesized. The shape memory effect and mechanical properties are found comparable to those of bulk alloy.

(ii) The synthesized films show the preferential orientation of Ni-Ti alloy corresponding to austenite and martensite phases. It has been revealed that the precise control on deposition parameters could be used to manipulate the transformation temperatures. Furthermore, films exhibit the good crystallinity and uniform growth.

(iii) The incorporation of implanted Ag ions into the Ni-Ti SMAs matrix modified the structure of Ni-Ti, which subsequently changes the phase transformation path and transition temperatures.

(iv) Ion implantation of Ni-Ti films at different fluence leads to the formation of R-phase which is found to be very advantageous for the two ways shape memory effect.

(v) Increase in fluence of implanted Ag ions shifts the martensite transformation towards lower temperature.

(vi) Mechanical properties of implanted Ni-Ti thin films are improved Ag ions implantation. A better shape recovery in terms of higher recoverable strain was attainable with the increase in the fluence of Ag ions in Ni-Ti matrix.

(vii) The structural and mechanical properties of nanocrystalline Ni-Ti thin films are found to be dependent on ion fluence and their corresponding energies. The films irradiated by 120 MeV Au ions show the complete amorphization behavior, however, in case of the films irradiated by 100 MeV Ag and 90 MeV Ni ions partial amorphization is seen.

(viii) The preferential orientation of sputtered Ni-Ti films is also influenced by the application of SHI irradiation. It has been observed that the precise control of the electronic energy of the bombarding ions could be used as a tool to modify the various properties of materials. Further, the films irradiated by 120 MeV Au ions exhibit the non-metallic behavior at room temperature.

(ix) The optimization of the irradiation fluence and species leads to the growth of hard precipitation and ductile phase on graded Ni-Ti films. This could be useful for the fabrication of the films with higher ductility and superior mechanical properties.

(x) The preferential growth of <110> orientated grains of austenite phase from the beginning of the deposition is observed. This is ascribed to the fact that most of the body centred cubic structure grow with minimum surface energy.

(xi) The Ag ion irradiated Ni-Ti thin film exhibits improved mechanical properties and excellent wear resistance by grain boundaries and dislocation interaction in comparison to pristine film, while the Ni ion irradiation at higher fluence results in the decrease of mechanical strength.

(xii) 90 MeV Ni ion irradiated magnetron sputter Ni-Ti films show the modification in crystallite size. The increase in fluence of irradiation ions (1×10^{12} to 1×10^{13} ions/cm^2) decreases the crystallite size (from 31.57 nm to 18.52 nm). This is because of the defragmentation of grains due to the deposition of very high energy into the Ni-Ti films.

(xiii) The increase in 90 MeV Ni ion fluence results in the change in surface roughness of irradiated Ni-Ti films. The surface smoothing increases with increasing the ion fluence.

(xiv) The structural, electrical, morphological and mechanical properties of Ni-Ti films can be tuned by making use of SHI irradiation/implantation; however, high fluence could degrade their shape memory properties.

(xv) Shape memory characteristic of the alloy degrades at high energy ion irradiation condition. In contrary, ion irradiation at low fluences with a proper ion beam leads to higher ductility.

6.2 Future prospects

Depending on above results and discussions, it is evident that there are many possible extensions and opportunities of the present work for further research and development, some of them can be given as:

(i) The electrochemical measurement of Ni-Ti SMAs based alloy at high temperature needs to be made to understand the corrosive behavior of Ni-Ti thin films.

(ii) The temperature dependent XRD measurement could be performed on pristine and irradiated Ni-Ti SMAs across the transition temperature. This experiment will provide the information of microstructure and amount of phase change from one crystal structure to another (martensite to austenite content). The temperature dependent XRD measurement of binary and irradiated/implanted films may be helpful to understand the mechanism of tuning of the transformation temperature of Ni-Ti SMAs films.

(iii) A systematic study on the variation of thickness and dimension is required. This study would be important for the microactuator devices.

(iv) In addition, the effect of implantation of ions of various gases (Ar, N_2, C and O_2 etc.) in Ni-Ti thin film needs to be investigated in detail.

References

[1] I. Chopra, Review of state of art of smart structures and integrated systems, AIAA J. **40**, 2145-2187 (2002).

[2] C.E. Borroni-Bird, Smarter vehicles. Smart structures and materials: industrial and commercial applications of smart structures technologies, San Diego, CA, (1997).

[3] C.Q. Chen, Y.P. Shen, Smart Mater. Struct. **8**, 403-409 (1997).

[4] C.A. Jaeger and C.A. Rogers, in ‘‘Proceedings of the ARO Workshop on Smart Materials, Structures and Mathematical Issues’’, ARO, Washington, (1988).

[5] P.F. Gobin, J. Tatibouet, in “Proceedings of the 3rd International Conference on Intelligent Materials” Technomic, Lancaster, (1996).

[6] T. Takagil, J. Intelligent Mater. System Struct. **1**, 149-156 (1990).

[7] J. Hu, S. Liu, Macromolecules **43,** 8315-8330 (2010).

[8] M. Salehi, M. Hamedi, S.H. Nohouji, J. Arghavani, Smart Mater. Struct. **23**, 025001 (2014).

[9] H.S. Tzou, H.J. Lee, S.M. Arnold, Mech. Adv. Mater. Struct. **11**, 367-393 (2004).

[10] M. Kohl, E. Just, W. Pfleging, S. Miyazaki, Sens. Actuators A **83**, 208-213 (2000).

[11] A. Emre, O.E. Ozbulut, H.E. Karaca, Smart Mater. Struct. **24**, 075020 (2015).

[12] K. Otsuka, X. Rena, Prog. Mater. Sci. **50**, 511-678 (2005).

[13] Y. Cheng, W. Cai, H.T. Li, Y.F. Zheng, L.C. Zhao, Surf. Coat. Technol. **186**, 346-352 (2004).

[14] W.J. Buehler, J.W. Gilfrich, R.C. Wiley, J. Appl. Phys. **34**, 1475-1477 (1963).

[15] F.E. Wang, W.J. Buehler, S.J. Pickart, J. Appl. Phys. **36**, 3232-3239 (1965).

[16] Johnson Matthey Medical Components. Nitinol technical properties. http://jmmedical.com/resources/221/Nitinol-Technical-Properties.html.

[17] D.E. Hodgson, H.W. Ming, J.B. Robert, Shape memory alloys Metal Handbook, **2**, 10th ed., ASM International, Materials Park, (1990).

[18] K. Otsuka, T. Kakeshita, Science and Technology of Shape-Memory Alloys: New Developments, MRS Bull. **27**, 91-100 (2002).

[19] H. Sitepu, W.W. Schmahl, D.M. Toebbens, Textures and Microstructures **35**, 185-195 (2003).

[20] D. Shindo, Y. Murakami, T. Ohba, MRS Bull. **27**, 121-127 (2002).

[21] T. Goryczka, H. Morawiec, J. Alloys Compd. **367**, 137-141 (2004).

[22] T. Waitz, V. Kazykhanov, H.P. Karnthaler, Acta Mater. **52**, 137-147 (2004).

[23] Ed Gerstner, Shape-memory alloys, Nature.com (2002).

[24] K.C. Atli, I. Karaman, R.D. Noebec, D. Gaydosh, Mater. Sci. Eng. A **560**, 653-666 (2013).

[25] D.A. Porter, K.E. Easterling, Phase Transformations in Metals and Alloys, Chapman & Hall, (1992).

[26] M. Bendahan, K. Aguir, J.L. Seguin, H. Carchano, Sens. Actuators **74**, 242-245 (1999).

[27] A. Gyobu, Y. Kawamura, T. Saburi, M. Asai, Mater. Sci. Eng. A **312**, 227-231 (2001).

[28] J.J. Gill, D.T. Chang, L.A. Momoda, G.P. Carman, Sens. Actuators **93**, 148-156 (2001).

[29] Y.Q. Fu, H.J. Du, Mater. Sci. Eng. A **342**, 236-244 (2003).

[30] N. Bayat, S. Sanjabi, Z.H. Barber Surf. Coat. Technol. **206**, 4075-4078 (2012).

[31] S. Miyazaki, A. Ishida, Mater. Sci. Eng. A **273-275**, 106-133 (1999).

[32] P. Krulevitch, A. P. Lee, P. B. Ramsey, J. C. Trevino, J. Hamilton, M. A. Northrup. J. Microelectromechanical Systems **5,** 270-282 (1996).

[33] F. Auricchio, R.L. Taylor, J. Lubliner, Comput. Methods Appl. Mech. Eng. **146**, 281-312 (1997).

[34] D.C. Lagoudas, Pseudoelastic loading path http://smart.tamu.edu/overview/ smaintro/simple/ pseudoelastic.html.

[35] Matsumoto H. J Alloys Compd **350,** 213-217 (2003).

[36] M. Nishida, C.M. Wayman, T. Honma, Metall. Trans. **17A**, 1505-1515 (1986).

[37] Y. Kudoh, M. Tokonami, S. Miyazaki, K. Otsuka, Acta Metall. **33**, 2048-2057 (1985).

[38] X. B. Wang, B. Verlinden, J. Van Humbeeck, Mat. Sci. and Tech. **30**, 2049-2056 (2014).

[39] G. M. Michal, R. Sinclair, Acta Crystallogr. B **37**, 1803-1807 (1981).

[40] T. Saburi, K. Otsuka, C.M. Wayman (Eds). Cambridge University Press. pp. 49-96 1998.

[41] T. Hara, T. Ohba, K. Otsuka, M. Nishida, Mater. Trans. **38**, 277-284 (1997).

[42] D. Wan, K. Komvopoulos, J. Mater. Res. **20**, 1606-1612 (2005).

[43] Nunomura, Y. Kaneno, H. Tsuda, T. Takasugi, Intermetallics **12,** 389-399 (2004).

[44] W. Tang, Metall. Mater. Trans. **28A**, 537-544 (1997).

[45] H. Kahn, M.A. Huff, A.H. Heuer, J. Micromech. Microeng. **8**, 213-221 (1998).

[46] Y. Kaynak, H. Tobe, R.D. Noebe, H.E. Karaca, I.S. Jawahir, Scripta Materialia **74**, 60-63 (2014).

[47] Y.Q. Fu, J.K. Luo, A.J. Flewitt, Inter. J. Nano-manufacturing (2009).

[48] H. Richard Wolf, H. Arthur, Micro. stems, **4**, 206-212 (1995).

[49] Chen WW, Wu Q, Kang JH, Winfree NA. Int J Solids Struct **38**, 8989-98 (2001).

[50] Z. G. Wei, R. Sandstroröm, S. Miyazaki, **33**, 3743-3762 (1998).

[51] . H. Horikawa, H. Tamura, Y. Okamoto, H. Hamanaka, T. Miura, MRS Int Mtg Adv Mater, **9**, 195 (1989)

[52] K. Otsuka, X. Ren, Mater. Sci. Eng. A **273-275**, 89-105 (1999).

[53] J. V. Humbeeck, Adv. Eng. Mater. **3**, 837-850 (2001).

[54] J. V. Humbeeck, R. Stalmans, Shape Memory Alloys Types and Functionalities; Wiley: 951 (2002).

[55] J.H. Sui , W. Cai, Appl. Surf. Sci. **253**, 2050-2055 (2006).

[56] J. D. Bush, A. D. Johnson, C. H. Lee, Stevenson, J. Appl. Phys. **68(12),** 6224-6228 (1990).

[57] J. L. Brimhall, H. E. Kissinger, A. R. Pelton, Radiat. Eff. Defects Solids, **90**, 241-258 (1985).

[58] C. Chluba, W. Ge, R. L. de Miranda, J. Strobel, L. Kienle, E. Quandt, M. Wuttig, Science, **348**, 1004-1007 (2015).

[59] S. Klaumunzer, M. D. Hou, G. Schumacher, Phys. Rev. Lett. **57**, 850-853 (1986).

[60] S. Klaumunzer, Nucl. Instr. and Meth. B **244,** 1-6 (2006).

[61] A. H. Zhang and Jing Zhu, Phys. Rev. B **74**, 045425-0454256 (2006).

[62] C. D. Orleans, J. P. Stoquert, C. Estoumes, C. Cerruti, J. J. Grob, J. L. Guille, F. Haas, D. Muller and M. R. Plouet, Phys. Rev. B **67,** 220101-220104 (2003).

[63] E. Valentin, H. Bernas, C. Ricolleau, F. Creuzet, Phys. Rev. Lett. 86, 99-102 (2001).

[64] Ekmel Ozbay, Science **311**, 189-193 (2006).

[65] P. Mukherjee, R. Bhattacharya, Nancy Bone, Yean K. Lee, C. R. Patra, S. Wang, Lichun Lu, C. Secreto, P. C Banetjee, M. J. Yaszemski, N. E. Kay and D. Mukhopadhyay, Jour. of Nanobiotechnology **5**, 1-13 (2007).

[66] M. Kumar, S. A. Khan, F. Singh, A. Tripathi, D. K. Avashti, A. C. Pandey, Nucl. Instr. Meth. in Phys. Res. B **256,** 323-328 (2007).

[67] D. K. Avasthi, W. Assmann, H. Nolte, H. D. Mieskes, H. Huber, E. T. Subramaniyam, A. Tripathi, S. Ghosh, Nucl. Instr. Meth. in Phys. Res. B **156**, 143-148 (1999) .

[68] T. Som, B. Satpati, 0. P. Sinha, N.C. Mishra and D. Kanjilal, Nucl. lnstr. Meth. in Phys. Res. B **244**, 213-220 (2006).

[69] J. Prakash, A. Tripathi, S. A. Khan, J. C. Pivin, F. Singh, J. Tripathi, S. Kumar, D. K. Avasthi, Vacuum **84**, 1255-1257 (2010).

[70] K. Awazu, X. Wang, M. Fujimaki and J. Tominaga, H. Aiba, Y. Ohki, T. Komatsubara, Phys. Rev. B **78,** 054102-054108 (2008).

[71] J. C. Pivin, G. Roger, M.A. Garcia, F. Singh, D. K. Avasthi, Nucl. Instr. And Meth. in Phys. Res. B **215**, 373-384 (2004).

[72] B. Schmidt, K. H. Heinig, A. Muckich, C. Akhmadaliev, Nucl. Instr. and Meth. In Phys. Res. B **267**, 1345-1348 (2009).

[73] J. Penninkhof, T. Van Dillen, S. Roorda, C. Graf, A. van Blaaderen, A.M. Vredenberg A. Polman, Nucl. Instr. and Meth. B **242**, 506-508 (2006).

[74] M. Toulemonde, J. M. Costantini, Ch. Dufour, A. Meftah, E. Paumier, F. Studer, Nucl. Instr. and Meth. B **116**, 37-42 (1996).

[75] S. Miyazaki, K. Otsuka, Development of shape memory alloys, ISIJ International, 29, 353 (1989).

[76] Zhu, S. L., X. J. Yang, et al. Mater. Sci. Eng., C, **28(8):** 1271-1275 (2008).

[77] L. Maissel and R. Giang, Handbook of Thin Film Technology (McGrawHill, New York, 1970), pp. 28-29.

[78] A.R. Pelton, J. Mater. Eng. Perform. **20,** 613-617 (2011).

[79] Raniecki B, Lexcelent C. Eur. J. Mech. A Solids **185,** 17-20 (1998).

[80] S. Mandl, A. Fleischer, D. Manova, B. Rauschenbach, Surf. Coat. Technol. **200**, 6225-6229 (2006).

[81] Y.Fu, H.Du, W. Huang, S. Zhang, M. Ha, Sens. Actuators A **112**, 395-408 (2004).

[82] H. Zhang, Y. Cheng, Y. Zheng Surf. Coat. Technol. **201,** 6857-6860 (2007).

[83] Ju X, Dong H. Surf. Coat. Technol. **201**, 1542-1547 (2006).

[84] D. Wever, A. Veldhuizen, M. Sanders, J. Schakenrad, Van Horn J. Biomaterials **18,** 1115-1120 (1997).

[85] S. Mandl, J.K.L. Lindner, Nucl. Instrum. Methods B **249**, 355-357 (2006).

[86] N. Smith, G. Antoun, A. Ellis, W. Crone, Appl. S. **35**, 1307-1312 (2004).

[87] A. Kumar, D. Singh, D. Kaur, Sensors and Actuators A **178**, 57-63 (2012).

[88] A. Kumar, D. Singh, D. Kaur Surf. Coat. Technol. **203**, 1596-1603 (2009).

[89] A. Ishida, M. Sato, Acta Materialia **51**, 5571-5578 (2003).

[90] S. Sanjabi, Z.H. Barber, Surf. Coat. Technol. **204**, 1299-1304 (2010).

[91] B. Naveen Kumar Reddy, N.K. Udayashankar, Surfaces and Interfaces **5**, 62-71 (2016).

[92] L.B. Tong, Y.H. Li, F.L. Meng, H.W. Tian, W.T. Zheng, Y.M. Wang, J. Alloys Compd. **494**, 166-168 (2010).

[93] A. Barbu, Dunlop, Hardouin Duparc, G. Jaskierowicz, N. Lorenzelli, Nucl. Instrum. Methods Phys. Res., Sect. B **145**, 354-372 (1998).

[94] T. LaGrange, C. Abromeit, R. Gotthardt, Mater. Sci. Eng. A **438-440**, 521-526 (2006).

[95] T. LaGrange, R. Gotthardt, Scripta Mater. **50**, 231-236 (2004).

[96] Florent Goldberg, Emile J. Knystautas, Thin Solid Films **342,** 67-73 (1999).

[97] R.F. Konopleva, I.V. Nazarkin, V.L. Solovei, V.A. Cheknov, S.P. Belyaev, A.E. Rajov, Physics of Solid State **40,** 1550-1554 (1998).

[98] R. Vishnoi, R. Singhal, K. Asokan, D. Kanjilal, D. Kaur, Thin Solid Films **520**, 1631-1637 (2011).

[99] Z.G. Wang, X.T. Zu, Y. Huo, S. Zhu, X.W. Wei, L.M. Wang, Nucl. Instrum. Methods Phys. Res., Sect. B **215,** 436-442 (2004).

[100] X.T. Zu, F.R. Wan, S. Zhu, L.M. Wang, Physica B **351,** 59-62 (2004).

[101] X.T. Zu , L.B. Lin , Z.G. Wang , S. Zhu , L.P. You, L.M. Wang , Y. Huo J. Alloys Compd. **351**, 87-90 (2003).

[102] Z.G. Wang , X.T. Zu, L.J. Liu, S. Zhu, Y. Huo, L.B. Lin, X.D. Feng, L.M. Wang , Nucl. Instrum. Methods Phys. Res., Sect. B **211**, 239-243 (2003).

[103] Naveed Afzal, I.M. Ghauri, F.E. Mubarik, F. Amin, Physica B **406**, 8-11 (2011).

[104] M. Yousaf, M. A. Arif, I. Ali, S. Ahmad, G. M. Mustafa, Naveed Afzal, I. M. Ghauri, Mater. Today **2**, 5622-5626 (2015).

[105] N. Ikenaga, Y. Kishi, Z. Yajima, N. Sakudo, S. Nakano, H. Ogiso, Nucl. Instrum. Methods Phys. Res., Sect. B **267**, 1509-1513 (2009).

[106] T. Zhao, Y. Li, Y. Xiang, X. Zhao, T. Zhang, Surf. Coat. Technol. **205**, 4404-4410 (2011).

[107] H. Pelletiera, D. Mullerb, P. Millea, J.J. Grob, Surf. Coat. Technol. **158-159**, 309-317 (2002).

[108] H. Pelletiera, D. Mullerb, P. Millea, J.J. Grob, Surf. Coat. Technol. **158-159**, 301-308 (2002).

[109] M.R. Gorji, S. Sanjabi, Z.H. Barber, Micro & Nano Letters **7**, 641-645 (2012).

[110] T. Zhao, Y. Li, Y. Liu, X. Zhao J Mech. Behav. biomed **13**, 174-184 (2012).

[111] S. Kucharski, N. Levintant-Zayonts, J. Luckner, Mater. Des. **56**, 671-679 (2014).

[112] Y. Li, T. Zhao, S. Wei, Y. Xiang, H.Chen, Mater. Sci. Eng., C **30**, 1227-1235 (2010).

[113] N. Levintant, Vacuum **81**, 1283-1287 (2007).

[114] R.M. Oliveira, B.B. Fernandes, F.C. Carreri, J.A.N. Goncalves, M. Ueda, M.M.N.F. Silva, M.M. Silva, L. Pichon, E.N. Camargo, J. Otubo, Appl. Surf. Sci. **263**, 763-768 (2012).

[115] N.L. Zayonts, S. Kucharski, Vacuum **83,** 220-223 (2009).

[116] V.G. Kotnur, G.C.A.M. Janssen, Surf. Coat. Technol. **211**, 167-171 (2012).

[117] S.K. Sharma, H.S. Vijaya, S. Mohan, Phys. Proc. **10**, 44-51 (2010).

[118] N. Choudhary, D.K. Kharat, D. Kaur, Solid State Phenom. **185,** 25-27 (2012).

[119] H. Thomas, Funakubo H, Shape memory alloy. New York: Gordon and Breach Science Publishers; 1987.

[120] Y. Sekiguchi, K. Funami, T. Funakubo, Proc 32nd Materials Society Annual Conf, 1983. p. 65 [in Japanase].

[121] J.J. Kim, P. Moine, D.A. Stevenson D.A. Scripta Metal. **20**, 243-248 (1986).

[122] Y. Fu, H. Du, W. Huang, S. Zhang, and M. Hu. Sens. Actuators, A. **112,** 396-408 (2004).

[123] R. Behrisch (ed.) (1981). Sputtering by Particle bombardment: Springer, Berlin. ISBN 978-3-540-10521-3.

[124] R. Behrisch and W. Eckstein (eds.). Sputtering by Particle bombardment: Experiments and Computer Calculations from Threshold to MeV Energies. Springer, Berlin (2007).

[125] P. Sigmund, Nucl. Instr. Meth. Phys. Res. B **27,** 1-20 (1987).

[126] T. Schenkel; Briere, M. Schmidt-Böcking, H. Bethge, K. Schneider, Phys. Rev. Lett. **78 (12),** 2481-2484 (1997).

[127] M. Sporn, Libiseller, G. Neidhart, T. Schmid, M. Aumayr, F. Winter, H.P. Varga, P. Grether, M. Niemann, D. Stolterfoht Phys. Rev. Lett. **79 (5),** 945-948 (1997).

[128] T. Neidhart, F. Pichler, F. Aumayr, H.P. Winter, M. Schmid, P. Varga, Phys. Rev. Lett. **74 (26),** 5280-5283 (1995).

[129] T. A. Schoolcraft and B. J. Garrison, Journal of the American Chemical Society. **113** (22), 8221-8228 (1991).

[130] A. Rockett, "Sputter deposition of thin films", University of Illinois, U.S.A., 1998.

[131] S. Chapman, T. G. Cowling, The mathematical theory of non-uniform gases, 3rd. edition, Cambridge University Press, 1990, ISBN 0-521-40844-X, p. 88.

[132] D. Kanjial, Current Science **80**, 1560 (2001).

[133] D.K. Avasthi and G.K. Mehta, Swift Heavy Ions for Materials Engineering and Nanostructuring, Springer Science & Business Media, 2011.

[134] S. Klaumunzer, Nucl. Instr. and Meth. B **225**, 136-146 (2004).

[135] D. Kanjilal, S. Chopra, M. M. Narayanan, I. S. Iyer, V. Jha, R. Joshi, S.K. Datta, Nucl. Instr. and Meth. A **238,** 97-100 (1993).

[136] D.K. Avasthi and W. Assmann, Current Science **80**, 1532-1541 (2001).

[137] http://www.iuac.ernet.in/infrastructure/accelerators/pelletron/Accelerator.htm

[138] H. Goldstein, Classical Mechanics, Addison-Wesley, Reading, MA (1959).

[139] L. C. Feldman, J. W. Mayer, Fundamentals of Surfaces and Thin Film Analysis, North Holland, New York, Chapter 2, Atomic Collisions and Backscattering Spectrometry (1986) 13.

[140] W. K. Chu, J. W. Mayer and M. A. Nico let, Backscattering Spectrometry, Academic Press, New York (1978).

[141] K. Oura, V.G. Lifshits, A.A. Saranin, A.V. Zotov, Surface Science: An Introduction. Springer-Verlag. ISBN 3-540-00545-5 (2003).

[142] B.D. Cullity, Elements of X-Ray Diffraction, Addison-Wesley, Reading, MA, (1970).

[143] A. Dahshan, K.A. Aly, J. Non-Cryst. Solids **408**, 62-65 (2015).

[144] G. Binnig, C. Quate and G. Gerber, Phys. Rev. Lett. **56**, 930-933 (1986).

[145] P. Echlin, D.C. Joy, C. Fiori, E. Lifshin, Scanning Electron Microscopy and X-Ray Microanalysis, ed. by Goldstein J. I. and Newbury D. E., Plenum, New York, (1981).

[146] Z. L. Wang, Journal of Physical Chemistry. B. **104**, 1153-1175 (2000).

[147] J. Pawley, Scanning. **19**, 324-336 (1997).

[148] Brandon D. and Kaplan W. D. Microstructural Characterization of Materials, John Wiley and Sons Ltd., England, (2008).

[149] P.J. Goodhew, T. Humpreys, R. Branland: Electron Miscroscopy and analysis Third edition, pp 122-166-(Taylor & Francis Group), 2001.

[150] M. T. P. Postek, K.S. Howard, A. T. Johnson, K.L.Mc Miche: Scanning Electron Microscopy (Ladd Research Industries, 83 Holly court, Williston, Vermont, (2001).

[151] Masato Yamashita: J. Appl Phys., **42**, 695-668 (2002).

[152] S. Brodowski,Wu. Amelung, Lu. Haumaier C. Abetzc, W. Zech Geodema **128**, 116-129 (2005)

[153] A. J. D’Alfonso, B. Freitag, D. Klenov, L. J. AllenPhy. ReV. B **81**, 100-105 (2010).

[154] H. Thomas, S. Thomas, R.V. Ramanujan, D. K. Avasthi, I.A. Omari, S. Harthi M.R. Anantharaman Nucl. Instrum. Methods Phys. Res. Sect. B **287**, 85-90 (2012).

[155] K.H., Ken; P.C., Gregory Thin Solid Films **370**, 18-29 2000.

[156] W.C. Oliver, G.M. Pharr, J. Mater. Res. **7**, 1564-1583 (1992).

[157] X. Cai, H. Bangert, Thin solid films **264**, 59-71 (1995).

[158] C.L. Chu, T. Hu, S.L. Wu, Y.S. Dong, L.H. Yin, Y.P. Pu, P.H. Lin, C.Y. Chung, K.W.K. Yeung, P.K. Chu, Acta Biomater. **3**, 795-806 (2007).

[159] C.W. Chan, H.C. Man, T.M. Yue, Corrosion Science **56,** 158-167 (2012).

[160] Y. Cheng, W. Cai, H.T. Li, Y.F. Zheng, J. Mater. Sci. **41**, 4961-4964 (2006).

[161] Z.D. Cui, H.C. Man, X.J. Yang Surf. & Coat. Tech. **192**, 347-353 (2005).

[162] L. Tan, R.A. Dodd, W.C. Crone, Biomaterials **24**, 3931-3939 (2003).

[163] Y. Li, S.B. Wei, X.Q. Cheng, T. Zhang, G.A. Cheng, Surf. & Coat. Tech. **202**, 3017-3022 (2008).

[164] André Anders, et al., Handbook of plasma immersion ion implantation and deposition, Ed, John Wiley and Sons, New York, (2000).

[165] A. Gupta, R. Singhal, N. Jagdish, D.K. Avasthi J. Mater. Res. **26**, 2901-2906 (2011**)**.

[166] Q.Z. An, K. Feng, H. Lu, X. Cai1, T. Sun, P.K. Chu Trans. Nonferrous Met. Soc. China, **25**, 1944-1949 (2015).

[167] V. Kumar, R. Singhal, R. Vishnoi, M. Gupta, P. Sharma, M.K. Banerjee, K. Asokan, H. Sharma, A. Gupta, D. Kanjilal, Adv. Mat. Lett. **8(4),** 486-492 (2017).

[168] J.F. Ziegler, J.P. Biersack, V. Littmark, The stopping and range of ions in solids, New York: Pergamon, (1985).

[169] W.O. Adeoya, M.H. Ali, J.C. Muller, P. Siffert, Appl. Phys. Lett. **50**, 1736-1738 (1987).

[170] Y.F. Zheng, B.B. Zhang, B.L. Wang, Y.B. Wang, L. Li, Q.B. Yang, L.S. Cui, Acta Biomater. **7**, 2758-2767 (2011).

[171] Warren BE. X-ray diffraction. Reading, MA: Addison-Wesley; 1986

[172] A.A. Akl, A.S. Hassanien, Superlattices and Microstruct. **85,** 67-81 (2015).

[173] J.M. Zhang, F. Ma, X. Ke Surf. Interface Anal. **35**, 662-666 (2003).

[174] A.K. Lowsk, J.C. Cki, A. Fahmi, B. Beker, Dalton Trans. **47**, 6825-6831 (2008).

[175] S. Sanjabi, Sayed K.S., Karen A.Y., Zoe H.B., Thin Solid Films **491**, 190-196 (2005).

[176] A. Gyobu, Y. Kawamura, H. Horikawa, T. Saburi, Mater. Sci. Eng., A, **273-275**, 749-753 (1999).

[177] H.S. Zhang, J.L. Endrino, A. Anders, Appl. Surf. Sci. **255**, 2551-2556 (2008).

[178] Yijun Zhang,Yang-Tse Cheng, J. Appl. Phys. **98**, 033505-4 (2005).

[179] Gall K, Sehitoglu H. Int J Plasticity **15**, 69-92 (1999).

[180] M.C. Mei, L. Gang, L. Jain, Zhanglide, Mater. Sci. Eng. A **127**, 85-89 (1990).

[181] Mohamed Ali, M.S.; Takahata, K. Sens. Actuators A Phys. **163**, 363-372 (2010).

[182] A. D. Johnson. J. Micromachin, 4, 34-41 (1999).

[183] M. Mohri, M.N. Ahmadabadi, J. Ivanisenko, Adv. Eng. Mater. **17**, 856-865 (2015).

[184] C. M. Wayman, Prog. Mater. Sci. **36**, 203-224 (1992).

[185] N. Choudhary, D.K. Kharat, D. Kaur, Surf. & Coat. Tech. **205**, 3387-3396 (2011).

[186] R. Vishnoi, R. Singhal, D. Kaur, J. Nanopart Res. **13**, 3975-3990 (2011).

[187] J.Y. He, H. Wang, H.L. Huang, X.D. Xu, M.W. Chen, Y. Wu, X.J. Liu, T.G. Nieh, K. An, Z.P. Lu, Acta Mater. **102**, 187-196 (2016).

[188] A. Kreitcberg, V. Brailovski, S. Prokoshkin, D. Gunderov, M. Khomutov, K. Inaekyan, Mater. Sci. Eng. A, **622**, 21-29 (2015).

[189] T. LaGrange, R. Schaublin, D.S. Grummon, C. Abromeit, R. Gotthardt, Phil. Mag. **85 (4-7),** 577-587 (2005).

[190] Q J. Cheng, A. Aerdell, Nucl. Instr. Methods B **44**, 336-343 (1990).

[191] X. T. Zu, S. Zhu, X. Xiang, L. P. You, Y.Huo., L. M. Wang, *Mater. Sci. Eng., A*, **36**, 352-355 (2003).

[192] P. Moine, J. P. Rivieri, J. Chaumont, A. Pelton, R. Sinclair, Nucl. Instrum. Methods Phys. Res., Sect. B, **20**, 7-8 (1985).

[193] T. Czeppe, N. L. Zayonts, Z. Swiatek, M. Michalec, O. Bonchyk, G. Savitskij Vacuum **83**, 214-219 (2009).

[194] Y. Matsukawa, S. Ohnuki, Journal of Nuclear Materials **239**, 261-266 (1996).

[195] G. Shugar, J. Ballinger, Chemical Technician′ Ready Reference Handbook (McGraw-Hill; New York, 1996).

[196] H.P. Klug and L.E. Alexander, X-ray Diffraction Procedures for Polycrystalline and Amorphous Materials (Wiley, New York 1974).

[197] R. Singhal, D. Kabiraj, P.K. Kulriya, J.C. Pivin, R. Chandra, D.K. Avasthi, Plasmonic **8 (2),** 295-305 (2013).

[198] R. Singhal, R. Vishnoi, K. Asokan, D. Kanjilal, D. Kaur, Vacuum **89**, 215-219 (2013).

[199] M. Silva, L. Pichon, M. Drouet, J. Otubo, Surf. Coat. Technol. **211**, 209-212 (2012).

[200] H. Conrad, J. Narayan, K. Jung, Int. J. Refract. Met. Hard Mater. **23**, 301-305 (2005).

[201] T.W. Duerig, K.N. Melton, D. Stockel, C.M. Wayman, S.M. Fisher, Engineering Aspects of Shape Memory Alloys (Elsevier, 1990).

[202] Quinn RT, Kraft RW, Hertzberg R.W. Trans Amer. Soc. Metals **62**, 38-44 (1969).

[203] J. Otubo, O.D. Rigo, C. Moura Neto, M.J. Kaufman, P.R. Mei, J. Phys. IV França, **112**, 873-876 (2003).

[204] J. Lutz, J.K.L. Lindner, S. Mändl, Appl. Surf. Sci. **255,** 1107-1109 (2008).

[205] W. Tillmann, S. Momeni, Sens. Actuators A **221**, 9-14 (2015)

[206] R.M.S. Martins, N. Schell, H. Reuther, L. Pereira, K.K. Mahesh, R.J.C. Silva, F.M. Braz Fernandes, Thin Solid Films **519**, 122-128 (2010).

[207] S.R. Stock, B.D. Cullity, Elements of X-ray diffraction, third ed. Prentice Hall, New York, 2001.

[208] F. Lehnert, T. Haupl, B. Abel, S.G. Mayr, Materials & Design **112**, 512-518 (2016).

[209] P.D. Tall, S. Ndiaye, A.C. Beye, Z. Zong, W.O. Soboyejo, H.J. Lee , A.G. Ramirez, K. Rajan, Mater. Manuf. Process. **22**, 175-179 (2007).

[210] Victor Iliev Rizov, Materials and Design **27**, 947-954 (2006).

[211] H.J. Lee, H. Ni, D.T. Wu, A.G. Ramirez, Mater. Trans. **47(3),** 527-531 (2006)

[212] X. Huang, J.S. Juan, A.G. Ramirez, Scr. Mater **63**, 16-19 (2010).

Appendix-A

List of Publications

List of Publications

1. **Electronic excitation induced modifications of nanostructured Ni-Ti shape memory alloy thin films.**
   V. Kumar, R. Singhal, R. Vishnoi, M. Gupta, P. Sharma, M. K. Banerjee, K. Asokan, H. Sharma, A. Gupta, D. Kanjilal
   Advanced Materials Letters, 8(4), 486-492, 2017.
2. **Ag implantation-induced modification of Ni-Ti shape memory alloy thin films.**
   V. Kumar, R. Singhal, R. Vishnoi, M.K. Banerjee, M.C. Sharma, K. Asokan, M. Kumar
   Radiat Effects and Defects in Solids, 172, 629-642, 2017.
3. **Effect of crystallographic orientation on structural and mechanical behaviours of Ni-Ti thin films irradiated by Ag^{7+} ions**
   V. Kumar, R. Singhal
   Applied Physics A, 124, 328-338, 2018.
4. **Impact of SHI on structural and mechanical behaviour of intermetallic NiTi Thin films**
   V. Kumar, R. Singhal
   Physica B: Condensed Matter 546, 80–88, (2018)

Appendix-B

Research Articles

Research Article 2017, **8**(4), 486-492 Advanced Materials Letters

Electronic excitation induced modifications of nanostructured Ni-Ti shape memory alloy thin films

V. Kumar[1], R. Singhal[1]*, R. Vishnoi[2], M. Gupta[3], P. Sharma[1], M. K. Banerjee[4], K. Asokan[5], H. Sharma[1], A. Gupta[6], D. Kanjilal[5]

[1]*Department of Physics, Malaviya National Institute of Technology Jaipur, JLN Marg, Malviya Nagar, Jaipur 302017, India*
[2]*Department of Physics, Vardhman College, Bijnor, U.P. 246701, India*
[3]*UGC-DAE Consortium for Scientific Research, University Campus, Khandwa Road, Indore 452001, India*
[4]*Department of Mettalurgical and Materials Engineering, Malaviya National Institute of Technology Jaipur, JLN Marg, Malviya Nagar, Jaipur 302017, India*
[5]*Inter University Accelerator Centre, Aruna Asaf Ali Marg, New Delhi 110067, India*
[6]*Amity Center for Spintronic Materials, Amity University, Sector 125, Noida 201303, India*

*Corresponding author, E-mail: rsinghal.phy@mnit.ac.in

Received: 11 October 2015, Revised: 25 July 2016 and Accepted: 06 September 2016

DOI: 10.5185/amlett.2017.6211
www.vbripress.com/aml

Abstract

In the present work, the effects of 120 MeV Au ion irradiation at different fluences ranging from 1×10^{12} to 3×10^{13} ions/cm^2 on structural and electrical properties of thin films of Nickel titanium (Ni-Ti) shape memory alloys (SMAs) grown on Si substrate using DC magnetron co-sputtering is studied. The surface morphology, crystallization and phase transformation behaviour of these films were investigated using field emission scanning electron microscopy (FESEM), atomic force microscopy (AFM), X-ray diffraction (XRD) and Four-terminal resistivity measurement method. XRD pattern reveals that both the phases-martensite as well as austenite exist in the pristine film. Resistivity measurements revealed a two way transformation from cubic to rhombohedral and from rhombohedral to monoclinic phase in pristine film and decrease in its transformation temperature with increased fluence. At higher fluences 5×10^{12} and 1×10^{13} ions/cm^2, films showed non-metallic behaviour which could be due to the disorder occurring in these films due to ion impact and precipitate formation. The elemental composition of pristine film is determined by Rutherford backscattering spectroscopy. Copyright © 2017 VBRI Press.

Keywords: SMA, NiTi, SHI irradiation.

Introduction

Nowadays, the demand for micromachines has increased significantly in various fields such as biotechnology, aerospace, micro-electro-mechanical systems (MEMS), industries and various biomedical applications **[1-3]**. Thin films of Ni-Ti alloy can be used to produce such microactuators because of their unique properties such as large stress sustainability without deforming permanently **[4]**, low voltage controllability, biocompatibility, shape memory behaviour etc. Also, the work output per unit volume of these films is quite large as compared to other micro-actuation mechanisms **[5]**. Recently, NiTiCu based ultralow-fatigue SMA films containing Ti_2Cu precipitates for 10 million transformation cycles were reported for artificial heart valve or elastocaloric cooling **[6]**. These unique properties in Ni-Ti films are due to their distinct crystalline structure (B2 at high temperature exhibiting austenite phase and monoclinic at low temperature exhibiting martensite phase) and phase transformation behaviour. The phase transformation is accompanied by significant changes in the structural and electrical properties of films, thus controlling the design and fabrication of micro-actuators and out of several methods one of the effective ways to produce phase transformation in shape memory alloys is high energy ion irradiation.

The effect of different type of perturbations such as ion beam irradiation, electron irradiation and proton irradiation on shape memory alloys has been investigated by many groups. Moine *et al*. studied 250 and 390 keV Ni ions implantation induced amorphization on bulk martensitic Ti-Ni alloy **[7]**. It was reported that at a temperature of 300 K, the fluence required to transform the martensitic transformation to amorphous state was 0.1 dpa whereas at a temperature of 77 K, the required dose was found to be on high side ~ 0.18 dpa and the reasoning was given in terms of the stabilization of martensite phase at lower temperature. Another report was given by Brimhall *et al*., who irradiated the Ni-Ti alloy by 2.5 MeV Ni ion beam and 6 MeV Ti ion beam at a dose of ~ 0.2 dpa and observed a complete amorphization of Ni-Ti austenitic phase after ion irradiation **[8]**. They concluded that amorphization of the phase was possible without complete chemical disordering. Zu *et al.* observed the amorphization of Ti-Ni-Cu alloy samples which were irradiated by 400 keV Xe ions at a dose of 0.4 dpa **[9]**. Vishnoi *et al.* observed phase transformation at low fluence ($6x10^{12}$ ions/cm^2) and amorphization at high fluence ($3x10^{13}$ ions/cm^2) in Ni-Mn-Sn ferromagnetic SMA thin films using 200 MeV Au ions **[10]** while Singhal *et al.* observed phase transformation at slightly higher fluence ($1x10^{13}$ ions/cm^2) in Ni-Mn-Sn film of different composition using 120 MeV Ag ions **[11]**. Pelletier *et al.* studied the phase transformation in Ni-Ti wire by using 1.5 MeV Ar ions to increase the life time of endodontic instrument. They observed the completely amorphization of martensite phase at a fluence of $5x10^{17}$ ions/cm^2, while the austenite phase was partially amorphized **[12]**. Lagrange *et al.* also studied the suppression of martensite phase in Ni-Ti thin films irradiated by 5 MeV Ni ions to develop the shape memory thin films actuator. They observed that martensite phase was first transformed into austenite phase and then become amorphized **[13]**. Ikenaga *et al.* studied 3 MeV Cu ion implanted bulk Ti-Ni films and they observed amorphous region at a fluence of 10^{14} ions/cm^2 at 300 K substrate temperature, but in case of 100 K it did not appear even at 10^{15} ions/cm^2 **[14]**. They observed that the sample implanted at 100 K, ion implanted region showed crystallinity however sample implanted at 300 K modified to amorphous.

It is well understood from these studies that the properties of SMA can be significantly modified using ion irradiation techniques. Among all types of ion irradiation, SHI irradiation is of special significance since SHI is a very useful tool for modifying the properties of films, foils and surface of bulk solids. SHI transfers its energy to the material mainly by inelastic collision which causes electronic excitation of the atoms in the material and produces long narrow disordered region along its path called track whose length and diameter depend on the types and energy of ion beam used to irradiate the material. The mechanism of transfer of electronic excitation to the displacement of lattice atoms could be understood by commonly known models such as Coulomb explosion model **[15]** and thermal spike model **[16]**. Though, it is difficult to produce tracks in metals due to the large number of mobile conduction electrons present in them which shield the space charge produced by the ionization of metal atoms by incoming swift heavy ions and by spreading the energy deposited by these ions very rapidly, however, formation of tracks by heavy ions was reported in metals such as Ni_3B **[17]**, $NiZr_2$ **[18]**, Ni-Ti **[19]** shape memory alloy etc.

Thus, with reference to the above mentioned studies and to the best of our knowledge, there are few reports of SHI irradiation on bulk Ni-Ti but there are no such reports in case of Ni-Ti metallic thin films which are very much needed to understand the effects of SHI interaction with Ni-Ti films since they are more promising candidates for various applications as compared to bulk due to their various distinguished characteristics and to explore how the transformation temperatures can be controlled by ion irradiation making them useful for different applications.

Therefore, in this study, we report the preliminary work done by using SHI irradiation on Ni-Ti films. The present work is focussed on ion-beam induced modifications of 120 MeV Au ion irradiated Ni-Ti sputter deposited thin films which are investigated using X-ray diffraction, Rutherford Backscattering spectroscopy, atomic force microscopy, Field emission scanning electron microscopy and Electrical resistivity measurements.

The main objective of the present study is to investigate the effects of SHI on both phases, austenite as well martensite phase simultaneously at room temperature for the future application of these material in harsh environment such space or nuclear reactor. In present experiment, we also investigated the critical value of fluence for shape memory behaviours. Below this critical fluence Ni-Ti films show the SMA behaviour. Irradiation at low fluence below the critical value creates the defect in the materials in a control manner which increase the vacancies diffusion and this diffusion of vacancies lead to higher mobility.

The schematic of the work presented in manuscript is shown in **Fig. 1**. The modifications in the structural and electrical properties against SHI at different ions fluences of 120 MeV energy were characterized by FESEM, AFM, XRD and four-terminal resistivity measurement. The measurement showed the disorder produced in microstructure in Ni-Ti films strongly dependent upon the ion fluences and at a higher fluence of 3×10^{13} ions/cm^2, both phase's austenite as well as martensite was completely disappeared due to huge amount of electronic energy deposited by SHI in Ni-Ti matrix.

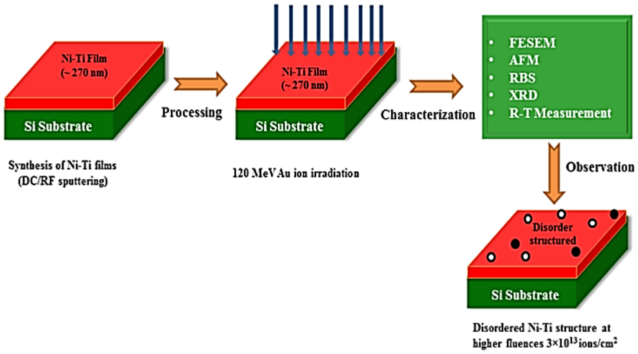

Fig. 1. Schematic diagram of Ni-Ti thin films deposited at 550 ˚C and irradiated at different fluences.

Experimental

Ni-Ti films were deposited by direct current magnetron sputtering technique on Si substrates by using an AJA Int. Inc. make ATC Orion-8 series sputtering system. Two separate targets of Ni and Ti were used for thin film deposition. The arrangement of rotation of substrate in horizontal plane was also possible during film deposition for better uniformity. The substrates were first cleaned in an ultrasonic bath using a mixture of distilled water and trichloroethylene in 4:1 ratio and then they were washed with acetone. High purity nickel (99.9%, 50 mm diameter and 2 mm thickness) and titanium (99.9%, 50 mm diameter and 3 mm thickness) targets were used for film deposition. The Ar pressure was regulated to be 0.13 Pa. The target to substrate distance was fixed approximately 16 cm. Before deposition, a base pressure of 2×10^{-7} Torr was achieved and sputter cleaning of both the Si substrate and target (Ni at 50 W and Ti at 100 W for 10 minutes) was done. After cleaning, the deposition was performed for 1 hour 40 minutes using direct current powers of 50 W for Ni and 100 W for Ti. During deposition, the pressure was kept constant at 3×10^{-3} Torr using a dynamic throttling valve and substrate temperature was kept constant at 550^{o}C. Substrate holder was rotated at 60 rpm in a horizontal plane to deposit films of uniform composition. The thickness of all the deposited films was approximately 270 nm. Post-annealing was not performed after film deposition. These Ni-Ti films on Si substrate were irradiated with 120 MeV Au ion beam at IUAC New Delhi, India using 15 UD pelletron accelerator facility. Ion fluence was varied from 1×10^{12} to 3×10^{13} ions/cm^2. The electronic energy loss S_e and nuclear energy loss S_n calculated for Ni-Ti SMA using 120 MeV Au ions was $\sim3.1\times10^3$ and 5.3×10^1 eV/Å, respectively, and the range of Au ions in Ni-Ti was ~7.6 μm as calculated by SRIM programme **[20]**, which was found to be much higher than the film thickness, so most of the Au ions after passing through the film get buried into the Si substrate.

The surface morphology and microstructure of the films were studied using FESEM (Nova Nano FE-SEM 450 FEI) and AFM using a Bruker make Nanoscope v system with a Si_3N_4 cantilever in noncontact mode. The thickness and elemental composition of the films were measured using Rutherford backscattering spectrometer. The orientation, crystallinity and room temperature phase of the pristine and irradiated films were studied using X-ray diffractometer (Bruker D8 Advance) equipped with Cu Kα x-ray source in θ-2θ geometry having a scan speed of 0.6 ^{o}/min. The electrical resistivity of Ni-Ti films at different temperatures was measured using four probe method over a temperature range from 100 to 400 K. The temperature of the film was measured by using Lake Shore thermocouple and temperature ramp was set at 2 K/minute during heating and cooling cycles. The contacts on the films were made by using silver paint.

Results and discussion

Structural properties

Field emission scanning electron microscopy

The surface properties of pristine and 120 MeV ion irradiated Ni-Ti films were determined by FE-SEM. **Fig. 2(a)** to **2(e)** show the FE-SEM micrographs of pristine and irradiated films at different fluences ranging from 1×10^{12} to 3×10^{13} ions/cm^2. It is clear from these images that different shaped grains such as pyramidical and spherical, are formed and the grain size first increases with increase in the ion fluence, remain constant up to a certain fluence and then decreases first gradually and then considerably with further increase in the fluence. **Fig. 2(a)** shows that in the pristine film pyramidical and spherical shaped grains are observed depicting the presence of both austenite and martensite phases in the films. But, the pyramidical grains are quite large in number as compared to spherical grains due to the dominance of austenite phase in the film. **Fig. 2(b)** shows diffused pyramidical and spherical grains present in the film irradiated at a fluence of 1×10^{12} ions/cm^2. The grain size increases but the number of pyramidical grains decreases while that of spherical grains increases due to the decrease of austenite phase and slight increment of martensite phase in the film in accordance with the XRD data which is later shows decrease in the intensity of (110) peak depicting austenite phase while broadening and slight increase in the intensity of (002) peak depicting martensite phase. With increase in fluence to 5×10^{12} ions/cm^2 (**Fig. 2(c)**), FESEM micrograph show grains of similar morphology and constant size as found in film irradiated at fluence 1×10^{12} ions/cm^2. At further increased fluence of 1×10^{13} ions/cm^2, smaller grains with diffused grain boundaries are observed (**Fig. 2(d)**). As the fluence is increased to 3×10^{13} ions/cm^2 (**Fig. 2(e)**), the grain size decreases considerably to the extent that surface morphology of the film completely disappears and a smooth film appears which may be due to the amorphization of the film at a fluence of 3×10^{13} ions/cm^2.

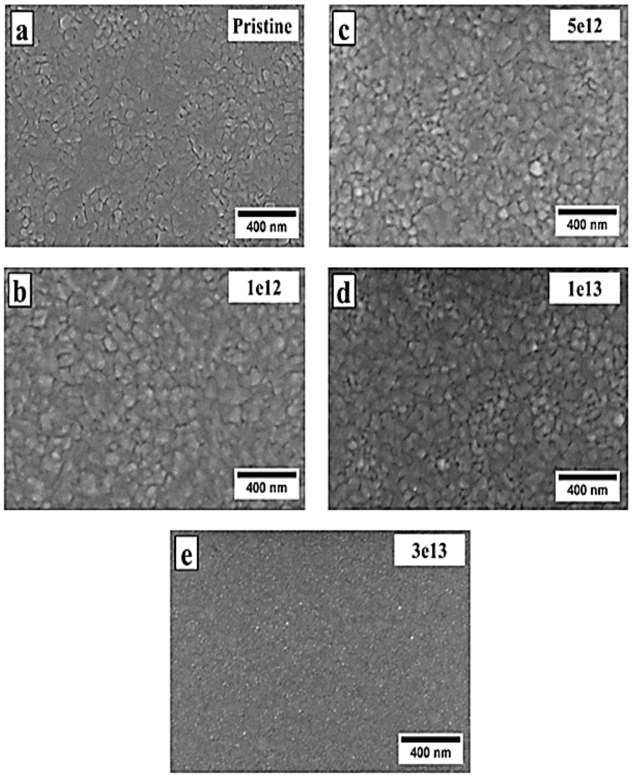

Fig. 2. FESEM images of pristine and 120 MeV Au ion irradiated Ni-Ti thin films at different fluences.

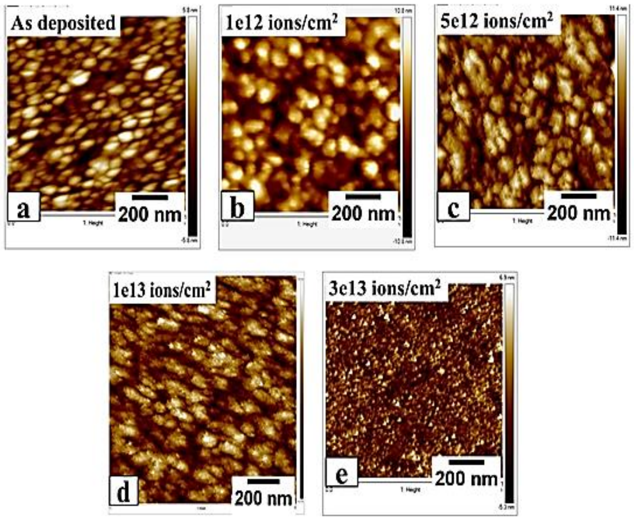

Fig. 3. AFM images of pristine and 120 MeV Au ion irradiated Ni-Ti thin films at different fluences.

Atomic force microscopy

Apart from FESEM, the surface morphology (grain size and surface roughness) of all the films was also analyzed using AFM. **Fig. 3(a)** to **(e)** shows the two dimensional AFM images of as- deposited and 120 MeV Au ion irradiated Ni-Ti SMA films at a scale of 1µm×1µm. The root-mean-square roughness (R_{rms}) of the surfaces of the films was obtained from AFM scans over film areas of 2µm×2µm by scanning three times, each time at a different location for every film. R_{rms} of the films was calculated using the following formula,

$$R_{rms} = \sqrt{\frac{\sum Z_i^2}{N}}$$

where, R_{rms} is the root mean square roughness taken from the mean image data plane and Z_i is the current Z value, Z is the Peak-to-valley difference in height values within the analyzed region, N is the number of points within the box cursor in nm. The average values of surface roughness of as deposited and irradiated films at different fluences 1×10^{12}, 5×10^{12}, 1×10^{13} and 3×10^{13} ions/cm^2 was found to be ~ 2.9 nm, ~ 3.98 nm, ~ 3.85 nm, ~ 3.76 nm and 1.88 nm respectively. It was observed that root mean square surface roughness first increases with increase in fluence to 1×10^{12} ions/ cm^2 due to the increased intensity of martensite phase in the film and then it again decreases but to a smaller extent for films irradiated at 5×10^{12} and 1×10^{13} ions/ cm^2 respectively, whereas it decreases considerably for film irradiated at 3×10^{13} ions/cm^2 due to the complete amorphization of the film resulting in the disappearance of both the austenite and martensite phases, in accordance with the FESEM result as reported in **Fig. 2**. The sizes of the grains calculated by AFM also show similar behaviour as calculated by FESEM images.

Rutherford backscattering spectroscopy

The major problem in using Ni-Ti films for various applications is the difficulty in controlling their chemical composition. The transformation temperatures of Ni-Ti also depend considerably on the composition of films. A slight change in the composition results in a remarkable change in the transformation temperatures and thus the various properties of the films.

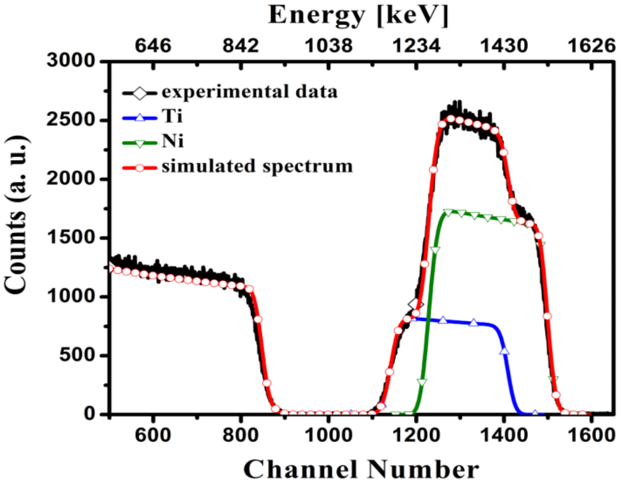

Fig. 4. RBS spectra (2 MeV He$^+$) perform on as deposited film shows Ni and Ti edges for the channel number in the range of 1100-1500 range.

So formation of desired composition in the films and also accurate determination of composition in the films after formation is very essential. Rutherford backscattering spectroscopy (RBS) is an efficient method to determine the composition of the films as well as film thickness, atomic species present in the films and their concentration. **Fig. 4** shows Rutherford backscattering spectrum of as deposited Ni-Ti film on Si substrate. In order to measure the film thickness and to determine the atomic concentration of metals in the film, the RBS spectrum was simulated by SIMNRA **[21]**, and a fit is shown in **Fig. 4** by continuous line. The Ni atomic fraction was calculated 56.7 at. % and Ti was found to be 43.3 at. %. The films thickness simulated by SIMNRA was found to be ~ 270 nm.

X-ray diffraction

Fig. 5 shows the room temperature X-ray diffraction (XRD) pattern of Ni-Ti pristine film and also of the films irradiated by 120 MeV Au ions at different fluences ranging from 1×10^{12} to 3×10^{13} ions/cm^2. In addition to substrate peak, XRD pattern reveals that both the phases, austenite (B2) as well as martensite (B19') exist in the pristine sample. No traces of other phases like Ti_2Ni and Ti_3Ni_4 were observed in XRD pattern of these films. The planes corresponding to austenite and martensitic structure are marked by their Miller indices. The most intense peak at 2θ=42.5° which is due to the (110) fundamental reflection corresponds to cubic austenite structure, and the peak at 2θ=43.9° which is due to (002) fundamental reflection corresponds to monoclinic martensite structure. The peaks $(\bar{1}36)$, $(1\bar{3}6)$ and $(0\bar{4}4)$ corresponds to naturally oxidized Si substrate. The film irradiated at a fluence of 1×10^{12} ions/cm^2 shows decrease in the intensity of (110) peak (corresponding to B2 phase) and the (002) peak, corresponding to B19', becomes broad. It indicates the damage of austenite structure in the film upon ion irradiation. With increase in the fluence to 5×10^{12} ions/cm^2, the peak intensity of both the phases decreases. With further increase in fluence to 1×10^{13} ions/cm^2, the intensity of these peaks decreases considerably. The decrease in intensity of both the phases at this fluence shows the partial amorphization of the austenite and martensite phase and suppression of phase transformation by the electronic energy deposition in Ni-Ti regime. At a much higher fluence of 3×10^{13} ions/cm^2, all the peaks are vanished and the film gets completely amorphized due to excessive ion impact. Amorphization by electronic excitation and ionization is also possible, where the energy of the incoming ion is transferred to the atoms of lattice via electron-electron and electron-phonon coupling. Such electron excitations can also cause local heating followed by a rapid quenching (thermal spikes) producing lattice distortions which are so drastic that they relax into an amorphous state **[22]**.

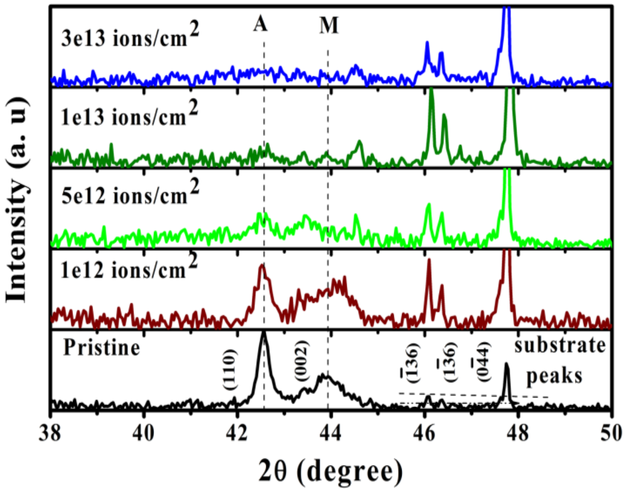

Fig. 5. X-ray diffraction spectra of pristine and 120 MeV Au ion irradiated Ni-Ti thin films at different fluences.

The XRD pattern shows the crystalline to amorphous phase transformation of Ni-Ti thin films by SHI irradiation at a fluence of 3×10^{13} ions/cm^2. The suppression of both the phases under the SHI irradiation has been observed by introduction of lattice defects and high strain generation by the bombardment of Au ions on Ni-Ti films. The amorphization of materials depends on the irradiation conditions such as ion fluence, irradiation temperature and nature of the ions as reported by several authors [**23**, **24**]. In the case of electron and proton irradiation, it has been well established in the literature that irradiation cause stress field and lattice disorder in the materials [**25**]. The lattice disorder by electronic excitation produces the point defect (vacancy and interstitial pairs) which is evenly distributed in the material and suppress the transformation temperature and cause amorphization. Irradiation at critical fluences, produce isolated amorphous zone in a crystalline material and density of these amorphous zones is continuously increased with increase the fluences and at a higher fluence these amorphous zone starts to overlap and at a critical fluence, material become amorphous.

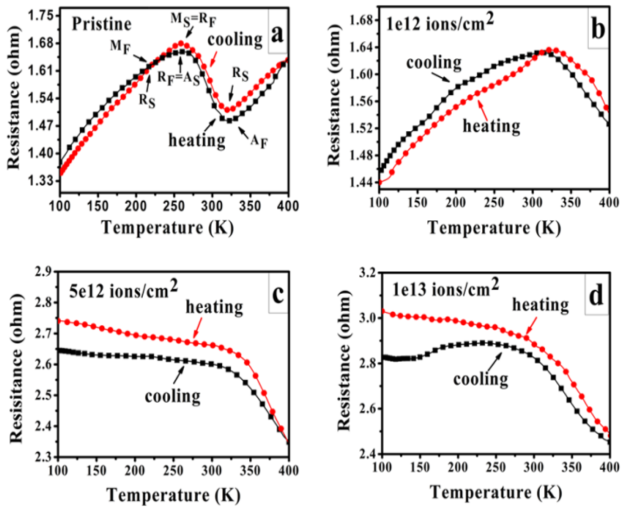

Fig. 6. Electrical resistance versus temperature (R-T) curves of pristine and 120 MeV Au ion irradiated Ni-Ti films, during heating and cooling cycle.

Electrical properties

The variation of electrical resistance with temperature is an effective method for determining the formation of various phases in shape memory alloys thin films and studying their phase transformation behaviour since the high temperature ordered austenite phase, intermediate R phase and low temperature disordered martensite phases are accompanied with changes in the electrical resistance due to their different crystal structures.

Fig. 6(a) to **(d)** show the electrical resistance versus temperature curves of pristine and 120 MeV Au ion irradiated Ni-Ti films, measured by four-terminal resistivity method during cooling and heating cycles in the temperature range 100-400 K. At the time of experiment, the condition of stationary equilibrium was maintained by cycling the temperature stepwise with a sufficient time interval at every data point. In figures 6(a) to (d) R_s, R_f, M_s, M_f and A_s, A_f, denote the start and finish temperatures of formation of the intermediate R phase and martensitic (B19') phase on cooling, and austenitic (B2) transformation on heating, respectively. **Fig. 6(a)** shows the electrical resistance versus temperature (R-T) curve of pristine Ni-Ti film. The pristine film shows a very clear two-step phase transformation B2↔R↔B19' during heating and cooling cycles. During heating cycle, electrical resistance of B2 phase was observed to increase with increase in the temperature because of the formation of R phase, but during cooling below 400 K, first the resistance value of B19' phase decreases linearly because of decrease in the intensity of electron-phonon interaction but at temperature below R_s (310 K), the electrical resistance again starts increasing with temperature because the austenite B19' phase gets distorted and starts transforming to R phase with higher electrical resistance, because in small sized grains the restriction imposed by the grain boundaries for the formation of R phase is small as compared to that offered for phase transformation from austenite to martensite phase **[26]**. On cooling the film further below R_f (260 K), the electrical resistance goes on decreasing with temperature because R phase to martensite transformation begins to occur which gets completed below M_f. Thus, during both heating and cooling cycles, formation of R phase was observed which possess higher electrical resistance in comparison to B2 and B19' phases. **Fig. 6(b)** shows the R-T curve of thin film irradiated at a fluence 1×10^{12} ions/cm^2, in which slightly different trend of electrical resistance was observed upon ion irradiation with 120 MeV Au ions. It was observed that irradiated film showed deteriorated hysteresis as compared to pristine film. Also, the R-T curves during heating and cooling cycles do not show the clear phase transformation behaviour. It could be due to the disorder occurring in the film due to ion impact as also confirmed by the decrease in intensity of ordered austenite phase from XRD data. R-T curves of films irradiated at fluences 5×10^{12} and 1×10^{13} ions/cm^2 as shown in figures 6(c) and (d) show the non-metallic behaviour of both the films without any indication of phase transformation during subsequent heating and cooling cycles. At higher fluence (1×10^{13} ions/cm^2) the energy deposited by incoming ions in the film due to the electronic stopping is quite large and leads to degradation of shape memory behaviour and complete amorphization of the films. In the present case, the incomplete phase transformation could be attributed to the following reasons; (a) large resistance force as compared to driving force could be generated due to the constraints imposed by inter-diffusion of film and substrate due to ion irradiation (b) large number of grain boundaries due to small grain size restrict the growth of martensitic phase during cooling (c) presence of intrinsic defects created by 120 MeV Au ions in Ni-Ti thin films at higher fluences.

Conclusion

In this study, a systematic and preliminary investigation on the effect of 120 MeV Au ions irradiation at different fluences ranging from 1×10^{12} to 3×10^{13} ions/cm^2 on Ni-Ti SMA thin films deposited by DC-magnetron co-sputtering system on Si substrate at 550 ^{o}C was carried out. FESEM and AFM micrographs revealed the successive changes in the surface morphology of the films with increase in fluence content. As the fluence increases, spherical shaped grains increases as compared to pyramidical ones due to change in phase and at considerable higher fluence of 3×10^{13} ion/cm^2, spherical grains also disappear due to the amorphization of the films at such high fluence. XRD measurements revealed the presence of both the phases, austenitic as well as martensitic phase in pristine sample. As the fluence of 120 MeV Au ion increases, crystallinity of the Ni-Ti SMAs decreases and at a fluence of 3×10^{13} ions/cm^2 complete amorphization occurred. The R-T measurements revealed that clear phase transformation from martensite to austenite phase and vice versa via R-phase was observed in pristine film during subsequent heating and cooling cycles. The R-T measurements also revealed the degradation of shape memory effect and occurrence of non-metallic behaviour of Ni-Ti films irradiated at higher fluences.

This study paved the way for exploring how the crystallinity and phase transformation temperatures of Ni-Ti nanocrystalline thin films can be controlled using ion irradiation in order to utilize them for applications.

Acknowledgements

One of the authors (V. Kumar) is thankful to the Technical Education Quality Improvement Programme (TEQIP), MNIT Jaipur for financial assistantship. The crew of Pelletron Accelerator group of IUAC New Delhi is highly acknowledged for providing stable beam of 120 MeV Au ions. Authors would like to acknowledge the help and support provided by Mr. Sunil Ojha for RBS measurements at IUAC New Delhi. Author is also thankful to UGC-DAE CSR Indore for synthesis of Ni-Ti thin films, and Materials Research Centre, MNIT Jaipur for providing characterization techniques such as AFM and FESEM. One of the authors (R. Singhal) highly acknowledges the financial support provided by DST New Delhi in terms of DST FAST Young Scientist project (SR/FTP/PS-081/2011). One of the authors (R. Vishnoi) highly acknowledges the financial support provided by DST New Delhi in terms of DST FAST Young Scientist project (SR/FTP/PS-029/2012).

References

1. Humbeeck, J. V. ; *Adv. Eng. Mater.* **2001**, 3, 837. **DOI:** 10.1002/1527-2648(200111)3:11<837::AID-ADEM837>3.0.CO;2-0
2. Humbeeck, J. V, Stalmans, R.; Wiley: **2002**, 951. **DOI:** 10.1002/0471216275.esm073
3. Gill, J. J, Chang, D. T, Momoda, L. A, Carman, G. P.; *Sens. Actuat. A. Phys.,* **2001**, 93, 148. **DOI:** 10.1016/S0924-4247(01)00646-X
4. Bush, J. D., Johnson, A. D., Lee, C. H., Stevenson, D. A.; *J. Appl. Phys.,* **1990**, 68(12), 6224. **DOI:** 10.1063/1.346914
5. Krulevitch, P., Lee, A. P., Ramsey, P. B., Trevino, J. C., Hamilton, J., Northp, M. A.; *J. Microelectro-mech. Syst.,* **1996**, 5, 270. **DOI:** 10.1109/84.546407
6. Chluba, C.,Ge, W., Miranda, R. L. De, Strobel, J., Kienle, L., Quandt, E., Wuttig, M.; *Science,* **2015**, 348, 1004. **DOI:** 10.1126/science.1261164
7. Moine, P.; Jaoen, C. *J. Alloys Compd.* **1993**, 194, 373. **DOI:** 10.1016/0925-8388(93)90022-F
8. Brimhall, J., Kissinger, H., Pelton, A.; *Radiat. Eff. Defects Solids,* **1985**, 90, 241. **DOI:** 10.1080/00337578508222535
9. Zu, X. T., Zhu, S., Xiang, X., You, L. P., Huo., Y., Wang, L. M.; *Mater. Sci. Eng., A,* **2003**, 36, 352. **DOI:** 10.1016/S0921-5093(03)00635-X
10. Vishnoi, R., Singhal, R., Asokan, K., Kanjilal, D., Kaur, D.; *Appl. Phys. A,* **2012**, 107, 925. **DOI:** 10.1007/s00339-012-6826-5
11. Singhal, R., Vishnoi, R., Asokan, K., Kanjilal, D., Kaur, D.; *Vacuum,* **2013**, 89, 215. **DOI:** 10.1016/j.vacuum.2012.05.017
12. Pelletier, H., Muller, D., Millea, P., Grob, J. J.; *Surface and Coatings Technology,* **2002**, 301, 158. **DOI:** 10.1016/S0257-8972(02)00187-1
13. LaGrange, T., Gotthardt, R.; *Scripta Materialia,* **2004**, 50, 231. **DOI:** 10.1016/j.scriptamat.2003.09.017
14. Ikenaga, N., Kishi, Y., Yajima, Z., Sakudo, N., Nakano, S., Ogiso, H.; *Nucl. Instrum. Methods Phys. Res., Sect. B,* **2009**, 267, 1509. **DOI:** 10.1016/j.nimb.2009.01.077

15. Leuser, D., Dunlop, A.; *Radiat. Eff. Defects Solids*, **1993**, 126, 163.
DOI: 10.1080/10420159308219701
16. Szenes, G.; *Phys. Rev. B*, **1995**, 51, 8026.
DOI: http://dx.doi.org/10.1103/PhysRevB.51.8026
17. Audouard, A., Balanzat, E., Bouffard; Jousset, J. C., Chamberod, A., Dunlop, A., Lesueur, D., Fuchs, G., Spohr, R., Vetter ; *J. Phys. Rev. Lett.*, **1990**, 65, 875.
DOI: http://dx.doi.org/10.1103/PhysRevLett.65.875
18. Barbu, A., Dunlop, A., Lesueur, D., Averback, R. S.; *Europhys. Lett.* **1991**, 15, 37.
DOI: http://dx.doi.org/10.1209/0295-5075/15/1/007
19. Dunlop, A., Lusueur, D., Barbu; A. *J. Nucl. Mater.*, **1993**, 205, 426.
DOI: 10.1016/0022-3115(93)90106-9
20. Zeigler, J. F., Biersack, J. P.; Springer US: New York, **1985**.
DOI: 10.1007/978-1-4615-8103-1_3
21. Adeoya, O, Ali, M. H., Muller, J. C., Siffert, P., *Appl. Phys. Lett.*, **1987**, 50, 1736.
DOI: 10.1063/1.97732
22. Lagrange, T., Schaublin, R., Grummon, D. S., Abromeit, C., Gotthardt, R.; *Philos. Mag.*, **2005**, 85, 577.
DOI: 10.1080/02678370412331320107
23. Moine, P., Rivieri, J. P., Chaumont, J., Pelton, A., Sinclair, R.; *Nucl. Instrum. Methods Phys. Res., Sect. B*, **1985**, 7-8, 20.
DOI: 10.1016/0168-583X(85)90523-3
24. Czeppe, T., Zayonts, N. L., Swiatek, Z., Michalec, M., Bonchyk, O., Savitskij, G.; *Vacuum*, **2009**, 83, S214.
DOI: 10.1016/j.vacuum.2009.01.066
25. Matsukawa, Y., Ohnuki, S.; *Journal of Nuclear Materials*, **1996**, 239, 261.
DOI: 10.1016/S0022-3115(96)00428-X
26. Waitz, T., Kazykhanov, V., Karnthaler, H. P.; *Acta Mater.*, **2004**, 52, 137.
DOI: 10.1016/j.actamat.2003.08.036

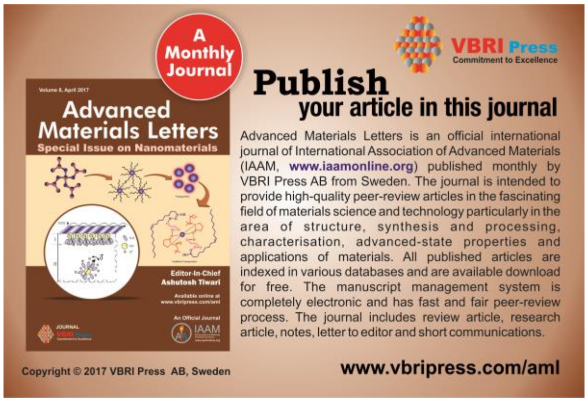

RADIATION EFFECTS & DEFECTS IN SOLIDS, 2017
VOL. 172, NOS. 7–8, 629–642
https://doi.org/10.1080/10420150.2017.1377711

Ag implantation-induced modification of Ni–Ti shape memory alloy thin films

V. Kumar[a], R. Singhal[a], R. Vishnoi[a], M.K. Banerjee[b], M.C. Sharma[c], K. Asokan[d] and M. Kumar[e]

[a]Department of Physics, Malaviya National Institute of Technology Jaipur, Jaipur, India; [b]Department of Metallurgical & Materials Engineering, Malaviya National Institute of Technology JLN Marg, Jaipur, India; [c]National Institute of Solar Energy, Gurgaon, India; [d]Inter University Accelerator Centre, New Delhi, India; [e]Nanotechnology Application Centre, University of Allahabad, Allahabad, India

ABSTRACT
Nanocrystalline thin films of Ni–Ti shape memory alloy are deposited on an Si substrate by the DC-magnetron co-sputtering technique and 120 keV Ag ions are implanted at different fluences. The thickness and composition of the pristine films are determined by Rutherford Backscattering Spectrometry (RBS). X-Ray diffraction (XRD), atomic force microscopy (AFM) and four-point probe resistivity methods have been used to study the structural, morphological and electrical transport properties. XRD analysis has revealed the existence of martensitic and austenite phases in the pristine film and also evidenced the structural changes in Ag-implanted Ni–Ti films at different fluences. AFM studies have revealed that surface roughness and grain size of Ni–Ti films have decreased with an increase in ion fluence. The modifications in the mechanical behaviour of implanted Ni–Ti films w.r.t pristine film is determined by using a Nano-indentation tester at room temperature. Higher hardness and the ratio of higher hardness (H) to elastic modulus (E_r) are observed for the film implanted at an optimized fluence of 9×10^{15} ions/cm^2. This improvement in mechanical behaviour could be understood in terms of grain refinement and dislocation induced by the Ag ion implantation in the Ni–Ti thin films.

ARTICLE HISTORY
Received 10 January 2017
Accepted 6 September 2017

KEYWORDS
Ni–Ti alloy; DC-magnetron co-sputtering; ion implantation; nano-indentation; surface morphology; shape memory alloy

1. Introduction

Ni–Ti shape memory alloy (SMA) thin films are promising material in shape memory applications and superelasticity due to their phase transformations between austenite and martensite phases. Shape memory behaviour of this material is used in micro devices for micro-electromechanical systems (MEMS) such as microsensors and micro-actuators (*1–3*). On the other hand, superelasticity is used in biomedical applications mainly for neurovascular stents such as arterial stents and endovascular stents in blood vessels (*4,5*). The limitation in mechanical properties of Ni–Ti such as hardness, corrosion and wear resistance make it difficult to be used in orthodontic and MEMS applications. Therefore, it is essential to improve the surface properties (*e.g.* wear resistance, hardness and biocompatibility) of

CONTACT V. Kumar ✉ vks8361@gmail.com

Ni–Ti thin film for various applications. In order to enhance Ni–Ti properties, various surface modification techniques such as oxidation treatment (*6*), gas nitriding (*7*), various coating (*8*), laser melting (*9*), alkaline treatment and ion implantation techniques have been performed on Ni–Ti alloy (*10*,*11*). The critical challenge for coating techniques focuses on the binding strength because of the problem of delamination. However, for surface modification of metals and alloys, ion implantation is a precise technique, which endows Ni–Ti SMA with new modified surface layer with ability to retain its superelastic and shape memory behaviour in the thin films. The modified surface also affects the structural, electrical and mechanical properties by the presence of foreign ions (*12*,*13*).

It has been reported that the mechanical properties of the materials are strongly dependent upon the defect density, grain refinement and precipitation, which lead to increase in resistance of materials against plastic deformation. However, these treatments result in a change in martensite transformation temperature by changing the internal stress and chemical composition of the matrix (*14*,*15*). There are few reports (*11*,*16*–*21*) on microstructure and tribological properties of NiTi SMA implanted by different metallic ion beams. In above reports, authors have reported improvement in tribological and biomedical properties of Ni–Ti alloy. Kaur et al. reported the improvement in electrical and mechanical properties of Ni–Ti thin films by addition of W in Ni–Ti Matrix. The improvement in mechanical properties was attributed to the grain refinement of Ni–Ti thin films by W addition (*22*). Oh et al. investigated the effect of Ag addition to Ni–Ti alloy on micro-hardness, phase transformation temperature and corrosion behaviour for medical and dental application. Arc melting, homogenization, hot rolling and solution heat treatment were performed to prepare the Ni–Ti–Ag specimens. Ag addition in cast alloy increased the transformation temperature range to 373 Kelvin (K) and stabilized the martensite phase at room temperature along with the improved mechanical properties (*21*). Singhal et al. investigated the effect of Ag ions on Au nanoparticles embedded in fullerene C_{70} matrix in order to tune the surface plasmon resonance frequency (SPR). They observed that tuning of SPR wavelength was due to phase transformation of fullerene into amorphous carbon with increase of fluences (*23*).

Therefore, silver is the most promising element because it possesses many advantages such as excellent biocompatibility, good antibacterial ability and thermal stability. It also exhibits good corrosion resistance because of the formation of the oxide layer with Ti (*i.e.* TiO_2) (*24*–*27*). However, to the best of our knowledge, the effect of Ag implantation on phase transformation behaviour and mechanical properties of Ni–Ti thin films prepared by the dc-magnetron co-sputtering technique has not been reported. In the present study, Ni–Ti thin films were implanted with 120 keV Ag ions at different fluences ranging from 3×10^{15} to 3×10^{16} ions/cm^2. The correlation between the microstructure and mechanical properties of Ni–Ti thin films after implantation has been discussed in terms of crystallite size and dislocation density.

2. Experimental details

Ni–Ti thin films were deposited on Si substrate using the DC-magnetron co-sputtering technique. To achieve the uniform growth of Ni–Ti films, Si substrate was rotated (60 rpm) in the horizontal plane of the targets. High-purity targets of Ni (99.99%) and Ti (99.99%) were used in this study. The substrates were cleaned in an ultrasonic bath containing a mixture

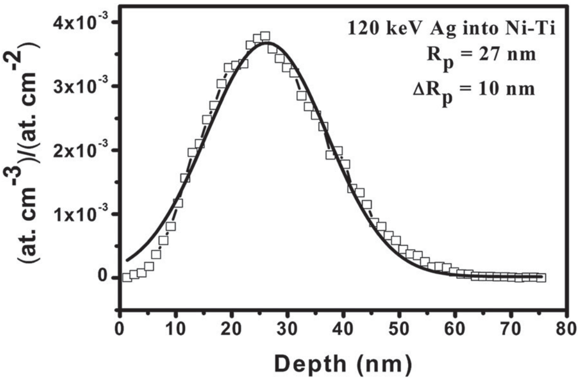

Figure 1. Depth distribution of Ag atoms in Ni–Ti films simulated by TRIM computer code for ten thousand 120 keV Ag ions.

of (1:4) trichloroethylene and distilled water, respectively. Before deposition, the sputtering chamber was evacuated to a base pressure of about 2×10^{-7} torr, while during deposition the pressure was kept at 3×10^{-3} torr. The pressure of Ar gas (99.99 at.%) was regulated to be 9×10^{-3} torr inside the chamber before deposition and sputtering of both the targets and Si substrate for 10 minutes was performed for cleaning. After cleaning, the deposition was performed for 1 hour 40 minutes using direct current powers of 100 W for Ti and 50 W for Ni target. The target to substrate holder distance was fixed at approximately 16 cm. During deposition the substrate temperature was kept at 823 K. Prepared Ni–Ti thin films were implanted by 120 keV Ag ions (negative ion) using an MC-SNICS ion source in the Low Energy Ion Beam Facility (LEIBF) of the Inter-University Accelerator Centre (IUAC), New Delhi. During implantation, the samples' stage in the implantation chamber was kept under a pressure of $\sim 6 \times 10^{-7}$ torr. In the case of 120 keV Ag ions, the electronic and nuclear stopping power (S_e and S_n) in Ni–Ti thin film were calculated using SRIM code (*28*). The range of Ag ions was calculated by SRIM and found to be ~ 27.1 nm, where range denotes the maximum distance up to which Ag ions can penetrate in to the film. The theoretical distribution of Ag ions was calculated by using TRIM 2008 computer simulation for ten thousand ions (*28*). Assuming a normal Gaussian distribution, the values of projected ion range R_p and the standard variation ΔR_p was obtained as shown in Figure 1. Moreover, Figure 2 shows the SRIM simulation of ion trajectory (1000 Ag ions) for 120 keV Ag ions and defect production by implanted ions in 270 nm film thickness. The separate histograms of Ni and Ti show the production of vacancies by implanted ions in the entire thickness. It is noticed that the defects generated by incoming ions are in the range of energy of bombarded ions. The calculated number of vacancies for Ni is found to be 1.3×10^{24} for the fluence of 3×10^{15} and for the fluence of 9×10^{15} and 3×10^{16} ions/cm^2; the number of vacancies are 4.0×10^{24} and 1.3×10^{25} ions/cm^3, respectively. Similarly, Ti vacancies created at different fluences of 3×10^{15}, 9×10^{15} and 3×10^{16} ions/cm^2 are found to be 1.0×10^{24}, 3.1×10^{24} and 1.0×10^{25} ions/cm^3, respectively. Thus, a higher number of vacancies and hence a higher damage is produced in Ni–Ti thin films.

The atomic concentration and thickness of the pristine film were measured by Rutherford Backscattering Spectrometry (RBS). The RBS was performed using 2 MeV He^{2+} ions on

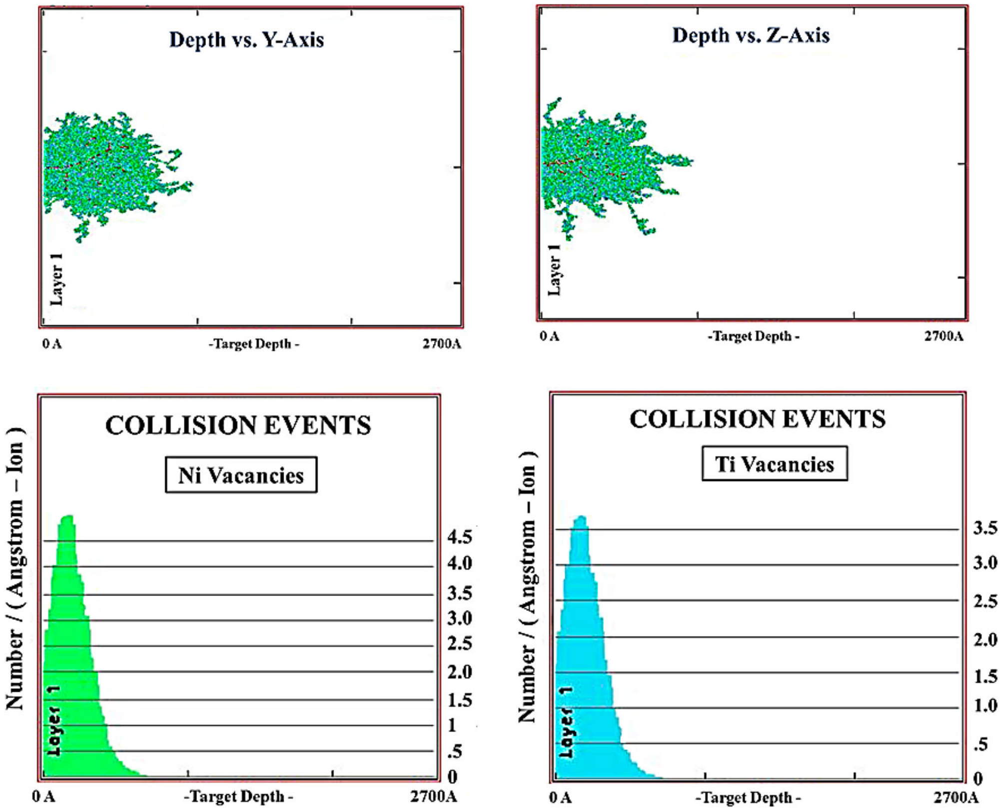

Figure 2. TRIM simulation for 1000 Ag ion of 120 keV energy in Ni–Ti film showing the ion trajectory for defects' production by the energetic implanted ions in 270 nm thickness. The histograms of Ni and Ti showing the vacancies created by the passage of 120 keV Ag ions in Ni–Ti films.

pristine Ni–Ti film. The structural and crystallographic orientation of Ni–Ti films were analyzed by an X-ray diffractometer (Bruker D8 Advance) with a Cu-Kα1 radiation source of wavelength 1.54 Å. These measurements were carried out in a 2θ range of 35–52° at a scan speed of 0.6°/minute. Furthermore, the surface morphology and the roughness of pristine and implanted Ni–Ti films have been investigated using AFM (Bruker Nanoscope *V*) in the non-contact mode.

To study the phase transformation of pristine and implanted films, four-point probe electrical resistivity measurement was used in a temperature range of 100 K to 400 K, with a heating/cooling rate of 2 K/minute. These measurements were carried out in a liquid nitrogen cryostat using a standard Keithley source meter and a temperature controller. For electrical characterization, contacts over films were made with silver paste. The mechanical properties of the pristine and implanted films were measured by using a CSM instrument Nano-indentation tester equipped with a Berkovich diamond tip.

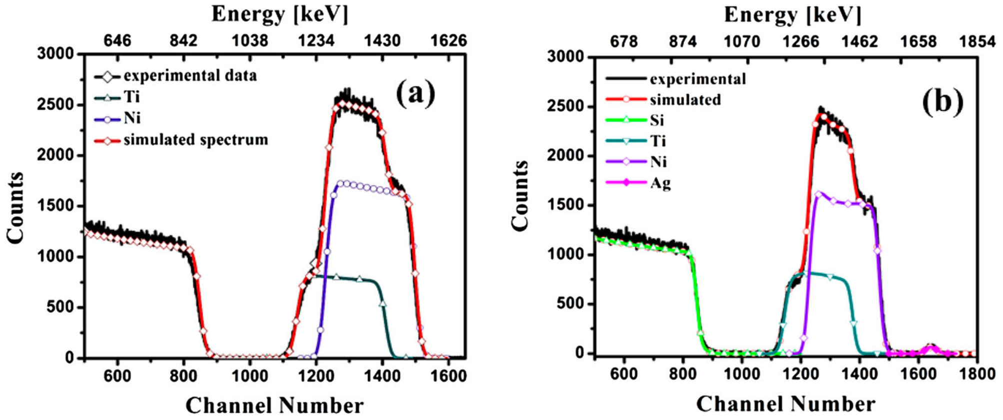

Figure 3. RBS spectrum for NiTi pristine film (a) and implanted film at a fluence of 3 × 10^{16} ions/cm^2 (b) along with SIMNRA simulation.

3. Results and discussions

3.1. Rutherford backscattering spectrometry

RBS is used to determine the film thickness, atomic species and their atomic concentration. Figure 3(a) displays the RBS spectrum of pristine Ni–Ti film on Si substrate at normal incidence with detector positioned at 165° scattering angle. In order to measure the film thickness and quantify the atomic concentration of metals in film, the RBS spectrum was simulated by SIMNRA (*29*), and a fit is shown in Figure 3. The Ni atomic concentration was calculated to be $\sim$56.7 at% and Ti was found to be $\sim$43.3 at%. The thickness of the film, estimated by SIMNRA simulation is found to be $\sim$270 nm. Furthermore, the film implanted at a fluence of 3 × 10^{16} ions/cm^2 was also characterized by using RBS to know the preferential sputtering in implanted film. The Ni-to-Ti ratio for the pristine and implanted films decreases from 1.3 to 1.26 at%; this change suggests that there is preferential sputtering in the Ni–Ti system during implantation process. Hence the variation in concentration of Ni from 56.7 in pristine to 55.2% in implanted film is attributed; consequently, the preferential sputtering of Ni atoms over Ti atoms takes place.

3.2. Structural properties

(a) *X-ray diffraction*

XRD pattern of Ni–Ti pristine film and also of those implanted by 120 keV Ag ions at fluences of 3 × 10^{15}, 9 × 10^{15} and 3 × 10^{16} ions/cm^2, respectively, are shown in Figure 4. XRD pattern reveals that both the phases, austenite phase (*A*) (cubic; JCPDS file no. 65-5537) as well as martensite phase (*M*) (monoclinic; JCPDS file no. 77-2170), were formed in Ni–Ti pristine films deposited at 823 K, and planes corresponding to their structure are marked by corresponding Miller indices. The most intense peak at $2\theta = 42.5°$ is due to the (110) fundamental reflection corresponding to cubic structure and the peak at $2\theta = 43.9°$, which is due to (002) fundamental reflection corresponding to monoclinic structure, respectively. Moreover, a small peak at 43.2° was observed due to Ni_4Ti_3 precipitation phase corresponding

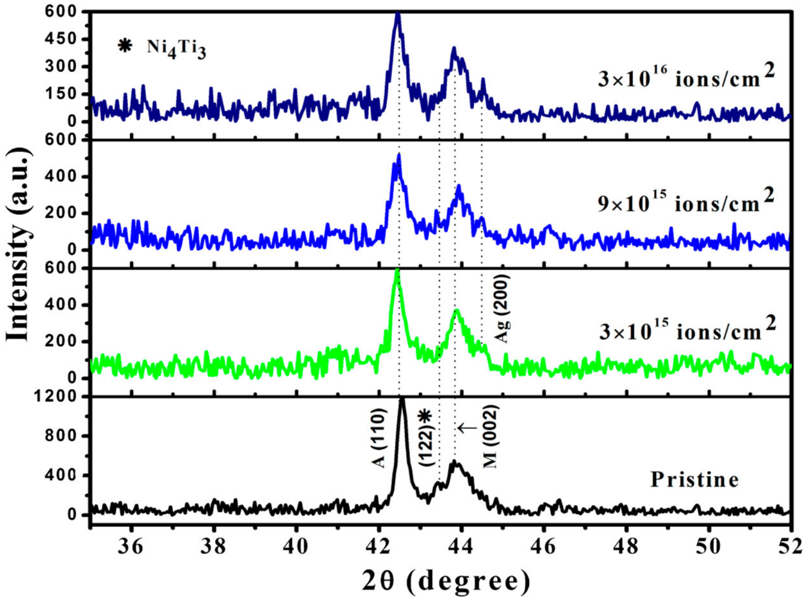

Figure 4. XRD spectra of pristine and 120 keV Ag ions implanted Ni–Ti thin films deposited at 823 K by using the DC-magnetron co-sputtering technique.

to (122) fundamental reflection. The evolution of the XRD peak with implantation fluences exhibits different trends. Figure 4 shows that at the lowest fluence of 3×10^{15} ions/cm^2, a small peak at $2\theta = 44.5°$ arises corresponding to Ag (200) plane (JCPDS file no. 03-0921), indicating the structural change produced by the implanted ions (*30*).

The mean crystallographic crystallite size (*D*) of the pristine and implanted thin films was calculated from the XRD data corresponding to austenite (110) and Ag (200) peaks by applying Scherrer's formula (*31*).

$$D = \frac{0.9\lambda}{\beta \cos\theta}, \tag{1}$$

where λ is the wavelength of Cu-Kα ($\lambda = 0.154$ nm) radiation, β and θ are full width at half maxima (FWHM) and Bragg's angle, respectively. The calculated value of crystallite size for the pristine film is 32.7 nm and for the films implanted at different fluences 3×10^{15}, 9×10^{15}, and 3×10^{16} ions/cm^2 is found to be 30.2, 20.6 and 23.7 nm, respectively, as summarized in Table 1. Also, the crystallite size corresponding to Ag (200) peak at fluences of 9×10^{15}, 3×10^{16} ions/cm^2 is calculated and found to be 22 and 27 nm, respectively. The crystallite size corresponding to film implanted at a fluence of 3×10^{15} ions/cm^2 by Ag ions could not be calculated due to small Ag signal.

The microstrain (ε) of pristine and implanted Ni–Ti thin films at different fluences was calculated by using the following equation (*32*,*33*):

$$\varepsilon = \frac{\beta_G \cot\theta}{4}, \tag{2}$$

where β_G is FWHM (in radian) and θ = angle of diffraction, respectively. The calculated values of microstrain were observed to increase with a decrease in the crystallite size up

Table 1. Microstructural parameters of pristine and implanted Ni–Ti thin films at different fluences.

Fluence (ions/cm^2)	2θ (degree)	FWHM (degree)	Crystallite size (D) (nm) along (110) peak	Microstrain (ε)% along (110) peak	Dislocation density (δ) $\times$ (10^{15} line/m^2)	Average. surface roughness (R_{rms}) (nm)
Pristine	42.56	0.26	32.7	0.29	0.93	2.14
3×10^{15}	42.44	0.28	30.2	0.31	1.09	1.18
9×10^{15}	42.46	0.41	20.6	0.46	2.35	0.80
3×10^{16}	42.46	0.35	23.7	0.40	1.78	0.37

to a fluence of 9×10^{15} ions/cm^2 and it decreases at higher fluence of 3×10^{16} ions/cm^2. The calculated values of microstrain in pristine film are 0.29 and for the films implanted at different fluences 3×10^{15}, 9×10^{15}, 3×10^{16} ions/cm^2 was found to be 0.31, 0.46 and 0.40, respectively, as reported in Table 1. The film implanted at higher fluence (3×10^{16} ions/cm^2) shows an increase in crystallite size, which was calculated corresponding to (110) plane. Moreover, a simultaneous increase in intensity indicates improvement in crystallinity of Ni–Ti thin films. Therefore, it can be concluded that at higher fluence, film releases strain energy, which is primarily responsible for the growth of (110) plane, because most of the body-centred cubic orientations have a lower surface energy (*34*). The peak broadening in XRD lines without affecting the peak position could be due to the non-uniform displacement of atoms after implantation with respect to their lattice position.

The dislocation density (δ) of the pristine and implanted thin films was calculated from the crystallite size (D) using the following relation (*35*), and values are shown in Table 1.

$$\delta = \frac{1}{D^2} \text{ lines/m}^2. \tag{3}$$

The dislocation density is defined as the length of dislocation per unit volume, while the dislocation is a line defect. The calculated values of dislocation density were strongly dependent upon the amount of defects produced by the Ag ions.

The XRD data for the pristine and films implanted at different fluences were obtained at room temperature (300 K). The XRD data (Figure 4) show the presence of Ni_4Ti_3 phase at 43.2° (JCPDF file no. 39-1113) in the film deposited at 823 K and also in the films implanted at different fluences. The presence of Ni-rich (Ni_4Ti_3) phase in Ni–Ti films leads to the formation of R phase as reported by Sanjabi et al. (*36*) and Gyobu et al. (*37*). Due to the existence of Ni_4Ti_3 precipitate phase, we have R-phase in the present result, which was further confirmed by electrical resistivity versus temperature curves (Figure 6) in both heating and cooling cycles.

(b) *Atomic force microscopy*

The surface morphology of pristine and Ag implanted films at different fluences of 3×10^{15}, 9×10^{15} and 3×10^{16} ions/cm^2, respectively, was analyzed by AFM. Figures 5(a)–(d) shows the two-dimensional AFM images of pristine and implanted thin films with a scan area of 1 µm × 1 µm. AFM images clearly show the change in morphology of films with an increase in incident ions per unit area on the films. The root means square (R_{rms}) surface roughness of Ni–Ti pristine and implanted films are given in Table 1. The root means square surface

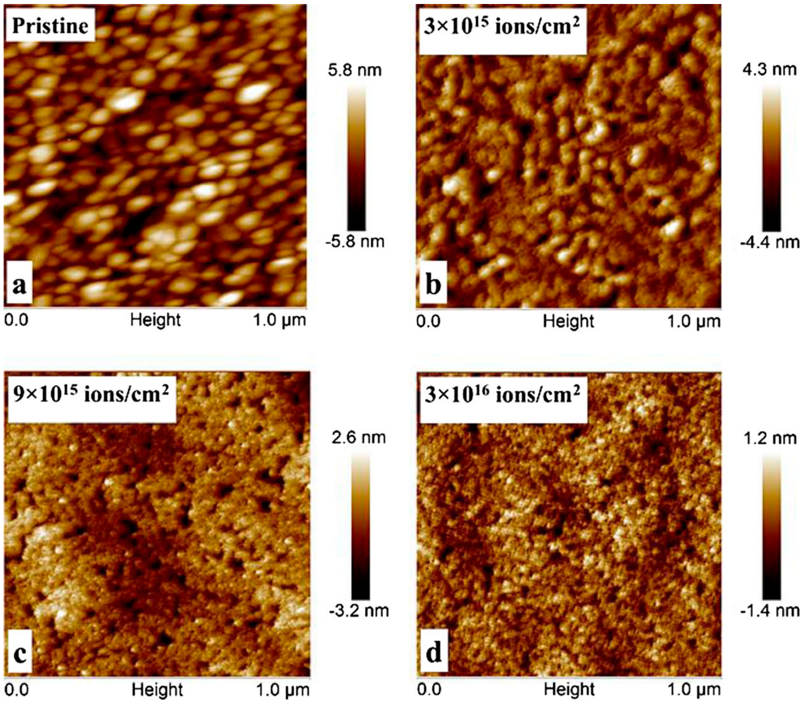

Figure 5. AFM surface micrograph of Ni–Ti thin films over a scan area 1 × 1 µm; (a) pristine Ni–Ti film, (b) Ni–Ti film implanted at 3×10^{15} ions/cm^2, (c) Ni–Ti films implanted at 9×10^{15} ions/cm^2 and (d) Ni–Ti thin film implanted at higher fluence 3×10^{16} ions/cm^2.

roughness was calculated based on the calculation of standard deviation in peak to valley difference in height within image area as reported in ref. (*38*).

$$R_{\mathrm{rms}} = \left[\frac{1}{N} \sum_{i=1}^{N} |Z^i - \overline{Z}|^2 \right]^{1/2}, \tag{4}$$

where $\overline{Z}$mean height distance and N is the number of surface height data. The R_{rms} value of pristine films is ∼2.14 nm and for the films implanted at different fluences, it is found to be ∼1.09, ∼0.80 and ∼0.37 nm, respectively. The R_{rms} values of surface roughness calculated by AFM images were observed to decrease with an increase in ion fluences, which could be due to a decrease in crystallite size and an increase in XRD peak broadening.

3.3. Electrical transport properties

Phase transformation behaviour of pristine and 120 keV Ag-implanted thin films at different fluences 3×10^{15}, 9×10^{15} and 3×10^{16} ions/cm^2 was characterized by the four-point probe resistivity method. Figure 6(a)–(d) shows the resistivity versus temperature curves of pristine and implanted thin films at different fluences during heating and cooling cycles. At the time of experiment, the condition of stationary equilibrium was maintained by cycling the temperature stepwise with a sufficient time interval between every data point. In Figures 6(a)–(d), R_s, R_f, M_s and M_f denotes the start and finish temperature of formation of

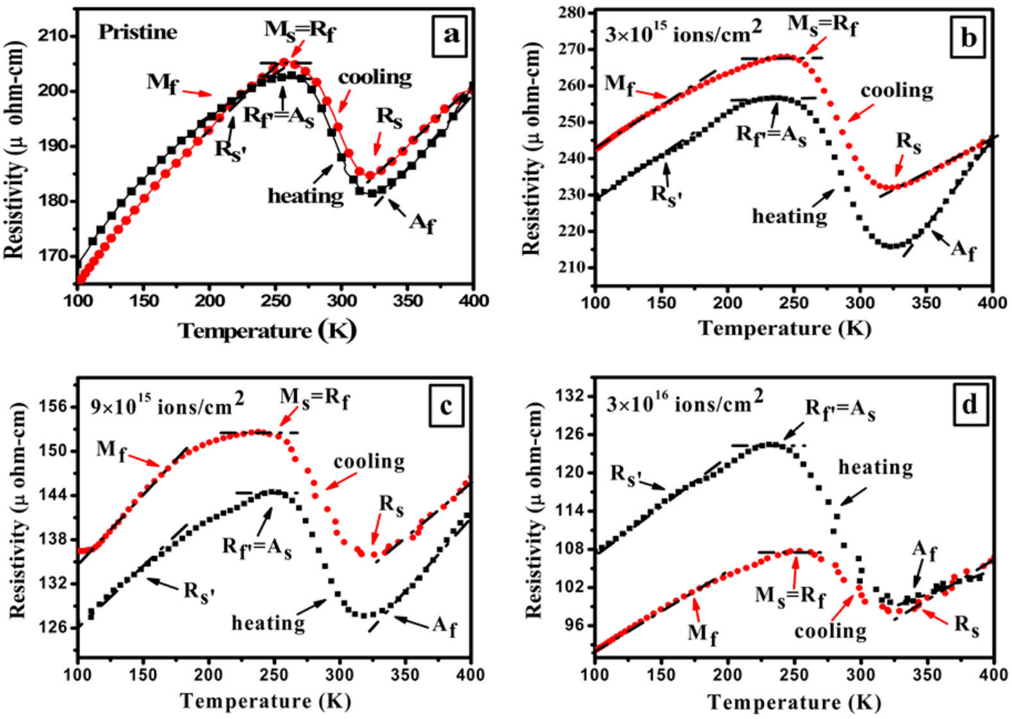

Figure 6. Electrical resistivity versus temperature curves of Ni–Ti pristine and implanted thin films at different fluences during heating and cooling cycles.

intermediate R phase (36), martensitic phase (B'_{19}) on cooling and R'_s, R'_f, A_s and A_f denotes the R phase, austenite phase (B_2) on heating, respectively. It was observed that austenite, martensitic and R phase are present in Ni–Ti pristine films and also in the films implanted at different fluences, as shown in Figures 6(a)–(d). A linear decrease of resistivity values was observed after implantation in Ni–Ti thin films with continuous increase in the fluence; it may be explained as follows; during implantation, vacancy diffusion is increased and this increased diffusion of vacancies leads to the decrease in the resistivity values (39). Figure 6(a) shows the resistivity versus temperature curves of pristine Ni–Ti film deposited at 823 K, which reveals two-step phase transformation from martensitic (B'_{19}) to austenitic phase (B_2) and vice versa via R phase, during heating and cooling cycles. It was observed that upon heating, the value of electrical resistivity increases with an increase in the temperature up to 260 K because of the formation of R phase, but after phase transformation of martensite to austenite, the value of resistivity is found to decrease. The resistivity of films was measured by using the following equation (40):

$$\rho = \frac{\pi t}{\ln 2}\left(\frac{V}{I}\right),$$

where V is the voltage, I current and t film thickness.

During heating and cooling cycles, R-phase transformation is observed in all the films implanted at different fluences. The formation of R-phase during phase transformation from austenite ($B_2 \leftrightarrow R$) induces significantly small transformation strain ($\sim 1\%$) when compared to the phase transformation from austenite to martensite ($B_2 \rightarrow B'_{19}$) phase transformation (~ 10%) (41). Decrease in strain by twinning plays an important role in the formation of R phase because it proceeds by nucleation and growth in parent phase. Therefore, the formation of R phase is a self-accommodation process, which occurs gradually in the parent phase with decreasing temperature. The presence of R-phase transformation in Ni–Ti shape memory alloy thin films are found to be very beneficial to the two ways shape memory effect which can remember both low and high temperatures shapes (42). Due to this unique property, Ni–Ti SMA is considered as a promising material for actuation of some MEMS devices such as microsensors and microswitches (3). Thin films of Ni–Ti SMA are very sensitive to environmental changes such as electrical field, magnetic field, stress and temperature and thus they can be used for microsensor applications (43). Other promising applications include optical fibre switching, probe tips for self-regulating equipment, fuel injectors, lens positioner, microrelay and switches embedded with on-chip circuit breakers to prevent overheating caused by accidental overload or short circuit, etc. (44). In present work, two-way shape memory effect occurs due to the following reasons: existence of Ni_4Ti_3 precipitate phase, intrinsic residual stress generation, higher Ni composition and biasing force generated by Si substrate.

A two-step phase transformation in Ni–Ti films takes place in the following procedure as reported by Mohri et al. (45):

$$A\text{- phase} \rightarrow R\text{- phase} \rightarrow M\text{- phase (during cooling cycles)},$$

$$M\text{- phase} \rightarrow R\text{- phase} \rightarrow A\text{- phase (during heating cycles)}.$$

Figure 6(b)–(d) accounts a two-step phase transformation (austenitic phase↔ martensitic phase via R phase and vice versa) in Ni–Ti films implanted at 3×10^{15}, 9×10^{15} and 3×10^{16} ions/cm^2, respectively, during heating and cooling cycles. The values of austenitic A_f (finish temperature of austenitic phase) and martensitic phase M_s (start martensitic phase temperature) calculated from resistivity versus temperature curves were found to be 321 and 260 K for pristine film, 323 and 253 K for film implanted at 3×10^{15} ions/cm^2, 320 and 252 K for the film implanted at 9×10^{15} ions/cm^2, 330 and 238 K for the film implanted at a fluence of 3×10^{16} ions/cm^2. The thermal hysteresis width is defined by the temperature difference between the A_f and M_s and found to be 61, 70, 68 and 92 K for the pristine and the films implanted at different fluences. From resistivity versus temperature curves, it appears that film implanted at a fluence of 3×10^{16} ions/cm^2 shows much larger hysteresis width in comparison to pristine Ni–Ti films, which could be due to the structural defect and change in the chemical composition after ion implantation (46). In case of the films implanted at different fluences at 3×10^{15}, 9×10^{15} and 3×10^{16} ions/cm^2, respectively, it is observed that hysteresis loop is not closed even at 100 K, which could be due to small grain size, lattice mismatching and intrinsic stress formed in films after implantation.

3.4. Mechanical properties

The mechanical properties of pristine and 120 keV Ag-implanted Ni–Ti films were determined by CSM Nano-indentation. Figure 7 (a)–(d) shows the indenter load versus displacement curves as a function of ion fluences taken at room temperature. These curves are used to calculate the basic mechanical properties such as indent depth recovery ratio (δ),

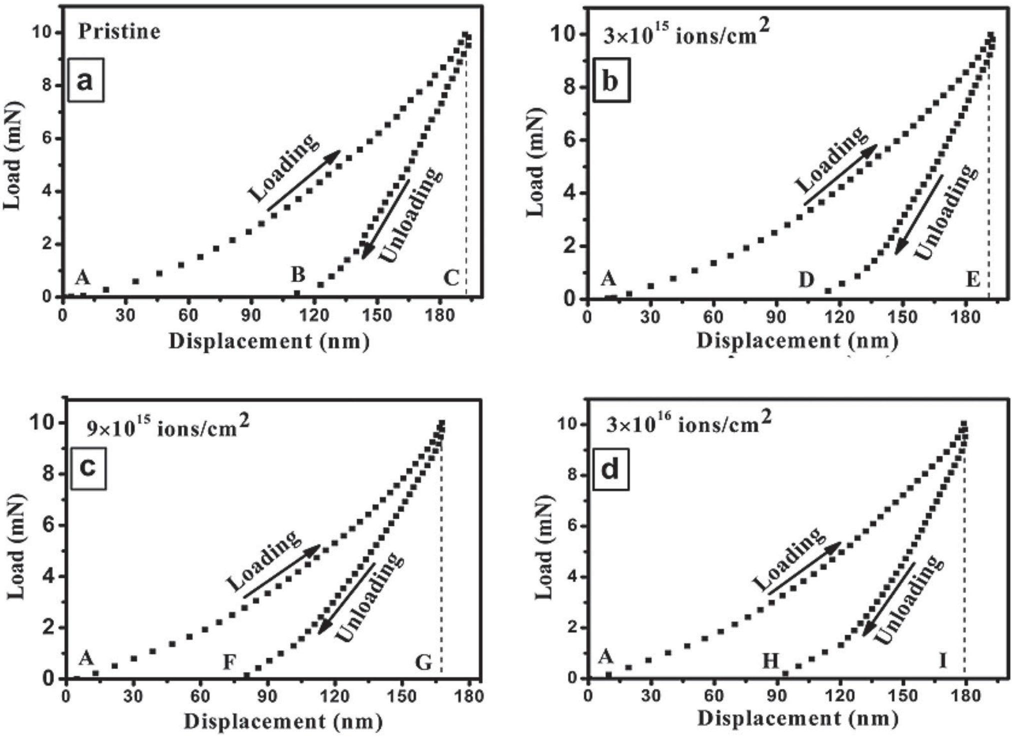

Figure 7. Load versus displacement curves of pristine and Ag-implanted Ni–Ti thin films at different fluences.

elastic modulus (E_r), hardness (H) and plastic resistance parameter (H/E_r). All results were calculated by using the Oliver and Pharr method (47):

The elastic modulus is defined by the equation:

$$E_r = \frac{S\sqrt{\pi}}{2\sqrt{A}},$$

where S (unloading stiffness) $= \mathrm{d}P/\mathrm{d}h$ and A is the projected contact area. The elastic modulus of the material is related to the modulus of elasticity by the following relation:

$$\frac{1}{E_r} = \frac{(1-v_i^2)}{E_i} + \frac{(1-v_s^2)}{E_S},$$

where subscript i represents the indenter material and subscript s corresponds to the sample material, and v is the Poisson's ratio. The hardness (H) of the material is expressed by the following formula:

$$H = \frac{P_{\max}}{A},$$

where $P_{\max}$ is the maximum load and A is the projected contact area. The obtained values by nano-indentation test are listed in Table 2. The elastic modulus of the pristine film was 161 GPa and for the films implanted at different fluences 3×10^{15}, 9×10^{15} and 3×10^{16}

Table 2. A comparison of hardness and elastic modulus of pristine and 120 keV Ag-implanted Ni–Ti thin films.

Fluence (ions/cm^2)	Total depth h_{max} (nm)	Residual depth h_r (nm)	Depth recovery ratio (δ)	Hardness H (GPa)	Elastic modulus E_r (GPa)	H/E_r
Pristine	192.3	112.3	0.41	17.7	161	0.10
3×10^{15}	190.6	114.2	0.40	20.1	164	0.12
9×10^{15}	167.4	80.9	0.51	28.2	173	0.16
3×10^{16}	178.9	94.2	0.47	22.3	170	0.13

ions/cm^2, respectively, it was found to be 164, 173 and 170 GPa, respectively, as mentioned in Table 2. The hardness of pristine film was 17.7 GPa and for the films implanted at 3×10^{15}, 9×10^{15} and 3×10^{16} ions/cm^2 respectively, it was found to be 20.1, 28.2 and 22.3 GPa, respectively. It has been observed that Ni–Ti film exhibits a higher value of hardness (28.2 GPa) at a fluence of 9×10^{15} ions/cm^2 in comparison to pristine ($H = 17.7$ GPa) film; this is ascribed to smaller crystallite size of implanted film compared to pristine films, which is also confirmed by XRD analysis. It is found that a decrease in crystallite size is almost 1.5 times lower than the pristine film. Similar behaviour was also reported by Choudhary and Vishnoi et al. in NiTi/PZT/TiO$_x$ heterostructures and NiMnSn thin films. They concluded that a large number of grain boundary leads to smaller crystallite size, which restricts the wear of the films to a large extent by acting as barriers to dislocation motion (*48*,*49*). It is also reported by several authors that smaller grain size and higher dislocation density increase the yield strength of the material (*50*,*51*). The Ni–Ti films implanted at a fluence of 9×10^{15} ions/cm^2 shows higher dislocation density and smaller crystallite size in comparison to the films implanted at different fluences as reported in Table 1. Hardness-to-elastic-modulus (H/E_r) ratio is also an important parameter to measure the elastic and elastic–plastic behaviour of thin films. A higher H/E_r value is found for the film implanted at a fluence of 9×10^{15} ions/cm^2, which indicates small strain energy and better wear resistance to plastic deformation.

The indentation-induced superelastic effect can be characterized by depth recovery ratio, which is estimated from the load versus displacement curve by using the following relation (*39*):

$$\text{Depth recovery ratio } (\delta) = \frac{(h_{max} - h_r)}{h_{max}},$$

where h_{max} and h_r correspond to penetration depth at maximum load, residual displacement when load returned to zero during unloading, respectively. The values of h_{max} and h_r indicated by *C*, *E*, *G*, *I* and *B*, *D*, *F*, *H* respectively for different fluences are shown in Figures 7 (a)–(d), and the values of depth recovery (δ) for the pristine and implanted films are shown in Table 2. The h_r and h_{max} are the characteristics of elastic nature of the materials and hardness. The Lower the values of h_r, the higher is the elasticity of materials, and also lower values of h_{max} show higher hardness of materials.

4. Conclusions

Ag-ion implantation at different fluences leads to the formation of new phases in the film and causes significant changes in microstructural parameters. AFM study reveals changes in the surface roughness values with increases in ion fluence. It is concluded that a two-step phase transformation ($B_2 \leftrightarrow R \leftrightarrow B'_{19}$) takes place in Ni–Ti and Ni–Ti–Ag films during heating and cooling cycles. The film implanted at a fluence of 3×10^{16} ions/cm^2 shows the large thermal hysteresis during heating and cooling cycles due to the generation of structural defects in crystalline Ni–Ti matrix after the ion implantation. Significant improvement in mechanical properties is achieved in the film implanted at a fluence of 9×10^{15} ions/cm^2. Improved properties of Ni–Ti films pave the way for future MEMS application.

Acknowledgements

The authors acknowledge Ms. K. Devarani Devi and Mr Sunil Ojha at IUAC, New Delhi for their help and support to carry out ion implantation of Ni–Ti films. The author is also thankful to Dr M. Gupta of UGC-DAE CSR, Indore, for providing the characterization techniques such as XRD and synthesis of Ni–Ti thin films. Dr A. Gupta, Amity Center for Spintronic Materials, Amity University Noida is also acknowledged for their help and support.

Disclosure statement

No potential conflict of interest was reported by the authors.

Funding

One of the authors (R. Singhal) acknowledges the financial supports provided by Department of Science & Technology, New Delhi in terms of DST FAST Young Scientist project (SR/FTP/PS-081/2011).

References

(1) Xu, D.; Wang, L.; Ding, G.; Zhou, Y.; Yu, A.; Cai, B. *Sens. Actuators A* **2001,** *93,* 87–92.
(2) Brien, B.; Carroll, W.M.; Kelly, M.J. *Biomaterials* **2002,** *23,* 1739–1748.
(3) Fu, Y.; Du, H.; Huang, W.; Zhang, S.; Ha, M. *Sens. Actuators A* **2004,** *112,* 395–408.
(4) Grummon, D.S. *JOM* **2003,** *55,* 24–32.
(5) Weafer, F.M.; Bruzzi, M.S. *Int. J. Fatigue* **2016,** *82,* 730–736.
(6) Chu, C.L.; Hu, T., Wu; S.L., Dong; Y.S., Yin; L.H., Pu; Y.P., Lin; P.H., Chung; C.Y., Yeung; K.W.K., Chu; P.K *Acta Biomater.* **2007,** *3,* 795–806.
(7) Gorji, M.R.; Sanjabi, S.; Barber, Z.H. *Micro Nano Lett.* **2012,** *7,* 641–645.
(8) Cheng, Y.; Cai, W.; Li, H.T.; Zheng, Y.F. *J. Mater. Sci.* **2006,** *41,* 4961–4964.
(9) Cui, Z.D.; Man, H.C.; Yang, X.J. *Surf. Coat. Tech.* **2005,** *192,* 347–353.
(10) Tan, L.; Dodd, R.A.; Crone, W.C. *Biomaterials* **2003,** *24,* 3931–3939.
(11) Li, Y.; Wei, S.B.; Cheng, X.Q.; Zhang, T.; Cheng, G.A. *Surf. Coat. Tech.* **2008,** *202,* 3017–3022.
(12) Anders, A., Ed. *Handbook of Plasma Immersion Ion Implantation and Deposition*; John Wiley and Sons: New York, 2000.
(13) Gupta, A.; Singhal, R.; Jagdish, N.; Avasthi, D.K. *J. Mater. Res.* **2011,** *26,* 2901–2906.
(14) An, Q.Z.; Feng, K.; Lu, H.; Cai1, X.; Sun, T.; Chu, P.K. *Trans. Nonferrous Met. Soc. China* **2015,** *25,* 1944–1949.
(15) Kumar, V.; Singhal, R.; Vishnoi, R; Gupta, M.; Sharma, P.; Banerjee, M.K.; Asokan, K.; Sharma, H.; Gupta, A.; Kanjilal, D. *Adv. Mat. Lett.* **2017,** *8,* 486–492.
(16) Zhao, T.; Li, Y.; Liu, Y.; Zhao, X. *J. Mech. Behav. Biomed. Mater.* **2012,** *13,* 174–184.
(17) Chluba, C.; Ge, W.; de Miranda, R. L.; Strobel, J.; Kienle, L.; Quandt, E.; Wuttig, M. *Science* **2015,** *348,* 1004–1007.
(18) Zhao, T.; Li, Y.; Xia, Y.; Venkatraman, S.S.; Xiang, Y.; Zho, X. *Mater. Sci: Mater. Med.* **2013,** *24,* 105–114.
(19) Zhao, T.; Li, Y.; Xiang, Y.; Zhao, X.; Zhang, T. *Surf. Coat. Tech.* **2011,** *205,* 4404–4410.

(20) Singhal, R.; Kabiraj, D.; Kulriya, P.K.; Pivin, J.C.; Chandra, R.; Avasthi, D.K. *Plasmonics.* **2013,** *8,* 295–305.

(21) Oh, K.T.; Joo, U.H.; Park, G.H.; Hwang, C.J.; Kim, K.N. *J. Biomed Mater. Res. B Appl. Biomater.* **2006,** *76,* 306–314.

(22) Kaur, N.; Kaur, D. *Mater. Lett.* **2013,** *91,* 202–205.

(23) Singhal, R.; Pivin, J.C.; Avasthi, D.K. *J. Nanopart. Res.* **2013,** *15,* 1641.

(24) Luo, P.; Wang, S.N.; Zhao, T.T.; Li, Y. *Rare Met.* **2013,** *32,* 113–121.

(25) Melaiye, A.; Youngs, W.J. *Expert Opin* **2005,** *15,* 125–130.

(26) Singhal, R.; Pivin, J.C.; Chandra, R.; Avasthi, D.K. *Surf. Coat. Tech.* **2013,** *229,* 50–54.

(27) Babu, R.; Zhang, J.; Beckman, E.J.; Virji, M.; Pasculle, W.A.; Wells, A. *Biomaterials* **2006,** *27,* 4304–4314.

(28) Ziegler, J.F.; Biersack, J.P.; Littmark, V. *The Stopping and Range of Ions in Solids*; Pergamon: New York, 1985.

(29) Adeoya, W.O.; Ali, M.H.; Muller, J.C.; Siffert, P. *Appl. Phys. Lett.* **1987,** *50,* 1736–1738.

(30) Zheng, Y.F.; Zhang, B.B.; Wang, B.L.; Wang, Y.B.; Li, L.; Yang, Q.B.; Cui, L.S. *Acta Biomater.* **2011,** *7,* 2758–2767.

(31) Cullity, B.D. *Elements of X-Ray Diffraction*; Addison-Wesley: Reading, MA, 1970.

(32) Dahshan, A.; Aly, K.A. *J. Non-Cryst. Solids* **2015,** *408,* 62–65.

(33) Akl, A.A.; Hassanien, A.S. *Superlattices Microstruct.* **2015,** *85,* 67–81.

(34) Zhang, J.M.; Ma, F.; Xu, K.W. *Surf. Interface Anal.* **2003,** *35,* 662–666.

(35) Lowsk, A.K.; Cki, J.C.; Fahmi, A.; Beker, B. *Dalton Trans.* **2008,** *47,* 6825–6831.

(36) Sanjabi, S.; Sayed, K.S.; Karen, A.Y.; Zoe, H.B. *Thin Solid Films* **2005,** *491,* 190–196.

(37) Gyobu, A.; Kawamura, Y.; Horikawa, H.; Saburi, T. *Mater. Sci. Eng. A* **1999,** *273–275,* 749–753.

(38) Zhang, H.S.; Endrino, J.L.; Anders, A. *Appl. Surf. Sci.* **2008,** *255,* 2551–2556.

(39) Vishnoi, R.; Singhal, R.; Asokan, K.; Kanjilal, D.; Kaur, D. *Thin Solid Films* **2011,** *520,* 1631–1637.

(40) K.H., Ken; Gregory, P.C. *Thin Solid Films* **2000,** *370,* 18–29.

(41) Waitz, T.; Kazykhanov, V.; Karnthaler, H.P. *Acta Mater.* **2004,** *52,* 137–147.

(42) Mei, M.C.; Gang, L.; Jain, L.; Lide, Z. *Mater. Sci. Eng. A* **1990,** *127,* 85–89.

(43) Bendahan, M.; Aguir, K.; Seguin, J.L.; Carchano, H. *Sens. Actuators* **1999,** *74,* 242–245.

(44) Johnson, A.D. *Micromach. Devices* **1999,** *4,* 1.

(45) Mohri, M.; Ahmadabadi, M.N.; Ivanisenko, J. *Adv. Eng. Mater.* **2015,** *17,* 856–865.

(46) Wayman, C. M. *Prog. Mater. Sci.* **1992,** *36,* 203–224.

(47) Oliver, W.C.; Pharr, G.M. *J. Mater. Res.* **1992,** *7,* 1564–1583.

(48) Choudhary, N.; Kharat, D.K.; Kaur, D. *Surf. Coat. Tech.* **2011,** *205,* 3387–3396.

(49) Vishnoi, R.; Singhal, R.; Kaur, D. *J. Nanopart Res.* **2011,** *13,* 3975–3990.

(50) He, J.Y.; Wang, H.; Huang, H.L.; Xu, X.D.; Chen, M.W.; Wu, Y.; Liu, X.J.; Nieh, T.G.; An, K.; Lu, Z.P. *Acta Mater.* **2016,** *102,* 187–196.

(51) Kreitcberg, A.; Brailovski, V.; Prokoshkin, S.; Gunderov, D.; Khomutov, M.; Inaekyan, K. *Mater. Sci. Eng. A* **2015,** *622,* 21–29.

Applied Physics A (2018) 124:328
https://doi.org/10.1007/s00339-018-1746-7

Applied Physics A
Materials Science & Processing

Effect of crystallographic orientation on structural and mechanical behaviors of Ni–Ti thin films irradiated by Ag^{7+} ions

Veeresh Kumar[1] · **Rahul Singhal**[1]

Received: 17 November 2017 / Accepted: 14 March 2018

Abstract

In the present study, thin films of Ni–Ti shape memory alloy have been grown on Si substrate by dc magnetron co-sputtering technique using separate sputter targets Ni and Ti. The prepared thin films have been irradiated by 100 MeV Ag^{7+} ions at three different fluences, which are 1×10^{12}, 5×10^{12}, and 1×10^{13} ions/cm^2. The elemental composition and depth profile of pristine film have been investigated by Rutherford backscattering spectrometry. The changes in crystal orientation, surface morphology, and mechanical properties of Ni–Ti thin films before and after irradiation have been studied by X-ray diffraction, atomic force microscopy, field-emission scanning electron microscopy, and nanoindentation techniques, respectively. X-ray diffraction measurement has revealed the existence of both austenite and martensite phases in pristine film and the formation of precipitate on the surface of the film after irradiation at an optimized fluence of 1×10^{13} ions/cm^2. Nanoindentation measurement has revealed improvement in mechanical properties of Ni–Ti thin films after ion irradiation via increasing hardness and Young modulus due to the formation of precipitate and ductile phase. The improvement in mechanical behavior could be explained in terms of precipitation hardening and structural change of Ni–Ti thin film after irradiation by Swift heavy ion irradiation.

1 Introduction

The shape memory behavior and superelasticity of Ni–Ti make it a promising material for micro-electro-mechanical system (MEMS) and biomedical applications [1, 2]. These unique properties are mainly due to the reversible phase transformations between low-temperature martensite and high-temperature austenite crystal structures, which can be achieved by variation in temperature and applied load [3, 4]. Nowadays, shape memory behavior of Ni–Ti alloy is commercially used for different applications such as coupling, sensors, actuators, and cellular phones antennas [5, 6]. Recently, Ni–Ti has attracted wide interest as a biomaterial, due to shape recovery behavior after deformation beyond its elastic limit either by heating or by removing the applied load [7].

In the form of thin film, Ni–Ti shape memory alloy (SMA) have received significant interest of the scientific community due to their excellent properties for MEMS applications, such as high power density, high power-to-weight ratio, outstanding chemical resistance, pseudoelasticity (or superelasticity), and excellent biocompatibility [2, 8–10]. The work output per unit volume of SMA thin film is quite large in comparison to other micro-actuation mechanisms. Phase transformation in Ni–Ti SMA thin film is accompanied by significant changes in physical, electrical, chemical, and mechanical properties, such as shape recovery, thermal expansion coefficient, surface roughness, electrical resistivity, dielectric constant, yield stress, Young modulus, hardness, and damping [11, 12]. These changes can be fully utilized in design and fabrication of pumps and grippers for MEMS. Hence, it is essential to explore the mechanical properties of the SMA films.

Numerous attempts have been made to enhance the properties of Ni–Ti through different surface modification techniques, such as gas nitriding [13], ion nitriding [14], heat oxidation [15], laser surface melting [16], and ion irradiation [17–19]. The critical challenge for ion or gas nitriding is the formation of the non-superelastic Ti_2Ni layer that limits its application in dentistry as reported by several authors [20, 21]. However, equilibrium precipitate phase of nickel and titanium Ni_3X, Ni_2X, Ni_4X_3, TiX, Ti_3X_4, and TiX_2 (where

✉ Veeresh Kumar
vks8361@gmail.com

[1] Department of Physics, Malaviya National Institute of Technology Jaipur, JLN Marg, Malviya Nagar, Jaipur 302017, India

X = Si, Ti, Sn, Al, V, Nb) are potential stable phases which contribute to enhancing the mechanical strength of Ni–Ti SMA [22]. Swift heavy ion (SHI) irradiation has unique capabilities for modification of surface layers on metals and alloys including their crystal structure, chemical composition, and physical and mechanical properties. SHI-induced damaging effects can benefit the shape memorial behavior and bias the shape recovery if the detrimental effects are more controlled [23]. It is reported that mechanical properties of the materials strongly depend upon the precipitation, defect density and grain refinement, which significantly increases the resistance of materials against plastic deformation. However, these treatments reduce the martensite transformation temperature by changing the internal stress and surface composition of the matrix [19, 24].

There are various studies of the effect of precipitation on structural, mechanical, and phase transformation behavior of SMAs. Nunomura et al. have thoroughly investigated the phase relation and microstructure of pseudo-ternary alloy based on Ni_3Ti, Ni_3Nb, and Ni_3Al [25]. The effect of annealing temperature on microstructure and mechanical properties of intermetallic Ni enriched NiTi films is reported by Reddy et al. [26]. They have observed the higher values of hardness due to the nucleation, growth process of grains, and segregation of Ni_3Ti precipitation phase at the higher annealing temperature. Recently, the influence of Ti_2Cu precipitate in NiTiCu-based ultralow-fatigue SMA films has been reported by Chluba et al. for 10 million transformation cycles for artificial heart valve or elastocaloric cooling [27]. Zu et al. have investigated the effect of 1.7 MeV electron irradiation on martensite phase transformation of NiTi alloy. The martensite temperature decreases with irradiation fluence due to relaxation of elastic stress around the Ni_4Ti_3 precipitate phase [17]. In addition, Ishida et al. have reported that Ni-51 at. pct and Ti-49 at. pct thin films exhibit the stable super elasticity and excellent shape memory effect [28]. In bulk NiTi alloy, the higher composition of Ni (55 to 60 at. pct) shows excellent properties such as high yield strength, non-magnetization, and high corrosion resistance at prominent temperature [29]. Moreover, formation of Ni_4Ti_3 and Ni_3Ti phases in NiTi alloy makes them chemically and structurally stable at higher annealing temperature [30]. Afzal et al. have studied the microstructure and mechanical behavior of 2 MeV proton beam irradiated Ni-rich-nitinol alloy [18]. The effect of different types of perturbations such as the electron, proton, and ion irradiation on microstructure, phase transformation, and mechanical properties have been reported in the literature [17, 18, 31], The purpose of the present study is improved the mechanical behavior of Ni–Ti films by Ag ion irradiation. The Ni composition (55 to 60 at. pct) is the best range to increase the mechanical behavior of alloy with higher mechanical strength and ductility [29]. The Ni-rich Ni–Ti films also undergo two-stage austenite to martensite phase via R-phase transformation because of the formation of the Ti_3Ni_4 precipitates [32]. Moreover, it is reported that Ni-rich composition of the Ni–Ti films exhibits stable superelasticity effect in addition to an excellent shape memory behavior [28]. Therefore, investigations on surface characteristic and mechanical behavior of 56.7 at.%Ni thin films, irradiated by SHI irradiation are not adequate and need to be explored in detail.

In the present study, we have used an innovative material modification technique namely SHI irradiation to engineer the surface structure and mechanical properties of Ni–Ti thin films [33]. The effect of energetic ions on material depends on the electronic energy, ion fluence, ion species, and temperature. It is well known that the energy loss of incident ions play a major role in the material modification that leads to the formation of lattice defects and excitation/ionization [33–35]. If S_e exceeds a threshold value 46 keV/nm, then there will be formation of track or amorphization of Ni–Ti bulk alloy, whereas if S_e = 32 keV/nm, no individual tracks formation can be observed at low fluence, only the monoclinic phase to cubic austenite phase transformation is observed at high fluences [36]. If $S_e \leq 17$ keV/ nm, swift heavy ions are unable to induce any visible structural modifications in Ni–Ti bulk alloy by electronic excitations [36]. Silver (Ag) is a potential metallic element to enhance the properties of SMA due to its exceptional mechanical properties of high strength, excellent thermal-driven ability, high mechanical damping and good superelasticity, etc. [3, 37–39]. Therefore, Ag ions with 120 MeV energy are used to observe the modification in Ni–Ti thin films. The value of S_e for Ag ions is 25 keV/nm, which is a moderate value, and therefore, it is enabled to modifications in Ni–Ti thin films. The Ni–Ti thin films irradiated at three optimized fluence of 1×10^{12}, 5×10^{12} and 1×10^{13} ions/cm^2 to observe structural and mechanical modifications.

The primary objective of the present study is to deposit the films with two different phases, ordered austenite and low-symmetry allotrope martensite phase with the higher composition of Ni. The films are irradiated at three different fluences by using SHI irradiation to promote the growth of hard Ni_3Ti precipitate which would enhance the mechanical behavior of Ni–Ti thin films. The results presented here to bring forth the understanding of the strengthening mechanisms and deformation behavior of Ni–Ti films by SHI irradiation. This study is also essential to investigate the effects of SHI irradiation on the shape memory alloy for future application of these materials in harsh radiation zones such as space or nuclear reactor. Figure 1 shows the schematic diagram of ion–solid interaction. A previous study on Ni–Ti thin films with composition (Ti-56.7 at.%Ni) has been done by the same author using 120 MeV Au ions irradiation to investigate the critical value of fluence and acceptable radiation limit for this composition [40]. Furthermore, the present

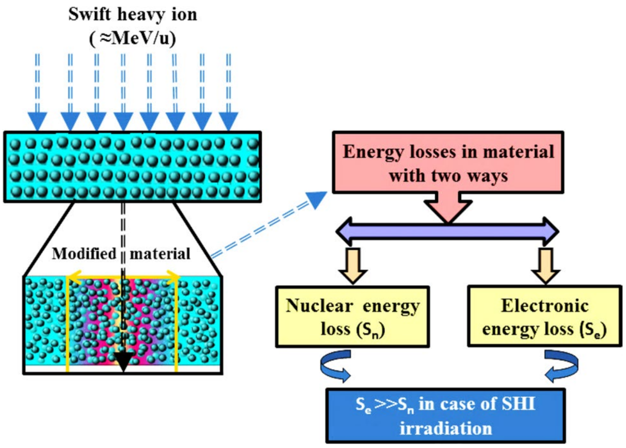

Fig. 1 Schematics diagram for ion–solid interaction for SHI

study has been performed to investigate the effect of SHI irradiation on structural and mechanical properties.

2 Experimental details

In the present study, we have deposited Ni–Ti thin film on 2-inch diameter Si (100) substrate (Matsurf Tech. Inc, USA) and after films deposition; substrate was divided into several 1×1 cm^2 small pieces for irradiation. The dimension of each film during the irradiation was 1×1 cm^2 in the irradiation chamber. Raster scanning (1×1 cm^2) of ion beam was done over the surface during irradiation to cover the complete area of the film. The Si wafer was attached to the substrate holder with the help of clips and rotated (60 rpm) in the horizontal plane of targets during deposition to achieve the uniform films growth. Before deposition, the Si substrate was first cleaned in a mixture of Trichloroethylene and distilled water (1:4) ratio in an ultrasonic bath and then washed with boiled acetone. High-purity Ti (99.9%) and Ni (99.9%) metal targets of 3 mm thick and 50 mm diameter (Neyco supplier, France) were used for deposition. The vacuum chamber was repeatedly flushed with argon gas for 10 min to minimize the possible contamination. Before deposition, a base pressure of 2×10^{-7} torr was achieved inside the vacuum chamber using a turbo molecular pump, while, during deposition, the pressure was kept at 3×10^{-3} torr using a dynamic throttling valve. The deposition was performed for 1 h 40 min using two different powers: 50 W for Ni and 100 W for Ti target respectively. All Ni–Ti thin films have been prepared in argon (~99.9%) atmosphere at 550 °C by an AJA Int. make ATC Orion-8 series sputtering system. The substrate holder to target distance was fixed about 16 cm.

The prepared Ni–Ti films were irradiated by 100 MeV Ag^{7+} ion beam at Inter University Accelerator Centre (IUAC), New Delhi, at room temperature using 15 UD Pelletron Tandem accelerator facility. During irradiation, a high vacuum of the order of $\sim 6 \times 10^{-7}$ torr was maintained inside the irradiation chamber. The values of nuclear energy loss (S_n) and electronic energy loss (S_e) were calculated by SRIM 2008 code [41] and found to be 0.01×10^3, 2.5×10^3 eV/Å, respectively. Moreover, the range of 100 MeV Ag ions in Ni–Ti films (density 6.14 g/cm^3) was also calculated by SRIM 2008 code and determined as 8.23 µm. The modifications in Ni–Ti films can be understood by S_e and S_n. When the SHI interact with the target of Ni–Ti film, it loses their energy into material by two different ways; (a) direct transfer of energy to target lattice by elastic collision, term is known as nuclear energy loss (S_n) and (b) transfer of energy of the incident ions to electrons of target atoms, term is called electronic energy loss (S_e). In high-energy regime (≈ MeV/u), energy transfer by incident ions causes the displacement of atoms in cylindrical zones around the ion path in the target material. In the present study, the calculated value of S_e is too high than that of S_n; that's why S_e dominates over S_n; therefore, modifications are mainly attributed due to S_e effect. The ion beam was scanned over an area of 1×1 cm^2 to achieve the uniform irradiation of Ni–Ti films and the beam current was kept constant at ~ 2 pnA (particle nanoampere).

The composition and thickness of the pristine film were measured by Rutherford backscattering spectrometry (RBS) technique. The crystal structure of the pristine and irradiated Ni–Ti thin films has been studied by X-ray diffractometer (Bruker D8 Advance). The XRD measurement is performed at an incident angle of 1° with Cu-K$_{\alpha 1}$ radiation source of wavelength 1.54 Å in Bragg–Brentano ($\theta/2\theta$) geometry at a scan rate of 0.6°/min at UGC-DAE-CSR Indore. Furthermore, the surface morphology of the films was investigated by AFM (Bruker Nanoscope V system) with a Si$_3$N$_4$ cantilever in tapping mode and field-emission scanning electron microscope (FESEM) with (Model:-TESCAN, MIRA II LMH) at IUAC, New Delhi.

The mechanical properties of pristine and irradiated Ni–Ti thin films have been investigated using the nanoindentation tester equipped (CSM Instruments) with a diamond Berkovich-type indenter tip. The test was performed in air at room temperature at different positions on films surface, and average hardness and Young modulus were calculated. Three nanoindentation tests are performed on pristine and irradiated films at different locations to calculate the average hardness and Young modulus values. Each indenter test consisted of 8-s linear load segment to a peak load, 10-s holding, and an 8-s linear unloading segments. The hold periods are used to reduce the time-dependent effects (creep effects) generate in the specimen.

3 Results and discussion

3.1 Rutherford backscattering spectrometry

RBS is a non-destructive technique and capable to determining both elemental composition and depth of a thin layer. Figure 2 shows simulated RBS spectrum along with depth profile of pristine Ni–Ti film deposited at 550 °C. The elemental stoichiometry and film thickness was estimated using the SIMNRA simulation of RBS data [42]. The composition of Ni and Ti present in the film was determined by He^{2+} ions with a beam of 2 MeV energy and at normal incidence with the detector positioned at 165° scattering angle. The calculated near surface concentration of Ti was found to be ~ 43.3 at% and Ni concentration was found to be ~ 56.7 at%. The thickness of the pristine film was found to be ~ 270 nm. The elemental composition versus depth profile for Ni and Ti is shown in Fig. 2b and it is showing the uniform distribution of Ni and Ti content through the film thickness.

3.2 Structural properties

3.2.1 X-ray diffraction

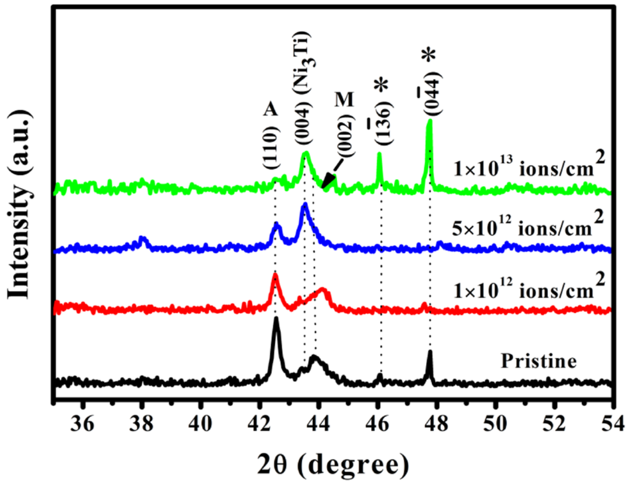

Fig. 3 XRD spectra of pristine and 100 MeV Ag^{7+} ion irradiated Ni–Ti thin films at different fluences

Figure 3 shows the room temperature XRD pattern of the pristine and irradiated Ni–Ti thin films at different fluences in the 2θ range of 35°–54°. The XRD pattern of pristine film deposited at 550 °C exhibits three phases: martensite (monoclinic; JCPDS file no. 77-2170), austenite (cubic; JCPDS file no. 65-5537), and the small amount of Ni_3Ti phase (hexagonal; JCPD file no. 65-2038). In addition to substrate peaks, XRD pattern of the pristine film shows the strong austenite peak at $2\theta = 42.5^\circ$corresponding to (110) fundamental reflection, martensite peak at $2\theta = 43.9°$ corresponding to (002) fundamental reflection, and a small amount of Ni enriched buried Ni_3Ti precipitate peak at $2\theta = 43.5°$ corresponding to (004) plane, respectively. Two other peaks observed in pristine films at 46° and 47.7° are corresponding to oxidized Si substrate [40]. During the cleaning process, solvent (boiled Acetone) may be left its residues in some cases which can affect the surface of Si [43]. After cleaning, the residues of Acetone may reside on the surface of the substrate, which could directly affect the oxygen concentration at the surface and responsible for the intensity variation of the peaks. The film irradiated at a fluence of 1×10^{12} ions/cm^2 shows decrease in intensity of both phases due to the phase transformation from austenite (110) and martensite (002) phase into Ni_3Ti phase on Ag ion bombardment. Furthermore, the film irradiated at a fluence of 5×10^{12} ions/cm^2 shows the dominance of Ni_3Ti phase with concurrent decrease in the intensity of austenite phase. The film irradiated at (5×10^{12} ions /cm^2) fluence shows the ordering of Ni_3Ti phase, which corresponds to hexagonal crystal structure of films. It is observed that film irradiated at this fluence releases strain energy which is primarily responsible for the ordering of (004) plane, because (004) plane of Ni–Ti possesses the minimum surface energy in accordance of basic crystal growth theory [44]. Furthermore, the film irradiated at a higher fluence of 1×10^{13} ions/cm^2 shows the dominance of Ni_3Ti phase and partial amorphization of austenite and

Fig. 2 RBS spectra (2 MeV He^{2+}) along with SIMNRA simulation (**a**) and depth profile (**b**) of Ni–Ti pristine film deposited at 550 °C

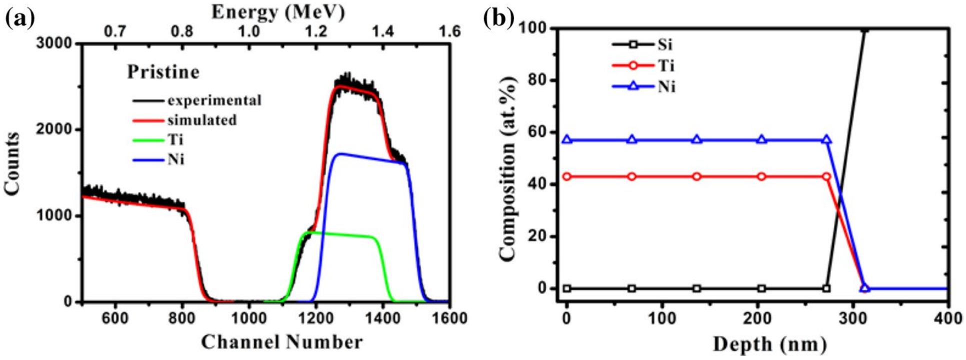

martensite phase. The decrease in intensity of austenite and martensite phase depends upon the amount of energy deposited in Ni–Ti films by the Ag^{7+} ions. When the SHI irradiation passes through the Ni–Ti film, it causes ionization and excitation of Ni–Ti atoms, which leads to the modifications in properties such as structure and phase. Such electronic excitations can also cause local heating followed by a rapid quenching (thermal spikes) which subsequently produces lattice distortions. These lattice distortions are so drastic and they relax into an amorphous state [31]. The modifications in materials structure or phases depend upon irradiation condition such as ion fluence, irradiation temperature, and the nature of ions as reported by several authors [3, 44]. The precipitation of phases and recrystallization of monoclinic into cubic phase by 2 MeV proton beam irradiation has also been observed by Afzal et al. [18] in Ni–Ti alloy at room temperature. The irradiation of Nitinol by proton beam produces small displacement cascade and thus generates vacancies, interstitials, or precipitates. Irradiation-induced defects in the material increase the shear movement of atoms and lead to increase in anti-phase boundary which decreases the martensite transformation.

3.2.2 Atomic force microscopy

The surface morphology (grain size and roughness) of pristine and Ag^{7+} irradiated Ni–Ti thin films at different fluences ranging from 1×10^{12} to 1×10^{13} ions/cm^2 is studied with AFM in tapping mode. Figure 4a–d shows two-dimensional AFM micrographs of pristine and irradiated Ni–Ti thin films at scan area of 1 μm^2. AFM micrograph of the pristine film (Fig. 4a) shows the very fine and dense grains of Ni–Ti with well-defined boundary. The film irradiated at a fluence of 1×10^{12} ions/cm^2 shows the change in surface morphology with fluence. Moreover, grains are non-uniformly distributed over the film surface due to electronic energy bombardment on Ni–Ti film. The modification of film surface can be understood on the reference of electronic energy deposited into the Ni–Ti thin film. When SHI pass through the Ni–Ti film, it loses its energy into the material followed by ionization and excitation of the atoms. Electronic energy deposited by SHI irradiation beyond a certain threshold ($S_e \sim 32$ keV/nm for Ni–Ti) can cause the significant movement of the atoms resulting into change in the crystal structure and surface roughness [36]. Furthermore, it is found that irradiation at higher fluence of 1×10^{13} ions/cm^2 decreases the grain size and promotes the agglomeration of the grains. The agglomeration of the grains is attributed to multiply ions impact turning on Ni–Ti film by SHI irradiation [45].

The average roughness (R_{avg}) and root-mean-square surface roughness (R_{rms}) of the pristine and irradiated Ni–Ti films are obtained from the AFM images of 1 μm × 1 μm scan area of films surface, three times at different position for each film, and it has been taken as an average

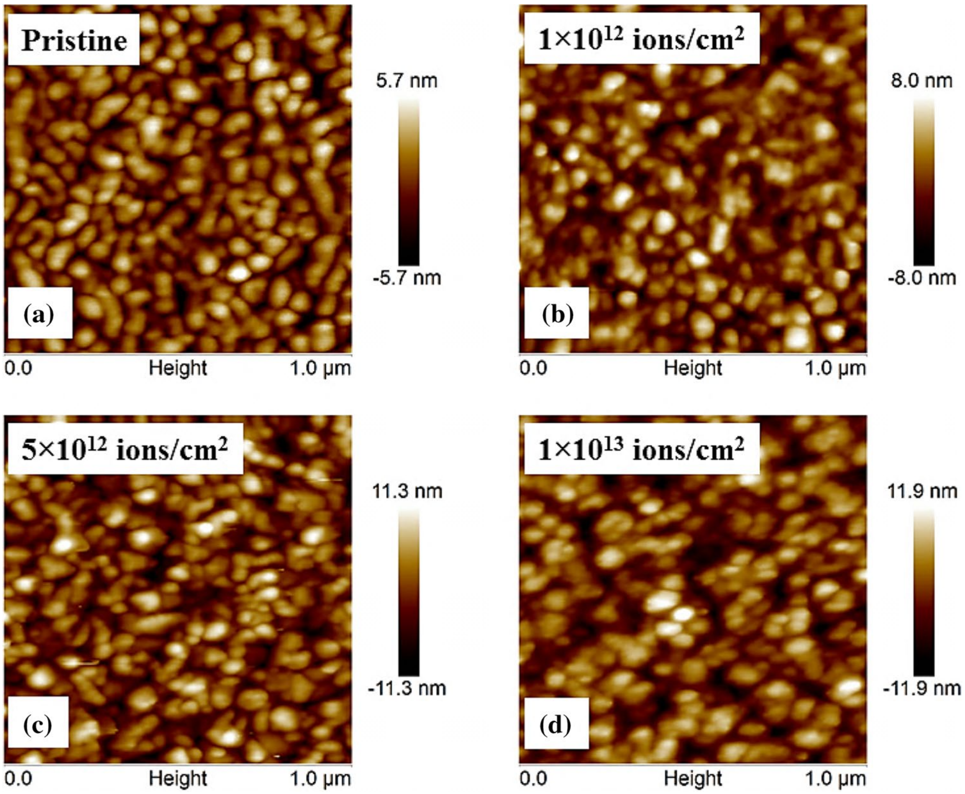

Fig. 4 AFM 2 D surface micrographs of pristine and 100 MeV Ag^{7+} ion irradiated Ni–Ti films at different fluences over a scan area of 1 × 1 μm^2

roughness estimated from AFM micrograph. The R_{avg} and R_{rms} are defined by the following equations [46]:

$$R_{avg} = \left[\frac{1}{N}\sum_{i=1}^{N} |Z_i - \overline{Z}|\right],$$

$$R_{rms} = \left[\frac{1}{N}\sum_{i=1}^{N} |Z_i - \overline{Z}|^2\right]^{1/2},$$

where $\overline{Z}$ is mean height distance and N is the number of surface height data. The R_{avg} and R_{rms} of the pristine and irradiated films are observed to increase with increasing the ion fluences. This could be due to agglomeration of grains and Ni_3Ti precipitate formation at higher fluences. The R_{avg} value of the pristine film is ~2.06 nm and for the films irradiated at different fluences found to be ~2.82, ~3.73 and ~4.10 nm, respectively. The R_{rms} values found to be ~1.61 nm for the pristine film and ~2.32, ~3.02, and ~3.35 nm for the films irradiated at three different fluences respectively. AFM results indicate that the surface morphology of the Ni–Ti films strongly depends upon the ion fluences, as shown in Fig. 5.

In the present study, the Ni–Ti films with same thickness are irradiated using different fluences. Different fluences have different effects on the surface of the grown films such as clustering of grains and formation of craters, etc. [47]. The surface morphology is changed with fluences with the simultaneous change in the Z-height of the sample. The Z-height of the sample depends upon the arrangement of grains and roughness of the films. The variation in roughness value of film also changes the Z-height of the film. In the present study, the Z- height of the four samples is different due to the difference in roughness values of the films.

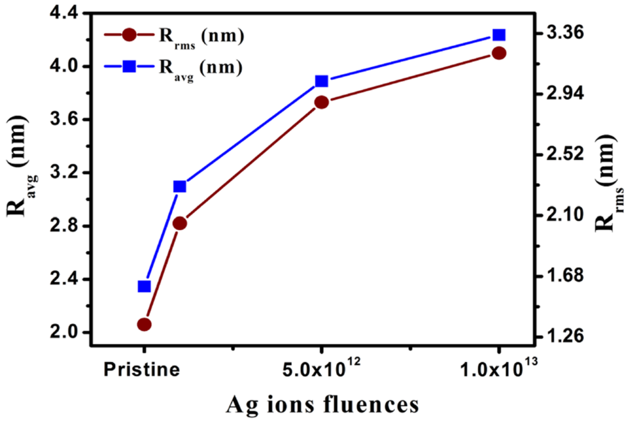

Fig. 5 Variation of R_{avg} and R_{rms} with different ion fluences

3.2.3 Field-emission scanning electron microscopy

Apart from AFM, the surface morphology of pristine and irradiated Ni–Ti thin films is also investigated by FESEM. Figure 6a–d shows the FESEM images of pristine and Ag^{7+} irradiated Ni–Ti thin film at different fluences ranging from 1×10^{12} to 1×10^{13} ions/cm^2. The FESEM micrographs have confirmed the change in surface morphology of Ni–Ti films with ion irradiation at different fluences. Figure 6a shows the dense granular morphology with nearly same granule sized in the pristine film deposited at 550 °C. In Fig. 6b, FESEM image of the irradiated film at a fluence of 1×10^{12} shows that the density of granular size grains decreases as fluence increases. These SHI-induced structural modifications are also supported by AFM analysis. Furthermore, the film irradiated at fluence of 5×10^{12} ions/cm^2 shows the diffused grains morphology of the film; however, it is possible to observe the boundary of grains. The grains of the films are seemed to be agglomerated at this fluence. With further increase in the fluence (1×10^{13} ions/cm^2), the granular morphology of film is completely disappeared and it becomes difficult to observe the boundary of grains. The agglomeration of the grains can be ascribed to the electronic energy deposited by the incoming ions in Ni–Ti regime [48, 49]. The surface features of the pristine and the films irradiated at different fluences of Ag ions have no evident defaults such as cracks and holes etc.

3.3 Nanoindentation

The change in crystal structure in nm-sized crystallites by SHI irradiation may play an important role to enhance the mechanical properties of nanocrystalline materials. Materials under the lattice contraction resist the large force, thus, decreasing the penetration depth of indentation and inhibiting the crack propagation [50]. This phenomenon leads to increase in toughness and hardness of materials; however, lattice expansion leads to opposite phenomena. Ni_3Ti precipitate increases the mechanical strength by promoting the interaction between grain boundaries and dislocation which subsequently increase the average hardness and Young modulus values.

The CSM nanoindentation has been used to characterize the mechanical properties of pristine and irradiated Ni–Ti films. Figure 7 shows the load versus displacement curves of pristine and the films irradiated at different fluences of 100 MeV Ag^{7+} ions. These curves are used to calculate the fundamental mechanical properties such as hardness (H), Young modulus (E_{eff}), and plastic resistance parameter (H/E_{eff}), etc. All results obtained by nanoindentation are analyzed using the Oliver and Pharr method [51] and listed in Table 1. The load–displacement curves (Fig. 7) show that the behavior of each film is consistent from test

Fig. 6 FESEM images of pristine and 100 MeV Ag^{7+} ion irradiated Ni–Ti films at different fluences

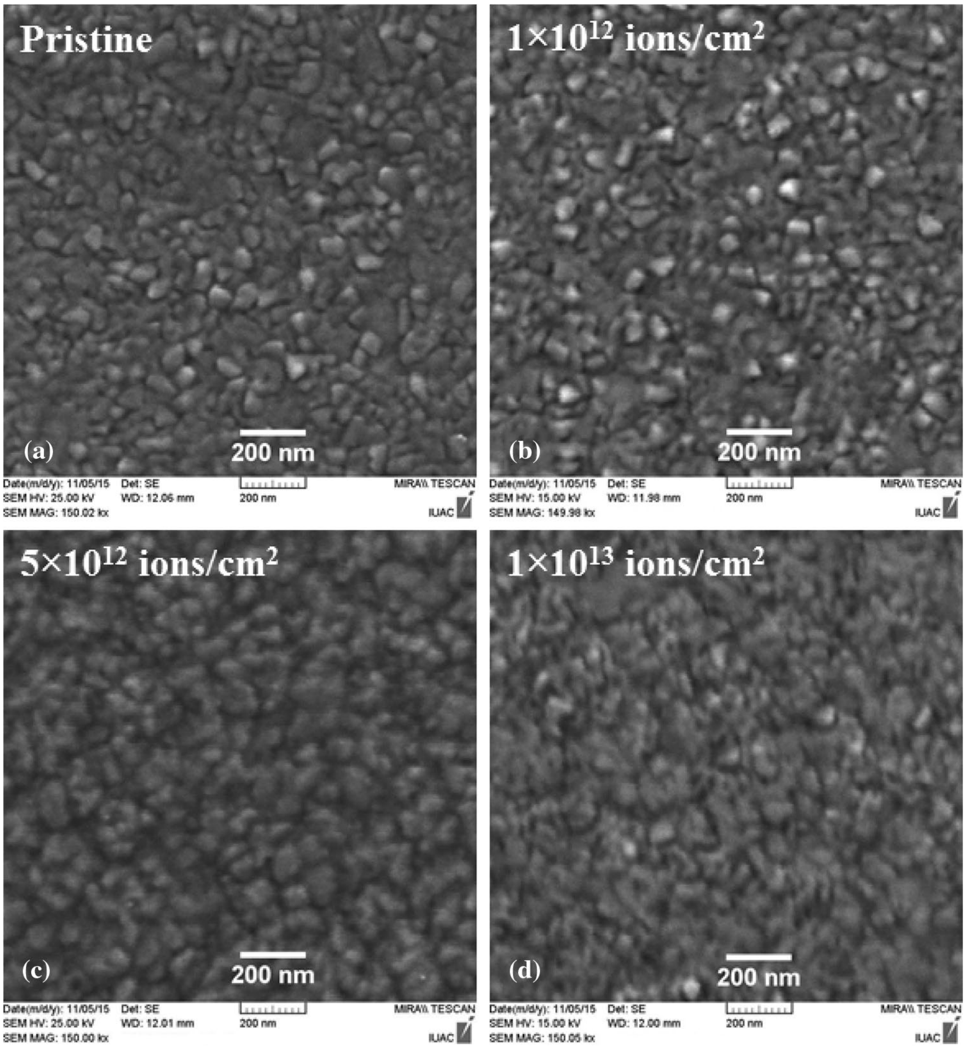

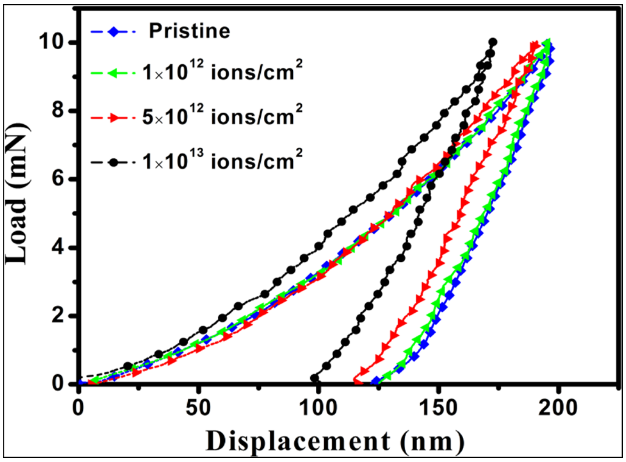

Fig. 7 Load versus depth profile of pristine and 100 MeV Ag^{7+} ion irradiated Ni–Ti films at different fluences

to test, indicating the homogeneous surface of the films over the area tested. The E_{eff} is a significant parameter of materials related to stiffness: the larger the value of E_{eff}, the stiffer the material. Furthermore, the H/E_{eff} is also an important parameter to differentiate in elastic and elastic–plastic nature of the materials. The higher value of H/E_{eff} shows higher elastic nature of material or higher resistance to plastic deformation, while the lower value of H/E_{eff} corresponds to its elastic–plastic behavior [52].

The Young modulus is calculated using the following relation:

$$E_{\text{eff}} = \frac{\sqrt{\pi}}{2}\frac{S}{\sqrt{A}},$$

where S is unloading stiffness at maximum load ($S = \frac{\mathrm{d}P}{\mathrm{d}h}$) and A is the projected contact area. The Young modulus of the material is related to the modulus of elasticity by the following relation:

Table 1 Comparison of hardness and Young modulus values of pristine and irradiated Ni–Ti thin films

Fluence (ions/cm^2)	Hardness H (GPa)	Young modulus E_{eff} (GPa)	H/E_{eff}	Average H (GPa)	Average E_{eff} (GPa)	Average (H/E_{eff})
Pristine	11.11	172.5	0.064	11.62 ± 1.07	172.62 ± 1.04	0.067 ± 0.005
	12.86	173.73	0.074			
	10.89	171.65	0.063			
1×10^{12}	11.47	171.36	0.066	12.81 ± 1.18	171.83 ± 3.32	0.074 ± 0.007
	13.71	168.77	0.081			
	13.24	175.37	0.075			
5×10^{12}	13.89	183.37	0.075	13.58 ± 0.27	181.81 ± 1.61	0.074 ± 0.001
	13.48	180.15	0.074			
	13.38	181.93	0.073			
1×10^{13}	14.89	176.94	0.084	16.12 ± 1.64	176.93 ± 1.96	0.090 ± 0.008
	17.99	178.90	0.100			
	15.48	174.97	0.88			

$$\frac{1}{E_{\mathrm{eff}}} = \frac{(1-\nu_{\mathrm{i}}^2)}{E_{\mathrm{i}}} + \frac{(1-\nu_{\mathrm{s}}^2)}{E_{\mathrm{S}}},$$

where subscript i represents the indenter material, subscript s corresponds to sample material, and ν is the Poisson's ratio. The hardness (H) of the deposited material is calculated by the following equation:

$$H = \frac{P_{\mathrm{max}}}{A},$$

where P_{max} is the maximum indenter load and A is the projected contact area at that load. Figure 8a, b shows the variation of hardness and Young modulus values for pristine and for the film irradiated at different fluences ranging from 1×10^{12} to 1×10^{13} ions/cm^2. From the figure, it depicts that hardness of Ni–Ti films is increase with the increase in ion fluence and the film irradiated at a fluence of 1×10^{13} ions/cm^2 shows the higher hardness value. The improvement in hardness of Ni–Ti films at different fluences is attributed to the formation of lattice disorder and the associated change in crystal structure. It is also reported that hardness of the metallic thin films increases vividly when the thickness of the deposited material falls below ~ 300 nm; and the hall Petch relation, obeyed by thin films, is also dependent on film thickness [53]. The formation of defects such as precipitation, dislocation, and irradiation-induced phase in material up to a certain limit contributes to increasing the resistivity and barrier strength. However, these treatments suppress the martensite transformation temperature by changing the internal stress and chemical composition of the Ni–Ti matrix [19, 54]. The hardness of pristine film is 11.62 ± 1.07 GPa and for the films irradiated at different fluences is found to be 12.81 ± 1.18, 13.58 ± 0.27, and 16.12 ± 1.64 GPa, respectively, as reported in Table 1. The Young modulus of the pristine film is 172.62 ± 1.04 GPa and for the films irradiated at different fluences are 171.83 ± 3.32, 181.81 ± 1.61, and 176.93 ± 1.96 GPa, respectively. The H/E_{eff} ratio is an important parameter to measure the material elastic and elastic–plastic behaviors. The higher value of H/E$_{\mathrm{eff}}$ ratio shows the excellent wear resistance and better films quality, while a lower value of H/E$_{\mathrm{eff}}$ reveals the large fraction of work is consumed in plastic deformation, and large strain energy is required while contacting a material [22]. A higher (H/

Fig. 8 Variation of hardness (**a**) and elastic modulus (**b**) of pristine and irradiated Ni–Ti films at different fluences of 100 MeV Ag^{7+} ions

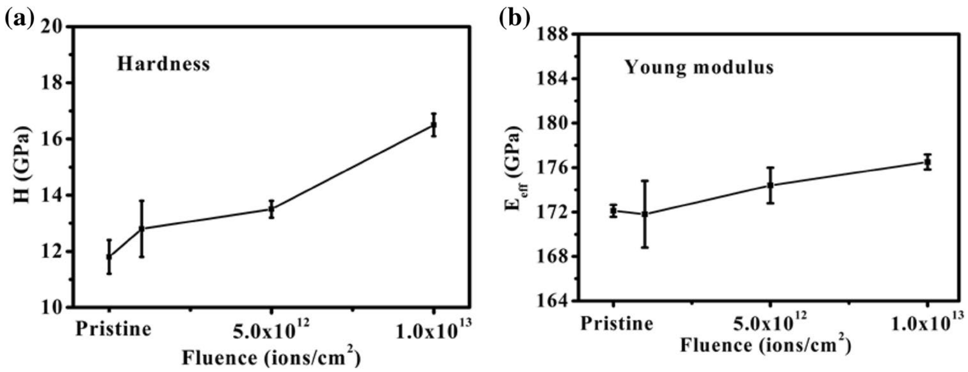

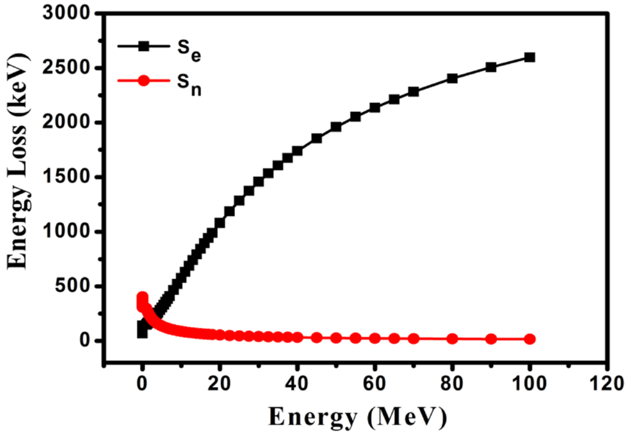

Fig. 9 SRIM simulation of nuclear (S_n) and electronic stopping (S_e) power versus energy for Ag^{7+} ions in Ni–Ti matrix

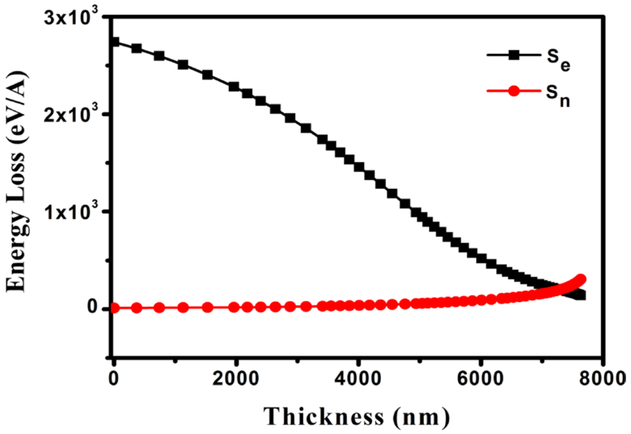

Fig. 10 SRIM simulation, the variation of electronic (S_e), and nuclear energy (S_n) loss of 100 MeV Ag^{7+} ions with thickness in Ni–Ti matrix

E_{eff}) value (0.090 ± 0.008) is obtained for the film irradiated at a fluence 1×10^{13} ions /cm^2. The higher value of H/E_{eff} shows the better wear resistance and small strain energy for deformation.

Figure 9 shows the variation of electronic (S_e) and nuclear stopping (S_n) power versus energy for 100 MeV Ag^{7+} ions calculated by SRIM program in Ni–Ti matrix. The strength of interaction between incident ions and target atom depends on charge, mass, and energy of the incident ions. The energy deposited by bombardment of ions can modify the structural and phase transformation properties of films. The electronic excitation and ionization of materials by SHI irradiation causes the significant displacement of atoms. When energetic ions pass through the Ni–Ti films, loses their energy via two independent processes; (a) nuclear stopping (S_n) loss: incident ions transfer energy to the target lattice by elastic collision and cause significant atomic displacements, which further results in creation of Frenkel defects (vacancies or interstitial), (b) electronic stopping (S_e) loss: incident ions transfer energy to the electrons of target atoms by inelastic collision known as electronic stopping loss. In the high-energy region (energy range of the order of ~ MeV), electronic stopping dominates over nuclear stopping and modifications are mainly due to the electronic stopping. In the present study, Ag ions are chosen due to its higher mass and energy regime. Figure 10 shows the variation of S_e and S_n with projected depth of ~ 800 nm at 100 MeV for Ag^{7+} ions, which is much larger than ~ 270 nm, and the film thickness of Ni–Ti films. Therefore, the effect of electronic stopping power on structural and mechanical properties of Ni–Ti films is anticipated to be uniform irradiation.

4 Conclusions

In the present study, effects of 100 MeV Ag^{7+} ion irradiation on structural, morphology, and mechanical behavior of Ni–Ti thin films have been investigated. XRD measurement reveals the change in crystal structure after irradiation and formation of buried Ni_3Ti precipitate phases at a fluence of 1×10^{13} ions/cm^2. XRD measurement also evidences that irradiation of Ni–Ti film at a higher fluence suppresses the austenite and martensite phase by introducing an intermediate Ni_3Ti precipitation phase. AFM and FESEM measurements show the change in surface morphology with fluence. The Ni–Ti films surface roughness increases with increase in ion fluence, which may be due to the ion irradiation-induced sputtering effects as confirmed by AFM. Nanoindentation measurement reveals that hardness and Young modulus of Ni–Ti thin films are improved as the ion fluences increases. The obtained results demonstrate that the ion irradiation of Ni–Ti films by 100 MeV Ag^{7+} ions leads to the formation of nickel enrich hard precipitate phase. Formation of precipitation phase reduces Ni concentration in the surface which contributes to potential mechanical applications.

Acknowledgements V. Kumar is very much thankful to Technical Education Quality Improvement Program (TEQUIP), MNIT Jaipur for the Ph.D. scholarship. R. Singhal acknowledges the financial supports provided by Department of Science & Technology, New Delhi in terms of DST FAST Young Scientist project (SR/FTP/PS-081/2011). The author would like to acknowledge Mr. Sunil Ojha and Mr. S.A. Khan from IUAC, New Delhi for their help and support in RBS and FESEM characterizations. The author is also acknowledging UGC-DAE CSR Indore, for synthesis and characterization of Ni–Ti thin films. The crew of pelletron accelerator IUAC, New Delhi is also highly acknowledged for providing the stable beam of 100 MeV Ag ions.

References

1. Y. Fu, W. Huang, H. Du, X. Huang, J. Tan, X. Gao, Surf. Coat. Technol. **145**, 107–112 (2001)
2. S. Miyazaki, A. Ishida, Mater. Sci. Eng. A **273–275**, 106–133 (1999)
3. K.T. Oh, U.H. Joo, G.H. Park, C.J. Hwang, K.N. Kim, J. Biomed. Mater. Res. B Appl. Biomater. **76**(2), 306–314 (2006)
4. J.H. Sui, W. Cai, Appl. Surf. Sci. **253**, 2050–2055 (2006)
5. K. Otsuka, T. Kakeshita, MRS Bull. **27**, 91–100 (2002)
6. K. Otsuka, X. Ren, Intermetallics **7**, 511–528 (1999)
7. M.M. Silva, L. Pichon, M. Drouet, J. Otubo, Surf. Coat. Technol. **211**, 209–212 (2012)
8. P. Krulevitch, P.B. Ramsey, D.M. Makowiecki, A.P. Lee, M.A. Northrup, G.C. Johnson, Thin Solid Films **274**, 101–105 (1996)
9. V. Kumar, R. Singhal, R. Vishnoi, M.K. Banerjee, M.C. Sharma, K. Asokan, M. Kumar, Radiat Eff. Defects Solids **172**, 629–642 (2017)
10. H. Richard, H.A. Wolf, J. Microelectromech. Syst. **4**, 206–212 (1995)
11. Y.Q. Fu, J.K. Luo, A.J. Flewitt, Inter. J. Nanomanufacturing **2**, 208–225 (2009)
12. Y. Fu, H. Du, W. Huang, S. Zhang, M. Hu, Sens. Actuators, A **112**, 395–408 (2004)
13. S.K. Wu, H.C. Lin, C.Y. Lee, Surf. Coat. Technol. **113**, 13–16 (1999)
14. F.M. El-Hossary, S.M. Khalil, M.A. Kassem, M.A. Lateef, K. Lotfy, JBAP **3**, (2014) 54–67
15. R.G. Vitchev, H. Kumar, B. Blanpain, J.V. Humbeeck, Biomaterials **23**, 4863–4871 (2002)
16. H.C. Man, Z.D. Cui, T.M. Yue, Scripta Mater. **45**, 1447–1453 (2001)
17. X.T. Zu, L.B. Lin, Z.G. Wang, S. Zhu, L.P. You, L.M. Wang, Y. Huo J. Alloys Compd. **351**, 87–90 (2003)
18. N. Afzal, I.M. Ghauri, F.E. Mubarik, F. Amin, Phys. B **406**, 8–11 (2011)
19. H. Pelletier, D. Muller, P. Mille, J.J. Grob, Surf. Coat. Technol. **158–159**, 301–308 (2002)
20. S.K. Wu, C.L. Chu, H.C. Lin, Surf. Coat. Technol. **92**, 197–205 (1997)
21. H.C. Lin, H.M. Liao, J.L. He, K.M. Lin, K.C. Chen, Surf. Coat. Technol. **92**, 178 (1997)
22. Y. Quinn, R.T. Kraft, R.W. Hertzberg, R.W. Trans Am. Soc. Metals **62**, 38–44 (1969)
23. T. Lagrange, C. Abromeit, R. Gotthardt, Mater. Sci. Eng. A **438–440**, 521–526 (2006)
24. Q.Z. An, K. Feng, H. Lu, X. Cai, T. Sun, P.K. Chu, Trans. Nonferrous Met. Soc. China **25**, 1944–1949 (2015)
25. Y. Nunomura, H. Kaneno, T. Tsuda, Takasugi, Intermetallics **12**, 389–399 (2004)
26. B. Naveen Kumar, N.K. Reddy, Udayashankar, Surf. Interfaces **5**, 62–71 (2016)
27. C. Chluba, W. Ge, R.L. Miranda, J. Strobel, L. Kienle, E. Quandt, M. Wuttig, Science **348**, 1004–1007 (2015)
28. A. Ishida, A. Takei, M. Sato, S. Miyazaki, Thin Solid Films **281–282**, 337–339 (1996)
29. D.J. Hart, J.T. Mooney, D.C. Lagoudas, F.T. Calkins, J.H. Mabe, Smart Mater. Struct. **19**, 01502 (2009)
30. Y. Nunomura, Y. Kaneno, H. Tsuda, T. Takasugi, Intermetallics **12**, 389–399 (2004)
31. T. Lagrange, R. Schaublin, D.S. .Grummon, C. Abromeit, R. Gotthardt, Philos. Mag. **85**, 577–587 (2005)
32. F.F. Gong, H.M. Shen, Y.N. Wang Mater. Lett. **25**, 13–16 (1995)
33. D.K. Avasthi, G.K. Mehta, swift heavy ions for materials engineering and nanostructuring. Springer Series in Materials Science, **145** (2011)
34. R. Kumar, S.B. Samanta, S.K. Arora, A. Gupta, D. Kanjilal, R. Pinto, A.V. Narlikar, Solid-State Commun. **12**, 805–810 (1998)
35. F. Studer, M. Toulemonde, Nucl. Instr. and Meth. B **65**, 560–567 (1992)
36. A. Barbu, A.H. Dunlop, G. Duparc, N. Jaskierowicz, Lorenzelli, Nucl. Instrum. Methods Phys. Res., Sect. B **145**, 354–372 (1998)
37. L. Shijie Hao, J. Cui, F. Jiang, X. Guo, D. Xiao, C. Jiang, Yu,. Brown, Zonghai Chen, Hua Zhou, Yandong Wang, YuZi Liu, Dennis E. Yang Ren, Sci. Rep. **4**, 1–6 (2014)
38. P. Luo, S.N. Wang, T.T. Zhao, Y. Li, Rare Met. **32**(2), 113–121 (2013)
39. R. Vishnoi, R. Singhal, K. Asokan, J.C. Pivin, D. Kanjilal, D. Kaur, Vacuum **89**, 190–196 (2013)
40. V. Kumar, R. Singhal, R. Vishnoi, M. Gupta, P. Sharma, M.K. Banerjee, K. Asokan, H. Sharma, A. Gupta, D. Kanjilal, Adv. Mat. Lett. **8**(4), 486–492 (2017)
41. J.F. Ziegler, J.P. Biersack, V. Littmark, The stopping and range of ions in solids. (Pergamon, New York, 1985)
42. W.O. Adeoya, M.H. Ali, J.C. Muller, P. Siffert, Appl. Phys. Lett. **50**, 1736–1738 (1987)
43. G. Shugar, J. Ballinger, Chemical Technician′ Ready reference handbook. (McGraw-Hill, New York, 1996)
44. H.P. Klug, L.E. Alexander, X-ray diffraction procedures for polycrystalline and amorphous materials. (Wiley, New York, 1974)
45. R. Singhal, D. Kabiraj, P.K. Kulriya, J.C. Pivin, R. Chandra, D.K. Avasthi, Plasmonic **8**(2), 295–305 (2013)
46. H.S. Zhang, J.L. Endrino, A. Anders, Appl. Surf. Sci. **255**, 2551–2556 (2008)
47. H. Pelletiera, D. Mullerb, P. Millea, J.J. Grob, Surf. Coat. Technol **158–159**, 301–308 (2002)
48. R. Singhal, R. Vishnoi, K. Asokan, D. Kanjilal, D. Kaur, Vacuum **89**, 215–219 (2013)
49. R. Vishnoi, R. Singhal, K. Asokan, D. Kanjilal, D. Kaur, Thin Solid Films **520**, 1631–1637 (2011)
50. M. Silva, L. Pichon, M. Drouet, J. Otubo, Surf. Coat. Technol. **211**, 209–212 (2012)
51. W.C. Oliver, G.M. Pharr, J. Mater. Res. **7**, 1564–1583 (1992)
52. H. Conrad, J. Narayan, K. Jung, Int. J. Refract. Met. Hard Mater. **23**, 301–305 (2005)
53. T.W. Duerig, K.N. Melton, D. Stockel, C.M. Wayman, S.M. Fisher, Engineering aspects of shape memory alloys (Elsevier, 1990)
54. H.J. Lee, H. Ni, D.T. Wu, A.G. Ramirez, Mater. Trans. **47**(3), 527–531 (2006)

Physica B: Condensed Matter 546 (2018) 80–88

Contents lists available at ScienceDirect

Physica B: Condensed Matter

journal homepage: www.elsevier.com/locate/physb

Impact of SHI on structural and mechanical behavior of intermetallic NiTi thin films

V. Kumar*, R. Singhal

Department of Physics, Malaviya National Institute of Technology Jaipur, JLN Marg, Malviya Nagar, Jaipur 302017, India

ARTICLE INFO

Keywords:
SMA
SHI irradiation
Electronic excitation
Nanoindentation

ABSTRACT

In the present investigation, nanocrystalline thin films of NiTi are grown on Si substrate by dc-magnetron co-sputtering using Ni and Ti sputtering targets. These as- grown NiTi thin films are irradiated by 90 MeV Ni ions with fluences 1×10^{12}, 3×10^{12}, 9×10^{12} and 1×10^{13} ions/cm^2, respectively. The elemental composition and depth profile of the pristine film are analyzed by Rutherford backscattering spectrometry. Further, structural, surface morphology and mechanical properties of these films are investigated by X-ray diffraction (XRD), atomic force microscopy (AFM) and nanoindentation techniques, respectively. X-ray diffraction result shows the presence of both austenite and martensite phases in the pristine film with the preferred growth of (110) orientation. The crystallite size is decreased with increase in the ion fluence as compared to pristine film. The AFM images confirm the variation in surface roughness values with the change in the incident ion fluence. The nanoindentation investigation has revealed the enhancement in the mechanical behavior of the NiTi films with ion fluences. The irradiated NiTi film at a fluence of 3×10^{12} ions/cm^2 exhibits higher hardness, elastic modulus and depth recovery ratio and therefore better wear-resistance as compared to other films. This result of nanoindentation indicates the higher ductility of NiTi film in comparison of pristine film and their applicability for Micro-electromechanically system applications (MEMS).

1. Introduction

In the present scenario, the demand for micromachines has increased significantly in various fields such as biomedical, aerospace, biotechnology, industries and various micro-electro-mechanical systems (MEMS) applications [1–3]. Thin films of NiTi have attracted significant research interest due to their excellent biocompatibility and mechanical properties. It is reported that NiTi thin films exhibit superelasticity and shape memory effect that are comparable to the bulk counterpart [4]. The physical origins of these two effects are due to the martensitic transformation between high symmetrical austenite (B_2) and low symmetrical or stress-induced martensite phases (B19′). The appropriate level of biocompatibility and high work output per unit volume of NiTi SMA make it suitable for MEMS-based biomedical and micro-actuators devices fabrication [5–7].

The growth of high purity, quality and stoichiometry NiTi thin film and modification of their properties under swift heavy ion (SHI) irradiation are of immense technological importance for MEMS applications [8,9]. The SHI irradiation technique has attracted the attention of research community for tuning the materials properties, which would be a rapid advancement in the field of materials science [10,11]. At present scenario, ion beam technology is a versatile technology for the development of miniaturized devices which require basic and fundamental understanding about the interaction between ions and matter [12–14]. The deposition of localized energy density into a specified volume is the main advantage of SHI irradiation over thermal equilibrium process [15]. Furthermore, the study of the interaction between ions and matter establishes an interdisciplinary connection between condensed and atomic physics.

As the beam of energetic ions passes through the material, it loses its energy into the material and significantly modifies the material properties. The modifications in material properties depend upon the energy deposited into the material by swift heavy ions; therefore a desired modification in material property could be achieved by choosing the particular beam and fluence, which is not possible by using any other technique [16,17]. The effects of different types of perturbations such as electron, proton, and ion irradiation on microstructure, phase transformation behavior and mechanical properties of bulk NiTi alloy have been reported in literature [18–20], But the investigation of surface characteristic and mechanical behavior of NiTi thin films irradiated with 90 MeV Ni ion irradiation are not adequate and needs to be investigated in detail.

---

* Corresponding author.
E-mail address: vks8361@gmail.com (V. Kumar).

https://doi.org/10.1016/j.physb.2018.07.029
Received 14 May 2018; Received in revised form 25 July 2018; Accepted 26 July 2018

In the present experiment the effect of SHI irradiation on the structural, topographical and mechanical property of NiTi thin films have been investigated. The SHI irradiation has demonstrated the enhancement of the various properties of nanocrystalline NiTi thin films up to certain fluences and decrements in the properties above that fluence. The variations in structural and mechanical properties at higher fluence are attributed to the grain boundary sliding by imparted of the SHI irradiation on the NiTi thin film, which is explained in detail. This study is also important to use NiTi SMA in a harsh space environment, as in the case of the device designed; the superior tribological and mechanical properties are required [21].

2. Experimental details

In present study, all the thin films of intermetallic NiTi alloy have been deposited by dc-magnetron co-sputtering technique on Si substrate in one deposition. The two separate high purity Ni (99.99%) and Ti (99.99%) targets (Neyco supplier, France) of 3 mm thick and 2-inch diameter have been used for films deposition. A base pressure of 2×10^{-7} torr has been achieved before deposition inside the vacuum chamber by using a rotary and turbo molecular pumps. The deposition has been performed under a pressure of 3×10^{-3} torr using a dynamic throttling valve. Before films deposition, the Si substrate has been cleaned in a mixture of Trichloroethylene and di-water in an ultrasonic bath and then cleaned with the boiled acetone. Further, the films deposition has been performed for 1 h 40 min by two different powers; 100 W for Ti and 50 W for Ni targets, respectively. The deposition of the films has been carried out in argon (~99.9%) atmosphere at the substrate temperature of 550 °C by an AJA Int. make ATC Orion-8 series sputtering system. After deposition, all the deposited thin films have been naturally cooled to room temperature by water cooling arrangement inbuilt to the sputtering system. The distance between the substrate and target holder is kept ~16 cm to get the uniform deposition.

The prepared NiTi thin films have been irradiated at Inter-University Accelerator Centre (IUAC), New Delhi at the room temperature with 90 MeV Ni ions at different fluences of 1×10^{12}, 3×10^{12}, 9×10^{12} and 1×10^{13} ions/cm^2 by 15 UD Tandem Accelerator. During irradiation, a high vacuum (6×10^{-7} torr) is maintained inside the irradiation chamber. The ion beam is focussed on the spot size 1×1 cm^2 over the film area using a magnetic scanner (raster scanning 1×1 cm^2). During the irradiation experiment, the beam current is kept ~2 pnA (particle nanoampere) and the charge state of the Ni ion is found 7+. The final energy of the ions coming out of the accelerator after the switching magnet can be calculated by following equation;

$$E = [E_{deck} + (1 + q)V_T]$$

where q is the charge state of ions after stripping, V_T is terminal potential in MV, and E_{deck} is the deck potential of MC-SNICS source. The electronic energy (S_e) and nuclear energy loss (S_n) have been calculated by the SRIM-2008 code and found to be 1.7×10^3 eV/Å, 0.003×10^3 eV/Å, correspondingly [22]. Furthermore, the range of 90 MeV Ni ions beam has also been calculated by SRIM 2008 computer code in NiTi matrix (density = 7.013 gm/cm^3) and determined as 8.23 μm. The calculated value of S_e is too high than that of S_n; therefore, modifications are mainly attributed due to S_e effect. The values of the fluences have been decided by measuring the charge arising on the film surface under the secondary electron suppressed geometry.

The composition of elements and depth profile of the pristine film have been estimated by Rutherford backscattering spectrometry (RBS). The room temperature crystal structure or phase of pristine and films irradiated at different fluences have been carried out by the Bruker D8 Advance X-ray diffractometer (XRD). The XRD characterization has been performed with a Cu K_α radiation of wavelength ($\lambda = 1.54$ Å) with a scan rate of 0.6°/minute at UGC-DAE-CSR Indore. Furthermore, surface features of the pristine and irradiated thin films have been characterized by atomic force microscopy (AFM) (Bruker Nanoscope V system) in tapping mode with a Si_3N_4 cantilever. The mechanical properties of the pristine and the irradiated NiTi thin films have been analyzed by nanoindentation tester equipped (CSM Instrument) with a diamond Berkovich Type indenter tip. Nanoindentation test has been performed on three different positions of the films surface to calculate the average hardness and elastic modulus values. Every nanoindentation test consisted of 8-sec linear loading segment to a peak load and 10-sec holding and again 8-sec linear unloading segments. Mostly the holding period has used to diminish the time-dependent effects (creep effects) caused by the specimen. All these characterizations have been done at room temperature before and after irradiation.

3. Results and discussion

3.1. Rutherford backscattering spectrometry

RBS is a non-destructive technique and it gives the precise estimation of the composition and thickness of the deposited film. The NiTi alloy thin film is very sensitive to the elemental composition and the composition uniformity over the surface. The phase transformation behavior and mechanical strength of the NiTi alloy also depend upon the elemental composition. A small variation in composition (0.1 at.%) could cause a shift in transformation temperature by around 10 °C; consequence shape memory effect occurred below or above room temperature [23]. The superelasticity behavior is also affected by the elemental composition of films. Therefore, the fabrication of the desired composition in the thin film and also the exact determination of the elemental composition of the films are very essential. Fig. 1(a)-(b) represents the simulated RBS spectrum and depth profile for the pristine film deposited on Si substrate at 550 °C. To obtain the film thickness and elemental composition present in the pristine film, the RBS data has been simulated by the SIMNRA software and the fitting of data is shown in Fig. 1(a) [24]. The simulated concentration of the Ti is found to ~43.3 at.% and the concentration of the Ni is found to be ~56.7 at.%. The estimated film thickness is found to be ~270 nm, respectively. Furthermore, Fig. 1(b) shows the graph of the atomic concentration of Ni and Ti versus depth of the film. This Fig. shows the uniform distribution of elements (Ni and Ti) content through the films thickness. A significant diffusion of NiTi into Si substrate (~39 nm) is also observed after the deposition. This diffusion possibly may be due to higher temperature deposition of Ni and Ti.

3.2. X-ray diffraction

Fig. 2 represents the room temperature X-ray diffraction pattern plotted for pristine and the irradiated NiTi thin films. The pristine and irradiated NiTi films represent the several diffraction peaks which indicate the polycrystalline nature of the films. The XRD pattern exhibits two major peaks corresponding to NiTi, in pristine and also in the films irradiated at different fluences. The XRD pattern of the pristine film deposited at 550 °C shows two sharp peaks corresponding to austenite and martensite phase. The XRD patterned of pristine film exhibits the austenite peak located at 2θ = 42.5° (JCPDS file no. 65-5537) corresponding to cubic (110) plane, and martensite peak at 43.9° (JCPDS file no. 77-2170) corresponding to monoclinic (002) plane, respectively. The presence of martensite phase at room temperature in the pristine film could be due to higher bi-axial stress. This type of behavior of martensite phase consistent with the data reported by Martins et al. [25]. The growth of austenite phase corresponding (110) plane in the pristine film could be due to the migration of atoms toward plane with lesser surface energy: here body-centered cubic crystal structure (bcc) which have minimum surface energy along the (110) plane. Due to the minimum surface energy, (110) plane should be favourable in bcc structures [26].

The NiTi thin film irradiated at fluences of 1×10^{12} ions/cm^2 shows

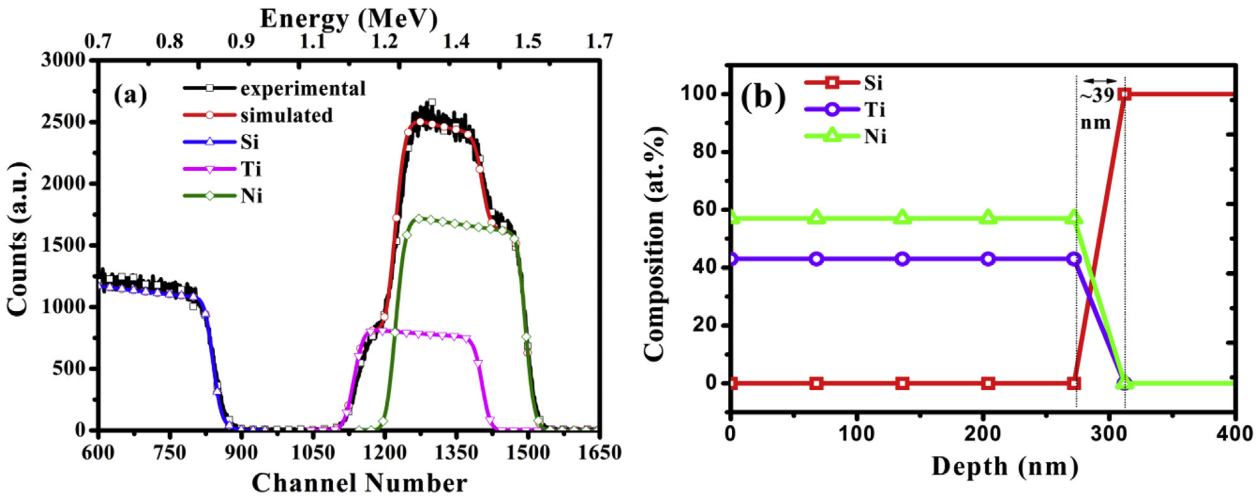

Fig. 1. RBS spectra along with SIMNRA simulation of NiTi pristine film deposited on Si substrate (a) and depth profile (b) performed by using 2 MeV He^{2+} ions.

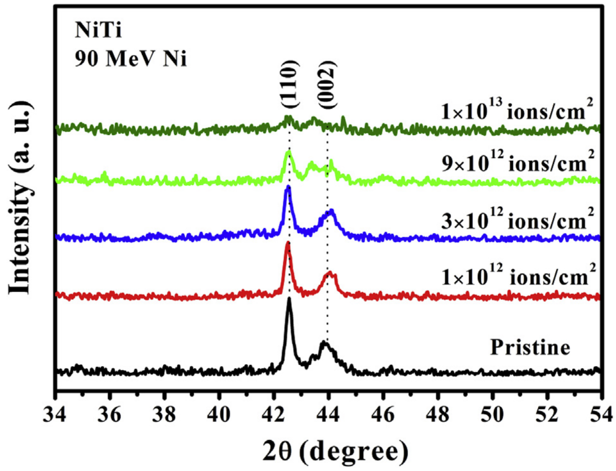

Fig. 2. XRD pattern of the pristine and 90 MeV Ni ions irradiated NiTi thin films.

the decrease in peak intensity of both austenite and martensite peaks correspond to (110) and (200) planes. Further increase in the fluence to 3×10^{12} ions/cm^2, the intensity of the austenite peak is decreasing and the peak corresponding to (200) plane became broad. The boarding of the (200) plane shows the less stability of the martensite phase against the SHI irradiation. This peak broadening also shows the partial amorphization of martensite phase at this fluence. With further increase in fluence to 9×10^{12} ions/cm^2, the intensity of both the phases decreases considerably. At the much higher fluence of 1×10^{13} ions/cm^2, decrease in the intensity of both peaks related to austenite and martensite phases shows the partial amorphization of both the phases. The decrease in crystallinity for both phases depends upon the amount of energy deposited by SHI irradiation in NiTi films by Ni ions. When the energetic ion is passing through the NiTi films, it produced ionization and excitation of alloy atoms, and it leads to modification in structural properties of the material. Such high electronic excitation can also produce local heating followed by rapid quenching (thermal spike) and producing lattice distortions, which are so drastic that the material relaxes into an amorphous state [27].

Furthermore, the average crystallite size (D) of the NiTi pristine and films irradiated at different fluences has been calculated from line broadening of the XRD lines, corresponding to austenite (110) plane after removing the instrumental broadening by using the Debye-Scherrer's formula [28];

$$D = \frac{K\lambda}{\beta \cos\theta} \tag{1}$$

where D = crystallite size, K = shape factor (0.9), β = integral half width, λ and θ are the wavelength of Cu-K$_\alpha$ (λ = 0.154 nm) radiation, and Bragg angle, respectively.

The calculated crystallite size (D) values for the pristine is 31.57 ± 1.1 and for the irradiated NiTi thin films at different fluences of 90 MeV Ni ions (1×10^{12}, 3×10^{12}, 9×10^{12} and 1×10^{13} ions/cm^2) are found to be 30.44 ± 1.2 nm, 28.41 ± 1.4 nm, 26.63 ± 1.4 nm and 18.52 ± 1.5 nm respectively and summarized in Table 1.

Furthermore, the strain (ε_{zz}) developed in pristine and irradiated NiTi thin films at different fluences of 90 MeV is calculated for the austenite (110) plane by the given relation [28]:

$$\varepsilon_{zz}(\%) = \frac{(a - a_0)}{a_0} \times 100 \tag{2}$$

where symbol 'a' represents the lattice parameter corresponds to strained NiTi films and 'a_0' represents the lattice parameter of unstrained bulk NiTi alloy. The lattice parameter 'a' of NiTi films have been calculated by the formula given below for cubic crystal structure [28]:

$$\frac{1}{d^2} = \frac{(h^2 + k^2 + l^2)}{a^2} \tag{3}$$

where d represents the interplanar distance calculated for the peak (110) by the Bragg condition, a represents the lattice parameter and h, k, l show the Miller indices.

The calculated values of lattice strain are observed to increase with an increase in the ion fluence as shown in Fig. 3. For the pristine thin

Table 1
Microstructural parameters of pristine and the films irradiated at different fluences of 90 MeV Ni ions.

Fluence (ions/cm^2)	2θ (degree)	FWHM (degree)	Crystallite size (D) (nm) along (110) peak	Lattice strain (ε)% along (110) peak	Dislocation density (δ) × (10^{15} line/m^2)
Pristine	42.56	0.27	31.57 ± 1.1	0.30	1.00
1×10^{12}	42.51	0.28	30.44 ± 1.2	0.31	1.07
3×10^{12}	42.52	0.30	28.41 ± 1.4	0.33	1.23
9×10^{12}	42.54	0.32	26.63 ± 1.4	0.36	1.41
1×10^{13}	42.52	0.46	18.52 ± 1.5	0.52	2.91

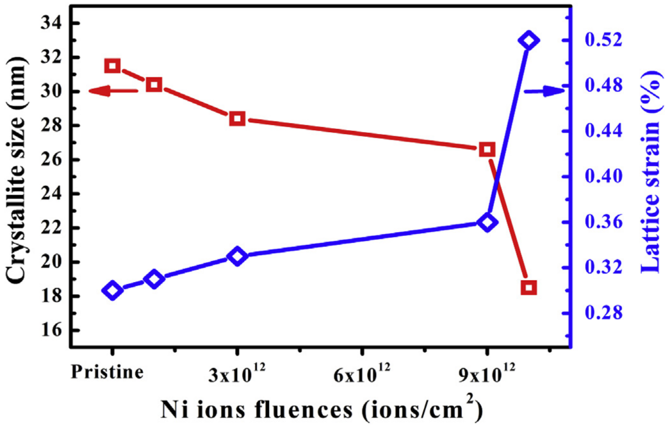

Fig. 3. Variation of crystallite size and lattice strain with fluences for the pristine and the films irradiated at different fluences of 90 MeV Ni ions.

film, the calculated strain value is 0.30 and for the films irradiated at different fluences 1×10^{12}, 3×10^{12}, 9×10^{12}, 1×10^{13} ions/cm^2 are found to be 0.31, 0.33 and 0.36 and 0.52 respectively as reported in Table 1. The calculated lattice parameters have been found to be smaller than the lattice parameters of bulk NiTi alloy, which suggest a lattice compression in the direction perpendicular to the film plane. This observation shows the compressive in plane stress in the films. The lattice strain values are increased with increase in ion fluence of 90 MeV Ni ion beam. This increasing in lattice strain values could be due to the increase in lattice defect, large number of grain boundaries and decrease of ordering of preferred orientation of NiTi films. The Fig. 3 represents the variation of crystallite size and lattice strain with ion fluences.

The dislocation density (δ) of the pristine and irradiated NiTi films at different fluences has been calculated from the crystallite size (D) using the given relation [29], and values are reported in Table 1:

$$\delta = \frac{1}{D^2}\ \text{lines/m}^2 \tag{4}$$

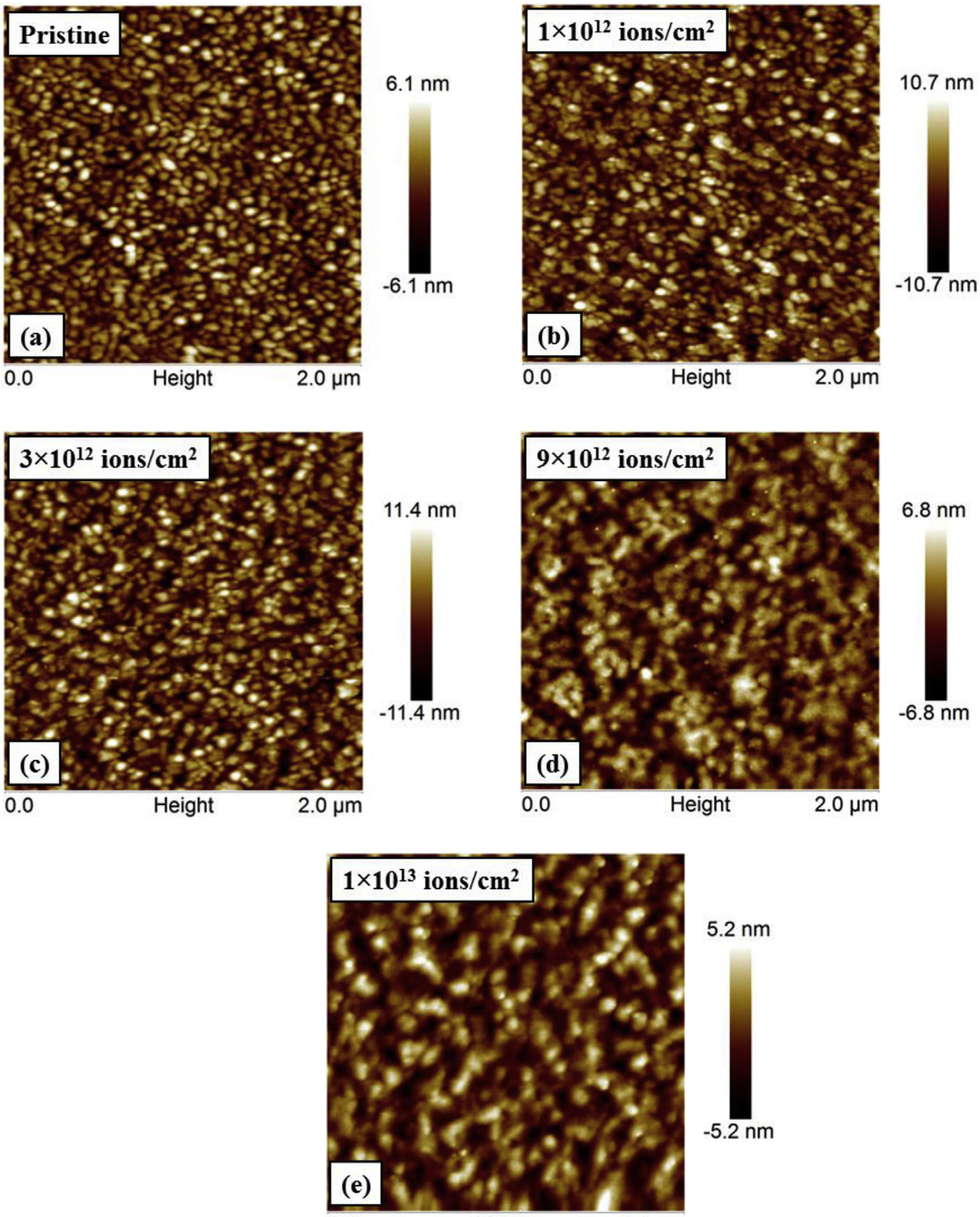

Fig. 4. AFM (2D) surface morphological micrographs over scan $2 \times 2\,\mu\text{m}^2$ areas for the pristine and irradiated NiTi thin films.

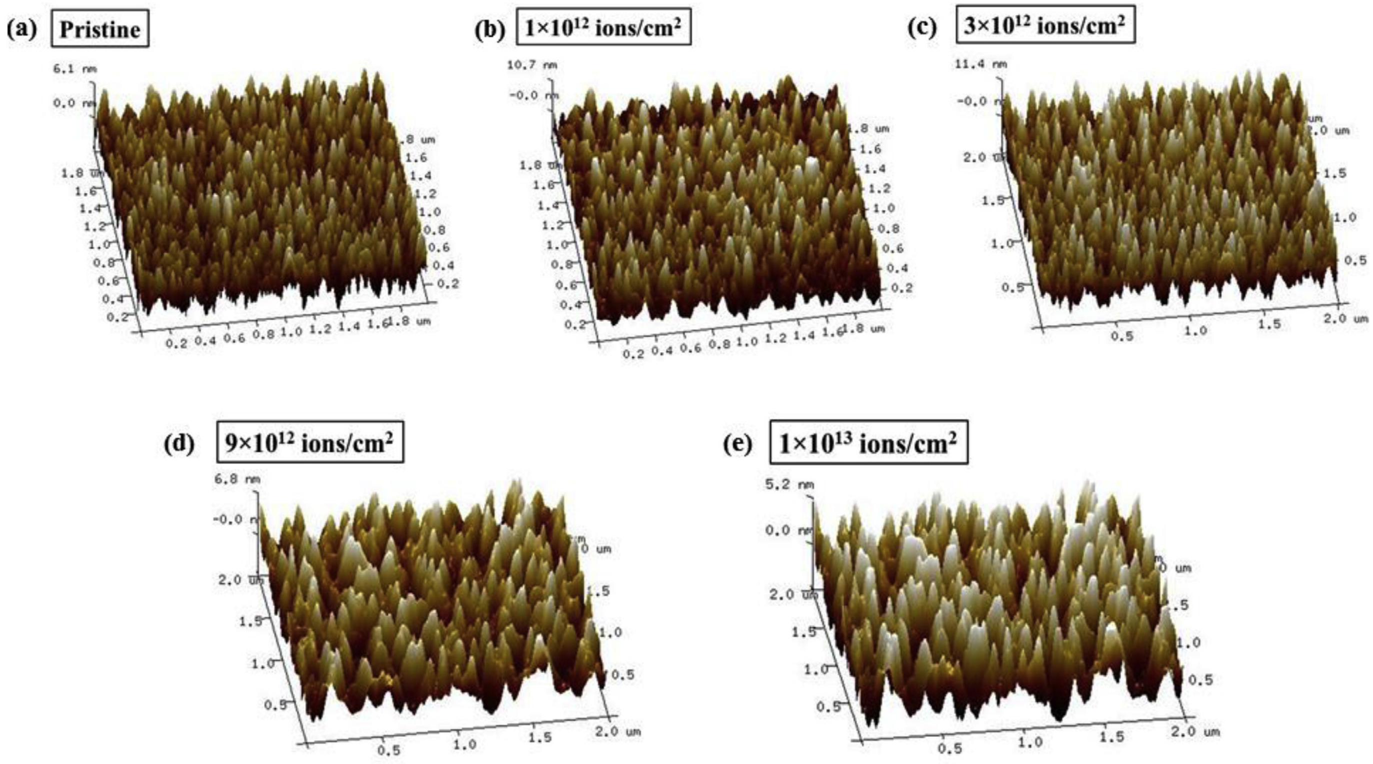

Fig. 5. AFM 3D micrographs of pristine and irradiated NiTi thin films.

The dislocation density is a line defect and it is defined as the length of dislocation per unit volume. The values of dislocation density are increased with increase in ion fluence and it strongly depends upon the amount of defects created by the incident Ni ions.

3.3. Atomic force microscopy

The topographical features of the pristine and irradiated NiTi thin films at different fluences ranging from 1×10^{12} to 1×10^{13} ions/cm^2 have been studied with AFM in tapping mode. Figs. 4(a)–(e) and 5(a)–(e) show two-dimensional and three-dimension representation of AFM micrographs for pristine and irradiated NiTi thin films on the scan area of $2 \times 2\,\mu\text{m}^2$. It is clear that from the AFM micrographs that film have different surface morphology at different fluences. The AFM micrograph of the pristine film (Fig. 4(a)) shows the very dense and fine grains with well define boundary of NiTi film deposited at 550 °C. The film irradiated at fluence of 1×10^{12} ions/cm^2 reveals the change in film morphology with fluence. Further, the film irradiated at 3×10^{12} ions/cm^2 represents the distorted grains on the film surface and crystalline grains are randomly distributed over the film surface. Further, increasing in fluence of 9×10^{12} ions/cm^2, the film shows the featureless grain growth and indicates no sharp grains formation. However, irradiation with 1×10^{13} ions/cm^2 (Fig. 4(d) and 4(e)) amorphous state like topography appeared. However, at this fluence some randomly distributed grains formed by the coalescence of adjacent grains due to the incident electronic energy deposition in NiTi matrix.

The topography features of the NiTi pristine and irradiated films are evaluated using average roughness (R_{avg}) and root-mean-square surface roughness (R_{rms}). The surface roughness of the films are calculated using AFM by scanning the areas of $2 \times 2\,\mu\text{m}^2$, over the film surface at three times each time at different position using the relation [30]:

$$R_{avg} = \left[\frac{1}{N}\sum_{i=1}^{N}|Z_i - \overline{Z}|\right], \tag{5}$$

$$R_{rms} = \left[\frac{1}{N}\sum_{i=1}^{N}|Z_i - \overline{Z}|^2\right]^{1/2} \tag{6}$$

where N represents the number of surface height data, and $\overline{Z}$ represent the mean height distance. The values of R_{avg} and R_{rms} of the films increases with the increase in the ion fluences up to 3×10^{12} ions/cm^2 and the values decrease considerably with an increase in the fluence. The R_{avg} value for the pristine film is ~2.14 and for the films irradiated at different fluences are found to be ~3.77 nm, ~4.31 nm, ~2.52 nm and ~1.75 nm, respectively, while the values of R_{rms} for the pristine and irradiated films are found to be ~1.81 nm, ~2.23 nm, ~3.89 nm, ~1.83 nm and ~1.32 nm respectively. It is observed that the small surface roughness contributed by the shallower depression exhibit smoother film surface and the higher surface roughness is most probably due to the ion irradiation induced sputtering effect [31].

3.4. Nanoindentation

Nanoindentation is a suitable tool to test the mechanical properties, i.e., elastic modulus, hardness and the extension of stress-induced phase transformation. It is employed to measure the penetration depth of an indenter into the film surface along with the applied load and also to measure the values of the area of contact depth and hardness of the materials deposited on the substrate [32,33]. Fig. 6(a)-(e) represents the load versus displacement curves for the pristine and the irradiated NiTi films.

The mechanical properties of NiTi thin films such as hardness and elastic modulus have been calculated using the load versus displacement graph (p-h) and analyzed by the Oliver and Pharr method [34]. Fig. 6(a)–(e) represents the load versus displacement curves for the pristine and irradiated NiTi thin films. The patterns of load versus displacement curves for all the films consistent from test to test, indicate that the surface of all the films is homogeneous over the areas tested. The load versus displacement graphs of all the films show the overall elastic-plastic response [35]. The unloading curves (plastic

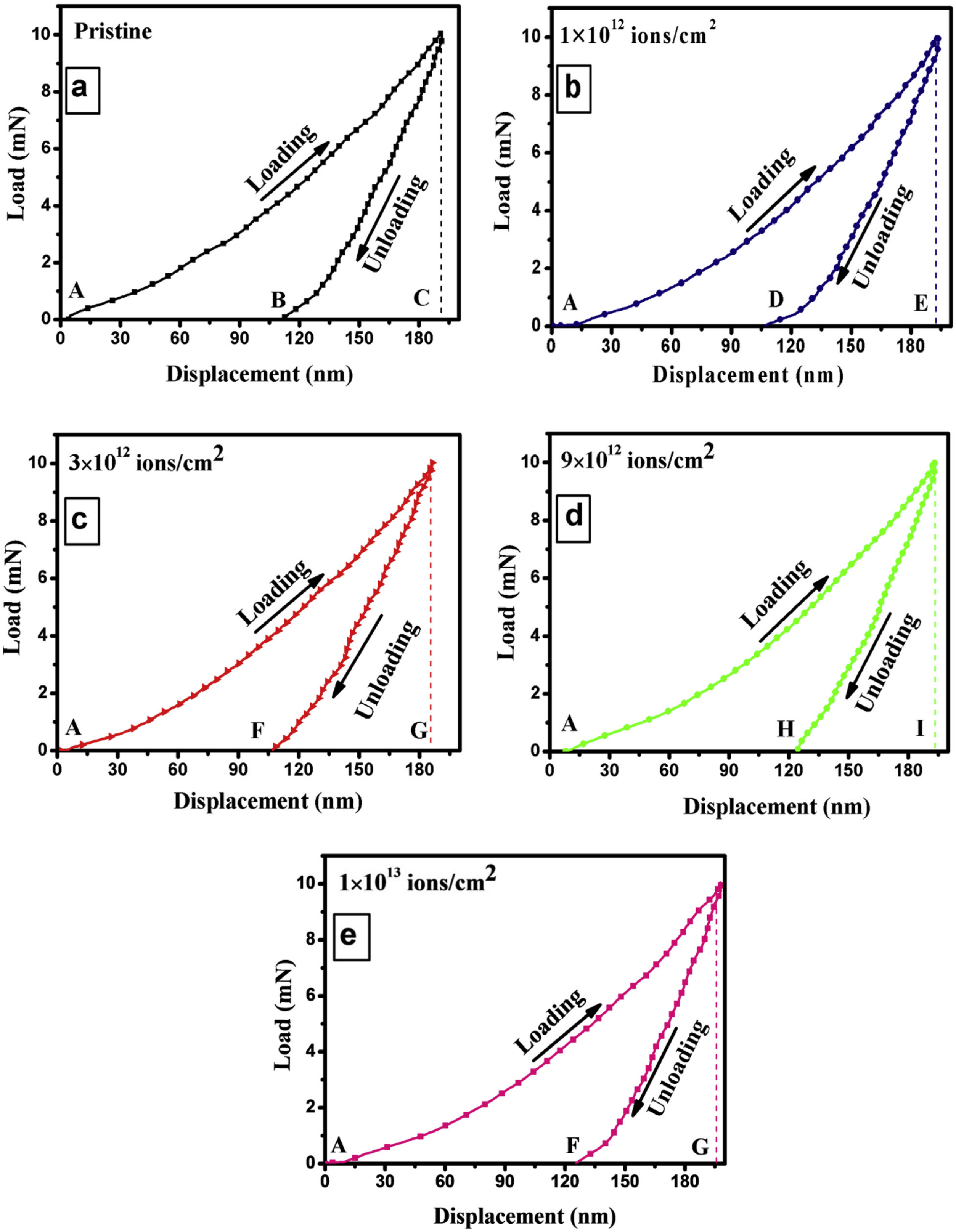

Fig. 6. Load versus displacement curves for pristine and 90 MeV Ni ion irradiated thin films.

response) of all the films are smooth demonstrating that stress of the films is recovery on relaxation during indentation withdraw.

The elastic modulus of the pristine and irradiated NiTi films is calculated by the following equation:

$$E_{eff} = \frac{\sqrt{\pi}}{2}\frac{S}{\sqrt{A_c}} \tag{7}$$

where S is unloading stiffness at maximum load ($S = \frac{dP}{dh}$) and A_c is the projected contact area and E_{eff} is the effective modulus of the material

Table 2
The various mechanical parameters calculated from nanoindentation for the pristine and for the films irradiated at different fluences of 90 MeV Ni ions.

Fluence (ions/cm^2)	Hardness H (GPa)	elastic modulus E_{eff} (GPa)	H/E_{eff}	Depth recovery ratio
Pristine	11.2 ± 0.40	155.5 ± 4.0	0.072 ± 0.001	0.41
1×10^{12}	11.4 ± 0.98	163.3 ± 2.6	0.069 ± 0.006	0.42
3×10^{12}	12.8 ± 0.93	169.4 ± 2.4	0.075 ± 0.006	0.42
9×10^{12}	10.9 ± 0.53	164.4 ± 3.9	0.066 ± 0.003	0.36
1×10^{13}	9.1 ± 0.48	167.4 ± 3.9	0.054 ± 0.003	0.34

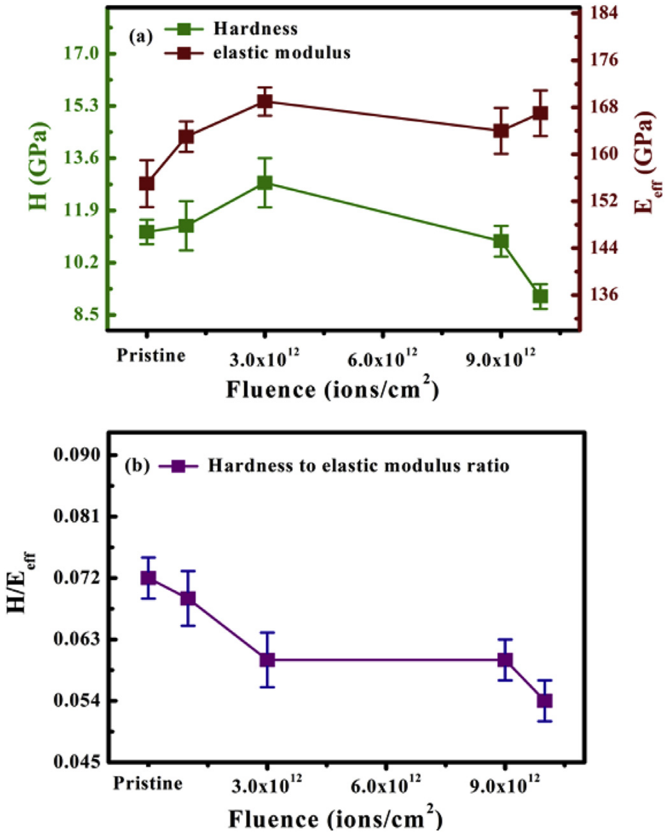

Fig. 7. Variation of hardness and elastic modulus (a), and hardness to elastic modulus ratio (b) with fluences for the pristine and irradiated NiTi thin films.

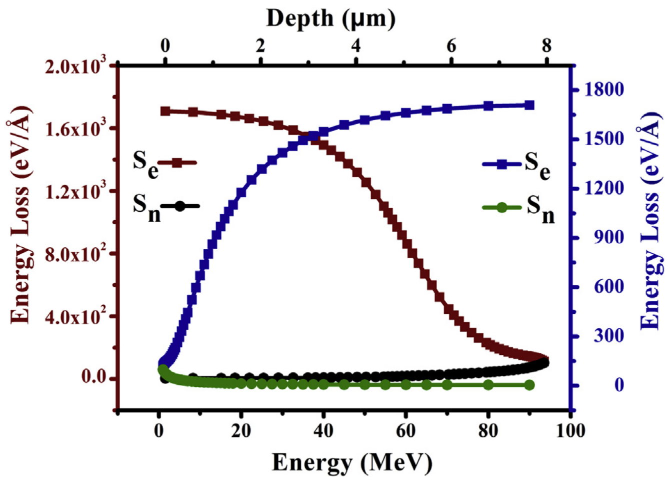

Fig. 8. SRIM simulation, variation of electronic (S_e) and nuclear stooping (S_n) powers with variation in depth and energy for NiTi thin film.

associated to the modulus of elasticity which is given by the following equation:

$$\frac{1}{E_{eff}} = \frac{(1 - \nu_i^2)}{E_i} + \frac{(1 - \nu_s^2)}{E_S} \tag{8}$$

where, subscript i represents the indenter material, and subscript s corresponds to film material and ν represents the Poisson's ratio. The films hardness (H) could be calculated by the following equation:

$$H = \frac{P_{\max}}{A} \tag{9}$$

where, $P_{\max}$ represent the maximum indenter load and A is the projected contact area at that load.

The calculated mechanical properties by nanoindentation measurement are shown in Table 2. The hardness of the NiTi pristine film is 11.26 ± 0.40 GPa and for the irradiated films are found to be 11.40 ± 0.98 GPa, 12.85 ± 0.93 GPa, 10.90 ± 0.53 GPa and 9.18 ± 0.48 GPa respectively. The elastic modulus of the pristine film is 155.57 ± 4.06 GPa and for the films irradiated at different fluence are found to be 163.39 ± 2.62 GPa, 169.4 ± 2.46 GPa, 164.46 ± 3.92 GPa and 167.46 ± 3.9 8 GPa respectively. The obtained values of the elastic modulus at different irradiated fluences follow the same trends as shown by the hardness. It is observed that irradiation has a significant effect on the mechanical behavior of the NiTi thin films. Irradiation of the films up to certain fluences leads to an increase in mechanical strength by grain boundary and dislocation interaction. At low fluences, hardness and elastic modulus of the films increase due to nucleation and propagation of dislocation, but at higher fluence the values of hardness is decreased.

Fig. 7(a)-(b) display the graphs of hardness, elastic modulus and hardness to elastic modulus ratio values versus ions fluences for the pristine and irradiated films. It illustrates that hardness of the NiTi films increase up to the fluences 3×10^{12} ions/cm^2 and after that the hardness of the films decreased with increase the fluences. The films irradiated at the fluences of 9×10^{12} and 1×10^{13} ions/cm^2 exhibit decrease in hardness and elastic modulus values with decreasing in grain size values with fluence. The observed decrease in hardness and elastic modulus values at higher fluence could be attributed to large number of grain boundaries generated by SHI irradiation. As it is reported that the decrease in grain size leads to the large number of grain boundary per unit volume, which enhance the volume fraction of material occupied by the grain boundaries and therefore decrease the hardness of the material [36]. The lower hardness of the films shows the smaller resistance to plastic deformation, i.e., higher tendency toward plastic deformation.

The significant feature to examine the behavior of wear resistance of the films is ascribed by the ratio of hardness to elastic modulus and it is also the major parameter to determine elastic and the elastic-plastic behavior of the films. Xu et al. observed that the deformation around the indenter surface arises due to the sink-in and piling-up and tendency of sink-in increase with increasing the value of H/E_{eff} ratio [37]. The film with higher H/E_{eff} ratio shows the smaller accumulation strain and leading into excellent the wear resistance, while the small value of (H/E) demonstrate more fraction of work consumed in the plastic deformation and more work is required for contracting a material. The NiTi film irradiated at a fluence of 3×10^{12} ions/cm^2 has the higher (H/E_{eff}) value (0.075 ± 0.006). This higher (H/E) value shows the small strain energy and better wear resistance for deformation.

The indentation induced superelastic effect is analysis using load versus depth curves, by the relation [38].

$$\text{Depth recovery ratio}(\delta) = \frac{(h_{\max} - h_r)}{h_{\max}} \tag{10}$$

where $h_{\max}$ is indentation penetration depth at maximum load, and h_r is corresponding to residual displacement when the load returned to zero during indentation withdrawal respectively. The values of depth recovery ratio are increased for the pristine, and the films irradiated up to the fluence of 3×10^{12} ions/cm^2 afterwards it decreases considerably for the films irradiated at fluence 9×10^{12} ions/cm^2 and 1×10^{13} ions/cm^2 as shown in Table 2. The increment in depth recovery ratio could be due to the higher hardness and higher degree of crystallization. However, the decrement is most probable due to lower hardness and irradiation induced defects.

Fig. 8 shows the combine graphs for electronic (S_e) and nuclear (S_n) stopping power versus energy (MeV) and depth for NiTi thin film with composition Ti-57.7 at.%Ni. The variation of S_e and S_n versus energy of the incident 90 MeV Ni ions is simulated by using TRIM 2008 code. The interaction between the incident ions and the target atoms depends upon the energy, mass and charge of the incident ions species. Sufficient energy provided by the incident ions to the target NiTi matrix can cause the significant moment of the atoms and result in the change in structural and phase transformations properties of the films. SHI irradiation deposits it is energy into the materials by two independent processes: one is electronic energy loss (S_e) and second is knows as nuclear energy loss (S_n). In electronic energy loss: ions of indent beam transfer their energy to the electrons of target atoms by inelastic collision and this terms known as the electronic energy loss. Nuclear energy loss: ions of incident beam deposited their energy into the material lattice by elastic collision and produced the significant movement of atoms result in the formation of Frenkel defects (vacancies or interstitial defect) and term knows as nuclear energy loss. In the high energy range (MeV/amu) electronic stopping dominates over the nuclear stopping potential and results in the modifications of material properties. Furthermore, Fig. 8 shows the penetration depth of the incident beam is much larger than the thickness of the films and therefore the incident beam could penetrate the NiTi films and buried into the Si substrate.

4. Conclusions

In the present study, systematic and preliminary investigations on the effect of 90 MeV Ni ions irradiation on the structural, morphological and mechanical behaviours of NiTi thin films have been investigated. NiTi thin films are deposited on Si substrate by dc-magnetron co-sputtering technique. The XRD pattern reveals the existence of both austenite and martensite phases in the films. As the fluence increases, the crystallinity of the films decreases and at higher fluence of 1×10^{13} ions/cm^2 the partial amorphization of the film occurs. Furthermore, AFM study reveals that R_{avg} and R_{rms} values of the NiTi films increase up to a fluence of 3×10^{12} ions/cm^2 due to the ions irradiation induce sputtering effect and after that these values are decreased due to the suppression of both the phases. Nanoindentation measurement has revealed that the film irradiated at a fluence of 3×10^{12} ions/cm^2 exhibit higher hardness, elastic modulus and depth recovery ratio values in comparison of the films irradiated at higher fluences. Significant enhancement in mechanical behavior of nanocrystalline NiTi thin films is observed with ion beam irradiation. Thus, the improved properties of Ni-Ti films pave the way for future MEMS application.

Acknowledgements

Veeresh Kumar is grateful to the Technical Education Quality Improvement Program (TEQUIP), MNIT Jaipur for providing the financial assistantship. The authors acknowledge Mr. Sunil Ojha and Dr. K. Asokan from IUAC, New Delhi, for their valuable suggestion and support during irradiation experiment. The financial support provide by Department of Science & Technology, New Delhi for this research work in terms of DST FAST Young Scientist project (SR/FTP/PS-081/2011) is highly acknowledged. The authors highly acknowledge Dr. M. Gupta, UGC-DAE CSR Indore, for the synthesis of NiTi thin films. The author is also highly acknowledged Dr. Manvendra Kumar, University of Allahabad, Allahabad for nanoindentation characterization. The crew of Pelletron accelerator of IUAC, New Delhi is highly acknowledged for the stable 90 MeV Ni ions beam.

References

[1] J. Van Humbeeck, R. Stalmans, Shape memory alloys, types and functionalities, Encycl. Smart Mater. John Wiley & Sons, Inc., Hoboken, NJ, USA, 2002, pp. 951–964, , https://doi.org/10.1002/0471216275.esm073.

[2] J. Van Humbeeck, Shape memory alloys: a material and a technology, Adv. Eng. Mater. 3 (2001) 837–850, https://doi.org/10.1002/1527-2648(200111)3:11<837::AID-ADEM837>3.0.CO;2-0.

[3] J.J. Gill, D.J. Chang, L.A. Momoda, G.P. Carman, Manufacturing issues of thin film NiTi microwrapper, Sens. Actuators A Phys. 93 (2001) 148–156, https://doi.org/10.1016/S0924-4247(01)00646-X.

[4] H.J. Lee, A.G. Ramirez, Crystallization and phase transformations in amorphous NiTi thin films for microelectromechanical systems, Appl. Phys. Lett. 85 (2004) 1146–1148, https://doi.org/10.1063/1.1783011.

[5] K.T. Oh, U.H. Joo, G.H. Park, C.J. Hwang, K.N. Kim, Effect of silver addition on the properties of nickel-titanium alloys for dental application, J. Biomed. Mater. Res. Part B Appl. Biomater. 76 (2006) 306–314, https://doi.org/10.1002/jbm.b.30369.

[6] V. Kumar, R. Singhal, R. Vishnoi, M.K. Banerjee, M.C. Sharma, K. Asokan, M. Kumar, Ag implantation-induced modification of Ni–Ti shape memory alloy thin films, Radiat. Eff. Defect Solid 172 (2017) 629–642, https://doi.org/10.1080/10420150.2017.1377711.

[7] S. Miyazaki, A. Ishida, Martensitic transformation and shape memory behavior in sputter-deposited TiNi-base thin films, Mater. Sci. Eng. A 273–275 (1999) 106–133, https://doi.org/10.1016/S0921-5093(99)00292-0.

[8] Y. Fu, H. Du, W. Huang, S. Zhang, M. Hu, TiNi-based thin films in MEMS applications: a review, Sens. Actuators A Phys. 112 (2004) 395–408, https://doi.org/10.1016/j.sna.2004.02.019.

[9] Y. Fu, H. Du, W. Huang, S. Zhang, M. Hu, TiNi-based thin films for MEMS applications, (n.d.). https://pdfs.semanticscholar.org/cd80/b10e65a7da79851013269ad1e90f68135b10.pdf (accessed March 10, 2018).

[10] M. Levalois, P. Bogdanski, M. Toulemonde, Induced damage by high energy heavy ion irradiation at the GANIL accelerator in semiconductor materials, Nucl. Inst. Methods Phys. Res. B. 63 (1992) 14–20, https://doi.org/10.1016/0168-583X(92)95160-S.

[11] A.P. Polonica, New possibilities of swift heavy ion implantation in material science and technology, Acta Phys. Pol. A 96 (1999) 239–244 http://przyrbwn.icm.edu.pl/APP/PDF/96/a096z2p06.pdf , Accessed date: 10 March 2018.

[12] S. Kuriakose, D.K. Avasthi, S. Mohapatra, Effects of swift heavy ion irradiation on structural, optical and photocatalytic properties of ZnO-CuO nanocomposites prepared by carbothermal evaporation method, Beilstein J. Nanotechnol. 6 (2015) 928–937, https://doi.org/10.3762/bjnano.6.96.

[13] M. Thakurdesai, A. Mahadkar, V. Bhattacharyya, Study of swift heavy ion irradiation induced nanophases of TiO_2, J. Nano Res. 24 (2013) 133–139, https://doi.org/10.4028/www.scientific.net/JNanoR.24.133.

[14] S. Klaumnzer, M.D. Hou, G. Schumacher, Coulomb explosions in a metallic glass due to the passage of fast heavy ions? Phys. Rev. Lett. 57 (1986) 850–853, https://doi.org/10.1103/PhysRevLett.57.850.

[15] V. Kumar, R. Singhal, Effect of crystallographic orientation on structural and mechanical behaviors of Ni–Ti thin films irradiated by Ag7 + ions, Appl. Phys. Mater. Sci. Process 124 (2018) 328, https://doi.org/10.1007/s00339-018-1746-7.

[16] J. Gierak, Focused ion beam technology and ultimate applications, Semicond. Sci. Technol. 24 (2009) 043001, , https://doi.org/10.1088/0268-1242/24/4/043001.

[17] E. Ozbay, Plasmonics: merging photonics and electronics at nanoscale dimensions, Science (80-.) 311 (2006) 189–193, https://doi.org/10.1126/science.1114849.

[18] N. Afzal, I.M. Ghauri, F.E. Mubarik, F. Amin, Mechanical response of proton beam irradiated nitinol, Phys. B Condens. Matter 406 (2011) 8–11, https://doi.org/10.1016/j.physb.2010.09.040.

[19] X.T. Zu, L.B. Lin, Z.G. Wang, S. Zhu, L.P. You, L.M. Wang, Y. Huo, Influence of electron irradiation on the martensitic transformation of a binary TiNi shape memory alloy, J. Alloys Compd. 351 (2003) 87–90, https://doi.org/10.1016/S0925-8388(02)01080-0.

[20] A.A. Al-Aql, Study of the influence of proton irradiation on the transformation temperature of Nitinol by electrical resistivity measurements, Phys. B Condens. Matter 239 (1997) 345–349, https://doi.org/10.1016/S0921-4526(97)00350-5.

[21] R.M. Oliveira, B.B. Fernandes, F.C. Carreri, J.A.N. Gonçalves, M. Ueda, M.M.N.F. Silva, M.M. Silva, L. Pichon, E.N. Camargo, J. Otubo, Surface modification of NiTi by plasma based ion implantation for application in harsh environments, Appl. Surf. Sci. 263 (2012) 763–768, https://doi.org/10.1016/j.apsusc.2012.09.161.

[22] J.P. Biersack, J.F. Ziegler, The stopping and range of ions in solids, Ion Implant. Tech. Springer Berlin Heidelberg, Berlin, Heidelberg, 1982, pp. 122–156, , https://doi.org/10.1007/978-3-642-68779-2_5.

[23] K. Otsuka, X. Ren, Physical metallurgy of Ti-Ni-based shape memory alloys, Prog. Mater. Sci. 50 (2005) 511–678, https://doi.org/10.1016/j.pmatsci.2004.10.001.

[24] W.O. Adekoya, M.H. Ali, J.C. Muller, P. Siffert, Direct evidence of recrystallization rate enhancement during rapid thermal annealing of phosphorus amorphized silicon layers, Appl. Phys. Lett. 50 (1987) 1736–1738, https://doi.org/10.1063/1.97732.

[25] R.M.S. Martins, N. Schell, H. Reuther, L. Pereira, K.K. Mahesh, R.J.C. Silva, F.M.B. Fernandes, Texture development, microstructure and phase transformation characteristics of sputtered Ni-Ti Shape Memory Alloy films grown on TiN < 111 > , Thin Solid Films 519 (2010) 122–128, https://doi.org/10.1016/j.tsf.2010.07.078.

[26] J.-M. Zhang, F. Ma, K.-W. Xu, Calculation of the surface energy of bcc metals by using the modified embedded-atom method, Surf. Interface Anal. 35 (2003) 662–666, https://doi.org/10.1002/sia.1587.

[27] A. Barbu, A. Dunlop, A. Hardouin Duparc, G. Jaskierowicz, N. Lorenzelli, Microstructural modifications induced by swift ions in the NiTi intermetallic compound, Nucl. Instrum. Methods Phys. Res. Sect. B Beam Interact. Mater. Atoms. 145 (1998) 354–372, https://doi.org/10.1016/S0168-583X(98)00408-X.

[28] N.W. Gregory, Elements of X-ray diffraction, J. Am. Chem. Soc. 79 (1957) 1773–1774, https://doi.org/10.1021/ja01564a077.

[29] A. Kropidłowska, J. Chojnacki, A. Fahmi, B. Becker, In search of molecular precursors for cadmium sulfide-new complexes with a sulfur-rich kernel: cadmium(ii) tri-tert-butoxysilanethiolates with additional diethyldithiocarbamato ligand, Dalton Trans. 2 (2008) 6825–6831, https://doi.org/10.1039/b806248j.

[30] H.S. Zhang, J.L. Endrino, A. Anders, Comparative surface and nano-tribological characteristics of nanocomposite diamond-like carbon thin films doped by silver, Appl. Surf. Sci. 255 (2008) 2551–2556, https://doi.org/10.1016/j.apsusc.2008.07.193.

[31] F.-X. Xiang, X.-L. Wang, S.-X. Dou, Transport evidence for the coexistence of the topological surface state and a two-dimensional electron gas in BiSbTe3 topological insulator, ArXiv Prepr 1404 (2014) 11 doi:10.1002/.

[32] S.A.S. Asif, K.J. Wahl, R.J. Colton, Nanoindentation and contact stiffness measurement using force modulation with a capacitive load-displacement transducer, Rev. Sci. Instrum. 70 (1999) 2408–2413, https://doi.org/10.1063/1.1149769.

[33] V. Králík, J. Němeček, Comparison of nanoindentation techniques for local mechanical quantification of aluminium alloy, Mater. Sci. Eng. A 618 (2014) 118–128, https://doi.org/10.1016/j.msea.2014.08.036.

[34] G.M. Pharr, An improved technique for determining hardness and elastic modulus using load and displacement sensing indentation experiments, J. Mater. Res. 7 (1992) 1564–1583, https://doi.org/10.1557/JMR.1992.1564.

[35] V.I. Rizov, Elastic-plastic response of structural foams subjected to localized static loads, Mater. Des. 27 (2006) 947–954, https://doi.org/10.1016/j.matdes.2005.02.013.

[36] R. Vishnoi, R. Singhal, D. Kaur, Thickness dependent phase transformation of magnetron-sputtered Ni-Mn-Sn ferromagnetic shape memory alloy thin films, J. Nanoparticle Res. 13 (2011) 3975–3990, https://doi.org/10.1007/s11051-011-0321-3.

[37] Z.H. Xu, J. Ågren, An analysis of piling-up or sinking-in behaviour of elastic-plastic materials under a sharp indentation, Philos. Mag. 84 (2004) 2367–2380, https://doi.org/10.1080/14786430410001690015.

[38] R. Vishnoi, R. Singhal, K. Asokan, D. Kanjilal, D. Kaur, Ion irradiation induced modifications of nanostructured Ni-Mn-Sn ferromagnetic shape memory alloy thin films, Thin Solid Films, 2011, pp. 1631–1637, , https://doi.org/10.1016/j.tsf.2011.08.021.

Bio-data

Veeresh Kumar
Research Scholar (Ph. D.)
Department of Physics
Malaviya National Institute of Technology, Jaipur.
Mob: 09897714276, 09694462695
Email: vks8361@gmail.com, 2013rph9002@mnit.ac.in

Academic Qualification:

Exam	Board/University	Division	Passing Year	Percentage/ CGPI	Subjects/Branch
B.Sc.	M.J.P. Rohilkhand University, Bareilly	Second	2005	59.48%	Physics, Mathematics
M.Sc.	M.J.P. Rohilkhand University, Bareilly	First	2009	61.58%	Physics
M.Tech.	National Institute of Technology Hamirpur (H.P)	First	2013	8.17	Materials Science & Engineering
Ph.D.	MNIT, Jaipur	……	pursuing	…….	Physics (Materials Science)

Research Work:

- As a Ph.D student currently working on "**Synthesis and Modification of Shape Memory Alloys Thin Films using Energetic Ions** in Malaviya National Institute of Technology, Jaipur.
- **"Optical studies of pulsed laser deposited ZnO" thin films** in M. Tech. (2011-13)

Academic Achievements:

- GATE -2011: AIR-690 GATE Score-367
- Receiving Institute fellowship for Ph.D. program under TEQIP-II sanctioned by MNIT, Jaipur.

Conferences/Workshops/School/Academic programs attended:

- Attended "**National Seminar on Role of Ion Beam in Materials Science and Acquaintance Programme on Ion Beam Facilities at IUAC New Delhi**" held on 20 Sep. 2013 at Department of Physics, C. C. S. University Meerut.
- Attended short term course on "**Frontier Materials**" held during Aug. 12-17, 2013 at Malaviya National Institute of Technology, Jaipur.
- Attended short term course on "**Nanotechnology and its Application**" held during Oct.7-11, 2013 at Malaviya National Institute of Technology, Jaipur.

- Presented a talk in "**Two days National workshop on Particle Accelerator for Interdisciplinary Research**" held during Feb. 18-19,2014 at Department of Pure &Applied Physics. G. G. V., Bilaspur (C.G).
- Attend National conference on "**Perspectives of physics in multidisciplinary research**" and presented a poster, which was held on 12-13 March 2014 at Department of physics, University of Rajasthan.
- I have attended a National Workshop on **"Advanced Functional Materials (AFM-2014)"** and **presented a poster,** which was held on 5th September 2014 at the Department of Metallurgical & Materials Engineering and Department of Physics, MNIT, Jaipur.
- I have attended a three days International School on "**Simulation of Ion-Beam Irradiation and its Effects**" which was held on 24th-26th October 2015, at Malaviya National Institute of Technology (MNIT) Jaipur organised by Inter University Accelerator Centre, New Delhi and MNIT Jaipur.
- I have attended an International Conference on "**Radiation Effects in Insulators (REI-18)"** and presented a poster, which was held in Hotel Royal Orchid, Jaipur during 26th to 31st October 2015 organized by Inter University Accelerator Centre, New Delhi.
- I have attended a workshop on "**Low energy Ion beam facility (LEIB)**" and presented a poster, which was held on 3th-4th November 2015 at Inter University Accelerator Centre, New Delhi.
- I have attended a national workshop on "**Ion Beam Induced Growth and Engineering of Materials**" which was held on 4-5th March 2016 at Kurukshetra University, Kurukshetra.

Personal Details:

Full name: -	Veeresh Kumar
Date of birth: -	02-07-1985
Sex:-	Male
Father's name: -	Sh. Digvijay singh
Mother's name:-	Smt. Santosh devi
Nationality:-	Indian
Marital status:-	Married
Permanent Address:-	Vill-Badhapur, post- Sharpur Putty Dist. Moradabad (Uttar Pradesh) Pin code: 244602

(Veeresh Kumar)